

ISSN: 0120-1425 • Diciembre de 2021

SERVICIO
GEOLOGICO
COLOMBIANO



volumen **48**
número 2

bg

Boletín Geológico

<https://revistas.sgc.gov.co/index.php/boletingeo>



Boletín Geológico
Vol. 48, n.º 2, 2021
Periodicidad semestral
ISSN impreso: 0120-1425
ISSN digital: 2711-1318
Servicio Geológico Colombiano

Oscar Paredes Zapata
Director general

Mario Andrés Cuéllar
Director de Geociencias Básicas

Marta Lucía Calvache Velasco
Directora de Geoamenazas

Gloria Prieto Rincón
Directora de Recursos Minerales

Hernán Olaya Dávila
Director de Asuntos Nucleares

Humberto Andrés Fuenzalida
Director de Hidrocarburos

Hernando Camargo
Director de Laboratorios

Victoria Díaz Acosta
Directora de Gestión de Información

Servicio Geológico Colombiano
Diagonal 53 n.º 34-53
Bogotá, Colombia
Teléfono: 220 0200, ext.: 3048
boletingeologico@sgc.gov.co

Mario Maya
Editor
Boletín Geológico

Comité editorial

Germán Alonso Bayona Chaparro
Cooperación Geológica Ares
Bogotá – Colombia

Matthias Bernet
Université Grenoble Alpes
Francia

Antoni Camprubí Cano
Universidad Nacional Autónoma de México
México

Iván Darío Correa Arango
Consultor
Medellín – Colombia

Thomas Heinrich Cramer
Universidad Nacional de Colombia
Bogotá – Colombia

Tobias Fischer
The University of New Mexico
Estados Unidos

Carlos Jaramillo
Instituto Smithsonian de Investigaciones
Tropicales
Panamá

John Makario Londoño
Servicio Geológico Colombiano
Manizales - Colombia

María Isabel Marín Cerón
Universidad EAFIT
Medellín – Colombia

Camilo Montes Rodríguez
Universidad del Norte
Barranquilla - Colombia

Héctor Mora Páez
Servicio Geológico Colombiano
Manizales - Colombia

Natalia Pardo
Universidad de los Andes
Bogotá – Colombia

Germán A. Prieto
Universidad Nacional de Colombia
Bogotá – Colombia

Yamirka Rojas Agramonte
Universität Kiel
Alemania

John Jairo Sánchez
Universidad Nacional de Colombia
Medellín – Colombia

Luigi Solari
Universidad Nacional Autónoma de México
México

Carlos Augusto Zuluaga Castrillón
Universidad Nacional de Colombia
Bogotá – Colombia

Corrección de estilo en español
Leonardo Paipilla

Traducción y corrección de estilo en
inglés
Peerwith y American Journal Experts

Diseño y diagramación
Leonardo Cuéllar V.

Diseño GIS
Cristian Hernández

Editora general
Carolina Hernández O.

Foto de cubierta
Parte frontal de una sección delgada
original con textos de Emil Grosse y
fotomicrografía en una sección delgada
de andesita hornbléndica del Cerro Tusa
Fondo: Cerro Tusa, Venecia, Antioquia,
Colombia
Fotografía de Velásquez et al. (2021)

Incluida en los siguientes
índices y bases de datos:

Ulrich
REDIB
GeoRef
Periódica
Google Scholar
Doaj
Sherpa Romeo

Página web:
<https://revistas.sgc.gov.co/index.php/boletingeo>

Esta obra está bajo licencia
internacional Creative Commons
Reconocimiento 4.0

Impresión
Imprenta Nacional de Colombia
Carrera 66 N.º 24-09



PBX: 457 8000
www.imprensa.gov.co
Bogotá, D. C., Colombia

Diciembre, 2021



CONTENIDO

- 3** Editorial
Mario **Maya**
- 7** Historical memory of the geology of Antioquia: Emil Grosse and The Carboniferous Tertiary of Antioquia
Memoria histórica de la geología antioqueña: Emil Grosse y El Terciario Carbonífero de Antioquia
Felipe **Velásquez Ruiz**, Marion **Weber Scharff**, Verónica **Botero Fernández**
- 41** Analytical solution of CO₂ mass flux measurement with Non-Dispersive Infrared sensors for soil in diffusive and advective-diffusive regime: Tool for the continuous and telemetric measurement of volcanic gases in an open chamber
Solución analítica de la medida de flujo de CO₂ con sensores infrarrojos no dispersivos para suelo en régimen difusivo y advectivo-difusivo: herramienta para la medida continua y telemétrica de gases volcánicos en cámara abierta
Nicolás **Oliveras**
- 61** The role of Rare Earth Elements in the deployment of wind energy in Colombia
El papel de los elementos de tierras raras en el despliegue de la energía eólica en Colombia
Carlos Andrés **Gallego**
- 81** Geological modeling of a hydrocarbon reservoir in the northeastern Llanos Orientales basin of Colombia
Modelamiento geológico de un yacimiento de hidrocarburos ubicado al noreste de la cuenca de los Llanos Orientales de Colombia
Laura Juliana **Rojas Cárdenas**, Indira **Molina**
- 95** Relevant aspects to the recognition of extensional environments in the field
Aspectos relevantes para el reconocimiento de ambientes extensionales en campo
Ana Milena **Suárez Arias**, Julián Andrés **López Isaza**, Anny Julieth **Forero Ortega**, Mario Andrés **Cuéllar Cárdenas**, Carlos Augusto **Quiroz Prada**, Lina María **Cetina Tarazona**, Oscar Freddy **Muñoz Rodríguez**, Luis Miguel **Aguirre Hoyos**, Nelson Ricardo **López Herrera**

- 107** Yuruma Formation (Barremian - lower Aptian?) In the Yuruma hill and Punta Espada, Alta Guajira, Uribia, Colombia
Formación Yuruma (Barremiano – Aptiano inferior?) en el cerro Yuruma y Punta Espada, Alta Guajira, Uribia, Colombia
Pedro **Patarroyo**
- 131** Seismic hazard assessment of the urban area of Ambato, Ecuador, in deterministic form
Evaluación de la peligrosidad sísmica del área urbana de Ambato, Ecuador, en forma determinística
Roberto **Aguar Falconi**, Paola **Serrano Moreta**
- 147** Editorial Policy
- 149** Instructions to Authors

EDITORIAL

Boletín *Geológico* published issue 48(2) in December 2021, with the following articles (Figure 1):

Velásquez et al. from *Universidad Nacional de Colombia, Facultad de Minas*, Medellín, present the *Terciario Carbonífero de Antioquia* (TCA), published by Dr. Jakob Emil Grosse in 1926, one of the most relevant classic works of Colombian geology in the first half of the XX century, in which its rigorous execution, excellent field control, and meticulousness in petrological and structural analyses stand out as one of the most valid and influential classic works, mainly for studies involving regional geology and economic geology.

Oliveras, Colombian consultant, presents two analytical solutions to measuring the carbon dioxide (CO₂) mass flux in a volcanic environment. CO₂ mass flux must be measured continuously and telemetrically to obtain a better understanding of the dynamics of volcanic degassing processes, contributing to the creation of a volcano behavioral model.

Gallego, from *Servicio Geológico Colombiano*, Bogotá, assesses the mineral demand in Colombia in the 2020-2050 period for the rare earth elements embedded in the deployment of wind power technologies in four different climate policy scenarios to establish whether they could face geological bottlenecks that could ultimately hamper the transition to a low-carbon economy.

Rojas and Molina, from *Universidad de los Andes*, Bogotá, characterize a hydrocarbon reservoir of two fields in the Carbonera Formation within the Llanos Orientales Basin of Colombia. This was conducted using well logs, the structural surface of the regional datum of the area, segments of the Yuca Fault and a local fault in the reservoir, the permeability equation, and J functions of the reservoir provided by the operating company.

Suarez et al., from *Servicio Geológico Colombiano*, Bogotá, propose a methodology for the recognition of extensional environments that integrates prefield photogeological interpretation, the establishment of a systematic process for data acquisition and structural analysis with a stereographic projection grid. Additionally, some basic concepts for the description and understanding of the structures and the mechanisms that generate them are included.

Patarroyo, from *Universidad Nacional de Colombia*, Bogotá, presents data on the lithostratigraphy, nomenclature and biostratigraphy of the Yuruma Formation at its type locality, as well as nearby outcrops located to the north in Punta Espada, Guajira Department, Colombia.

Aguiar and Serrano, from *Universidad de las Fuerzas Armadas ESPE* and *Universidad Laica Eloy Alfaro*, Ecuador, examine six models with strong motion equations. They determined the average spectra for soil profiles and proposed new spectral forms for the urban area of the city of Ambato.

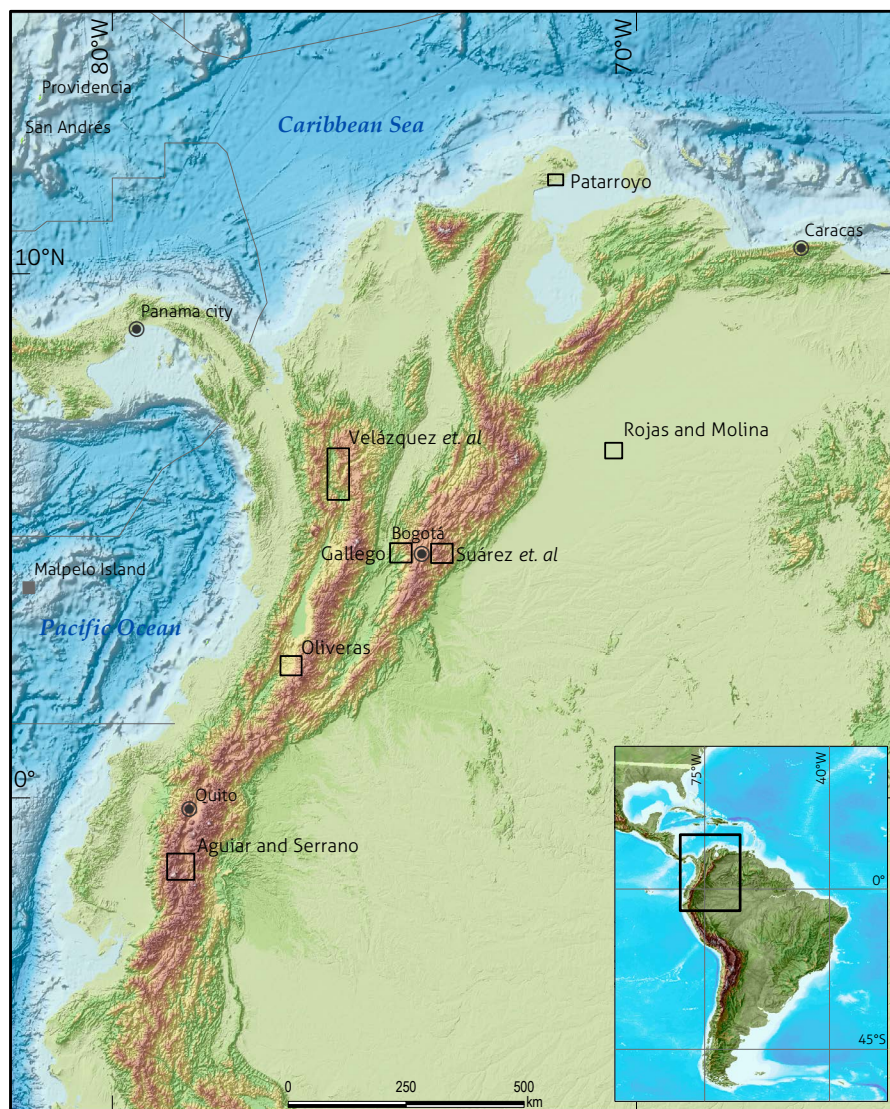


Figure 1. Location of the areas with contributions presented in *Boletín Geológico*, 48(2), 2021

Boletín Geológico acknowledges the collaboration of the following reviewers and their commitment to the peer-review process involved in this issue:

Agnes Mazot - GNS Science, New Zeland

Alejandra Tironi - Universidad Nacional del Centro de la Provincia de Buenos Aires, Argentina

Alejandro Beltrán - Universidad EAFIT, Colombia

Andrés Cárdenas - Universidad EAFIT, Colombia

Ángel Nieto Samaniego - Universidad Nacional Autónoma de México, México

Angélica Triana – Universidad Externado de Colombia y Universidad de los Andes, Colombia

Beatriz Aguirre - Universidad de Buenos Aires, Argentina

Berenice Solis - Universidad Nacional Autónoma de México, México

Camila Marques dos Santos - Centro de Desenvolvimento da Tecnologia Nuclear, Brazil
Camilo Ordóñez - Universidade Federal do Rio de Janeiro, Brazil
Carlos Guzmán - Universidad de Caldas, Colombia
Carlos Mario Echeverri - Universidade Federal Campina Grande, Brazil
César Mora - Cuencas Consultores, Colombia
Diana Ortega - Universidad EAFIT, Colombia
Fernanda Cravero - Centro de Tecnología de Recursos Minerales y Cerámica, Argentina
Gabriel París – Consultant, Colombia
Georgina Ibarra - Universidad Nacional Autónoma de México, México
Gustavo Hincapié - Universidad de Caldas, Colombia
Jorge López – LOGEA, Colombia
Leandro Rodríguez - Centro Regional de Sismología para América del Sur (CERESIS), Perú
Leda Sánchez Bettucci - Universidad de la República, Uruguay
Marcelo Assumpção - Universidad de Sao Paulo, Brazil
María Isabel Marín - Universidad EAFIT, Colombia
Mariana Jácome - Universidad Nacional Autónoma de México, México
Nelly Piragauta – Consultant, Colombia
Verónica Vennari – IDEVEA (UTN-CONICET), Argentina

Mario Maya
Editor

Boletín Geológico
boletingeologico@sgc.gov.co



Farallones de la Pintada, La Pintada, Antioquia, Colombia
Fotografía de Velásquez et al. (2021)



This work is distributed under the Creative Commons Attribution 4.0 License.

Received: February 24, 2021

Revision received: July 12, 2021

Accepted: July 24, 2021

Published on line: September 24, 2021

Historical memory of the geology of Antioquia: Emil Grosse and The Carboniferous Tertiary of Antioquia

Memoria histórica de la geología antioqueña: Emil Grosse y El Terciario Carbonífero de Antioquia

Felipe Velásquez Ruiz¹, Marion Weber Scharff², Verónica Botero Fernández²

1. Department of Geology and Millenium Nucleus for Metal Tracing along Subduction, FCFM, Universidad de Chile, Santiago, Chile.

2. Department of Geosciences and Environment, Universidad Nacional de Colombia, Medellín, Colombia.

Corresponding author: Felipe Velásquez, fevelasquezru@gmail.com

ABSTRACT

The Carboniferous Tertiary of Antioquia (TCA), published by Dr. Jakob Emil Grosse in 1926, is one of the most influential scientific results of the Ordinance 16 of 1918 of the Honorable Departmental Assembly of Antioquia. The work began with the main objective of quantifying the coal reserves of Antioquia, and showing their surface extension on a scale of 1:50 000, in a region that includes the Arma river to the Puente de Occidente and from the western side of the Cauca River to the Romeral lineament and the plains of Ovejas. As a result, extensive work comprising petrological, structural, and economic geology studies was published in a manuscript published in Spanish and German, plus four attached maps, including coal, gold, silver, kaolin, and carbonate mines, among others. In the present work, the four TCA maps were digitized at a scale of 1:50 000 with Bessel 1841 datum and created a unified file in .kml format, which can be used directly in field trips, via Google Earth on cell phones, tablets, or computers. The metadata associates the information in the TCA with the Servicio Geológico Colombiano for the year 2015. In addition, 480 thin sections were scanned, which were donated by Dr. Grosse to the Escuela Nacional de Minas and today are in the Museum of Geosciences of the Faculty of Mines of the Universidad Nacional de Colombia. The geospatial information contained in each thin section was interpreted and georeferenced, obtaining, as a result, a list with north and west geographic coordinates, in degrees, minutes, and seconds. This unpublished information is available in the supplementary material of this article. Finally, nine field trips were made to the places referenced in 23 photographs of the TCA between 1920 and 1923 to take their current equivalent and thus carry out a multi-temporal analysis of the TCA.

Keywords: Amagá Formation, geological heritage, museum of geosciences, Colombia.

RESUMEN

El Terciario Carbonífero de Antioquia (TCA), publicado por el Dr. Jakob Emil Grosse en 1926, es el resultado geocientífico más influyente de la Ordenanza 16 de 1918, de la Honorable Asamblea Departamental de Antioquia. El trabajo se comenzó con el objetivo principal de cuantificar las reservas de carbón del departamento y mostrar su extensión superficial en un mapa en escala 1:50 000, para la región comprendida desde el río Arma hasta el puente de Occidente y desde la margen oriental del río Cauca hasta la cuchilla del Romeral y los llanos de Ovejas. Como resultado, se publicó una extensa obra que comprende estudios petro-lógicos, estructurales y de geología económica, en un manuscrito publicado en español y alemán, más cuatro mapas adjuntos, en los cuales, además del carbón, también se cartografiaron las minas de oro, plata, caolín, carbonatos, entre otros. En el presente trabajo, se digitalizaron los cuatro mapas del TCA en escala 1:50 000, con datum Bessel 1841, y se creó un archivo unificado en formato .kml, el cual puede ser usado directamente en campo, vía Google Earth, mediante celular, tablet o computador, y cuyos metadatos asocian la información del TCA con su equivalente del Servicio Geológico Colombiano del año 2015. Además, se escanearon 480 secciones delgadas, que pertenecen a las colecciones patrimoniales del Museo de Geociencias de la Facultad de Minas, de la Universidad Nacional de Colombia. La información geoespacial contenida en cada lámina se interpretó y se georreferenció, obteniendo como resultado un listado con coordenadas geográficas norte y oeste, en grados, minutos y segundos, información inédita y disponible en el material suplementario del presente artículo. Finalmente, se realizaron 9 salidas de campo a los lugares referenciados en 23 fotografías del TCA entre 1920 y 1923, para registrar su equivalente actual y de este modo realizar un análisis multi-temporal del TCA.

Palabras clave: Formación Amagá, patrimonio geológico, museo de geociencias, Colombia.

1. INTRODUCTION

In 1918, the Honorable Departmental Assembly of Antioquia established that the governor's office would have the geographical and geological charts and maps of the department drawn up and published, per Ordinance No. 16 of April 6, 1918, for which a board called the Junta del Mapa de Antioquia (Zuluaga et al., 2005) was created. As a consequence of this ordinance, and by recommendation of the Antioquia Railroad, the Escuela Nacional de Minas, the mining company El Zancudo and some private individuals, Dr. Robert Scheibe, professor at the Technical School of Charlottenburg, was asked to lead the project. Among several difficulties, Dr. Scheibe listed that there was a lack of topographic material and scientific base material, and the problem of the mountainous configuration of the terrain, with inaccessible virgin forest areas, to carry out the requested assignment effectively.

Thus, on the recommendation of Dr. Scheibe and Dr. Juan de la Cruz Posada, professor at the Escuela Nacional de Minas in Medellín at that time (Posada, 1936), Dr. Jakob Emil Grosse, a student of Professor Scheibe in Charlottenburg (Germany), was hired to quantify the coal reserves and show their surface extent on a 1:50 000 scale plan, mainly for the Antioquia Railway project. In this way, Dr. Grosse produced a classic book of

Antioquian geology, *The Carboniferous Tertiary of Antioquia* (TCA) (Grosse, 1926), with four associated maps at 1:50 000 scale (Figure 1), for the region between the Arma River and the West Bridge, from the eastern bank of the Cauca River to the Romeral cleaver and the Ovejas plains.

Few studies of this type were carried out prior to the TCA in the carboniferous zone of Antioquia. Nevertheless, there are some geological records on the western foothills of the Central Cordillera. For example, in 1831, the Frenchman Boussingault contributed to understanding the Heliconia salt flats. Likewise, around 1834 and 1860, the Germans Reinhold and Degenhardt studied the regions of Titiribí, Amagá, and Heliconia, and the rector of the Escuela Nacional de Minas at that time, Tulio Ospina, before he died in Panama in 1921, wrote one of the first reviews on Colombian geology (Grosse, 1926). These works contributed significantly to the knowledge of the geology of that region, although there was still a lack of detailed topographic, geological, and structural geological information. In turn, Dr. Robert Scheibe made in 1919 a first draft with geological information of the area, which served as a guide to the map made later by Dr. Grosse (Castro, 2018), although the information was not published due to his death in early 1923 in Bogotá.

Thus, in two years in the field and with one assistant, three laborers, three saddle mules, and five pack mules, Dr. Grosse

faced the task of the Honorable Departmental Assembly. As a final result, the coal reserves were quantified and the mines of gold, silver, kaolin, carbonates and other industrial minerals were mapped. From this work, 480 rock samples and thin sections of rocks are kept in the Faculty of Mines of the Universidad Nacional de Colombia, Medellín, which are currently part of the Faculty Petrographic Collection of the Museum of Geosciences.

Since then, Dr. Grosse's geological collection has had to face the passage of time, with various periods of affectation that reflect the history of the collections of the Faculty of Mines. The present work aims to update the information of the geological and geo-spatial sampler of the four maps, thin sections, and photographic records of the TCA, showing it in an unpublished and open access way utilizing the supplementary material associated with the manuscript.

2. METHODS

2.1. Digitization of the TCA maps

The cartographic base of the TCA is composed of four maps at a scale of 1:50 000 (Figure 1a), which cover the central zone of plates 130, 146, and 166 (at a scale of 1:100 000) of the Instituto Geográfico Agustín Codazzi (IGAC, 2004, 2005a, 2005b). The legend located on map 4 of the TCA does not specify the coordinate system used and only refers to the fact that "Dr. Emil Grosse and Ing. Tulio Arbeláez G. have made a topographic base of the map (Grosse, 1926)". In addition, the company where the maps were produced and printed is named: "Berliner Lithogr. Institut. Julius Mosen, Berlin W35, Posdamersir 110 engraving and printing". Taking into account the above, the Bessel projection (1841), which was widely used in the late 19th and early 20th century, was used for digitizing these maps. In the process of digitalization and transformation of datums, it was observed that, for the World Geodetic System (WGS 84) projection system, the polygons in ArcGIS with Bessel 1841 datum present an offset of 37 km to the E and an areal decrease of approximately 45-50%, specifically for the central zone of Antioquia. Subsequently, the files generated in .shp format were transformed to .kml format to visualize the layers in Google Earth. At the same time, to corroborate that the digitized information effectively coincided with the relief of the area, the

geomorphology of the Cauca river was used, which presents different meanders for the TCA area, facilitating a refinement of the transformed version of the unified map. As a result, from the four initial 1:50 000 scale maps with Bessel 1841 datum of the TCA, a generalized map was created in .kml format (Figure 1b; Supplementary Material 1), which can be used directly in the field, via Google Earth, through cell phone, tablet or computer. To complement the digitization of the generalized map of the TCA, we proceeded to elaborate its current equivalent, based on the Geological Map of Antioquia (González, 1999), its explanatory memory (González, 2001), and the geology and metadata of the Geological Map of Colombia (Gómez et al., 2015). The extracted polygon was also generated in .kml format (supplementary material 2).

2.2. Cataloguing, transcription and georeferencing of TCA thin sections

The Museum of Geosciences of the Faculty of Mines of the Universidad Nacional de Colombia, Medellín, contains part of the hand samples and thin sections of the TCA. In the present research project, the thin sections were specifically cataloged and transcribed. The TCA rock flakes collection comprises 480 thin sections, of which 456 were analyzed because the remaining 24 flakes were in poor condition. The plates were produced by the German company Voigt & Hochgesang of Göttingen, and contain information from three different inventories (Figures 2a and 2b): the first one associated with Emil Grosse's personal catalogue, located at the top right of each plate; a second inventory copied in red, at the top and bottom of each plate, possibly associated with an inventory of the Escuela Nacional de Minas; and an inventory corresponding to the Universidad Nacional de Colombia, with the numbering located at the front of each plate (Figure 2b). In addition to the inventories, the plates contain Grosse's lithological classification, located at the top of the slide of each specimen, and the description of the location, located at the bottom of each thin section. Subsequently, the location of each slide was interpreted to associate them with IGAC plates 130, 146, and 166 and to generate the current coordinates in the WGS 84 system. As a result, an updated layer of sampling points was obtained for each specimen collected by Grosse in the TCA, available in .kml format and associated with supplementary material 3 of this paper.

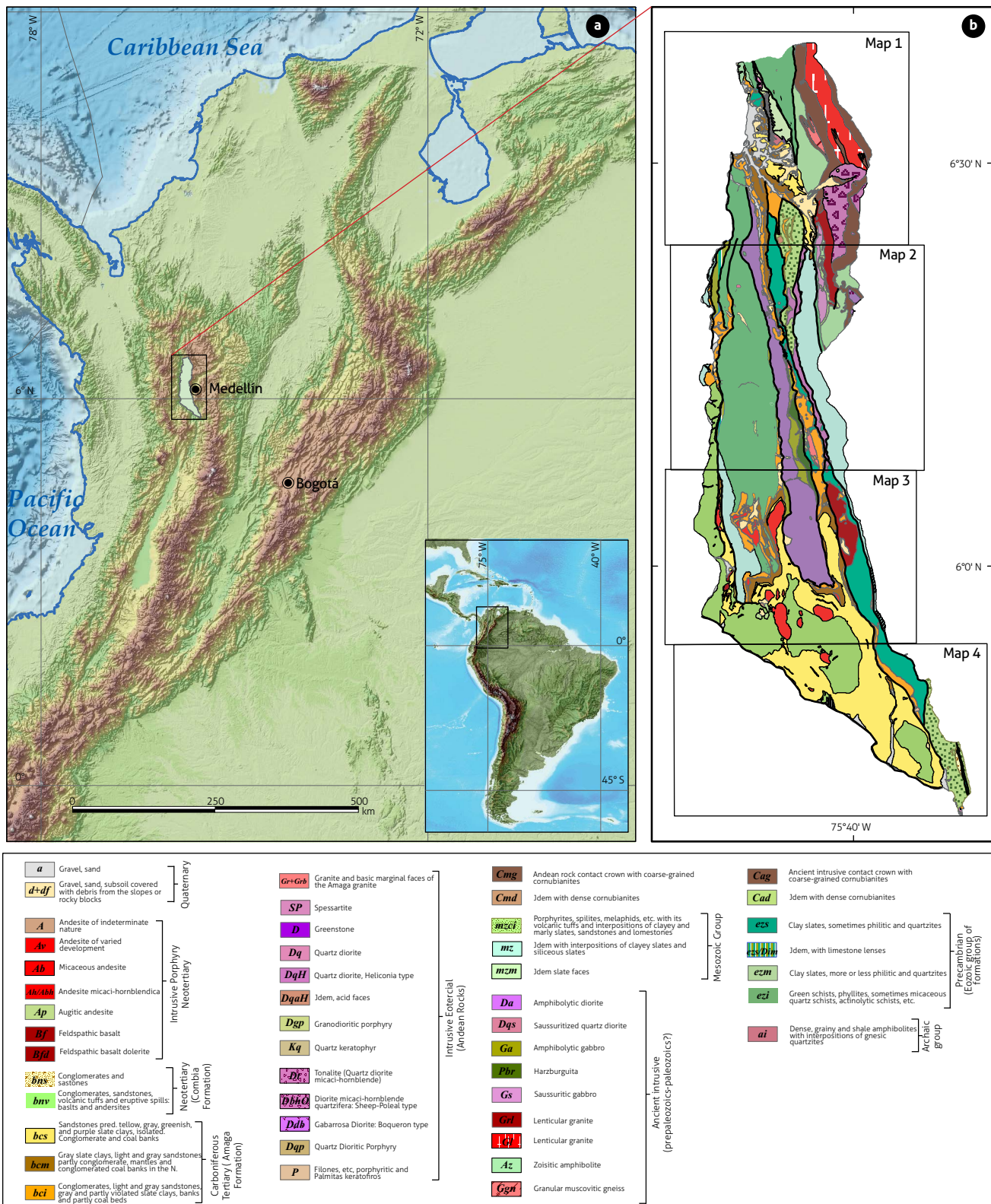


Figure 1. a) General tectonic framework and configuration of the four TCA maps; b) Digitized geological map of the TCA (Grosse, 1926) in the WGS 84 system (Supplementary Material 1)

2.3. Fieldwork and multi-temporal analysis of TCA images

As a complement to the cartographic and petrographic work, we took nine field trips to the referenced locations of 23 photographs recorded by Dr. Grosse in the TCA between 1920 and 1922 to show geoforms, lithologies, and overthrusts (fault zones for Grosse). To georeference them, the location des-

cribed in the legends of the samples was interpreted, and their respective north and west coordinates in the WGS 84 system were generated. To corroborate that the information was reliable, the points were refined in the field. A current photographic record was taken of the landscape images reported in the TCA to show some significant changes in the landscape over a century.

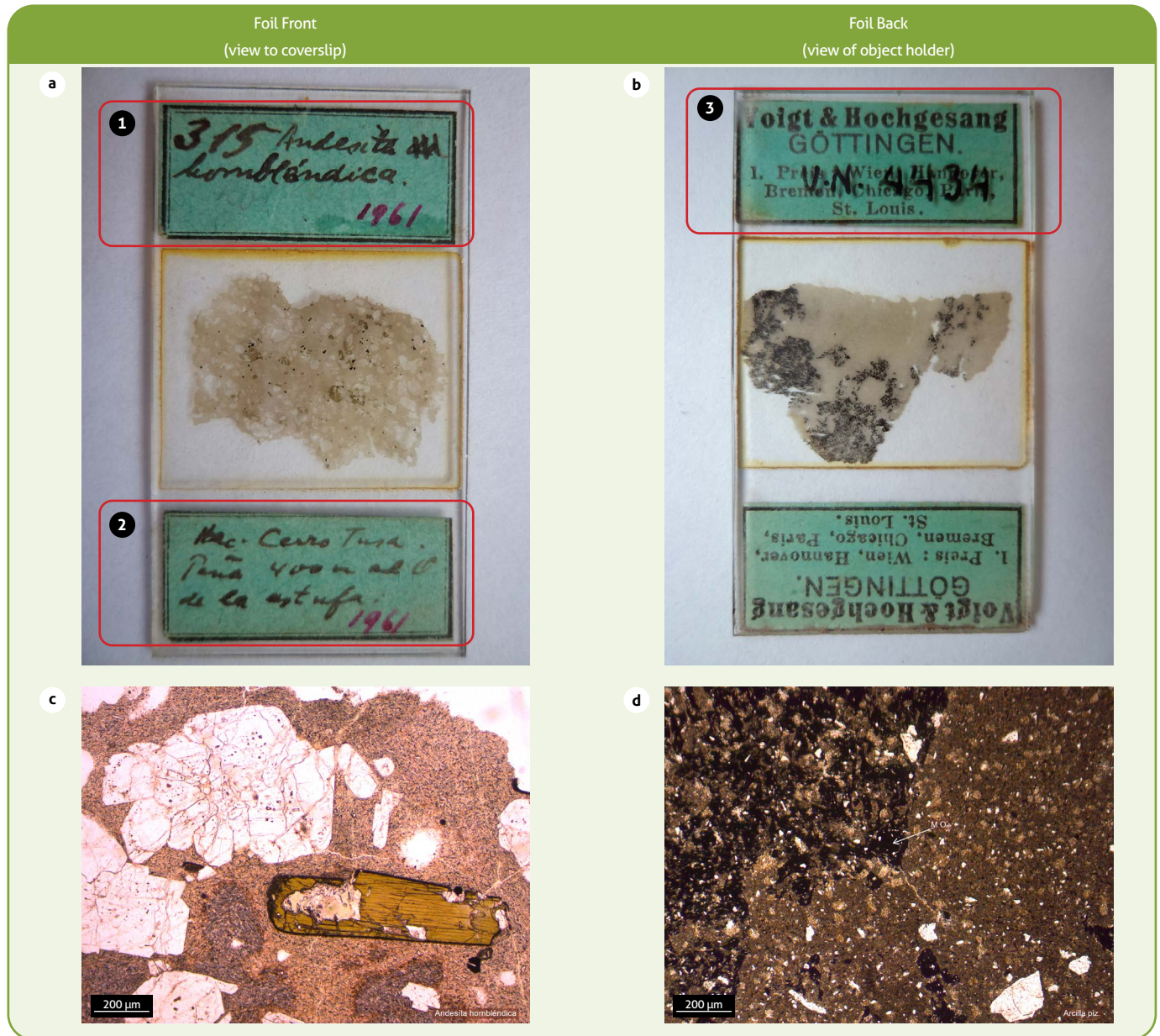


Figure 2. a) Front part of an original thin section specimen from the TCA with 1) Grosse's numbering, lithological classification of the specimen, and numbering of the Escuela Nacional de Minas; 2) Location of the specimen; b) Front part of the thin section with the name of the German factory Voigt & Hochgesang, Göttingen and 3) Catalogue of the Universidad Nacional de Colombia; c and d) are photomicrographs of the thin section in a and b, classified as hornblende andesite, located in Cerro Tusa, and a clay (arcillolite) with organic matter from the Amagá Formation, respectively.

3. RESULTS AND DISCUSSION

3.1. Map of the TCA, a current look at a classic work of cartography

The TCA maps have been, since their production, a classic work of geological reading and bibliographic analysis for the western zone of influence of the Central Cordillera, involving key lithostratigraphic units for the understanding of pre- and post-Andean evolution such as the Cajamarca Complex, the Quebradagrande Complex, and the Combia Formation, among others (c.f. Blanco-Quintero et al., 2014; Maya and González, 1995; Weber et al., 2020). Furthermore, this work also has relevance in the tectonic framework of the area because the work details in detail the Cauca-Romeral fault system, where Grosse approaches with fault mapping and satellite systems, named at the time as *overthrust*, from the German word *Überschiebung*, where "Über" means "over" (e.g., Romeral, San Jerónimo, Cauca E, etc.), mapped simultaneously with the topographic survey, and since then they have been the basis for the tectonic understanding of the area in several works of geodynamics and terrain (c.f. Cediel et al., 2003; Etayo-Serna et al., 1983; Restrepo and Toussaint, 2020; Toussaint and Restrepo, 2020).

On the other hand, one of the mining-economic implications was the mapping of small-scale *pits* and *pits* of metallic and non-metallic projects, such as gold, silver, kaolin, carbonates, among others. These later had a revolution in terms of exploration and mining in the middle belt of Cauca (Sillitoe, 2008), specifically in the polymetallic Au-Ag-Cu deposits, such as Buriticá, Cerro Vetas, La Mina and Nuevo Chaquiro, among others (Bartos et al., 2017; Lesage et al., 2013). Thus, since 1921, where coal was the focus of the TCA because of its strategic nature, the TCA maps became the geological basis par excellence for the lithological, structural, and mining understanding of the area.

In the geographic context, the four TCA maps cover the western end of the Central Cordillera of Colombia, between the Arma River in the south to the municipality of Olaya in the north, and between the Cauca River in the west to the Romeral cleaver range and the plains of Ovejas to the east. The studied zone covers an area of approximately 106 km long and 24 km wide (Figure 1a), configured in a south-north direction as follows: (1) Poblano plate, from 5° 41' 22"N bordering the Arma River, to 5° 53'54"N south of the municipalities of Venecia and Fredonia, between 75° 38'37"W and 75° 49'25"W; (2) Titiribí plate, between 5° 53'54"N south of the municipalities of Venecia and

Fredonia, to 6° 07'05"N south of the municipalities of Armenia and Angelópolis, from 75° 39'16"W and 75° 51'30"W; (3) Heliconia plate, between 6° 23'07"N south of the municipality of San Jerónimo and 6° 07'05"N south of the municipalities of Armenia and Angelópolis, in between 75° 37'26"W to 75° 51'54"W and; (4) Sopetrán plate, from 6° 23'07"N south of the municipality of San Jerónimo to 6° 39'00"N in the municipality of Olaya (formerly Sacaojal), between 75° 31'14"W and 75° 48'56"W.

Since its creation, the Bessel ellipsoid (1841) has been widely used in geodesy. Its function is based on various meridian arcs and data from continental geodetic networks of Europe, Russia and India's British Survey. In the early 20th century, such an ellipsoid was probably used by Emil Grosse for the production of the TCA maps. However, unfortunately, it is not accurately confirmed in Emil Grosse's cartographic information. On map 4 where the legend is reported, it is stated that "the topographic base of the map has been surveyed by Dr. Emil Grosse and Ing. Tulio Arbeláez G." (Grosse, 1926), without any additional information, and for this reason, in the present work the four TCA maps were digitized in that ellipsoid to WGS 84 datum, resulting in a unified map available in .kml format for viewing in Google Earth. The final map projected to WGS 84 was spatially and areally optimal. For example, the silhouette and meanders of the Cauca River conform to the western edge of the map (Figure 3), and likewise, the Romeral blade conforms to the eastern side of the map.

The TCA map has not undergone significant cartographic modifications in mapping lithologic units or mapping regional and local faults. However, the changes have been modifications in the definition of lithostratigraphic units and radiometric ages, partly due to the evolution of geochronological techniques. The most significant changes occurred in metamorphic and intrusive igneous rocks of the pre-Cenozoic age. For example, for the metamorphic rocks east of the Sopetrán and Romeral overthrusts (e.g., Romeral fault system), Emil Grosse separates contact aureoles (coronas in the original text), slates, and graphitic schists into independent units, while the three units are united in what is now called the Cajamarca Complex (González, 2001). A second example is found in the "Carboniferous Tertiary of Antioquia" concept, now called the Amagá Formation (González, 2001).

On the other hand, the most significant advance in geological knowledge in the TCA area is the radiometric ages of the pre-Cenozoic lithostratigraphic units. Results from U-Pb, Sm-Nd, and Ar-Ar dating have shown that the ages of the li-

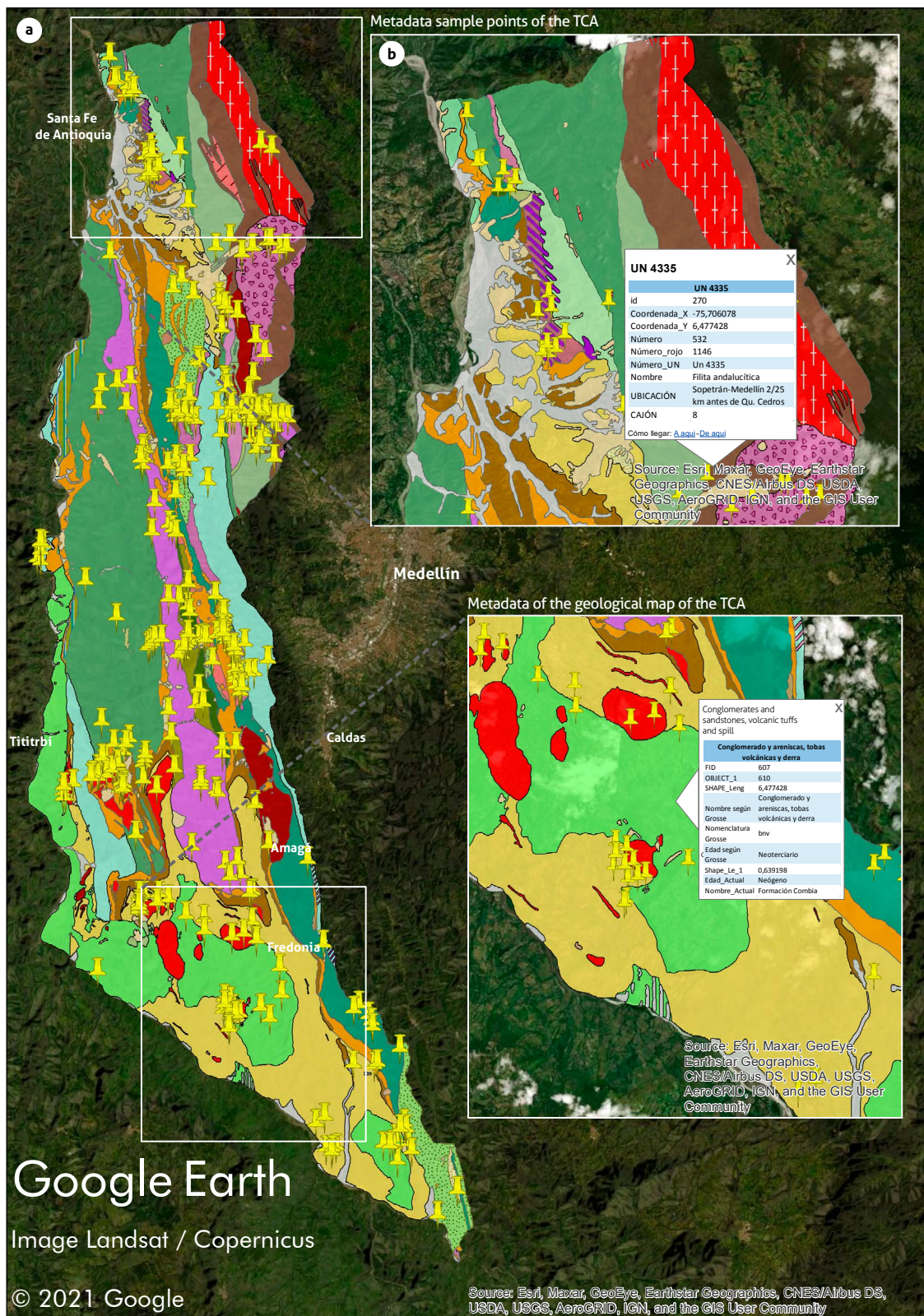


Figure 3. a) View of the geological map of the TCA in .kml format, in the Google Earth platform, with the location of the 456 cataloged and georeferenced rock thin section samples; b) Detailed metadata information of each thin section, showing the N and W coordinates, its numbering in the three different catalogs, name of the sample and location described by Dr. Grosse.

thostratigraphic units of the TCA range from 300 Ma to the Quaternary (Gómez et al., 2015), while for Grosse, the Cajamarca Complex, the Arquía Complex, the Sucre Amphibolites, the Sinifaná Metasedimentites, and the Angelópolis Ultramafites are assigned a Precambrian age (Grosse, 1926), following the recommendations of Dr. Robert Scheibe and his unpublished geological sketch of the area. This is because radiometric dating only had a profound development after World War II (White, 2013).

In the early 1920s, without the availability of radiometric dating and with an incipient advance on palynological studies at that time, Emil Grosse assigned an Eotertiary age to the Amagá Formation, an age approximate to those suggested by Van der Hammen (1958), who assigned a Middle Oligocene age to the Lower Member, based on palynomorphs found in claystones and coals, while Eocene palynomorphs are reported by Londoño et al. (2013) and Ramírez et al., (2015), proposing a middle to upper Eocene depositional interval for the Lower Member and middle to late Miocene age for the Upper Member. However, the age of the Amagá Formation remains controversial, and for example, Montes et al. (2015) and Lara et al. (2018) assign an age between ca. 15-13 Ma for the end of the Amagá Formation deposition. Similarly, Grosse assigned a Neotertiary age to the Combia Formation, which is temporally similar to the Miocene ages obtained by González (2001), Jaramillo et al. (2019), and

Weber et al. (2020). For this reason, the Grosse ages and the updated ages were taken into account to generate the metadata of the digitized layers, as shown in Figure 3.

3.2. Catalogue and interpretation of TCA thin sections

The geological sample collection of the TCA comprises hand specimens and thin sections, which were distributed among three academic institutions, including 1) the collection of the Royal Technical High School in Charlottenburg (Berlin Academy of Mines); 2) the Geological Institute of the University of Bonn and 3) the sample collection of the Escuela Nacional de Minas in Medellín, nowadays at the Faculty of Mines of the Universidad Nacional de Colombia in Medellín. For the thin section collection, a complete catalogue of the rock specimens was made, and thus, the information contained in the written part of the plates was transcribed (Figures 2a and 2b; Table 1). The collection of plates comprises 480 specimens, of which 456 are in good condition for petrographic analysis. The Emil Grosse collection was used for teaching until the 1990s at the University, and it is possible that this meant losses over time; furthermore, thin sections were not made for all hand specimens. On the other hand, the numbering of the 480 specimens assigned by Dr. Grosse for each plate ranges from number 1 to number 628, plus 7 alphabetically numbered plates; thus, to date, about 75% of the initially donated plates are preserved.

Table 1. Transcription translation to English, and interpretation of the TCA thin sections donated by Grosse to the Escuela Nacional de Minas

Sample No. (E. Grosse numbering, located at the top left)	Sample No. (located at the bottom right, in red)	Sample No. in UN catalog (located at the top of the section)	Transcription of the sample description by E. Grosse (i.e. upper thin section box).	Transcription of the location of the rock sample (i.e. bottom box of the thin section)	Interpretation of the north coordinate, based on the location description	Interpretation of the west coordinate, according to the location description
1	1798	N.A.	Candela Mountains. Hornblende augitic andesite	Hac. La Suiza; Block in the sleeve of the m	06° 04' 16,11"	75° 48' 16,37"
2	1796	UN 4422	Candela Mountains. Gabarro granite in the andesite	Hac. La Suiza; Block in the sleeve of the m	05° 54' 35,11"	75° 48' 29,29"
4	1756	UN 4406	Corcobado. Hornblende Andesite	1300 m S of Porvenir	05° 52' 54,41"	75° 42' 12,20"
5	1795	N.A.	Hornblende Andesite. Candela Mountains	La Suiza, blocks in the sleeve of the m	N.A.	N.A.
6	1759	UN 4409	Corcobado, Andesita hornblende	1200 m S of Porvenir. From the contact	05° 53' 14,49"	75° 42' 21,16"
8	1771	UN 4412	Arc. Piz. Modules at 5 cm from the contact	1200 m S of Porvenir	05° 52' 37,99"	75° 41' 54,71"
9	1790	UN 4419	Corcobado. Arc piz. Stained	550 m SW of Porvenir	05° 53' 22,23"	75° 42' 36,42"
10	1772	UN 4413	Corcobado. Arc. Piz. Modulated 20 cm	1200 m S of Porvenir	05° 52' 48,69"	75° 42' 39,26"
11	1774	UN 4415	Corcobado. Arc piz. Modulated 1 m from the contact	1200 m S of Porvenir C° to Cauca (sic.)	05° 52' 31,88"	75° 42' 19,41"

Missing numbers were specimens donated to other national and international academic institutions. Supplementary Material 4 presents detailed information on the 456 cataloged plates.

The information contained in the plates was transcribed as it appears in each specimen (i.e., *sensu stricto*, Table 1). In addition, the location of each plate was interpreted and georeferenced in the WGS 84 system, resulting in a list with geographical coordinates north and west, in degrees, minutes, and seconds (Table 1). This information is unpublished and allows us to unify geographically and with greater accuracy the samples of the TCA with the samples of the current literature. The information described above is detailed in supplementary materials 3 and 4, attached to this article. Subsequently, a photographic record was made of each specimen, and their respective photomicrographs were taken (Figures 2c and 2d) in a Leica petrographic microscope with a Leica DMC camera. In the photographic recording process, it was observed that the thin sections of the TCA are in good condition for future petrographic analysis. The slides have coverslips, which do not allow for electron microprobe analysis; however, the hand specimens are preserved in the Faculty of Mines of the Universidad Nacional de Colombia, Medellín.

To complement the transcription and interpretation of the information contained in all the available plates of the TCA, a photographic record of them was made, and their respective microphotography was taken, with plane-polarized light and crossed polarizers, to show graphically and in an unpublished way the color plates of the TCA manuscript (Figure 4a). The TCA map comprises 70 lithological units mapped by Grosse, equivalent to 18 lithostratigraphic units (Table 2), currently recognized by the Servicio Geológico Colombiano (Gómez et al., 2015). A single lithostratigraphic unit comprises one or several lithological units of the TCA. For example, for Grosse,

there are 13 different units of Neotertiary porphyritic intrusive rocks, which he separates in his map in detail, according to the different textural and mineral variations (e.g., andesite of indeterminate nature, andesite of varied development, micaceous andesite, hornblende andesite, augitic andesite, feldspathic basalt, augitic basalt, among others). At the same time, the Geological Survey corresponds to a unified group called Porphyritic Hypoabyssal Rocks (Figure 8c). In some cases, we have lithological units that are currently in disuse or do not have their equivalent in the regional literature because of their chemical implications; for example, Grosse uses the term *keratophyre* probably to refer to a volcanic rock of intermediate composition, which may have plagioclase richer in sodium than trachyte (Schermerhorn, 1973). Consider the terms *malchite* and *ebresite* used at the time by Grosse, but which have no equivalence today for classifying rocks.

Finally, 17 plates were selected from a total of 480 specimens, corresponding to 17 lithostratigraphic units (Quaternary alluvium and terraces were omitted), to generate the color photomicrographs of the original TCA specimens (Figures 4 to 8), where we listed 1) the metamorphic units, corresponding to Sucre Amphibolite, Palmitas Gneiss, Cajamarca Complex, Arquía Complex; 2) the Amagá Formation, Combia Formation and Sinifaná Metasedimentites; and 3) the igneous lithostratigraphic units, namely, Belmira Syntectonic Gneissic Intrusive, Quebradagrande Complex, Altavista Stock, Amagá Stock, Angelópolis Ultramaftes, Ovejas Batholith, Pueblito Gabbro, Pueblito Diorite, Heliconia Diorite, and Porphyritic Hypoabyssal Rocks.

Table 2. List of lithostratigraphic units mapped in the TCA and comparative ages assigned by Grosse vs. present ages

Lithological unit (Emil Grosse, 1926)	Lithostratigraphic Unit (Servicio Geológico Colombiano)	Age according to Grosse (1926)	Age updated	Figure No.
Zoisitic amphibolite	Amphibolites of Sucre	Pre Paleozoic	Paleozoic (González, 2001)	Figure 4b
Contact phyllite, contact crowns, shales and graphitic schists	Cajamarca Complex	Precambrian	240-230 Ma (Vinasco et al., 2006); 157-146 Ma (Blanco-Quintero et al., 2014).	Figure 5c
Lenticular granite, lenticular granite	Palmitas Gneiss	Pre Paleozoic	Permo-Triassic (González, 2001)	Figure 4c
Clay shales, phyllites and quartzites	Sinifaná Metasedimentites	Precambrian	Ordovician (González, 2001); Late Carboniferous to Early Triassic (Martens et al., 2012).	Figure 4d
Epidotized and uralitized diorite	Stock of Amagá	Eotertiary	221 Ma (Pérez, 1967); 232 Ma (Restrepo et al., 1991); Triassic (González, 2001).	Figure 6b
Peridotite (serpentine) - peridotite (harzburgite)	Ultramafites of Angelópolis	Pre Paleozoic	Lower Cretaceous; 166 Ma (González, 2001; Toussaint and Restrepo, 1978).	Figure 6c
Amphibolytic Gabbro	Pueblito Gabbro	Paleozoic	Lower Cretaceous; 166 Ma (González, 2001; Toussaint and Restrepo, 1978).	Figure 7a
Porphyritic diorite	Diorite of Pueblito	Paleozoic	Lower Cretaceous; 166 Ma (González, 2001; Toussaint and Restrepo, 1978).	Figure 7b
Augitic diorite	Altavista Stock	Eotertiary	Lower Cretaceous (González, 2001); 97 Ma (Cardona et al., 2020)	Figure 6a
Actinolytic shale	Arquia Complex	Precambrian	Lower Cretaceous; 137-112 Ma (Toussaint, 1996; Villagómez et al., 2011).	Figure 5a
Tufa agglomeratic	Quebradagrande Complex	Mesozoic	Lower Cretaceous; 105 Ma (González, 2001; Nivia et al., 2006; Toussaint and Restrepo, 1978).	Figure 5b
Quartz diorite, Idem acidic facies, keratophyric facies, basic facies	Diorite of Heliconia	Eotertiary	Upper Cretaceous (González, 2001)	Figure 7c
Lenticular granite	Gnesic Syntectonic Intrusive of Belmira	Pre Paleozoic	Permo-Triassic (González, 2001)	Figure 6d
Tonalite, quartziferous micaci-hornblende diorite: Ovejas-Poleal type	Batholith of Ovejas	Eotertiary	Upper Cretaceous (González, 2001)	Figure 6d
Carboniferous Tertiary of Antioquia (bcs, bcm, bci)	Amagá Formation	Tertiary	Middle Oligocene (Van de Hammen, 1958); Middle Eocene to Late Miocene (Londoño et al., 2013; Ramírez et al., 2015); end of deposition, ca. 15-13 Ma (Montes et al., 2015; Lara et al., 2018)	Figure 8a
Conglomerates, sandstones, volcanic tuffs, and eruptive spills (bns, bnv)	Combia Formation	Neotertiary	Neogene (~10-6 Ma) (González, 2001; Jaramillo et al., 2019; Weber, 2020).	Figure 8b
Andesite, micaceous andesite, hornblende andesite, augitic andesite, feldspathic basalt, augitic basalt, etc. (13 units in the TCA)	Neotertiary porphyry	Neotertiary	Neogene (González, 2001)	Figure 8c
Rubble, gravel, sand and subsoil covered with detrital detritus of the rocky slopes or boulders (a, df, d)	Recent alluvium and alluvial terraces	Quaternary	Quaternary (González, 2001; Mejía, 1984; Jaramillo-Zapata et al., 2014).	N.A.

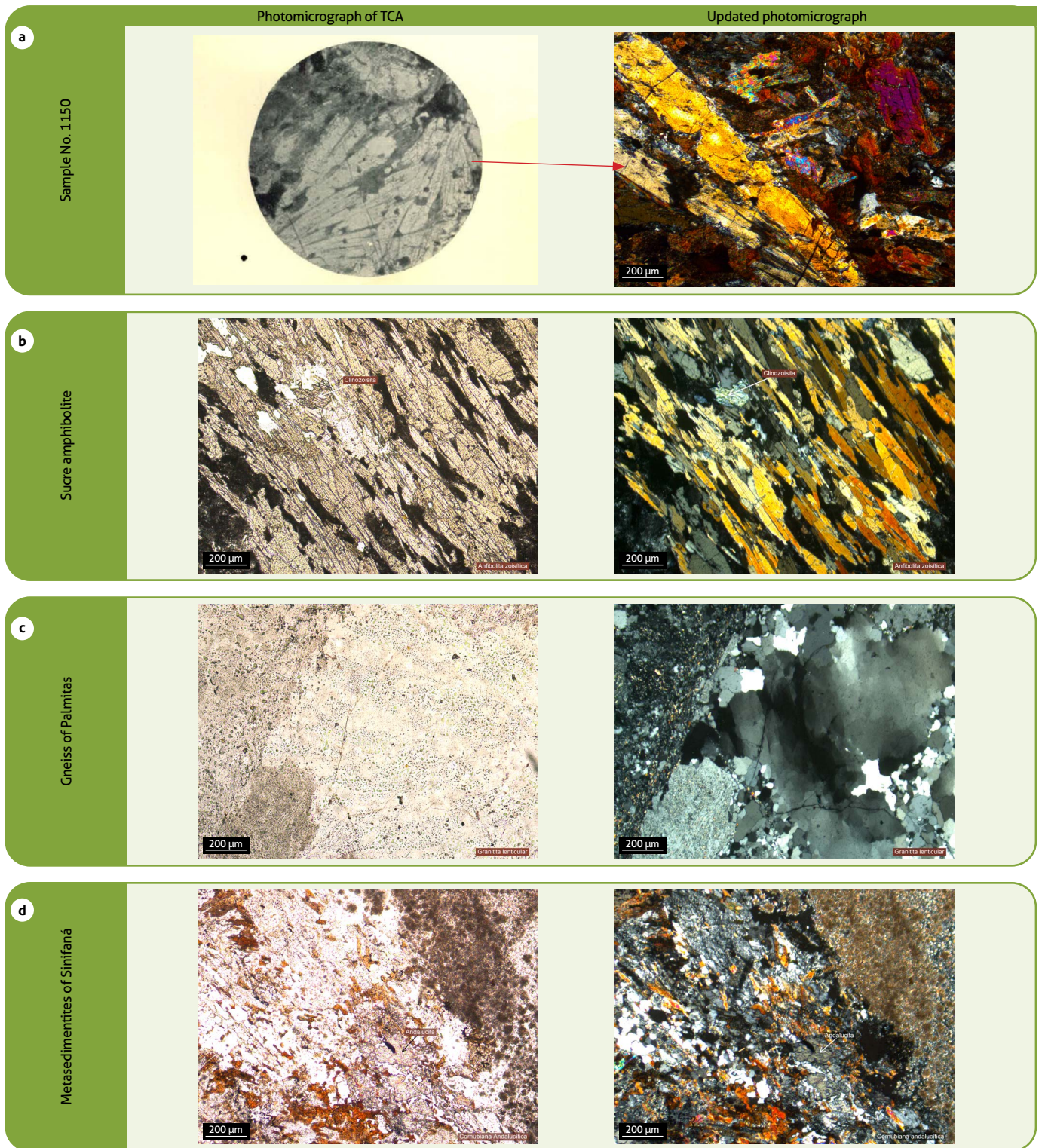


Figure 4. a) Photomicrograph of an andalusite and mica cornubian from the Cajamarca Complex, taken in shades of gray by Emil Grosse, compared with a color microphotograph of the same thin section, taken in the present work. Sample No. 1150 in Grosse's catalog; b-d) Pairs of photomicrographs with plane-polarized light and crossed polarizers, cataloged and transcribed according to Emil Grosse, corresponding to the following metamorphic lithostratigraphic units: b) Sucre amphibolite, sample No. 560, described as a sample of the Sucre Complex, sample No. 560, described as a "zoisitic amphibolite"; c) Gneiss of Palmitas, sample No. 476, catalogued as a "lenticular granite"; d) Metasedimentites of Sinifaná, sample No. 510, defined as a "cornubian andalusite".

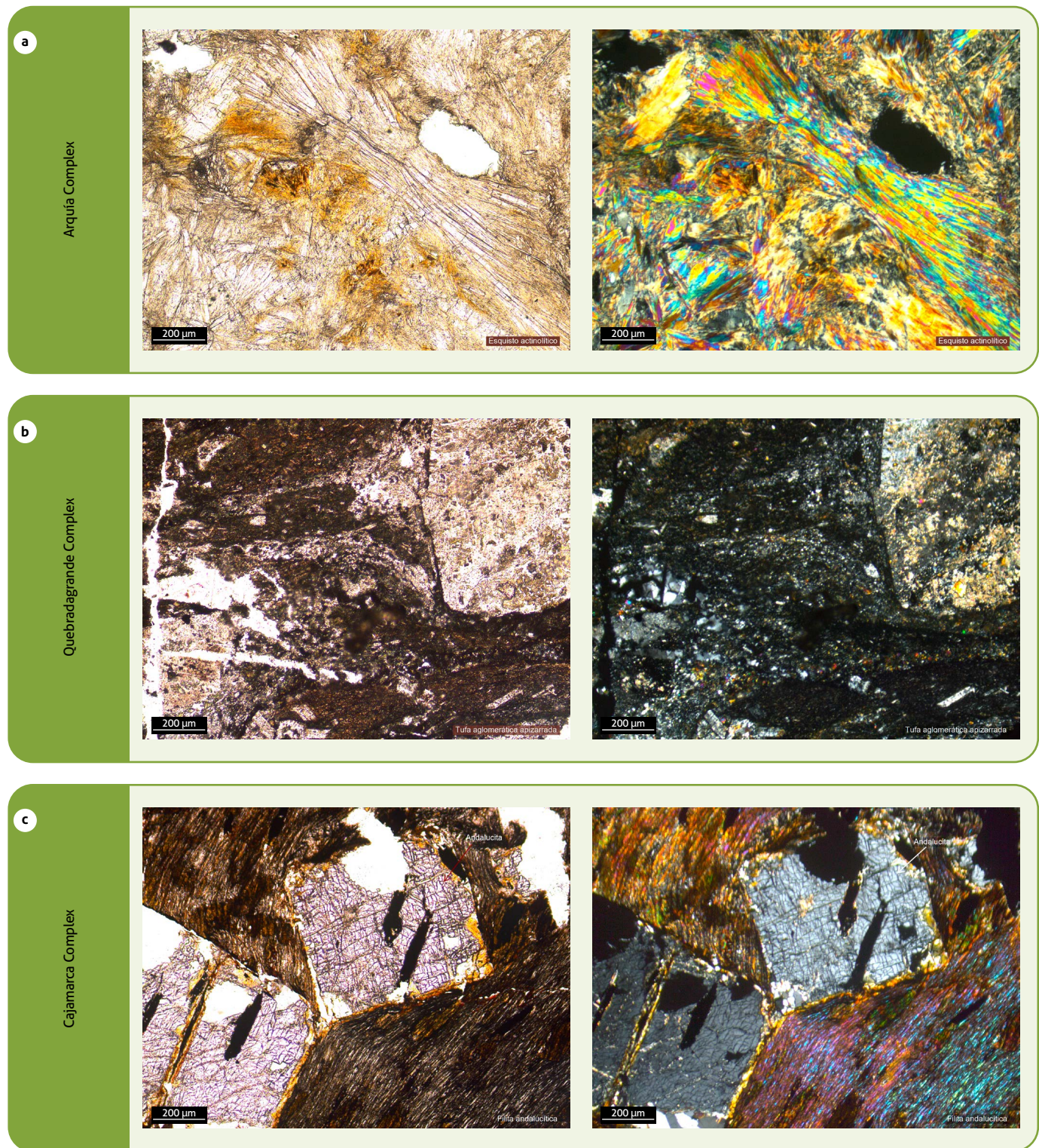


Figure 5. Pairs of photomicrographs with plane-polarized light and crossed polarizers, cataloged and transcribed according to Emil Grosse, corresponding to lithostratigraphic units denominated as complexes

a) Arquía Complex, sample No. 287, described as an “actinolitic schist”; b) Quebradagrande Complex, sample No. 733, cataloged as an “agglomeratic tuff”; c) Cajamarca Complex Unit, sample No. 532, defined as a “contact phyllite”; d) Cajamarca Complex Unit, sample No. 532, defined as a “contact phyllite”; e) Quebradagrande Complex, sample No. 733, defined as an “agglomeratic tuff”.

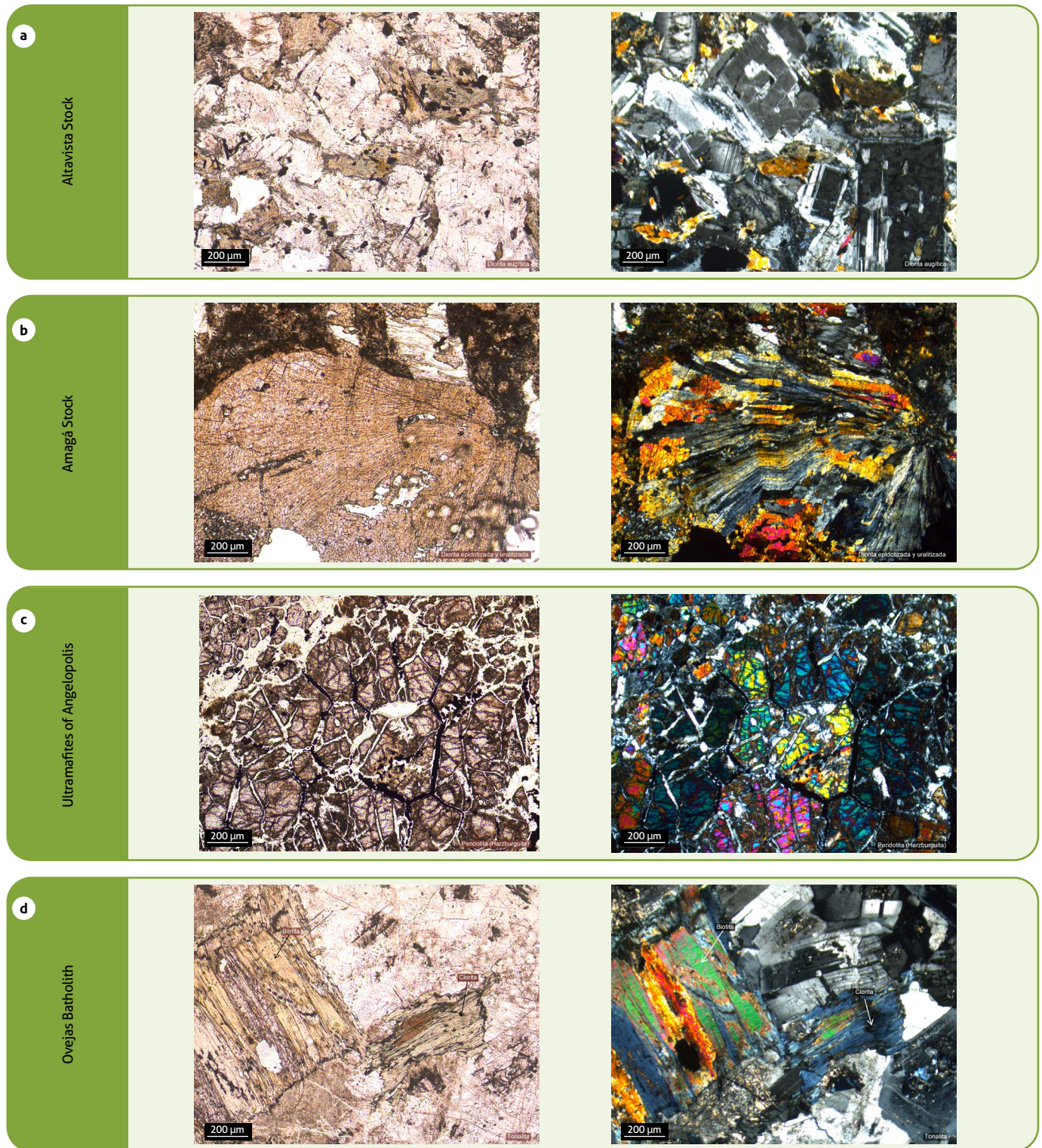


Figure 6. Pairs of photomicrographs with plane-polarized light and crossed polarizers, cataloged and transcribed according to Emil Grosse, corresponding to intrusive igneous lithostratigraphic units
 a) Altavista Stock, sample No. 497, described as an “augitic diorite”; b) Amagá Stock, sample No. 406, defined as an “epidotized and uralitized diorite”; c) Ultramafites of Angelópolis, sample No. 535, catalogued as a “peridotite (harzburgite)”; d) Batolito de Ovejas, sample No. 522, corresponding to a “tonalite”.

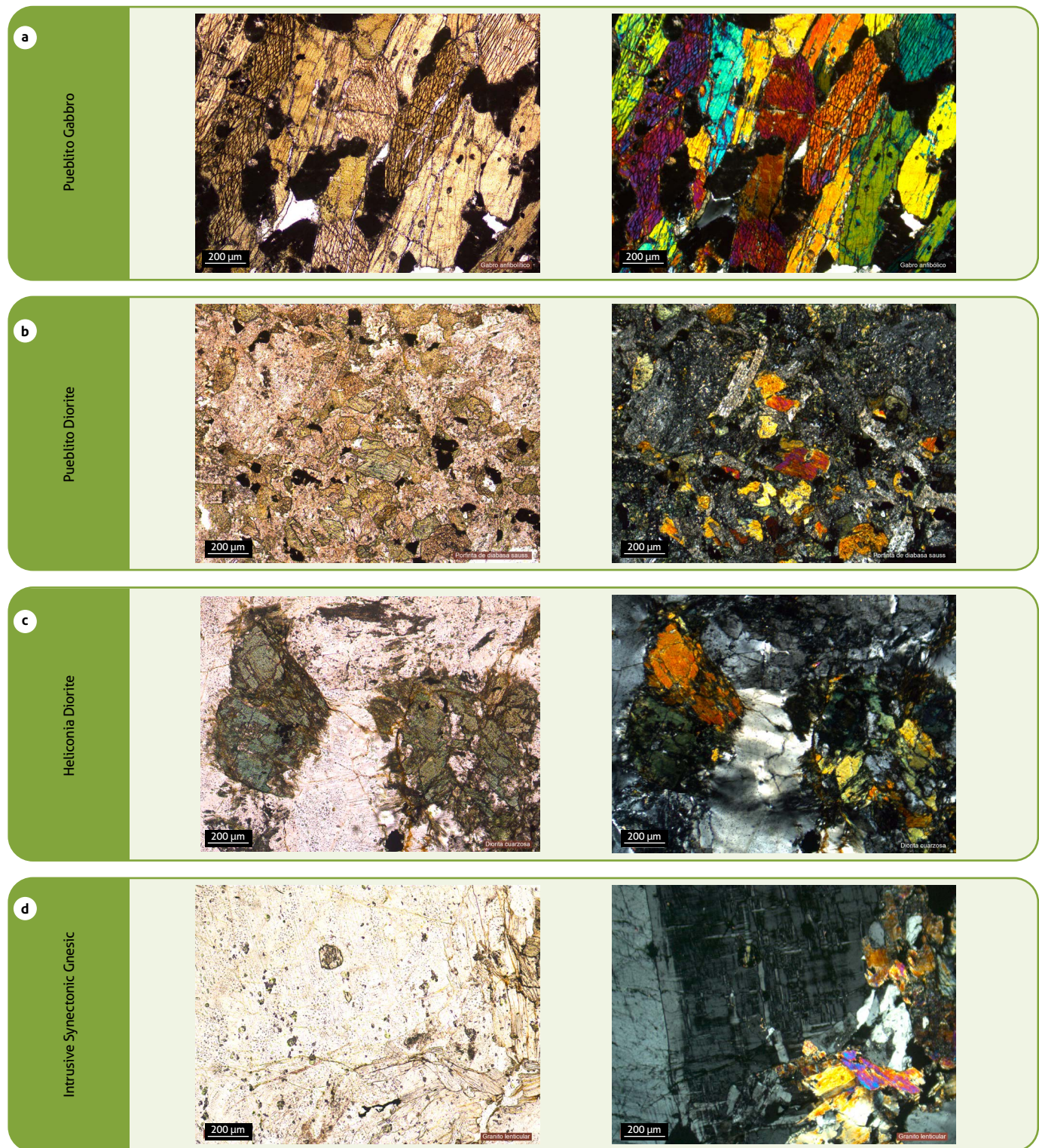


Figure 7. Pairs of photomicrographs with plane-polarized light and crossed polarizers, cataloged and transcribed according to Emil Grosse, corresponding to intrusive igneous lithostratigraphic units a) Pueblito Gabbro, sample No. 300, described as an “amphibolitic gabbro”; b) Pueblito Diorite, sample No. 449, defined as a “porphyritic diorite”; c) Heliconia Diorite, sample No. 389, corresponding to a “quartz diorite”; d) Intrusive Syntectonic Gnesic, sample No. 551, defined as a “lenticular granite”.

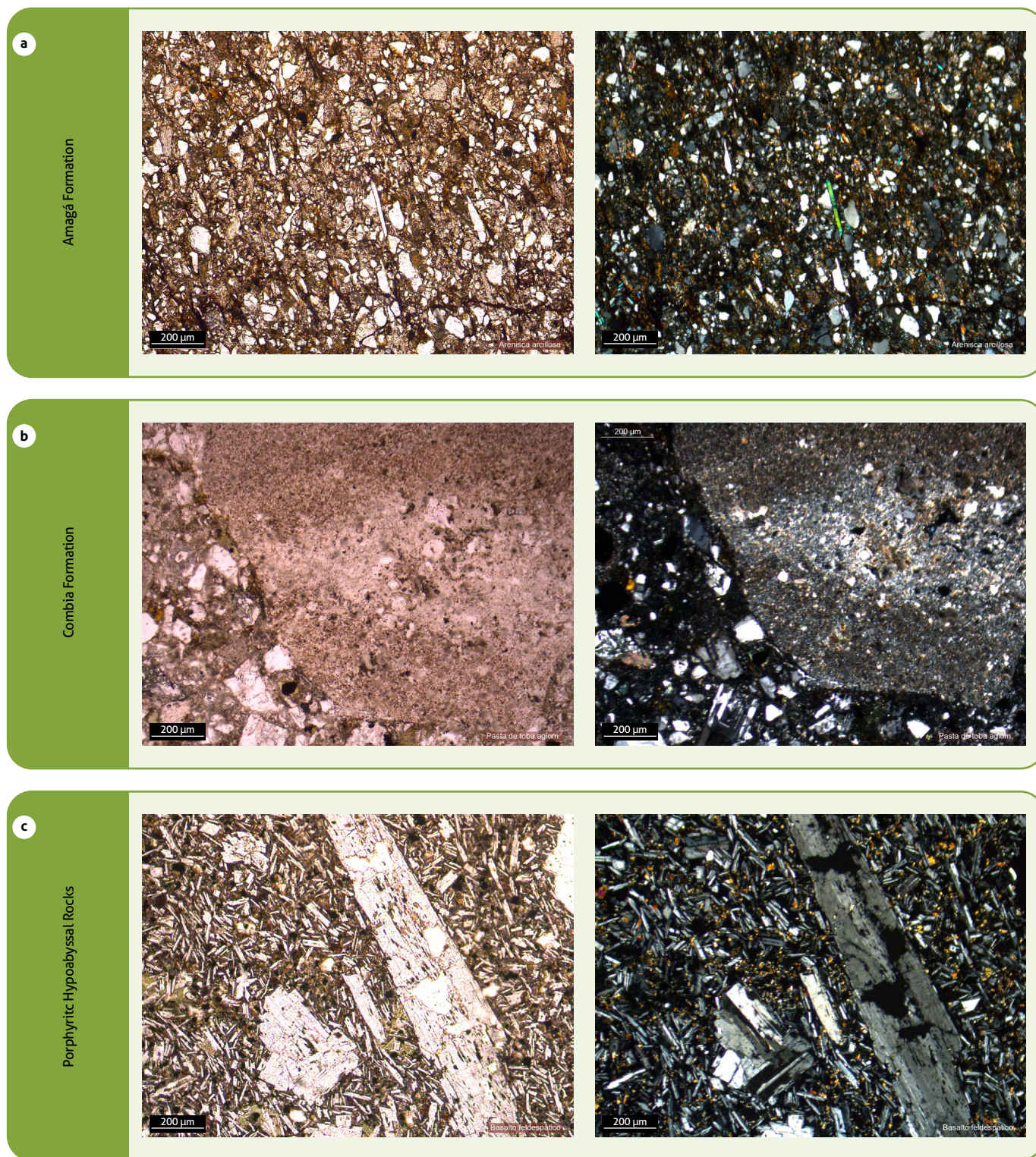


Figure 8. Pairs of photomicrographs with plane-polarized light and crossed polarizers, cataloged and transcribed according to Emil Grosse, corresponding to Tertiary lithostratigraphic units
 a) Amagá Formation (Carboniferous Tertiary of Antioquia), specimen No. 391, described as a “clayey sandstone”; b) Combia Formation, sample No. 62, defined as a paste of “agglomeratic tuff”; c) Porphyritic Hypoabyssal Rocks, sample No. 48, corresponding to a “feldspathic basalt”.

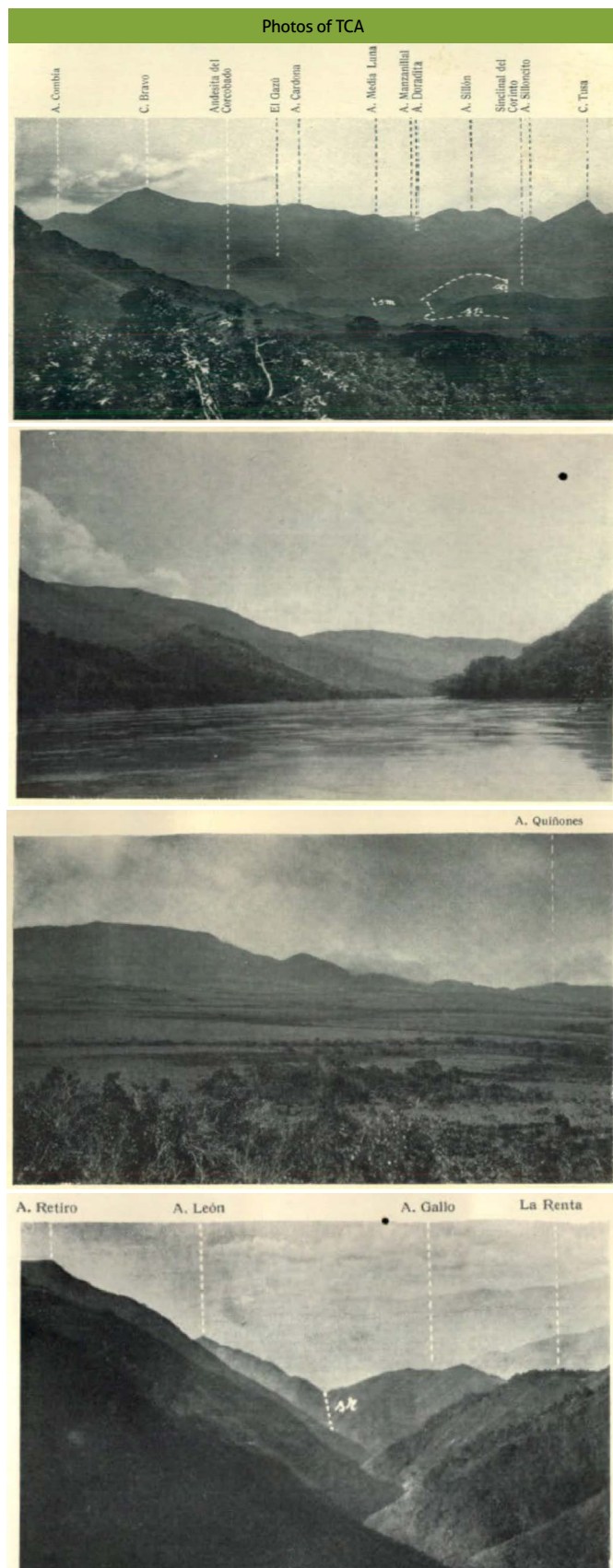
3.3. Multitemporal analysis of TCA images

To complement the cartographic, petrological, and structural work, Dr. Grosse left a photographic record of the most outstanding geomorphological features of the area associated with the TCA, which include: the great canyon of the Cauca River and its associated first- and second-order tributaries, the cliffs of La Pintada, Tusa hill, Bravo hill, the plains of Ovejas and the Boquerón area near the hill of Padre Amaya. The photographs show mainly landscapes of important geological information, taken from the highest altitude points in the area, such as the Alto de Quiñonez, Palo Blanco and Retiro, high and low slope hills, such as the Guayabal hill or the Monte Grande hill (Figures 9l and 9o), as well as the Cauca River and the Sinifaná, Nuarque and La Clara streams (Figures 9a, 9c, 9f, and 9g), and finally the urban centers of the municipalities of Ebéjico, Heliconia, and Sopetrán (Figures 9j and 9l). These photographs show in detail the most outstanding geomorphological and morphodynamic features of the area, such as the traces of faults and the formation of geofoms in silhouettes, sand bars, and meanders of rivers and their tributaries, plains, and lithological changes.

In order to take the exact photos where Dr. Grosse made his record, the description of the photograph was analyzed, and despite not having coordinates tied to the Bessel 1841 datum, it was possible to establish key reference points such as heights, hills, rivers, and streams, areas that were later corroborated in the field. The most difficult areas to find the exact location of were the first- and second-order streams and tributaries (e.g., Grosse's description: "the Las Juntas stream near the mouth of the Amagá stream"). Such descriptions were complicated at the beginning of the expedition due to the absence of a key reference point, such as hills, ridges, or high ground. However, satisfactory results were obtained in the end, resulting in

a photograph taken of the same point in the TCA, one hundred years after its publication (Figure 9b). The last problem encountered in taking photographs was that the access was restricted in many areas of interest because they were private properties or industrial areas.

When comparing the photographs, it can be seen that many of the rural and forested areas have remained little modified by man. For example, conservation of the landscape is evident in the Tablazo area of the Amagá-Heliconia watershed, and the high Gramal and Blanquizar cleaver in the municipality of Ebéjico (Figure 9n-o), and little anthropic intervention is observed in the alluvial terraces near the mouth of the Amagá stream in the Cauca river (Figure 9b). It is also observed that in some cases, there has been an increase in the vegetation and tree cover: for example, there is an increase in trees in the plains of Ovejas on the road between Bello and Sopetrán (Figure 9c), on the right margin of the western bridge of Santa Fe de Antioquia (Figure 9e) and in the high El Frisol, near the old road from Medellín to Sopetrán (Figure 9h). It is to be expected that the areas near the urban areas of the municipalities have a strong anthropic influence, such as road construction, fences, plantations and, in the specific case of Ebéjico, Sopetrán, and Heliconia, the increase of the urban limit, where the replacement of the houses in Tapia Pisada and Bahareque by brick and cement buildings can be observed (Figures 9c, 9j, and 9l). Finally, in the TCA photographs, there was little visibility of the overthrust zones (faults). In contrast, in the present photographs, the Amagá overthrust in the Heliconia basin can be better visualized (Figure 9i and 9j), the Sopetrán and La Sucumbí overthrusts on the Monte Grande hill, SW of Sopetrán (Figure 9l), and the Uvito and Piedecuesta overthrusts on the western slope of Roblal, in the Heliconia basin (Figure 9m).



Photos of TCA



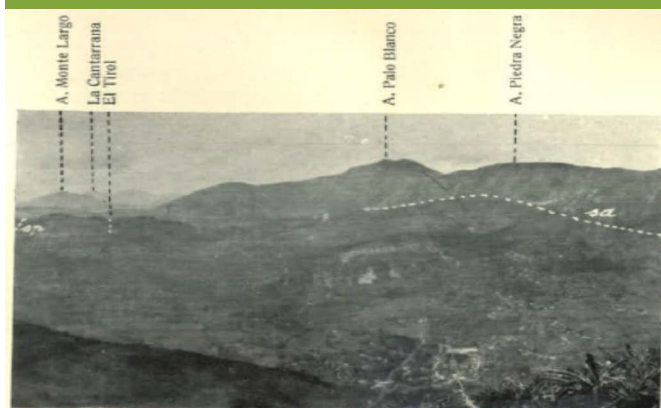
Catedral de Antioquia



Recent photos



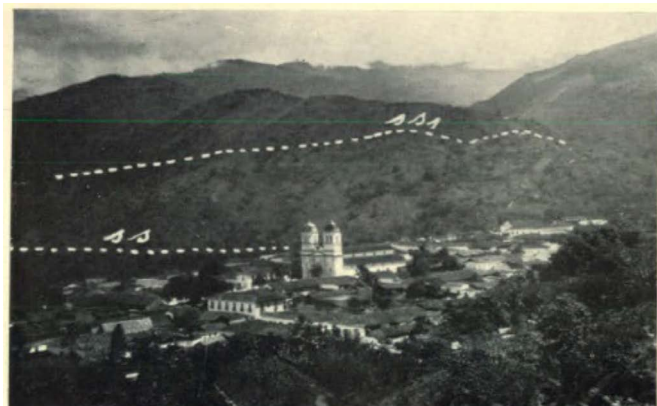
Photos of TCA



A. Piedra Negra



Boquerón de Yuna A. Picacho ● de la Enillada A. Pan de A. Palo Grande La Chapa



Recent photos



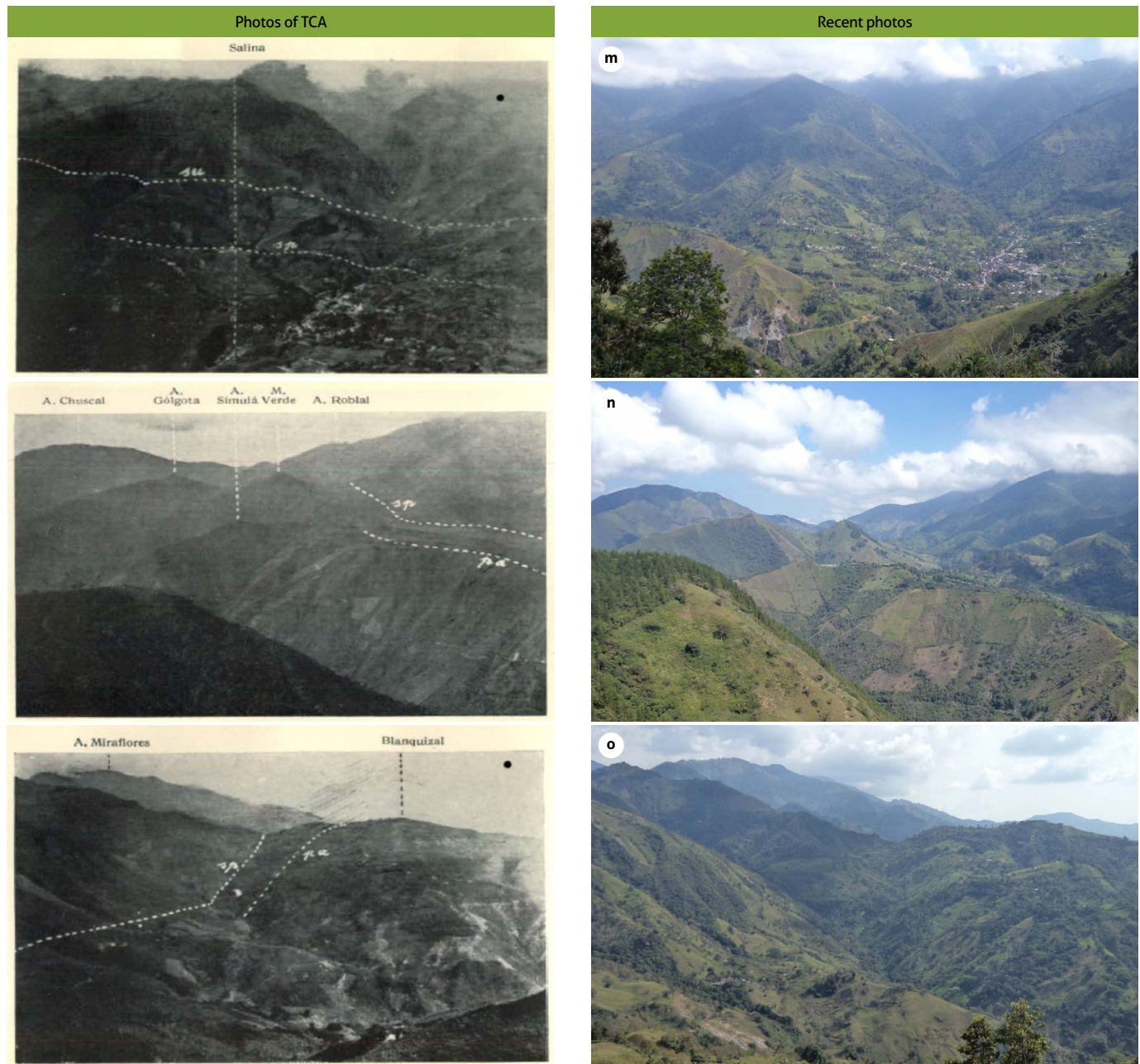


Figure 9. Pairs of photographs of the TCA taken by Emil Grosse and its present-day equivalent taken in the field
 a) the mountainous region south of Sinifaná creek, as seen from the Manchal; b) Cauca river between the Paso de los Pobres pass and the mouth of Amagá creek; c) the Ovejas plains, as seen from the east (Bello-Sopetrán road); d) view along the Zaguá creek valley, from the Corral descent to Zaguá creek; e) view of the Cauca river and the Occidente bridge (right bank); f) bend of Nuarque creek, seen from upper Palo Grande; g) cut of Nuarque creek, near the buttress sector, seen from upper Palo Grande; h) La Frisola creek and upper Venteadero, seen to the south of upper El Frisol; i) Heliconia and the Heliconia-Amagá basin, S of Guaca creek, seen from the W foot of upper El Roblal; j) Heliconia basin S of Guaca creek, seen from the W foot of El Roblal; k) Sopetrán basin seen from a terrace SW of Sopetrán; l) Sopetrán on a terrace, Monte Grande hill and Sopetrana creek, seen SW of Sopetrán; m) view of the Heliconia basin, from the W slope of Roblal and Aburreña creek, seen from the upper El Calvario; n) El Tablazo and the furrow that continues the Amagá-Heliconia basin; o) W slope of the upper Gramal and Blanquizal, seen from the Guayabal hill.

4. CONCLUSIONS

The TCA is one of the most relevant classic works of the Antioquian and Colombian geology of the first half of the XX century, in which its rigorous execution, excellent field control, and meticulousness in the petrological and structural analyses stand out as one of the most valid and influential classic works, mainly for studies involving regional geology and economic geology.

In the research work presented, the four 1:50 000 scale maps of the TCA were digitized, and the cartographic projection was transferred, and linked to the WGS 84 datum to work digitally in the field. In addition, the sample of thin sections donated by Dr. Emil Grosse to the Escuela Nacional de Minas, now in the Museum of Geosciences, was cataloged. This catalog represents 75% of the total number of thin sections generated for the TCA.

The work carried out allows comparing the maps obtained 100 years ago with the current maps. The most important changes correspond to the results of geochronological dating for the 70 lithological units mapped by Grosse and in the subsequent conformation of 18 lithostratigraphic units recognized by the Servicio Geológico Colombiano, associated with the TCA study area. Likewise, a record of 480 photos of plates and photomicrographs was made to the collection of thin sections of Grosse, unpublished images of high patrimonial value. A multi-temporal analysis, carried out with the photographic record of the TCA, showed that, in a 100-year interval, there had been no significant anthropic change for the rural areas, and an increase in the vegetation and tree cover was observed. On the other hand, a high anthropic influence was shown for the urban area, among which the construction of roads, fences, plantations, and the increase of the urban boundary stand out.

ACKNOWLEDGMENTS

The authors thank the Museo de Geociencias of the Facultad de Minas, Universidad Nacional de Colombia, Medellín, for providing the TCA samples for cataloging, scanning and taking photomicrographs of thin sections, and the Laboratorio de Petrografía de la Facultad de Minas, for the loan of the equipment. In addition, this work was supported by ANID-Subdirección de Capital Humano/Doctorado Nacional/2021-21210049. The authors thank the anonymous reviewers for their valuable comments and suggestions, which helped to improve the original manuscript.

Supplementary material

Supplementary data for this article can be found online at <https://doi.org/10.32685/0120-1425/bol.geol.48.2.2021.570>

REFERENCES

- Bartos, P. J., García, C., & Gil, J. (2017). The Nuevo Chaquiro Cu-Au-(Mo) Porphyry Deposit, Middle Cauca Belt, Colombia: Geology, Alteration, Mineralization. *Economic Geology*, 112(2), 275-294. <https://doi.org/10.2113/econgeo.112.2.275>
- Bessel, F. W. (1841). Ueber einen Fehler in der Berechnung der französischen Gradmessung und seinen Einfluß auf die Bestimmung der Figur der Erde. *Astronomische Nachrichten*, 19(438), 97-116. <https://doi.org/10.1002/asna.18420190702>
- Bissig, T., Leal-Mejía, H., Stevens, R. B., & Hart, C. J. R. (2017). High Sr/Y Magma Petrogenesis and the Link to Porphyry Mineralization as Revealed by Garnet-Bearing I-type Granodiorite Porphyries of the Middle Cauca Au-Cu Belt, Colombia. *Economic Geology*, 112(3), 551-568. <https://doi.org/10.2113/econgeo.112.3.551>
- Blanco-Quintero, I. F., García-Casco, A., Toro, L. M., Moreno, M., Ruiz, E. C., Vinasco, C. J., Cardona, A., Lázaro, C., & Morata, D. (2014). Late Jurassic Terrane Collision in the Northwestern Margin of Gondwana (Cajamarca Complex, Eastern Flank of the Central Cordillera, Colombia). *International Geology Review*, 56(15), 1852-1872. <https://doi.org/10.1080/00206814.2014.963710>
- Cardona, A., León, S., Jaramillo, J. S., Valencia, V., Zapata, S., Pardo-Trujillo, A., Schmitt, A. K., Mejía, D., & Arenas, J. C. (2020). Cretaceous Record from a Mariana- to an Andean-Type Margin in the Central Cordillera of the Colombian Andes. In J. Gómez & A. O. Pinilla-Pachón (eds.), *The Geology of Colombia, Volume 2, Mesozoic* (pp. 335-373). Publicaciones Geológicas Especiales 36. Servicio Geológico Colombiano. <https://doi.org/10.32685/pub.esp.36.2019.10>
- Castro, P. (2018, julio 18). *Robert Scheibe y el croquis geológico del sur de Antioquia (ca. 1919): Aportes alemanes en el desarrollo de la geología en Colombia* [Conference]. Cátedra Itinerante de Ciencias de la Tierra, EAFIT, Sociedad Colombiana de Geología, Medellín.
- Cediel, F., Shaw, R. P., & Cáceres, C. (2003). Tectonic Assembly of the Northern Andean Block. In C. Bartolini, R. T. Buffler, & J. Blickwede (eds.), *The circum-Gulf of Mexico and the Caribbean: Hydrocarbon habitats, basin formation,*

- and plate tectonics (pp. 815-848). American Association of Petroleum Geologists Memoir, 79.
- Etayo-Serna, F., Barrero, D., Lozano, H., Espinosa, A., González, H., Orrego, A., Ballesteros, I., Forero, H., Ramírez, C., Zambrano-Ortiz, F., Duque-Caro, H., Vargas, R., Núñez, A., Álvarez, J., Ropaín, C., Cardozo, E., Galvis, N., Sarmiento, L., Alberts, J. P., & ... Hodges, C. A. (1983). *Mapa de terrenos geológicos de Colombia*. Publicaciones Geológicas Especiales, 14. Ingeominas.
- González, H. (1999). *Geología del departamento de Antioquia. Escala 1:400 000*. Ingeominas.
- González, H. (2001). Memoria explicativa: Mapa geológico del departamento de Antioquia. Escala 1:400 000. Ingeominas.
- Grosse, E. (1926). *Estudio geológico del Terciario Carbonífero de Antioquia en la parte occidental de la cordillera Central de Colombia, entre el río Arma y Sacaoyal, ejecutado en los años de 1920-1923*. Dietrich Reimer.
- Instituto Geográfico Agustín Codazzi (IGAC). (2004). *Hoja n.º 130, Carta general. Escala 1:100 000*.
- Instituto Geográfico Agustín Codazzi (IGAC). (2005a). *Hoja n.º 146, Carta general. Escala 1:100 000*.
- Instituto Geográfico Agustín Codazzi (IGAC). (2005b). *Hoja n.º 166, Carta general. Escala 1:100 000*.
- Jaramillo, J. S., Cardona, A., Monsalve, G., Valencia, V., & León, S. (2019). Petrogenesis of the Late Miocene Combia Volcanic Complex, Northwestern Colombian Andes: Tectonic Implication of Short Term and Compositionally Heterogeneous Arc Magmatism. *Lithos*, 330-331, 194-220. <https://doi.org/10.1016/j.lithos.2019.02.017>
- Jaramillo-Zapata, J., Caballero, J., & Molina-Escobar, J. M. (2014). Patrimonio geológico y geodiversidad: bases para su definición en la zona andina de Colombia: caso Santa Fe de Antioquia. *Boletín Ciencias de la Tierra*, (35), 53-66.
- Lara, M., Salazar-Franco, A. M., & Silva-Tamayo, J. C. (2018). Provenance of the Cenozoic Siliciclastic Intramontane Amagá Formation: Implications for the Early Miocene Collision between Central and South America. *Sedimentary Geology*, 373, 147-162. <https://doi.org/10.1016/j.sed-geo.2018.06.003>
- Lesage, G., Richards, J. P., Muehlenbachs, K., & Spell, T. L. (2013). Geochronology, Geochemistry, and Fluid Characterization of the Late Miocene Buriticá Gold Deposit, Antioquia Department, Colombia. *Economic Geology*, 108(5), 1067-1097. <https://doi.org/10.2113/econgeo.108.5.1067>
- Londoño, C. I., Sierra, G. M., & Marín-Cerón, M. I. (2013). ¿Por qué la Formación Amagá no puede ser Oligocena? [Memories]. XIV Congreso Colombiano de Geología y Primer Simposio de Exploradores, Bogotá.
- Martens, U., Restrepo J. J., & Solari, L. (2012). Sinifaná Metasedimentites and Relations with Cajamarca Paragneisses of the Central Cordillera of Colombia. *Boletín Ciencias de la Tierra*, (32), 99-110.
- Maya, M., & González, H. (1995). Unidades litodémicas en la cordillera Central de Colombia. *Boletín Geológico*, 35(2-3), 43-57.
- Mejía, N. (1984). *Geología y geoquímica de las planchas 130 (Santa Fe de Antioquia) 146 (Medellín occidental) escala 1:100 000, memoria explicativa*. Ingeominas.
- Montes, C., Cardona, A., Jaramillo, C., Pardo, A., Silva, J. C., Valencia, V., Ayala, L. C., Pérez-Ángel, L. C., Rodríguez-Parra, L. A., Ramírez, V., & Niño, H. (2015). Middle Miocene Closure of the Central American Seaway. *Science*, 348(6231), 226-229. <https://doi.org/10.1126/science.aaa2815>
- Nivia, A., Marriner, G., Kerr, A., & Tarney, J. (2006). The Quebradagrande Complex: A Lower Cretaceous Ensilic Marginal Basin in the Central Cordillera of the Colombian Andes. *Journal of South American Earth Sciences*, 21, 423-436. <https://doi.org/10.1016/j.jsames.2006.07.002>
- Pérez, A. (1967). Determinación de la edad absoluta de algunas rocas de Antioquia por métodos radioactivos. *Dyna*, 84, 27-31.
- Posada, J. C. (1936). Bosquejo geológico de Antioquia. *Anales de la Escuela Nacional de Minas*, 38, 1-50.
- Ramírez, E., Pardo-Trujillo, A., Plata, A., Vallejo, F., & Trejos, R. (2015). *Edad y ambiente de la Formación Amagá (sector de Santa Fe de Antioquia-Sopetrán) con base en evidencias palinológicas* [Memories]. XV Congreso Colombiano de Geología, Bucaramanga.
- Restrepo, J., Toussaint, J., González, H., Cordani, U., Kawashita, K., Linares, E., & Parica, E. (1991). *Precisiones geocronológicas sobre el occidente colombiano* [Memories]. Simposio sobre Magmatismo Andino y su marco tectónico, Manizales.
- Restrepo, J. J., & Toussaint, J. F. (2020). Tectonostratigraphic Terranes in Colombia: An Update. First Part: Continental Terranes. In J. Gómez, & D. Mateus-Zabala (eds.), *The Geology of Colombia, Volume 1, Proterozoic-Paleozoic* (pp. 37-63). Servicio Geológico Colombiano, Publicaciones Geológicas Especiales 35. <https://doi.org/10.32685/pub.esp.35.2019.03>

- Rodríguez-Vega, Y. J., & Chicangana-Bayona, Y. A. (2017). La enseñanza de la geología en la Escuela Nacional de Minas de Medellín, 1910-1937. *Boletín de Ciencias de la Tierra*, 42, 55-63.
- Schermerhorn, L. J. G. (1973). What is Keratophyre? *Lithos*, 6, 1-11. [https://doi.org/10.1016/0024-4937\(73\)90076-5](https://doi.org/10.1016/0024-4937(73)90076-5)
- SGC. (2021). *Museo Geológico Nacional José Royo y Gómez*. Servicio Geológico Colombiano. <https://www2.sgc.gov.co/museo-geologico/Paginas/museo.aspx>
- Sillitoe, R. (2008). Major Gold Deposits and Belts of the North and South American Cordillera: Distribution, Tectonomagmatic Settings and Metallogenetic Considerations. *Economic Geology*, 103(4), 633-687. <https://doi.org/10.2113/gsecongeo.103.4.663>
- Silva-Tamayo, J. C., Lara, M., & Salazar-Franco, A. M. (2020). Oligocene-Miocene Coal-Bearing Successions of the Amagá Formation, Antioquia, Colombia: Sedimentary Environments, Stratigraphy, and Tectonic Implications. In J. Gómez, & D. Mateus-Zabala (eds.), *The Geology of Colombia, Volume 3, Paleogene-Neogene* (pp. 331-353). Servicio Geológico Colombiano, Publicaciones Geológicas Especiales 37. <https://doi.org/10.32685/pub.esp.37.2019.11>
- Gómez, J., Montes, N. E., Almanza, M. F., Alcárcel, F. A., Madrid, C. A., & Diederix, H. (2015). *Geological Map of Colombia* (v. 30). International Union of Geological Sciences. <http://dx.doi.org/10.18814/epiugs/2017/v40i3/017023>
- Toussaint, J. F. (1996). *Evolución geológica de Colombia, 3: Cretácico*. Universidad Nacional de Colombia.
- Toussaint, J. F., & Restrepo, J. J. (1978). *Edad K-Ar de dos rocas básicas del flanco noroccidental de la Cordillera Central*. Publicaciones Especiales de Geología, 15.
- Toussaint, J. F., & Restrepo, J. J. (2020). Tectonostratigraphic Terranes in Colombia: An Update. Second Part: Oceanic Terranes. In J. Gómez, & A. O. Pinilla-Pachón (eds.), *The Geology of Colombia, Volume 2, Mesozoic* (pp. 237-260). Publicaciones Geológicas Especiales 36. Servicio Geológico Colombiano. <https://doi.org/10.32685/pub.esp.36.2019.07>
- Van der Hammen, T. (1958). Estratigrafía del Terciario y Maestritichiano y tectogénesis de los Andes Colombianos. *Boletín Geológico*, 6(1-3), 67-28.
- Villagómez, D., Spikings, R., Magna, T., Kammer, A., Winkler, W., & Beltrán, A. (2011). Geochronology, Geochemistry and Tectonic Evolution of the Western and Central Cordilleras of Colombia. *Lithos*, 125(3-4), 875-896. <https://doi.org/10.1016/j.lithos.2011.05.003>
- Vinasco, C., Cordani, U., González, H., Weber, M., & Peláez, C. (2006). Geochronological, Isotopic, and Geochemical Data from Permo-Triassic Granitic Gneisses and Granitoids of the Colombian Central Andes. *Journal of South American Earth Science*, 21(4), 355-371. <https://doi.org/10.1016/j.jsames.2006.07.007>
- Weber, M., Duque, J. F., Hoyos, S., Cárdenas-Rozo, A. L., Gómez, J., & Wilson, R. (2020). The Combia Volcanic Province: Miocene Post-Collisional Magmatism in the Northern Andes. In J. Gómez, & D. Mateus-Zabala (eds.), *The Geology of Colombia, Volume 3, Paleogene-Neogene* (pp. 355-394). Publicaciones Geológicas Especiales 37. Servicio Geológico Colombiano. <https://doi.org/10.32685/pub.esp.37.2019.12>
- White, W. (2013). *Geochemistry*. Wiley Blackwell.
- Zuluaga, D., Castro, P., Weber, M., Tobón, J. I., & Reyes, G. (2005). *El Dr. Emil Grosse y la elaboración de un texto geológico en Antioquia* [Memories]. X Congreso Colombiano de Geología, Bogotá.

SUPPLEMENTARY DATA 1

Digitized geological map of The Carboniferous Tertiary of Antioquia (Grosse, 1926) in the WGS 84 system.

SUPPLEMENTARY DATA 2

Geological map of the area. Taken from the Geological Map of Colombia (Gómez et al., 2015).

SUPPLEMENTARY DATA 3

Updated layer of sampling points was obtained for each specimen collected by Grosse (1926) in The Carboniferous Tertiary of Antioquia.

SUPPLEMENTARY DATA 4. TRANSCRIPTION IN SPANISH FROM THE ORIGINAL SAMPLES

N° de la muestra (Numeración de E. Grosse, ubicada en el extremo superior izquierdo)	N° de la muestra (ubicada en el extremo inferior derecho, en rojo)	N° de muestra en catálogo de la UN (ubicada en la parte anterior de la sección)	Transcripción de la descripción de la muestra, realizada por E. Grosse (i.e. recuadro superior de la sección delgada)	Transcripción de la ubicación de la muestra de roca (i.e. recuadro inferior de la sección delgada)	Interpretación de la Coordenada Norte, según la descripción de la ubicación en "E" (° ' ")	Interpretación de la Coordenada Oeste, según la descripción de la ubicación en "E" (° ' ")	Cajón
1	1798		Sierra Candela. Andesita hornbléndica augítica	Hac. La Suiza; Bloqueen la manga de la m	06 04 16,11	75 48 16,37	7
2	1796	UN 4422	Sierra Candela. Gabarro granudo en la andesita	Hac. La Suiza; Bloque en la manga de la m	05 54 35,11	75 48 29,29	7
4	1756	UN 4406	Corcobado, Andesita hornbléndica	1300 m al s de porvenir	05 52 54,41	75 42 12,20	7
5	1795		Andesita hornbléndica Sierra Candela	La Suiza, bloques en la manga de			7
6	1759	UN 4409	Corcobado, Andesita hornbléndica	1200 m al S de porvenir. Del contacto	05 53 14,49	75 42 21,16	7
8	1771	UN 4412	Arc. Piz. Modulos a 5 cm. Del contacto	1200 m al S de porvenir.	05 52 37,99	75 41 54,71	7
9	1790	UN 4419	Corcobado. Arc piz. Manchada	550 m al SO de Porvenir	05 53 22,23	75 42 36,42	7
10	1772	UN 4413	Corcobado Arc. Piz. Modulada 20cm	1200 m al S de Porvenir	05 52 48,69	75 42 39,26	7
11	1774	UN 4415	Corcobado. Arc piz. Modulada 1m "" del contacto	1200 m al S de porvenir C° al Cauca	05 52 31,88	75 42 19,41	7
12	1797	UN 4423	Sierra Candela; Andesita hornbl.	Hac. Corcobado I. Bloques cerca dela estufa	06 04 25,19	75 48 07,22	7
13	1809		Sierra Candela. Andesita hornbléndica augítica	Sierra Candela; término occidenj (Peña en la manga)	06 04 03,21	75 48 28,77	7
14	1810	UN 4426	Sierra Candela. Andesita hornbléndica augítica	Sierra Candela; término occidenj (Peña en la manga)	06 03 46,08	75 48 25,63	7
15	1773	UN 4414	Corcobado. Arc. Piz. modulada 30 cv del contacto	1200 m al S de Porvenir Camino al Cauca	05 52 49,47	75 42 23,99	7
16	1781	UN 4417	Corcobado. Arc. Piz. modulos a 5 m Del contacto	1200 m al S de Porvenir Camino al Cauca	05 52 02,68	75 42 22,06	7
17	1770	UN 4411	Corcobado. Arc piz. Modulos del contact	1200 m al S de porvenir. Camino al Cauca	05 52 34,44	75 42 06,10	7
18	1782	UN 4418	Corcobado. Arc. Piz. modulos a 5 m Del contacto	1200 m al S de Porvenir	05 53 05,82	75 42 36,79	7
19	1779	UN 4416	Corcobado. Arc. Piz. modulos a 3,5 m Del contacto	1200 m al S de Porvenir Camino al Cauca	05 51 57,85	75 42 24,40	7
20	1814	UN 4428	Pórfido augi	Mandal, Sabaletas; Bloques sueltos en el camino			7
21	608	UN 4152	Espilita	Amagá -Pta. De Bolombolo; unos 100 m de El lotero.			10
22	64	UN 4026	Anfibolita albitica con porfiroblastos de granate	Hac. La Cabaña, quebrada al E de Q. Guamo.	06 00 56,40	75 46 54,24	12
23	1831	UN 4434	Arcilla piz. Metam. Contacto. (silicificado?)	La Suiza, manda al NO de la casa de Hac.			7
24	611	UN 4155	Espilita; con esqueletos de plag. Y aug.	La Candela- Cauca			10
25	63	UN 4085?	Anfibolita albitica	Qu. Cantarrana; bac. Corcobado II.			12
26	755	UN 4205	Diorita cuarzosa micácea	Qu. Sinifaná C° Pte. Lolo	05 59 33,39	75 43 34,72	10
27			Andesita descompuesta	Punto de hallazgo desconocido			5
28	720	UN 4194	Tufa densa silificada	La Candela - Hollo grande (Titiribi)			10
35	1897	UN 4458	Andesita hornbléndica	Quebrada Doradita al O del Gazú	05 57 55,75	75 45 13,90	6
40	1741	UN 4399	Andesita hornbléndica	C. Tusa pié sept; de bloques sueltos	05 58 08,95	75 46 20,67	7
42	1757	UN 4407	Corcobado, Andesita hornbl.	5m Al S de Piedras Gordas.	06 03 04,19	75 45 45,74	7
43	1357	UN 4351	Arcilla pizarrosa (Tufita)	Titiribi-Pte. Soto. La punja			8
47	1596		Basalto feldespático Neoterc. tipo 1				8
48	1597		Basalto feldespático Neoterc. tipo 1	A. Medialuna derrumbe en el flanco NO, 2°. Derrumbe desde abejo			8
53	1883	UN 4448	Andesita hornbléndica	Morro Plancho; bloques al NE			7
54	1898		Andesita hornbléndica augítica	Hac. EL Amparo, al E de C. Brabo	05 56 54,98	75 41 20,23	6

N° de la muestra (Numeración de E. Grosse, ubicada en el extremo superior izquierdo)	N° de la muestra (ubicada en el extremo inferior derecho, en rojo)	N° de muestra en catálogo de la UN (ubicada en la parte anterior de la sección)	Transcripción de la descripción de la muestra, realizada por E. Grosse (i.e. recuadro superior de la sección delgada)	Transcripción de la ubicación de la muestra de roca (i.e. recuadro inferior de la sección delgada)	Interpretación de la Coordenada Norte, según la descripción de la ubicación en "E" (°'")	Interpretación de la Coordenada Oeste, según la descripción de la ubicación en "E" (°'")	Cajón
56	1754	UN 4404	Andesita hornbléndica descompuesta	Alto Cardona			7
57	249	UN 4067	Diorita (de augita) anfibolítica	Cascajosa, falda suroccid.			12
58	292	UN 4078	Diorita anfibólica (con hornbl.)	Qu. NE de Venecia	06 00 22,90	75 44 08,13	11
60	1747	UN 4402	Andesita hornbléndica	C. Bravo SE Bloqueslevantados	05 56 11,68	75 42 15,86	7
61	1746	UN 4401	Andesita hornbléndica	C. Bravo P Oriental de la roca viva	05 56 21,23	75 41 43,15	7
62	1675		Neoterc. Pasta de toba aglom.	al SE de Venecia bloques sueltos	05 57 02,52	75 43 33,83	7
63			Neoterciario, Toba densa	Barranco al suroeste de Venecia	05 57 11,18	75 44 24,57	5
64			Toba de cristales	Barranco al sureste de Venecia	05 56 28,22	75 43 32,11	5
65	1738	UN 4398	Arenisca endurecida por cont. Con corindón	De la brecha al pi NO del A. Filón			7
66	1737	UN 4397	Arcilla piz. Endurecida p. cont. Con corindón	De la brecha al pi NO del A. Filón			7
67	1682	UN. 4389	Neoterc. Basalto Hipersténico Bomba de toba agl.	Fredonia-Puente Iglesias despues de las casas del alto Caubrá	05 53 31,70	75 39 57,74	7
68	1042	UN 4302	Cuarzodiorita de biotita				8
69	1050	UN 4306	Keratofiro cuarzoso	Fredonia-Caldas 100 m antes de la Qu. Sinifaná			8
70	1047		Diorita augítica	Fredonia - Caldas 20´ antes de Qu. Sinifaná	05 59 06,24	75 41 53,23	8
71			Aplita de diorita cuarzosa	tredoma-caldas mas mantos al sur de la quebrada sinifaná	05 59 45,16	75 38 45,62	5
72	1049	UN 4305	Aplita de diorita	Fredonia-Caldas; 75m antes de Qu. Sinifaná	05 59 00,65	75 42 21,31	8
73	1727	UN 4394	Andesita micácea	A. Sillón pié NO bloques sueltos			7
77	1046		Diorita cuarzosa	Fredonia-La Fonda? -Caldas 10´ al S de Qu. Piedras Verdes	05 55 52,14	75 38 01,08	8
78	1704.		Neoterc. Toba de cenizas	Fredonia-A.Caubra Alt. 1875.	05 52 55,72	75 40 55,72	7
82	1703		Neoterc. Toba de cenizas	Fredonia-A.Caubra Alt. 1860.	05 52 24,33	75 40 30,43	7
90	2004	UN 4504	Basalto feldespático	Loma entre poblanco inferior y Cauca; 9° dique desde el Cauca	5 46 22,21	75 37 54,36	6
91	2005	UN 4505	Basalto feldespático	Loma entre poblanco inf y Cauca 7° dique en la loma desde el Cauca	5 46 27,57	75 37 26,08	6
92	2006	UN 4505	Basalto feldespático	Loma entre rio poblanco inf y Cauca, 8° dique desde el Cauca	5 46 22,37	75 37 35,92	6
95	2001	UN 4502	Basalto feldespático	Loma entre Poblanco inf y Cauca, 12° dique desde el Cauca	5 46 12,39	75 37 38,12	6
101	427	UN 4118	Peridotita (Harzburgita)	Qu. De Las Lomas. (Poblanco)	5 50 17,13	75 35 37,91	11
102	426	UN 4117	Roca de diálaga; filoncitos dentro de peridotita	Qu. De Las Lomas. (Poblanco)	5 50 12,93	75 35 40,24	11
103	429	UN 4119	Caliza cristalina; del contacto de la serp	Qu. De las Lomas (Poblanco)	5 50 19,61	75 35 31,66	11
106	1613	UN 4363	Basalto feldespático Neoterc. tipo 3	Sta. Bárbara- Pte. De la Pintada; 2 km al SSO de cruce de la Qu. Saladita			8
107	1615	UN 4365	Neoterc. Basalto feldespático	A. Llano grande; bloques magnéticos en la punta			8
108	1615a	UN 4366	Neoterc. Basalto feldespático. Tipo 4	A. Llano grande; bloques magnéticos en la punta			8
109	430	UN 4120	Peridotita (serpentina)	C° de S. Bárbara Pto. De la pintada; 1 km al S de Qu. Las Lomas			11
113	2001	UN 5403	Basalto feldespático	Loma entre poblanco inferior y Cauca 6° dique desde el Cauca	5 47 34,00	75 38 22,69	6
116	2008	UN4508	Basalto feldespático	Loma entre poblanco y Cauca, 1° dique desde el Cauca en la loma	5 47 51,92	75 37 58,62	6
117	2/71.		Dacita	Farallon sept oriental	05 58 10,40	75 45 39,54	5
118	18		Andesita hornbléndica	Farallón merid. Pié occidental de bloque suelto.	05 57 47,24	75 45 44,24	12
119	1616		Basalto feldespático Neoterc. tipo 4	C. Amarillo, borde sept	05 45 46,64	75 34 35,25	8
120	1617	UN 4368	Basalto feldespático Neoterc. tipo 4	C° De la Pintada-Damasco falda oriental; derrame intermedio	05 46 52,41	75 34 41,17	8
123	1614	UN 4364?	Basalto feldespático Neoterc. tipo 3	Cimarrones. Barranco occidental. 2° derrame			8
124	1610		Basalto feldespático Neoterc. tipo 3	Pte. De la pintada-Damasco derrame 2° inf en la falda oriental Cimarronas	05 46 37,10	75 34 49,22	8
127	1612	UN 4362	Basalto feldespático Neoterc. tipo 3	Pte. De la pintada-Damasco; cima de la 3a subida	05 46 32,90	75 35 15,32	8
128	1611	UN 4361	Basalto feldespático Neoterc. tipo 3	Pte. De la pintada-Damasco; pié de la 3°	05 46 31,33	75 34 55,86	8
129	696	UN 4186	Toba aglom de porfirita (sauss)	Qu. Garrapata. Salados. (Damasco)	05 47 34,56	75 34 15,62	10
132	697	UN 4187	Toba de porfirita aglomerática (sauss).	Qu. Garrapata, Salados (Damasco)	05 46 37,57	75 34 04,81	10
133	644	UN 4164	Tufa densa	Qu. Garrapata; Salados. Damasco	05 46 15,39	75 33 56,56	10
137	694	UN 4185	Toba de porfirita aglomerática (sauss).	Damasco-Pte de la plantada; lado oriental de la quiebra.	05 47 19,83	75 34 11,43	10
138	605	UN 4151	Pizarra silíceas	Damasco-Buey	05 47 20,50	75 34 28,05	11
140	462	UN 4129	Gabro sauss (con prenitita)	Qu. Morro Azul; C° S. Bárbara a Manizales	05 52 33,07	75 35 55,22	11
141	469	UN 4131	(Gabro apiz) Esquisto de gabro.	C° S. Bárbara- Manizales; salida hacia arriba? De la Qu. Morro Azul.	05 52 16,43	75 35 48,07	11
142	468	UN 4130	Segregación básica dentro de gabro sauss. Dial. Bronc. Magn. Ilm. Pirroti.	Qu. Matasano; C° S. Bárbara- Manizales	05 53 03,05	75 36 22,88	11
143	461	UN 4128	Gabro sauss	Qu. Matasano; C° S. Bárbara- Manizales	05 52 01,29	75 35 44,88	11

N° de la muestra (Numeración de E. Grosse, ubicada en el extremo superior izquierdo)	N° de la muestra (ubicada en el extremo inferior derecho, en rojo)	N° de muestra en catálogo de la UN (ubicada en la parte anterior de la sección)	Transcripción de la descripción de la muestra, realizada por E. Grosse (i.e. recuadro superior de la sección delgada)	Transcripción de la ubicación de la muestra de roca (i.e. recuadro inferior de la sección delgada)	Interpretación de la Coordenada Norte, según la descripción de la ubicación en "E" (" " ")	Interpretación de la Coordenada Oeste, según la descripción de la ubicación en "E" (" " ")	Cajón
145	470	UN 4135	(Gabro apiz) Esquisto de gabro	C° S. Bárbara- Manizález; entre la Qu. Matasano Y qu. M. Azul (mitad)	05 52 48,45	75 36 37,59	11
146	65	UN 4027	esquisto verde	C° S. Bárbara Manizales, entre la qu. Las Juntas y Qu. Matasano (mitad)	05 44 25,43	75 31 48,70	12
147	630	UN 4158	Porfírita augítica (saussuritizada)	S. Bárbara - Manizales; 17 m al N del Río Arma	05 43 17,71	75 32 44,07	10
200	135	UN 4044	Cuarcita aso??quintada, lecho de la granitita	Qu. Trujá, al E del puente del ferrocarril			12
204	769	UN 4211	Gabro básico dentro de granitita	De un bloque presentado. Qu. Amagá	06 04 01,20	75 44 56,24	10
205	770	UN 4212	(Granitita). Segregación básica (gabro).	F.C. Amagá; carrilera; pedazo de balasto	06 02 24,49	75 41 11,93	10
213	246	UN 4064	Diorita (de augita) anfibolítica	Desembocadura de la Qu. Gualú (Amagá)			12
214	315	UN 4083	Pegmatita de diorita saussurítica	Troso suelto al oriente del A. piedra pelona			11
216	1371	UN 4353	Jaspis de porcelana	Hac. Los Micos. Qu. Mica inf. (titiribi)	06 04 15,17	75 46 23,60	8
217	1387	UN 4356	Arc. Piz; fundida por un incendio de manto	Est. Angelópolis del FC de Amagá	06 05 04,22	75 42 05,26	8
218	245	UN 4063	Diorita (de augita) anfibolítica	Vertiente merid. De la qu. Amagá N del alto piedras	06 03 00,46	75 43 00,93	12
220	771	UN 4213	(Granitita). Segregación básica (gabro).	F.C. Amagá; pedazo de balasto	06 02 18,87	75 41 12,57	10
224	803		Pizarra	Alto polca; faldam meridional; pedazos sueltos			10
226	657	UN 4166	Porfírita augítica (saussuritizada)	Angelópolis - La Estrella; falda occid del Romeral	06 08 28,27	75 41 13,96	10
227	398	UN 4111	Peridotita (Harzburgita)	Falda oriental de la loma de Cantarana			11
229	399	UN 4112	Peridotita (Harzburgita)	Qu. La Vieja; al NO de Angelópolis			11
230	688	UN 4181	Toba de porfírita aglomerática saussuritizada	Angelópolis - La Estrella. Vert. Occid. Del Romeral.	06 08 27,65	75 41 31,10	10
231	708	UN 4190	Tufa de cristales epidotizada	Angelópolis-La Estrella; Vertiente Occidental del Romeral	06 08 21,50	75 41 51,46	10
232	965		Keratofiro cuarzoso	A. del derrumbe bloq. Suelto en la falda sept. Angelópolis	7 07 50,95	76 41 49,44	9
233	886		Diorita cuarzosa	Alto del derrumbe; ped suelto en la falda sept. Angelópolis	06 08 24,04	75 42 05,85	9
234	964	UN 4076	Keratofiro cuarzoso	Angelópolis-La Istulla Falda occidl del A. 1500 m al NE de Apolis.	8 07 50,95	77 41 49,44	9
234	29i	UN 4076	Diorita anfibólica (con hornbl)	Amagá- Titiribi. 350 m al N de Piedras Gordas	06 03 13,47	75 43 42,63	11
235	887		Diorita cuarzosa porfirítica	Alto del derrumbe; ped suelto en la falda occid Angelópolis	06 08 30,35	75 42 04,72	9
236	910		Roca de biot. Aug. Y hornbl. Descompuesta (fac. bás) de diorita	A. del derrumbe. Parte media del derrumbe. Angelópolis.	06 08 09,25	75 42 05,58	9
237	871		Diorita sauss de grano fino	A. del derrumbe bloq. Suelto en la falda sept. Angelópolis	06 08 18,73	75 42 05,87	9
238	966		Keratofiro cuarzoso	A. del derrumbe bloq. Suelto en la falda sept. Angelópolis	06 07 50,95	75 41 49,44	9
239	974		Keratofiro				9
241	709	UN 4191	Toba de cristales	Angelópolis-Caldas.Pié del Romeral.	06 07 47,94	75 41 49,00	10
242	714	UN 4192	Tufa densa	Angelópolis-Caldas.Pié del Romeral.	06 07 47,94	75 41 49,00	10
243	342	UN 4091	Gabro anfibólico				11
244	344	UN 4094	Gabro anfibolítico	Angelópolis - Titiribi al E de Matasano	06 06 57,62	75 43 56,40	11
245	401	UN 4114	Peridotita (Harzburgita)	Cantarana; C° viejo de Angelópolis - Titiribi	06 04 41,43	75 42 42,59	11
246	400	UN 4113	Peridotita (Harzburgita)	Cantarana; C° nueva de Angelópolis - Titiribi	06 05 04,00	75 42 43,79	11
247	804		Pizarra nica	Alto Polca; falda SO; pedazos sueltos			10
248	833		Roca cornea micácea (cornubianita)	Qu. Ramirez; 100 m abajo del contacto de granito			10
249	834		Roca cornea micácea (cornubianita)	Descenso al salado en la qu. Ramirez			10
250	835		Roca cornea micácea (cornubianita)	Qu. Ramirez 150 m arriba del salado			10
252	343	UN 4093	Gabro anfibolítico	1,8 km al O de Angelópolis	06 07 02,47	75 43 36,27	11
253	909		Diorita cuarzo-augítica; De la diorita tipo de Helic.	Qu. Ramirez; 500 m arriba del C° Angelópolis-Pueblito	06 08 54,00	75 42 07,43	9
254	935		Aplita de diorita; epidotizada; filoncito	Qu. Ramirez; 500 m arriba del c° Angelópolis-Medellín	06 08 36,45	75 42 08,45	9
255	934		Aplita de diorita; epidot; filon	Qu. Ramirez; 500 m arriba del c° Angelópolis-Medellín			9
256	1024	UN 4297	Roca de epidota	Qu. Ramirez; 500 m arriba del C° de llegada a pueblito	06 09 36,50	75 42 18,37	9
258	2052		Granodiorita cataclástica	Cuchilla al O del salado en la Q. Ramirez, parte sept. De angelópolis	06 07 32,57	75 41 55,59	6
259	938		Aplita de diorita; epidotizada; filoncito	Qu. Ramirez; 600 m arriba del c° Angelópolis-Medellín	06 09 26,99	75 42 05,26	9
260	962		Keratofiro cuarzoso	Angelópolis-Pueblito; unos 30 m arriba del camino en la Qu. Ramirez.	06 07 52,90	75 42 04,88	9
261	764	UN 4210	Granitita	Qu. Quinta. 600 m arriba de la desemb.			10
262	773	UN 4214	Facies básica marginal de la granitita	Qu. Quinta?; 600 m arriba de la desemb.			10
265	800		Roca cornea micácea (cornubianita)	Qu. Quisita?; Lado norte; pocos metros arriba de la desemb.			10
266	685	UN 4179	Toba densa de porfírita epidotizada	Qu. Quiritú Guijarro (Ángelópolis)			10
270	436	UN 4121	Serpentina apizarrada	Cuerpo pequeño al E de Morro Plancho. A' polis.			11
271	346	UN 4096	Gabro anfibolítico	Pie SO de Morro Plancho	06 07 45,12	75 43 48,02	11

N° de la muestra (Numeración de E. Grosse, ubicada en el extremo superior izquierdo)	N° de la muestra (ubicada en el extremo inferior derecho, en rojo)	N° de muestra en catálogo de la UN (ubicada en la parte anterior de la sección)	Transcripción de la descripción de la muestra, realizada por E. Grosse (i.e. recuadro superior de la sección delgada)	Transcripción de la ubicación de la muestra de roca (i.e. recuadro inferior de la sección delgada)	Interpretación de la Coordenada Norte, según la descripción de la ubicación en "E" (°'")	Interpretación de la Coordenada Oeste, según la descripción de la ubicación en "E" (°'")	Cajón
272	250	UN 4068	Diorita anfibolítica	A. Partudo. Falda oriental.			12
274	978		Keratófiro	Depresión 1500 m al SE del Alto Delgadito			9
275	977		Keratófiro	Depresión 1500 m al SE del Alto Delgadito			9
276	832	UN 4227	Pórfido cuarzosos; fácies marginal de la granitita	A. Montelargo; falda merid.			10
277	2050		Granodiorita aplastada	400 m antes de la desembocadura de la quebrada Santa Barbara	06 00 03,20	75 40 36,67	6
278	360	UN 4099	Gabro anfibólico	Pueblito - Armenia 200 m al SO de la Quiebra	06 09 16,26	75 44 34,72	11
279	365	UN 4101	Gabro anfibolítico	Armenia - Pueblito, 175 m SO de la Quiebra	06 09 19,50	75 44 45,79	11
280	366	UN 4102	Gabro anfibolítico	Amagá - Pueblito 175 m SO de la Quiebra	05 59 44,69	75 42 00,87	11
281	96	UN 4039	Esquisto actinolítico	Armenia-Pueblito; al SE de A. Mojones.	06 09 39,96	75 46 09,44	12
284	371	UN 4105	Gabro saussurítico	Armenia - Pueblito, 500 m SO de la Quiebra	06 09 55,33	75 44 15,25	11
285	66	UN 4028	Anfibolita albitica	A. Caracol; cima SO; falda oriental			12
286	370	UN 4104	Gabro saussurítico	Armenia - Pueblito; 450 m al SO de la Quiebra	06 09 46 87	75 44 23,55	11
287	87	UN 4038	Esquisto actinolítico	Armenia-Pueblito; al SE de A. Mojones.	06 09 45,31	75 46 04,53	12
288	40	UN 4019	Filita calcárea	Titiribí-A' polis. Pte. Taparral.	06 05 23,69	75 47 01,70	12
289	48	UN 4022	Filita graffítica	Caracol falda oriental del alto SE.			12
290	67	UN 4029	Anfibolita albitica	Alto Caracol cima SO; falda oriental			12
291	68	UN 4030	Anfibolita albitica	Armenia-Pueblito; al SE del A. Mojones.	06 09 51,39	75 45 57,81	12
293	2061		Diorita anfibólica aplastada	Qu. de las Ánimas; cerca del límite diorita - terc. carb.	06 07 35,11	75 41 53,10	5
294	372	UN 4106	Gabro saussurítico	Armenia - Pueblito; 450 m al SO de la Quiebra	06 09 46 87	75 44 23,55	11
295	35	UN 4017	Filita micácea	Armenia - Pueblito al SE del alto Mojones	06 09 59,94	75 45 51,17	12
296	373	UN 4107	Gabro saussurítico	Armenia-Pueblito; 400 m al SO de la Quiebra	06 09 40,03	75 44 28,51	11
297	260	UN 4069	Diorita anfibolítica	Armenia- Pueblito Falda occidental del Alto Palo Blanco	06 06 41,06	75 45 12,46	12
298	39	UN 4018	Filita calcárea	Qu. Montoya, desembocadura.			12
300	361	UN 4100	Gabro anfibolítico	Lecho de la Qu. Amagá, al NNE de piedras Gordas.	06 05 30,73	75 45 05,09	11
301	1191		Anfibolita albitica; globa en porfido diorítico	Armenia-Paso de cangrejo; 1 700 km después de Arm.	06 11 03,10	75 47 37,20	8
302	1187		Pórfido cuarzodiorítico	Armenia-Paso del Cangrejo; 1100 m después de Armenia	06 14 24,64	75 51 00,55	8
303	1188		Porfido cuarzodiorítico	Armenia- Paso del cangrejo; 1100 m después de Jm.	06 13 45,52	75 51 17,21	8
304	1189		Pórfido cuarzodiorítico	1500 m antes de Armenia.	06 10 02,12	75 45 30,82	8
305	1190		Anfibolita albitica En pórfido diorítico	Armenia- Paso de cangrejo; 1700m después de Jm.	06 12 42,38	75 49 03,54	8
307	1964	UN 4484	Andesita hornbléndica	cerro castillo			6
309	579	UN 4149	Brecha	Titiribí-Balsal; descanza al "			11
310	610	UN 4154	Espilita	Titiribí-Paso de los pobres; 1 km antes de bolomb.	06 03 21,46	75 49 37,35	10
311	678	UN 4175	Hialodiabasa	Titiribí - Balsal; esquina 880 m al O de Cucaracho			10
314	1962	UN 4482	Andesita hornbléndica	Cerro Tusa, peña 400 m al O de la estufa	05 58 0,15	75 46 32,11	6
315	1961	UN 4481	Andesita hornbléndica	Cerro Tusa, peña a 400 m al oeste de la estufa	05 58 06,75	75 46 31,90	6
316	1959	UN 4480	Andesita augítica-hornblendífera	A. organos			6
319	1963	UN 4483	Andesita hornbléndica-argílica	A. buena vista vertiente SO Qu. Narezo			6
321	1679	UN 4388	Neoterc. Basalto Bomba de toba agl.	A. Buenavista (SO de C. Tusa) falda NO	05 57 29,35	75 46 29,81	7
322	1677		Neoterc. Basalto. Bomba de una toba aglom.	A. Buenavista (SO de C. Tusa) falda NO	05 57 21,95	75 46 29,80	7
323	1678		Neoterc. Basalto feldespático. Bomba de una toba aglom.	A. Buenavista (SO de C. Tusa); pié sept bloques sueltos	05 57 25,25	75 46 34,92	7
324	232-75		Madera fosil de los micos	de la capa de ceniza arriba del A. escudradero			5
325	1664		Andesita augítica, pasta de una toba aglomerática	A. Buenavista (SO de C. Tusa); Falda NO	05 57 43,60	75 46 34,50	7
327	1352	UN 4352	Arcilla Piz. En nodulito de contacto	Titiribí-paso delos pobres; 30m al Nde Qu. Chorros	06 04 31,22	75 48 16,42	8
328	1391	UN 4357	Arcilla piz. Tostada por incendio de manto	Titiribí- La Alp 30 m antes de terreno Junta	06 03 03,42	75 47 28,24	8
329	1742	UN 4400	Andesita hornbléndica	C. Tusa ; pié SO de la roca viva	05 57 34,01	75 46 31,89	7
333	247	UN 4065	Diorita (de augita) anfibolítica	Amagá-Titiribí 1,5 km al O de Amagá	06 02 50,48	75 42 54,81	12
335	29i	UN 4077	Diorita anfibólica (con hornbl.)	Amagá- Titiribí. 350 m al N de Piedras Gordas	06 03 32,72	75 43 42,04	11
337	312	UN 4082	Diorita anfibólica gneisica	200 m al N de Piedras Gordas, Amagá - Titiribí	06 03 22,00	75 43 41,93	11
338	1842	UN 4440	Sierra Vetas. Gabro básico en la andesita hornbl.	Titiribí, Paso de los pobres Qu. Chorros	06 03 45,41	75 48 03,93	7
339	1843	UN 4441	Sierra Vetas. Andesita hornbl. Con inclusion de filita	Titiribí paso del. 15 m al E de Q Maul??	06 03 37,84	75 48 29,83	7
340	1861	UN 4444	Esquisto verde (Precambrico)	Q. Chorros 10 m al E de la au De Sierra Vetas.			7

N° de la muestra (Numeración de E. Grosse, ubicada en el extremo superior izquierdo)	N° de la muestra (ubicada en el extremo inferior derecho, en rojo)	N° de muestra en catálogo de la UN (ubicada en la parte anterior de la sección)	Transcripción de la descripción de la muestra, realizada por E. Grosse (i.e. recuadro superior de la sección delgada)	Transcripción de la ubicación de la muestra de roca (i.e. recuadro inferior de la sección delgada)	Interpretación de la Coordenada Norte, según la descripción de la ubicación en "E" (" " ")	Interpretación de la Coordenada Oeste, según la descripción de la ubicación en "E" (" " ")	Cajón
341	1839	UN 4438	Sierra Vetas. Andesita augítica hornblendífera	Q. Chorros. Pié del salto unos 50 m al E del C° Titiribi-Cauca	06 02 39,49	75 49 58,23	7
342	1835	UN 4436	Sierra Vetas. Andesita micaciaugítica	Qu. Murial alt. 1425 m.	06 03 43,95	75 48 44,42	7
343	1919	UN 4466	Arcosa, en contacto con un silo	titiribi - p viejo, 550m al N de T	06 04 05,11	75 47 38,32	6
344	1914	UN 4464	Andesita hornbléndica	Qu Media1100 m al so de titiribi, silo A	06 03 08,01	75 47 21,00	6
345	1838	UN 4437	Sierra Vetas. Andesita hornbléndica	Titiribi paso del. 15 m al E de Q Maul	06 03 37,15	75 48 47,76	7
346	1832	UN 4435	Sierra Vetas. Andesita micacihornbléndica	Titiribi- hoyo 700 m al SE del morro Vetas	06 02 55,21	75 50 06,71	7
347	1903	UN 4461	Arc. Piz mandrada	Titiribi - los Alpes, 40 m después de la quebrada las Juntas	06 04 48,22	75 47 17,21	6
348	1901	UN 4460	Andesita hornbléndica alterada	Titiribi-los-alpes 40 m después de la quebrada las juntas	06 03 26,01	75 47 24,55	6
349	1910.	UN 4463	Arenisca endurecida	Titiribi - los Alpes lado sept. De la 1 cañada después de la quebrada las Juntas	06 04 16,28	75 47 33,63	6
350	1905	UN 4462	Andesita	Titiribi los alpes, despues de la quebrada las juntas	06 03 20,16	75 47 20,66	6
351	1918	UN 4465	Andesita hornbléndica	Titiribi Paso de los potres, 440 m al NO de Titiribi, silo	06 03 59,58	75 47 47,93	6
352	1811	UN 4427	Sierra Candela Andesita augítica.	400 m al S de Titiribi sel contacto contra arcilla piz	06 03 24,48	75 47 23,79	7
353	1841	UN 4433	Sierra Vetas. Andesita alterada. Silo detás de acrilla pizarrosa terciaria	Barranco al SE alO. De M. Vetas			7
354	1794	UN 4420	Sierra Candela. Andesita hornbléndica	Falda oriental del A. Suiza. (al O de la V. finá)			7
355	1827	UN 4431	Andesita augítica	Alto (falda occid.) 500 m al S del puerto sobre quebrada Juntas Titiribi	06 03 18,45	75 47 16,02	7
356	1830	UN 4433	Arenisca endurecida terciaria	Del contacto sept. De la andesita			7
357	1828	UN 4432	Adinola, del contacto de andesita	Del contacto sept. De la andesita			7
358	1818		Brecha de andesita	Qu. Juntas. 1200 m al SE de Titiribi	06 03 11,93	75 47 21,43	7
359	1819	UN 4430	Brecha de andesita	Qu. Juntas. 1200 m al SE de Titiribi	06 03 07,04	75 47 19,32	7
360	1844	UN 4442	Sierra Vetas. Andesita alterada				7
361	2083		Andesita propilitizada				5
362	1845	UN 4443	Sierra Vetas. Andesita propilitizada y sericitizada	M. altos Chorros			7
363	57	UN 4024	Anfibolita albitica	Filón Lodos roca encajante soc judep.			12
364	50	UN 4023	Anfibolita albitica	Zancudo; Pastelillo-Judip.	06 05 10,80	75 47 45,24	12
365	2064		Esquisto verde	Quebrada Juntas	06 05 10,17	75 47 10,53	5
366	670	UN 4172	Diabasa sauss con prenitá	Loma del Algorr; 1125 m al sup de "La Meseta"	06 18 22,15	75 46 17,03	10
367	609	UN 4153	Espilita				10
368	1372	UN 4354	Jaspis de porcelana	Hac. Los Micos Qu. Mica inf. Titiribi	06 04 27,31	75 46 18,36	8
369	1374	UN 4355	Arcilla pis. tostada	Hac. Los Micos; Altico al S de peña blanca	06 03 30,17	75 46 22,25	8
372				100 m al sur de la fabr. de azúcar de la hacienda los micos			5
373	42	UN 4020	Anfibolita albiti-calcárea	Qu. Amagá debajo de la desembocadura de la q. Peñitas.	06 06 10,60	75 48 18,58	12
375	378	UN 4108	Pegmatita de gabro anfibolítica	Heliconia - conta; cerca del límite contra la diorita	06 15 21,49	75 45 10,88	11
376	348	UN 4097	Gabro anfibolítico	Heliconia - Cauca	06 11 53,61	75 44 42,99	11
377	421	UN 4116	Jadeitita	Falda oriental del A. Calvario. Heliconia	06 11 34,00	75 44 18,38	11
378	446	UN 4124	Peridotita (serpentina)	S. José; C° de Heliconia a Sevilla	06 15 08,03	75 45 01,57	11
380	414	UN 4115	Roca de diálaga; filoncitos dentro de peridotita	Falda oriental del A. Calvario. Heliconia	06 11 16,21	75 44 13,36	11
381	846	UN 4227	Granitita cataclástica	Qu. Matasano. Del salado Heliconia.	06 12 36,26	75 44 17,87	10
382	2053		Granito milonitizado	Quebrada sabaleta abajo del camino Heliconia Pueblito	06 11 17,47	75 42 43,56	6
383	821	UN 4226	Granitita	Qu. Horcona; sa lado Superior	06 08 59,90	75 43 09,84	10
384	2057		Tect granitita condensa	Heliconia -Sevilla; Camino viejo entre Qu. Porquera y Sn José	06 14 55,90	75 44 51,88	5
385	261	UN 4070	Diorita (de augita) anfibolítica	Heliconia-Cauca. Cerca de la anfibolita	06 11 55,41	75 45 12,40	12
386	385	UN 4109	Roca de anfíbol	Pueblito - Armenia; límite entre peridotita y gabro anfibolítico	06 10 02,75	75 43 47,01	11
387	853		Diorita cuarzosa (Tipo de Heliconia)	El Uvito. 1750 m al ESE de Heliconia	06 12 03,63	75 43 01,86	9
388	869		Diorita cuarzosa (Tipo de Helic) sauss	Qu. Sabaletas; al NE de Pueblito	06 11 13,11	75 42 35,31	9
389	856	UN 4231	Diorita cuarzosa (Tipo de Heliconia)	Qu. Sabaletas al NE de Pueblito	06 10 49,77	75 42 45,75	9
390	857	UN 4232	Diorita cuarzosa (Tipo de Helic)	Qu. Sabaletas al NE de Pueblito	06 11 01,19	75 42 38,05	9
391	984		Arenisca arcillosa; metam por cont. Del límite contra la diorita	Pueblito-Medellín; Pié de la loma.	06 10 05,77	75 43 35,15	9
392	983		Arenisca arcillosa; metam por cont. Del límite contra la diorita	Pueblito-Medellín; Pié de la loma.	06 10 01,85	75 43 29,07	9
393	69	UN 4031	Esquisto verde (prob. Diorita fac. básica apizarrada)	Pueblito - Medellín 1675 m al NE de P. (capilla)	06 10 13,00	75 42 58,79	12
394	1017	UN 4295	Keratofiro apizarrado	Pueblito-Medellín	06 10 33,16	75 42 41,86	9
395	879		Diorita cuarzosa (tipo Hel) facies (aplítica) ácida	Pueblito-Medellín	06 09 57,03	75 42 29,11	9

N° de la muestra (Numeración de E. Grosse, ubicada en el extremo superior izquierdo)	N° de la muestra (ubicada en el extremo inferior derecho, en rojo)	N° de muestra en catálogo de la UN (ubicada en la parte anterior de la sección)	Transcripción de la descripción de la muestra, realizada por E. Grosse (i.e. recuadro superior de la sección delgada)	Transcripción de la ubicación de la muestra de roca (i.e. recuadro inferior de la sección delgada)	Interpretación de la Coordenada Norte, según la descripción de la ubicación en "E" (°'")	Interpretación de la Coordenada Oeste, según la descripción de la ubicación en "E" (°'")	Cajón
396	976		Keratofiro	Pueblito-Medellín	06 10 33,16	75 42 41,86	9
398	937		Aplita de diorita; epidot filoncito	Pueblito-Medellín	06 10 11,88	75 42 31,54	9
399	956		Keratofiro cuarzoso	Pueblito-Medellín, nido dentro de diorita	06 10 33,16	75 42 41,86	9
401	936		Aplita de diorita; epid; filoncito	Pueblito-Medellín	06 10 06,13	75 42 33,09	9
402	1016	UN 4294	Keratofiro cuarzoso, apizarrado	Pueblito-Medellín	06 10 33,16	75 42 41,86	9
403	1018	UN 4296	Keratofiro cuarzoso, cataclástico	Qu. Horcona; 30 m arriba del			9
404	844	UN 4228	Gabro olivínico metam	Qu. Sabaletas; abajo del C° Pueblito - Heliconia; terraño dentro de granito	06 10 16,12	15 44 18,00	10
405	707	UN 4189	Tufa de cristales; completam. Descomp (epidotizada)	Qu. Horcona; parte sup pié del Romeral	06 09 51,04	75 41 41,02	10
406	686	UN 4180	(diorita, porfírita) epidotizada y uralitizada	Qu. Horcona, Parte sup	06 09 39,36	75 42 09,96	10
407	715	UN 4193	Tufa densa; epidotizada	Qu. Malpaso; poco al O del pié del Romeral	06 07 47,94	75 41 49,00	10
408	662	UN 4168	Porfírita augítica (saussuritizada)	Qu. Sabaletas; al NE de Pueblito	06 11 13,99	75 42 39,23	10
409	439	UN 4122	Roca corneana del contacto de la serpentina	Lomo al E de Morro Plancho (Angelópolis)			11
410	263	UN 4071	Diorita anfíbolítica	2750 m al NO de Ebéjico; vert. Oriental de la qu. Llaná	06 20 50,56	75 47 09,31	12
411	28	UN 4015	Filita sericítica.	Qu. Pitirú; al E de Sevilla			12
412	669	UN 4171	Diabasa (Probabl)	Murrapel - Canoas			10
413	999	UN 4291	Porfírita diabásica; saussuritizada	Ebéjico-San Sebastian 50 m al E del límite contra el terciario carb.	06 20 30,29	75 44 57,16	9
414	636	UN 4161	Porfírita labradorítica (Saussuritizada) ((Keratofiro)	La Comunidad pié occidental del A. Cedro. Ebéjico	06 18 07,89	75 44 45,98	10
415	692	UN 4184	Tufa de porfírita aglomerática	Ebéjico - Medellín; 1600 m al N de A. Canoas.	06 17 19,51	75 43 22,81	10
416	1007		Diorita apizarrada	Qu. Zaguá; 1900m al S de la desembocadura	06 20 16,27	75 44 53,34	9
417	454	UN 4125	Peridotita (serpentina)	Qu. Juan Vaquero, al E del C° de Ebéjico a Sopetrán	06 22 2,19	75 46 58,91	11
418	2072		Diorita	Quebrada Zaguá, a 3/50m de la desembocadura	06 20 10,87	75 43 56 98	5
419	287	UN 4074	Diorita cuarzosa anfíbolítica	A. Chuscal. Borde oriental.	06 23 16,72	75 40 45,13	12
420	23i	UN 4060	Granodiorita matamórfica	Heliconia - Ebéjico; 500 m al NO del cruzamiento de la qu. La Clara	06 16 20,91	75 45 51,26	12
421	950		Porfírita cuarzosa (Preñitizada)	Qu. Zaguá; 3150 m al sur de la desembocadura.	06 20 49,94	75 44 56,62	9
422	322	UN 4084	Beresita	Depresión entre el Alto Chuscal y A. d las Brisas	06 14 59,33	75 45 58,43	11
423	70	UN 4032	Anfibolita albítica	Loma de Quirimará, Alto Palo Blanco falda NO	06 21 42,81	75 48 19,80	12
424	681	UN 4178	Keratofiro	Ebéjico-S. Jerónimo (C° sup); Falda del A. Gramal.	06 20 27,76	75 44 12,30	10
425	30i	UN 4079	Diorita (de augita) anfíbolítica, apizarrada.	Loma de Quirimará límite sur entre el precámbrico.	06 20 06,27	75 47 02,87	11
426	906		Diorita uralitizada (facies básica) de diorita	Ebéjico-S. Sebastian falda occid. del A. Gramal	06 20 17,14	75 44 24,66	9
427	905		Roca de augita uralitizada; segregación básica dentro de diorita	Ebéjico-S. Sebastián; falda NE del Alto Gramal			9
428	1006	UN 4292	Diorita apizarrada	Ebéjico-S. Sebastián; prte sup de la falda occid. Del Alto Gramal.	06 20 30,62	75 44 27,12	9
429	723	UN 4196	Porfírita labradorítica epidotizada	Ebéjico - Medellín 2° cañada antes de la qu. Enselma	06 17 44,45	75 44 27,01	10
431	233	UN 4061	Granodiorita gnésica metamórfica	Qu. Juan Capitán; 2 km al SSE de Ebéjico	06 18 54,85	75 46 22,37	12
432	959		Keratofiro cuarzoso	Ebéjico-Medellín; 75 m después del límite Paltos--form Porfíritas			9
433	888		Diorita cuarzosa (Tipo de Heliconia) facies ácida	Alto de Cedro. Falda NO; C° viejo de Ebéjico a Medellín	06 18 22,43	75 44 51,10	9
436	947		Keratofiro cuarzoso	Qu. Jeferina; al N del A. denrimo			9
437	946		Keratofiro cuarzoso	Qu. Lafarina; al N del A.			9
438	679	UN 4176	Keratofiro cuarzoso	Alto Retiro; falda merid (Ebéjico)	06 21 47,76	75 44 32,90	10
439	691	UN 4183	Toba de porfírita aglomerática (Keratofiro)	Ebéjico- Medellín; 2600 m al SE de Eb	06 18 4,14	75 45 14,99	10
440	998	UN 4290	Porfírita metamorfosea por contacto	Loma de Miraflores Falda sept.			9
441	997	UN 4289	Porfírita labradorítica metamorfosea por contacto; aglomerada	Loma de Miraflores Falda NO (Ebéjico)	06 18 25,93	75 44 12,14	9
442	908		Diorita augítica (uralitizada; cataclástica fac. bas de diorita)	Oíé occid. Del Alto Buena Vista en frente del A. Churimó			9
443	996	UN 4288	Porfírita metamorfosea por contacto	Cuchilla de Miraflores; vert. Sept			9
444	889		Diorita cuarzosa (Tipo de Heliconia) facies ácida	Ebéjico-S. Sebastian; 100 m al E del tunel terciario carbonífero-from de porfírita	06 20 28,23	75 44 50,63	9
445	890		Diorita cuarzosa (Tipo de Helic) facies ácida	Ebéjico-Medellín; 200 m al S de la Qu. Honda	06 18 47,06	75 46 17,57	9
446	911	UN 4166	Diorita cuarzosa saussuritizada	Qu. Lefarri Del A diurn			9
447	679a	UN 4177	Keratofiro	Alto Retiro; vertiente occid.			10
448	675	UN 4173	Diabasa porfírita sauss. (Diorita porfírita terc.)	Ebéjico - Medellín 80 m antes de qu. Enselma	06 18 26,30	75 46 22,11	10
449	676	UN 4174	Porfírita de diabasa sauss. (prob. Diorita porfírita)	Ebéjico - Medellín 10 m antes de Qu. Enselma	06 18 26,30	75 46 22,11	10
450	867		Diorita saussuritizada	Ebéjico-Medellín; 150 m antes de qu. Honda	06 18 47,49	75 46 24,27	9

N° de la muestra (Numeración de E. Grosse, ubicada en el extremo superior izquierdo)	N° de la muestra (ubicada en el extremo inferior derecho, en rojo)	N° de muestra en catálogo de la UN (ubicada en la parte anterior de la sección)	Transcripción de la descripción de la muestra, realizada por E. Grosse (i.e. recuadro superior de la sección delgada)	Transcripción de la ubicación de la muestra de roca (i.e. recuadro inferior de la sección delgada)	Interpretación de la Coordenada Norte, según la descripción de la ubicación en "E" (°'")	Interpretación de la Coordenada Oeste, según la descripción de la ubicación en "E" (°'")	Cajón
509	1098	UN 4317	Diorita tipo de poleal	Alto Quiñones, Qu. Ramirez	06 20 33,03	75 44 47,89	8
510	1169	UN 4339	Cornubiana andalucítica	? Del A. Quiñones; arroyo 150 m al SSE de la parada	06 21 02,29	75 45 07,36	8
510	1169	UN 4339	Cornubiana andalucítica	Pié occid. Del Alto Quiñones; arroyo 150 m al SSE de la posada	06 20 53,19	75 45 08,48	8
511	651	UN 4165	Toba aglomerática epidotizada y prenitizada, etc.	Qu. Tambora S. Jerónimo	06 26 44,25	75 44 36,69	10
513	638	UN 4162		Ebéjico - S. Jerónimo (C° inf) 1650 m al N de la sucia			10
514	728	UN 4197	Porfírita epidotizada	S. Jerónimo - Ebéjico; vertiente sept de la Loma Hermosa.	06 26 15,42	75 44 59,30	10
515	971	UN 4145	Keratófiro (tal vez efusivo)	Loma Hermosa, Cresta			9
516	642	UN 4163	Queratófiro (facies marginal de un)	Loma Hermosa; Cresta.			10
517	658	UN 4167	Porfírita augítica	Loma Hermosa? 3100 m al SE de la cara de la hacienda			10
518	970		Keratófiro (tal vez efusivo)	Loma Hermosa, Cresta			9
519	690	UN 4182	Toba aglomerática de porfírita	Loma Hermosa (oeste)			10
520	2069		Porfírita brechoza	Quebrada Guaracú, 300m arriba del C° S. Jerónimo-Ebéjico	06 25 58,96	75 44 03,23	5
521	184	UN 4049	Cuarcita micácea micectada	Sopetrán-S. Pedro alt.			12
522	1070		Tonalita	Qu. Grande 550 m al NE de S. Jerónimo	06 28 11,66	75 41 19,22	8
523	203	UN 4050	Granitita (lenticular) apizarrada	Loma de Cabuyal 75 m al E del limite contra gabro.	06 25 06,75	75 42 00,87	12
525	4	UN 4002	Arcaico. Anfibolita esquistosa	Qu. Nuarque C° Córdoba Sucre 50 m antes	06 32 26,32	75 46 17,55	12
526	19	UN 4011	Roca de epidota, nidos dentro de anfibolitas	Sopetrán - Sucre; 6m al NE de la De la Qu. Yuná	06 31 28,47	75 46 02,87	12
527	1029	UN 4009	Diorita micácea (en prenit)	Córdoba-Suiza; 6 m en el tallo? De la falda antes de la qu. Yuná	06 31 31,61	75 46 11,24	9
528	13	UN 4009	Arcaico. Mesocuarcita Y hornbléndica	Córdoba - Sucre; 3 m en el techo de la falda antes de Qu. Yuná	06 32 41,40	75 44 59,18	12
530	1160	UN 4336	Cuarcita micacifeldespática	Sopetrán-Medellín. 750 m antes de qu. De los Arias	06 28 05,77	75 40 03 49	8
531	1161	UN 4337	Cuarcita micacifeldespática	Sopetrán-Medellín. 1 km al NO de cruzamiento en la Qu. de los Arias	06 28 11,50	75 39 45,15	8
532	1146	UN 4335	Filita andalucítica	Sopetrán-Medellín 2/25 km antes de Qu. Cedros.	06 28 38,74	75 42 21,88	8
533	1094		Epesartita; filoncito dentro de diorita tipo Poleal	Sopetrán-Medellín 250 m Antes de Qu. De Los Arias.	06 28 27,03	75 40 38,79	8
533	27	UN 4014	Filita sericitica	200 m al S de Sacaajal.	06 37 03,49	75 47 55,89	12
535	459	UN 4127	Peridotita (Harzburguita)	Qu. Tajami, Sucre.	06 35 18,83	75 47 12,47	11
537	98	UN 4040	Esquisto verde, roca ígnea metamórfica.	Qu. Barbudo al NE de Sacaonal.	06 37 11,31	75 47 01,64	12
538	99	UN 4041	Anfibolita albitica	Qu. Coldión; al SE del A. Tunalcito.			12
539	749	UN 4204	Toba densa metamórfica (apizarrada saussuritizada)	Qu. Potrera; abajo del precámbrico. Sucre.	06 35 29,63	75 46 44,56	10
541	52	UN 4037	Anfibolita albitica	150 m al E del galápago del A. Boquerón al E de Sacaonal.			12
542	732		Porfírita apizarrada (sauss)	Qu Nuarque. 600 m arriba del puente en el C° Córdoba - Sucre	06 32 34,88	75 45 55,62	10
543	730	UN 4198	Silex	Palogrande; falda merid.			10
544	3	UN 4001	Arcaico. Anfibolita esquistosa	Córdoba - Sucre 100 m después de qu. Nuarque	06 32 25,82	75 46 07,69	12
545	5	UN 4003	Arcaico; Anfibolita esquistosa.	Qu. Nuarque; 400 m al E de C° Sucre-Córdoba.	06 32 29,37	75 46 03,76	12
546	735	UN 4202	Esquisto verde (Precámbrico)	Sopetrán - Sta. Rosa; 450 m al E. de S.	06 30 14,08	75 44 17,89	10
547	1027	UN 4298		Alto busillada Falda occid.			9
548	11	UN 4007	Anfibolita densa alterada con nidos de cuarzo y zeolitas	Salado grande de Córdoba. Cerca de la pajón	06 31 35,60	75 45 52,30	12
549	1030	UN 4299	Keratófiro cuarzoso; apizarrado	Qu. Nuarque; 400 m al E del C° Sucre-Córdoba	06 32 51,96	75 46 02,07	9
550	110	UN 4042	Gneis moscovítico lenticular	Loma del Palo Grande- La. Pasaje Palo Grande.	06 31 55,54	75 45 40,04	12
551	157	UN 4045	Granito lenticular	Sopetrán - Belmira falda del alto de la Ceja.	06 32 57,95	75 40 55,63	12
552	168	UN 4046	Micacita inyectada	Sopetrán - Santa Rosa (L. de Monte Grande) 8,85 km al NE de S.	06 32 45,30	75 40 25,37	12
553	1087	UN 4314	Pegmatita	Camino de sop. a Medellín 700 m SO de Q. Grande	06 27 54,53	75 41 48,05	8
554	1091		Diorita micahornbléndica cuarcífera	C° de Sopetrá a Medellín; 200 m antes de Qu. Arias	06 28 27,14	75 40 29,49	8
556	1031	UN 4300	Diorita cuarzosa	Qu. Tajami (salto) al E de Sucre	06 35 44,10	75 47 05,26	9
557	1036	UN 4301	Grandiorita porfídica	Qu. Venturoza; Sucre	06 35 19,04	75 46 56,11	9
558	1082		Tonalita con diferenciaciones básicas	Camino de Fredonia a Medellín 425 m OSO de Qu. Cedros	06 00 28,30	75 40 34,13	8
559	23	UN 4013	Anfibolita zoisitica	Sucre - Sacaajal 1500 m NO de Sucre.	06 35 58,75	75 47 35,60	12
560	21	UN 4012	Anfibolita zoisitica	C° de Sucre a Sacaonal; 1500 m NO de Sucre	06 35 56,18	75 47 41,32	12
561	898		Diorita cuarzosa (Tipo de Heliconia) facies ácida	Ebéjico-S. Jerónimo (C° inferior)Pico? Al N de la Qu. Sucia	06 23 01,04	75 43 49,88	9
562	899		Keratófiro cuarzoso; facies marginal dela diorita de Helic.	Ebéjico-S. Jerónimo; lado meridional de la Qu. Sucia	06 22 48,83	75 43 39,87	9
563	897		Diorita cuarzosa, facies ácida. (Tipo de Helic)	Ebéjico-S Jerónimo; C° inferior. Lado meridional de la Qu. Sucia.	06 22 52,65	75 43 50,92	9
564	990	UN 4285	Diabasa porfíritica	Ebéjico-S. Jerónimo; C° inf lado merid. De la qu. Sucia	06 20 51,99	75 42 57,74	9

N° de la muestra (Numeración de E. Grosse, ubicada en el extremo superior izquierdo)	N° de la muestra (ubicada en el extremo inferior derecho, en rojo)	N° de muestra en catálogo de la UN (ubicada en la parte anterior de la sección)	Transcripción de la descripción de la muestra, realizada por E. Grosse (i.e. recuadro superior de la sección delgada)	Transcripción de la ubicación de la muestra de roca (i.e. recuadro inferior de la sección delgada)	Interpretación de la Coordenada Norte, según la descripción de la ubicación en "E" (" " " ")	Interpretación de la Coordenada Oeste, según la descripción de la ubicación en "E" (" " " ")	Cajón
565	1195	UN 4348	Gabro (estonctina Ofiolítica)	A. Leoncito; NO de paso de cangrejo	06 13 37,94	75 51 07,81	8
565	706	UN 4188		Angelópolis-Caldas			10
566	628	UN 4157	Espilita uralitizada por contacto de gabro; esqueletos de ural	A. Lencito al NO del paso del cangrejo	06 14 07,31	75 51 07,65	10
567	513		Diabasa(?) metamórfica con adinola inyectada	Qu. Inso; poco arriba del terciario, mid oeste			11
568	29	UN 4016	Filita sericítica.	Qu. Sucia; 2 km al E de S. Nicolás.			12
569	73	UN 4033	Anfibolita albítica	Qu. Sucia, 2 km al E de S. Nicolás.			12
570	74	UN 4034	Anfibolita albítica	Qu Sucia; lado norte vuelta grande al E de S. Nicolás			12
571	303	UN 4080	Diorita (de augita) anfibolítica, apizarrada.	Qu. Sucia, límite entre el precámbrico. Lado norte de la quebrada			11
572	304	UN 4081	Diorita (de augita) anfibolítica, apizarrada.	Qu. Sucia, límite entre el precámbrico.			11
573	526		piroxenita metamórfica	Paso de Jaramillo-Ebéjico; al sur del paso. (piroxenita metam)			11
574	531	UN 4147	piroxenita metamórfica	188 m al N S. Nicolás arriba des. Del Cauca.			11
575	521	UN 4145	Diabasa (?) metamórfica	Qu. Mandinga; parte inf.			11
576	132	UN 4043	Pizarra, arcillosa, filítica.	Qu. Mardriga. Parte inf			12
577	721	UN 4195	Tufa densa	Cauca; orilla oriental 1 km al N de qu. Perica			10
578	518	UN 4144	Diabasa metamórfica	Paso de cangrejo - Armenia 1,74 km al SE del paso	06 14 30,13	75 51 08,44	11
579	513	UN 4143	Diabasa metamórfica	Cuchilla al N de Q. Tuerta, 50 m al E del Terc. Carb.			11
581	861		Diorita cuarzosa (Tipo de Helic) gabrosa	Qu. Sucia; al E del A. Nicolas	06 27 51,25	75 47 54,08	9
583	331	UN 4087	Diorita cuarzosa saussuritizada	A. Morro de bloque suelto en el pié	06 02 39,56	75 50 04,58	11
584	335	UN 4089	Porfirita hornblendi-saussurítica	A. Morro (Quirimará) pié oriental del contacto.	06 20 54,53	75 48 28,91	11
585	334	UN 4088	Porfirita hornblendi-saussurítica	A. Morro (Quirimará) pié oriental del contacto.	06 20 53 64	75 48 27,30	11
586	339	UN 4090	Porfirita hornblendi-saussurítica	Loma La Cortada. (Barca de S. Jerónimo) act unos 900 m.			11
587	1583	UN 4150	Andesita de augita amidaloidea. Terc. sup.	Falda dept. del A. Arbolitos			9
588	1588		Andesita de aug.				8
588	326	UN 4086	Malchita saussuritizada	C° de la Loma de Quirimará. 360 m al SE de S. Nicolás			11
589	1867	UN 4445	Andesita Completamente alterada	C° de Titiribí al Morro	06 03 12,47	75 50 03,64	7
592	761	UN 4207	Granodiorita milonitizada	Qu. Amagá. Paso de C° Pobres-Amagá; 1000 m al E de Q. Balsala			10
595	1659	UN 4378	Aglomerado de hialobasalto	Derrame al NE de la Amaga			7
601	808		Cornubianita	Qu. Sinifaná unos 750 m arriba del C° Amagá - Frefonia	05 58 17,16	75 41 18,97	10
602	809	UN 4150?	Roca cornea micácea con partes arenosas	Qu. Sinifaná, unos 700 m arriba del C° Amagá - Fredonia	05 58 11,23	75 41 26,50	10
604	1669	4382 UN	Pasta de una toba aglomerada	Pte. Iglesias-Fredonia bloques en el camino.	05 54 45,73	75 40 03,14	7
606	1670	4383 UN	Neoterc. Pasta de una toba aglomerática	Magallizo 700m al SO del A. Triste.			7
607	1711	UN 4393	Neoterci. Tufita aglomerática	La Mona-Fredonia por la qu. Ganudra	05 56 03,31	75 41 07,65	7
608	1728	UN 4395	Andesita micácea	Qu. Arabí al S del A.Sillón			7
609	1731	UN 4396	Andesita hornbléndica	C° La Muza- Pueblito?; pié sep del altico al SE del A. Milindres			7
611	1618		Basalto feldespático Neoterciario tipo 4	A. Pueblo Hueco; Faldqa oriental			8
612	1619		Basalto feldespático, neoterciario.	A. Manzanillas			7
613	1577		Andesita de hornblenda. Terciario superior	De Alto de Osos en la qu. S. Cristobal			8
616	1750	UN 4403	Andesita hornbléndica	Morro Llaguo			7
617	1966	UN 4485	Andesita hornbléndica	A. de la torre peña en el SE			6
618	1948	UN 4476	Andesita hornbléndica	Filón (silo) al SO de M. Alegre			6
619	1878	UN 4446	Andesita hornbléndica alterada				7
624	1881	UN 4447	Adinola cerca del contacto de la andesita	Qu. San Cristobal al SE de la Mina			7
627	580	UN 4150	Esquisto silíceo	Pte. Soto - El Lotero			11
628	532	UN 4148	Diabasa metamórfica	Río Poblano donde entra el C° de Fredonia a Sta. Bárbara	5 51 01,97	75 34 28,79	11
2.	901	UN 4199	Diorita cuarzosa epidotizada (tipo de Helic.)	Pueblito-Medellín; 225m al NE de piea	06 10 19,11	75 42 40,39	9
620	1622	UN 4371	Basalto feldespático, neoterciario, isópago	Hac. Morrón			7
aa.	748		Tufa densa saussuritizada	Qu. Venturosa; unos 300 m arriba del C° Sucre-	06 35 31,83	75 46 48,57	10
d.	953		Keratofiro cuarzoso	Pueblito-Medellín; 800 m al NE de P.- Capilla	06 10 33,16	75 42 41,86	9
h.	904		Diorita de augita, uralitizada; (fac bas. De diorita)	Ebéjico-S. Jerónimo. El oriental bajada de el Corral a la Qu. Zaguá; trozo suelto	06 21 16,97	75 44 13,88	9
m.	14	UN 4010	Arcaico. Mesocarcita grafitica y hornbléndica.	Salado grande de Córdoba, pié de la falda al E de las fuentes.	06 31 42,05	75 46 04,47	12
n.	10	UN 4006	Arcaica. Anfibolita densa rica en feldespato				12

N° de la muestra (Numeración de E. Grosse, ubicada en el extremo superior izquierdo)	N° de la muestra (ubicada en el extremo inferior derecho, en rojo)	N° de muestra en catálogo de la UN (ubicada en la parte anterior de la sección)	Transcripción de la descripción de la muestra, realizada por E. Grosse (i.e. recuadro superior de la sección delgada)	Transcripción de la ubicación de la muestra de roca (i.e. recuadro inferior de la sección delgada)	Interpretación de la Coordenada Norte, según la descripción de la ubicación en "E" (°'")	Interpretación de la Coordenada Oeste, según la descripción de la ubicación en "E" (°'")	Cajón
x.	733	UN 4201	Tufa aglomerática apizarrada	Qu. Nuarque; unos 150 m arriba de la vuelta grande al E del camino Sopetrán - Sucre	06 32 32,74	75 45 58,26	10
z.	731		Porfírita labradorítica epidotizada	Lomo sept. del Alto Palo Grande			10
	1676	UN 43	Neoterc. Pasta de una toba aglomerática	A. Buenavista (SO de C. Tusa) falda NO.	05 57 35,89	75 46 34,09	7
	1137	UN 4334	Spessartita; filón dentro de granito lenticular	Palmitas-S. Sebastian; 250 m al SO de P. spt	06 20 38,83	75 41 36,55	8
	1321a	UN 4349	Guijarro del cgl. Completam. Dyc.	Barranco de Arraquía; S. Jerónimo			8
	1150	UN 529?	x	Sopetrán-Medellín 1350 m al SE de la Qu. Cedros			8
	1373	UN 4104?	Jaspis de porcelana	Hac. Los Micos. Qu. Mica inf. (titiribi)	06 04 40,85	75 46 16,78	8
	1579	UN 4083	Neoterc. Andesita augítica				9
	870		Diorita cuarzosa (Tipo de Helic) sauss	Pueblito-Medellín; 800 m al NE de P.- Capilla	06 10 19,11	75 42 40,39	9
	969		(sin nombre)	Camino por la cresta de la Loma Hermosa. 1900 m al SE de la casa de la hacienda			9
	973		(sin nombre)	Pueblito-Medellín 850 m al SE de P.			9
	903			Qu. Zaguá; 1900 m al S de la boca. Ebéjico			9
	902			Heliconia-Uvito; A. de las cruces 1650 m al ESE de Heliconia			9
	11?	UN 4008		Salado grande de Córdoba			12
	43	UN 4021	Esquisto sericiticuarcítico	C° Palmitas-Cano.; 50 m al O de Qu. Sucia.	06 19 35,70	75 42 46,40	12



Formación Amagá, La Pintada, Antioquia, Colombia
Fotografía de Velásquez et al. (2021)



This work is distributed under the Creative Commons Attribution 4.0 License.

Received: May 20, 2020

Revision received: July 26, 2021

Accepted: July 27, 2021

Published online: September 24, 2021

Analytical solution of CO₂ mass flux measurement with Non-Dispersive Infrared sensors for soil in diffusive and advective-diffusive regime: Tool for the continuous and telemetric measurement of volcanic gases in an open chamber

Solución analítica de la medida de flujo de CO₂ con sensores infrarrojos no dispersivos para suelo en régimen difusivo y advectivo-difusivo: herramienta para la medida continua y telemétrica de gases volcánicos en cámara abierta

Nicolás Oliveras¹

1. Consultant, Popayán, Colombia

Corresponding author: noliveras@schulerweage.com

ABSTRACT

Measuring the carbon dioxide (CO₂) mass flux in a volcanic environment is necessary for volcanic monitoring. CO₂ mass flux must be measured continuously and telemetrically to get, almost in real-time, a better understanding of the dynamics of the volcanic degassing processes, contributing to the building, together with other monitoring technics, of a volcano behavior model. This study presents two analytical solutions, 1) a simple diffuse solution and 2) an advective-diffusive solution, which both implement NDIR (Non-Dispersive Infrared Emitter) sensor arrays in an open chamber (diffusion chimney) and an exchange chamber (gas interchanger). The first system, for which the gas speed is negligible, despite being basic (with values reflected in the slope of an equation line), introduces mass flux calculations with a single sensor NDIR. For the second system, where the gas speed is part of the equation, another mathematical solution and three measuring points are required, which demands the system to include a second NDIR sensor for the correct mathematical solution of the equations system. In addition, an embedded system can automate the method by calibrating, controlling an agitation fan, and recording temperature, pressure, and mass flux in volcanic soils at the

Citation: Oliveras, N. (2021). Analytical solution of CO₂ mass flux measurement with Non-Dispersive Infrared sensors for soil in diffusive and advective-diffusive regime: Tool for the continuous and telemetric measurement of volcanic gases in an open chamber. *Boletín Geológico*, 48(2), 41-59. <https://doi.org/10.32685/0120-1425/bol.geol.48.2.2021.496>

surface. Since this theoretically proposed method needs to be tested, experimental data are expected to validate the measurement of CO_2 mass flux, which will be used as a helpful tool for volcanic monitoring.

Keywords: Volcanic monitoring, volcanic activity diagnosis, embedded system, CO_2 mass flux.

RESUMEN

La medición del flujo de dióxido de carbono (CO_2) en un ambiente volcánico es una necesidad para el monitoreo volcánico. El flujo de CO_2 se debe medir de manera continua y telemétrica para una mejor comprensión, casi en tiempo real, de la dinámica de los procesos de desgasificación volcánica, que contribuyan a la construcción de un modelo de comportamiento volcánico, junto con otras técnicas de monitoreo. Este documento presenta dos soluciones analíticas, la primera es una solución difusa simple y la segunda es la solución advectiva-difusiva, que implementan un arreglo de sensores NDIR (emisor de infrarrojo no dispersivo) en una cámara abierta (chimenea de difusión) y una cámara de intercambio (intercambiador de gases). El primer sistema, a pesar de ser básico (con valores reflejados en la pendiente de una línea de ecuación), y para el que la velocidad del gas es despreciable, permite introducir a expertos en este campo en los cálculos de flujo de este tipo con un solo sensor NDIR. Para el segundo sistema, donde la velocidad del gas es parte de la ecuación, se requiere otra solución matemática y tres puntos de medida, que exige la inclusión de un segundo sensor NDIR para la correcta solución matemática del sistema de ecuaciones. Un sistema embebido puede automatizar el método por calibración mediante el control de un ventilador de agitación, que registre la temperatura, la presión y la medición del flujo en suelos volcánicos en la superficie. Este método propuesto teóricamente necesita ser probado, por tanto se esperan aportes experimentales para validar la medida de flujo de CO_2 como una herramienta poderosa para el monitoreo volcánico.

Palabras clave: Monitoreo volcánico, diagnóstico de la actividad volcánica, sistema embebido, flujo de CO_2 .

1. INTRODUCTION

The Earth emits gases, which are specific and possibly measurable as soil gas emissions in certain geological environments such as volcanic areas. Some gases are related to changes in the volcanic activity allowing its evaluation. Soil gas emissions have also been investigated in earthquake areas and along active fault zones (Allard et al., 1991; Badalamenti et al., 1988, 1991; Diliberto et al., 1993; Giammanco et al., 1998; Chiodini and Frondini, 2001; Gerlach et al., 2001; Ciotoli et al., 2003). Active volcanoes have been monitored periodically through the measurements of soil gas emissions because it is a good sign of change in their activity, and in many volcanic areas, there have been different projects in order to obtain accurate measurements for this purpose (Wakita, 1996; Ciotoli et al., 1998; Guerra and Lombardi, 2001; Rogie et al., 2001; Spicák and Horálek, 2001; Salazar et al., 2002).

According to Sahimi (1995), diffusion and advection result from the two different processes of the gas flux through natural soil. There are several ways to measure the CO_2 flux. One method, for example, is the calculation of the CO_2 flux from the concentration gradients in the soil (Baubron et al., 1990).

In addition, it is possible to measure the absorption of CO_2 in a caustic solution, as in the alkali absorption method (Witkamp, 1966; Kirita, 1971; Anderson, 1973), or to measure the difference in CO_2 concentrations between the inlet and outlet air in a closed chamber, as in open flow infrared gas analysis (Witkamp and Frange, 1969; Nakadai et al., 1993).

In the dynamic concentration method (Gurrieri and Valenza, 1988; Giammanco et al., 1995), the measurement of the CO_2 content in a mixture of air and soil gas is obtained from a special probe. Gurrieri and Valenza (1988) deduced that the dynamic concentration is proportional to the soil CO_2 flux according to an empirical relationship. For example, Camarda et al. (2007) used the dynamic concentration technique in Vulcano, which belongs to the Aeolian Islands, in Italy.

Accurate measurement of CO_2 emission in a volcano's soil can be done with a "gas accumulation chamber" device which consists of a noninvasive CO_2 concentration measurer (such as the NDIR method) and a known volume chamber placed on the soil surface. The gas accumulates in the chamber, and it is registered using, for example, a West Systems instrument with a LICOR LI-800 Non-dispersive infrared CO_2 detector (Tonani and Miele, 1991; Bekku et al., 1955; Norman et al., 1992; Chio-

dini et al., 1998; West Systems, 2012). With the calculation of the accumulation slope with respect to the time and the system constants, it is possible to obtain the CO₂ mass flux from the sampled point. This technique, clearly manual and designed for research and monitoring (Hernández et al., 2001), needs complex automation for continuous and telemetric use to monitor a volcano status. The accumulation chamber technique has been used in volcanoes such as the Stromboli volcano (Inguaggiato et al., 2013), in the volcanic areas of Solfatara of Pozzuoli, and the Vesuvius volcano (Cardellini et al., 2003), all of these in Italy; El Chichón volcano in Mexico (Jácome et al., 2016); Mount Fuji volcano (Notsu et al., 2006) and Miyakejima volcano (Hernández et al., 2001), both in Japan.

On the other hand, some authors have mentioned open chamber measurement techniques (Janssens et al., 2000 and Camarda et al., 2007). However, they have not been popularized due to difficulties with wind impacts, pressure changes, and system size. This paper shows the analytical solution for the measurement of CO₂ mass flux, based on an open chamber (diffusion chimney (DC) in this paper) and an exchange chamber (gas interchanger (GI) in this paper). This study proposes a model to monitor the CO₂ mass flux in the soil for an active volcano, but it is also possible to use it for other purposes like agriculture. Furthermore, using one or two NDIR sensors capable of measuring CO₂ would make it possible to measure diffuse and advective-diffuse cases, respectively.

Using the newly proposed technique, a stations network could continuously measure CO₂ emitted at a specific volcano area per day. It could be validated with non-continuous and non-telemetric measurements, for instance, using the portable manual accumulation chamber instrument. This document proposes an analytical solution for this type of system. It takes advantage of the reduced number of mechanical parts required for their implementation, allowing an automatic and continuous measurement of CO₂ mass flux in volcanic soils.

The solution of a 3 × 3 equation system does not require knowledge of the soil characteristics that condition the speed of the gas that emerges due to advection-diffusion. The placement of two NDIR sensors inside the open chamber (diffusion chimney (DC) in this document) allows calculating this speed without affecting the CO₂ gradient. A new parameter called *N* will establish the state of the measurement system in a simplified way, defining the diffusive or advective-diffusive state and the inflection point. Additionally, new strategies are added in the design stage to minimize the difficulties already studied

by other authors of the opened chamber techniques and to advance the alternative designs of continuous CO₂ mass flux measuring equipment for volcanic applications with an open chamber.

2. DEFINITIONS

Diffusion chimney (DC): The tube that connects the soil with the gas interchanger (GI). It allows mixing of the CO₂ gas that emerges from the ground with the atmosphere so that its concentration slowly decreases until it reaches the GI. Ideally, the soil emits a very high concentration of CO₂ gas and it decreases to reach the natural environmental concentration of the air through the DC and the GI (Camarda et al., 2007). As will be seen in the theoretical example defined by the new factor *N* (defined below), the transition from a diffusive to a diffusive-advective flow will be a value of approximately $1.47 \frac{mg}{s \times m^2}$ (see section 7.4).

Gas interchanger (GI): A tube system with a diameter bigger than the DC with ventilation holes. A homogeneous sample of the external gas is stored within the volume as a reference concentration well with or without external airflow. The tube at the bottom is in contact with the transmitting DC of CO₂.

NDIR: The CO₂ sensor under the Non-Dispersive Infrared Emitter (NDIR) technique, which obtains the concentration of CO₂ (ppm) in the DC in one position.

CO₂ mass flux: defined as $J_i(z, C) \left[\frac{mg}{s \times m^2} \right]$ is the mass of CO₂ per time unit and per area unit, calculated from a physicochemical model that integrates diffusion and advection. CO₂ ass flux is obtained by measuring the CO₂ concentration using the NDIR sensors, recording their position within the DC, estimating the external reference concentration, and considering the system's constants and variables.

3. PRINCIPLES OF THE MEASUREMENT SYSTEM

The proposed system can detect CO₂ mass flux emissions by diffusion and advection by measuring the concentration of two NDIR sensors in a DC and the base level of environmental concentration of CO₂ in a GI. In low mass fluxes, the diffusion predominates and needs only one sensor. However, in high mass fluxes, the system is governed simultaneously by diffusion and advection (Gurrieri and Valenza, 1988) and requires the data of the two sensors.

3.1. Diffusion process

- » Each time there is a change of the CO_2 concentration in the soil, that is, the lower part of the DC, a diffusion process occurs between two gases (gas coming from the soil and gas in the air), reflected in mass flux (García, 2020). This air with a higher CO_2 concentration (higher molecular weight) occupies spaces in the upper air of the DC, where one of the CO_2 sensors is located (upper NDIR sensor), gradually reaching the external equilibrium concentration measure reference through the GI.
- » The above-mentioned process has two analyses:
 - Stationary: If the CO_2 emission is without variations in time, the diffusion will enter a stationary state. Removing the time variable from the system makes it possible to obtain the constant CO_2 mass flux.
 - Temporary: If the phenomenon's behavior is studied from the temporal point of view, it is possible to determine the linear measurements of the system's DC and the GI, adjusting it to the required sensitivity. Similarly, it is possible to get the response time of the system.

The above two analyses will be performed according to 1st and 2nd Fick's law, respectively, based on the mass transport phenomenon where no chemical reaction occurs within the physical kinetics of gases.

3.2. Advection process

- » When there is a significant change of pressure in the soil relative to the ambient air, the process of advection, also reflected in mass flux, is generated along with a diffusion process in the DC (Camarda et al., 2007). This process twists the diffusion line of the system, which requires an additional NDIR sensor (NDIR soil sensor) to solve the new system mathematically.
- » The above also has two analyses:
 - Stationary: If the CO_2 emission is without variations in time, it will have a behavior where the diffusion and advection enter a stationary state. Removing the time variable from the system makes it possible to obtain the constant CO_2 mass flux.
 - Temporary: If the phenomenon's behavior is studied from the temporal point of view, it is possible to determine the linear measurements of the system's DC and GI, adjusting it to the required sensitivity. Similarly, it is possible to obtain the response time of the system.

3.3. Advection-diffusion process

The mathematical model of the CO_2 mass flux meter is performed under the following laws and principles (Camarda et al., 2007):

- » For diffusion, according to Fick's 1st and 2nd laws.
- » For advection, according to Darcy's law.
- » The principle of mass conservation will be applied.
- » It will be considered that no chemical reaction occurs within the physical kinetics of gases.

4. THEORY

4.1. Diffusion

Diffusion is a phenomenon studied by physical chemistry, where systems that are not in equilibrium evolve to states, either chemically or physically, until reaching a new equilibrium (García, 2018). For this case, we will assume only the evolution to a physically stable state, where the thermodynamic variable of our system out of balance, can be described as in equation 1:

$$C_i = C_i(\vec{r}, t) \quad (1)$$

where:

- » C_i is the thermodynamic variable of the concentration of CO_2 , and for this document, unless otherwise stated, the concentration shall always refer to CO_2 .
- » \vec{r} is the position vector of the study concentration.
- » t is the time.

In 1855 Adolf Fick set two laws regarding the diffusion of two substances, which can be applied while the following conditions are satisfied:

- » The substances are at the same pressure.
- » The substances are at the same temperature.
- » The substances do not react chemically to each other.

A change in atmospheric pressure generates a mass current in the system, which must be measured by a pressure differential meter. Small changes in atmospheric pressure ($\sim 1 \text{ hPa}$) can generate large errors by increasing or underestimating the CO_2 mass flux. What happens is that the atmospheric pressure works like a pump that injects or sucks gas into the ground, di-

rectly affecting the mass flux measurement. With the inclusion of advection in the next section, we will see that this problem is solved with the calculation of the mass flux velocity and that the use of a differential pressure meter in the DC could correct this error in the instantaneous mass flux measurement.

Assume two containers that have a mixture of two substances A and B, with different concentrations of CO₂ at the same temperature T , and pressure P (see Figure 1.)

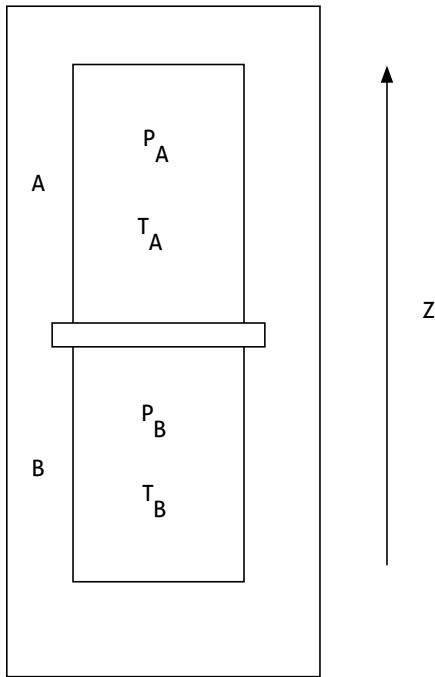


Figure 1. One-dimensional diffusion between two gases

The two substances are separated by an impermeable wall, which in an instant $t = 0$ is detached to allow the diffusion of the substance with the highest concentration B within the substance with the lowest concentration A. Thus, the molecular movement deletes the differences in concentration between the two substances, and this spontaneous decrease in concentration differences is called diffusion.

If the variable concentration is defined as C and the subscript A and B as indicators of the substance A and B, then C_A and C_B in the distance z change with the function of time. In Figure 2, C_A is equal to C_B after a certain amount of time ($t = \infty$). The Z-axis has been arranged horizontally for explanation.

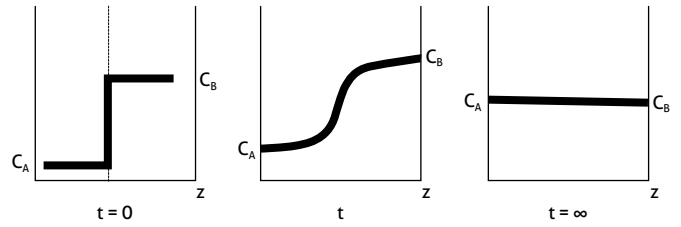


Figure 2. Diffusion without stable wells in the boundaries (Left) State for $t = 0$. (Center) Any value for $0 < t < \infty$. (Right) $t = \infty$

Diffusion is a macroscopic movement of the system's components due to the concentration gradient. In the proposed system, this diffusion disappears when the concentration differences are canceled, indicating that the system has reached equilibrium. If the concentration differences are kept within limits, they could reach a stationary state as in Figure 3.

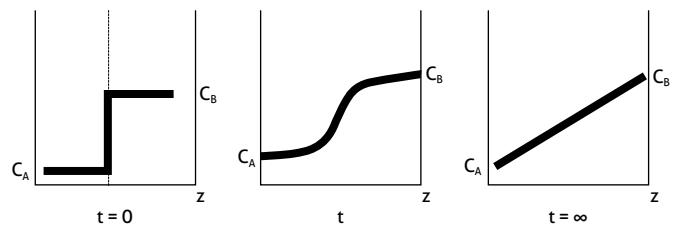


Figure 3. Diffusion with stable wells in the boundaries (Left) State for $t = 0$. (Center) Any value for $0 < t < \infty$. (Right) $t = \infty$

This new model would be achieved when the two boundaries are stable wells of A and B substances concentration in the study, allowing that at $t = \infty$ a stationary state occurs in the concentration at any point.

4.1.1. Fick's first law

Fick's first law applies to determine stationary behaviors of diffusion, and it states that the mass flux through a plane between two adjacent systems is proportional to the concentration gradient and unidimensionally is written as (Camarda et al., 2007):

$$J_{dif} = -D \frac{dC_i}{dz} \quad (2)$$

Where:

- » D is the diffusion coefficient in $\left[\frac{m^2}{s}\right]$. Note: D will be equal to air inwards CO_2 as from CO_2 to air for practical purposes.
- » C_i is the concentration in $\left[\frac{mg}{m^3}\right]$; therefore, the $[ppm]$ unit must be converted.
- » J_{dif} is the mass flux per diffusion at that point in $\left[\frac{mg}{s \times m^2}\right]$.

The value of D according to the conditions of pressure and temperature of the site different from $T_0 = 273.2^\circ K(0^\circ C)$ and $P_0 = 1013hPa$ is obtained from the following formula with $D_{(STP)} = 1.39 \times 10^{-5} \left[\frac{m^2}{s}\right]$ (Campbell, 1985):

$$D = D_{(STP)} \left(\frac{T}{T_0}\right)^{1.75} \left(\frac{P_0}{P}\right) \left[\frac{m^2}{s}\right] \quad (3)$$

Where:

- » $D_{(STP)}$ is the diffusion coefficient in pressure and temperature standard conditions.

4.1.2. Fick's second law

Fick's second law applies to determine the temporal behaviors of diffusion and is written as García (2020):

$$\frac{dC_i}{dt} = D \frac{d^2C_i}{dz^2} \quad (4)$$

Where:

- » D is the diffusion coefficient in $\left[\frac{m^2}{s}\right]$ and does not depend on either C_i or z .
- » C_i is the concentration in $\left[\frac{mg}{m^3}\right]$.

Because Fick's second law can determine the temporal behavior, this allows knowing the system's response time to a change of mass flux in a non-stationary state.

Equation 4 is a differential equation with infinite solutions, but one solution applies boundary solutions and can be adjusted to our problem (Busquets, 2011):

$$\frac{C_z - C_0}{C_s - C_0} = 1 - \text{ferr} \left(\frac{z}{2\sqrt{D \times t}} \right) \quad (5)$$

Where:

- » $\text{ferr}()$ is the error function of Gauss (Callister, 1995).
- » C_z is the concentration given by the sensor in $[ppm]$.

- » C_0 is the reference concentration in $[ppm]$.
- » C_s is the concentration in the boundary in $[ppm]$.
- » z is the distance to the point of interest in $[m]$.
- » D is the diffusion coefficient in $\left[\frac{m^2}{s}\right]$.
- » t , is the time in $[s]$.

4.2. Advection

Advection is the variation of a scalar property at a given point, such as pressure or temperature, by a vector field effect. Here, the advection process will be defined by the pressure gradient ∇P that generates a mass transport process (Camarda et al., 2006, 2007).

4.2.1. Darcy's law

In 1856 Henry Darcy published the formula that bears his name and is currently called Darcy's law, which defines how to measure this type of advective mass transport (Camarda et al., 2006, 2007). Darcy's law determines the velocity of a fluid as a function of pressure gradient:

$$v = - \frac{k}{\mu} \nabla P \quad (6)$$

Where:

- » v is the gas velocity in $\left[\frac{m}{s}\right]$.
- » k is the intrinsic permeability, which is the only function of the soil properties in $[m^2]$.
- » μ is the gas dynamic viscosity in $[Pa \times s]$.
- » ∇P is the pressure gradient in $\left[\frac{Pa}{m}\right]$.

As seen below, it will not be from this equation that v will be calculated to determine the CO_2 mass flux, but the analytical solution with the advantage of using two NDIR sensors. The mass flux due to advection is obtained knowing the concentration and speed:

$$J_{adv} = C_i v \quad (7)$$

Where:

- » C_i is the concentration in $\left[\frac{mg}{m^3}\right]$.
- » v is the gas speed in the diffusion chimney in $\left[\frac{m}{s}\right]$.
- » J_{adv} is the mass flux per advection at that point in $\left[\frac{mg}{s \times m^2}\right]$.

4.3. Advective-Diffusion theory

The simultaneous diffusion and advection processes are defined as the sum of the two mass fluxes acting simultaneously (Gurrieri and Valenza, 1988; Sahimi, 1995):

$$J_i = J_{dif} + J_{adv} \quad (8)$$

Using the definitions of equations 2 and 7, the mass fluxes remain as:

$$J_i = -D \frac{dC_i}{dz} + C_i v \quad (9)$$

The law of mass conservation must be considered to quantitatively describe a system where diffusion and advection occur simultaneously.

$$\nabla \cdot J_i + \frac{\partial C_i}{\partial t} = 0 \quad (10)$$

Where $\nabla \cdot J_i$ is the mass flux divergence J_i . By combining equations 9 and 10 and assuming that v and D are constant, the next equation is found:

$$v \nabla C_i - D \nabla^2 C_i = \frac{\partial C_i}{\partial t} \quad (11)$$

This is the equation for all problems where diffusion and advection are simultaneously involved. The one-dimensional equation to be applied to the DC would be:

$$v \frac{\partial C_i}{\partial z} - D \frac{\partial^2 C_i}{\partial z^2} = \frac{\partial C_i}{\partial t} \quad (12)$$

And in a stationary state:

$$v \frac{\partial C_i}{\partial z} - D \frac{\partial^2 C_i}{\partial z^2} = 0 \quad (13)$$

Which has a general solution (Isachenko et al., 1980):

$$C(z) = A \frac{D}{v} e^{\frac{v}{D}z} + B \quad (14)$$

Where A and B are constants that depend on the boundary conditions.

If this solution is tested to the two points model of concentration measurement, it is found that equations will be missing because apart from A and B , the value of v is also unknown. For this reason, it is necessary to place another NDIR sensor to

have three equations and solve the three variables of the system (see section 5.3. Equation's approach).

5. MASS FLUX METER OF CO₂ BY ADVECTION AND DIFFUSION

The CO₂ mass flux meter of CO₂ by diffusion and advection proposed in this study works with two coupled chambers where diffusion and advection occur in the DC. Also, in the GI, a rapid diffusion occurs with the atmospheric air. The advection product of the pressure gradient has significant effects for velocities v , which are greater than a numerical tenth of D , that is, $v > \frac{D}{10}$ for a normalized diffusion chimney $z = -1$.

5.1. Considerations

- » In the DC, the measurement is performed with two CO₂ sensors. In general, the DC is long, narrow, and has a much smaller volume than the GI.
- » The GI works as a reference well for the wind filter and external atmospheric concentration, allowing the diffusion to operate in quiet and isolated from the outside. In general, the GI is short, wide, and has a much larger volume than the DC.

Due to the dimensions and openings of the DC and GI, the system:

- » Can be at the same temperature everywhere.
- » There may be a pressure gradient that generates a mass flux, deforming the concentration distribution into the DC.

Equally, it is assumed that:

- » GI is bigger than DC.
- » There is no chemical reaction between the gases emitted by the soil and air.
- » A sensor is as close as possible to the ground on the DC and will be called a soil sensor.
- » A sensor is at the upper side and is generally one-third of the length of the DC measured from above. This sensor will be called the upper sensor.

The upper sensor arrangement in a third of the effective length is called the cubic solution position; the quadratic solution position is set when the sensor is placed in the middle

of the tube. This last solution position, although also valid, has little dynamic range as it will look mathematically.

5.2. The N parameter and the possible states of the system

On the way through the DC from the soil sensor to the atmospheric air (CO_2 concentration reference), a diffusive process occurs simultaneously, as there is a difference in concentration between the two points, and a diffusion-advection process can happen if there is simultaneously a significant pressure gradient. In this way, the DC and the GI will work as follows, generally for $z = -1$ (normalized to one meter), and the classification parameter N is defined as:

$$N = - \frac{D}{10 \times v \times z} \tag{15}$$

Which determines the status of the measurement system and is important to know whether the system is in a diffusive or advective-diffusive state.

The numerical simulation of equation 9 with the solutions of equation 14 for different system states provides interesting graphs interpreting the CO_2 concentration distribution along with the DC and the N parameter interpretation. These graphs are obtained for hypothetical speeds and solving only the unknowns A and B in a system of two equations with two variables knowing speed v . In sections 5.3. and 6.2. show the approach and solution of the equations that already consider the velocity v for an analytical solution that completes the system.

Possible states of the system, changing v and its relationship with the N parameter:

- » Without diffusion and advection ($N \gg 1, v \cong 0, z = -1$): when there is no difference in the CO_2 concentration between the ends of the DC, the limits of which are the air near the ground and the GI, there will not be a gradient triggering the movement of any molecules. Inside the GI will have a reference concentration given by the atmosphere. Therefore, at any time, the two NDIR CO_2 sensors will have a concentration in *ppm* of the same proportion. If there is no less likely diffusion, there will be the advection resulting from a large pressure gradient between the ground air and the atmospheric air. Figure 4 shows an illustrative graph where the two lines have been separated for demonstrative purposes.

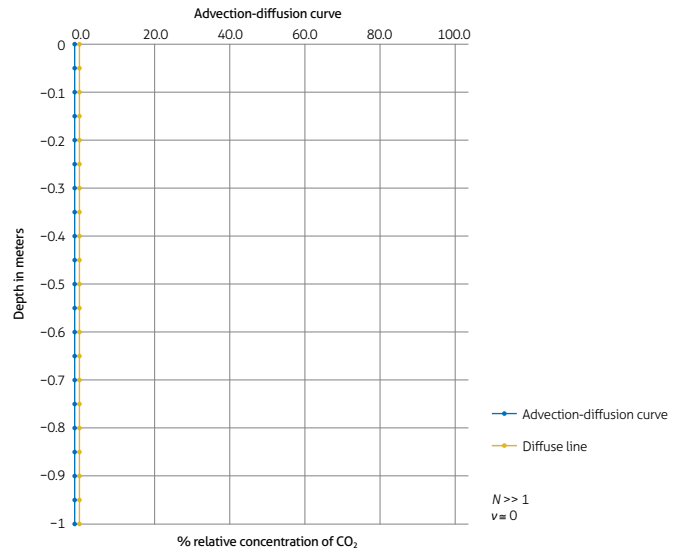


Figure 4. CO_2 percentage concentration with respect to depth for $v \cong 0$

- » With diffusion and without advection ($\infty \gg N > 1, 0 < v < \frac{D}{10}, z = -1$): when there is a CO_2 concentration difference between the ends of the DC whose limits are the soil and the GI, there will be a gradient that will mobilize CO_2 . Inside the GI will have a reference concentration given by the atmosphere. At $t > 0$, with the system's characteristics and under a continuous emission of CO_2 , the CO_2 NDIR sensors located inside the DC will record concentration changes. The difference in concentration in two environments works as a diffuser element of CO_2 (denser) to normal air (less dense), and the difference in this concentration between the soil sensor, the upper sensor, and the reference concentration given by the atmosphere is the essence of the mass flux meter. The point of $v = \frac{D}{10}$ was chosen so that the error difference between the only diffusive and the advective-diffusive models would be a maximum of 1%. See Figure 5.
- » With diffusion and advection ($1 \geq N > 0, v \geq \frac{D}{10}, z = -1$): when there is a significant pressure gradient of CO_2 between the air near the ground and the atmosphere, there will be a CO_2 mass flux between the DC and GI. This new mass flux is more significant than the CO_2 mass flux by diffusion. The effect on the diffusion line is to bend it upwards with a peak of about one-third relative to the diffusion line. This match allows for a higher dynamic range of the system

in the upper sensor, significantly decreasing system errors. The value of $N = 1$ or $v = \frac{-D}{10 \times z}$ is called diffusion to advection-diffusion transition and is the point that corresponds to a maximum error of 1% compared to a linear model using Fick's first law. Figures 6a and 6b show the case of $0 < N \leq 1$, $v > \frac{D}{10}$ and $N \approx 0$, $v \gg \frac{D}{10}$.

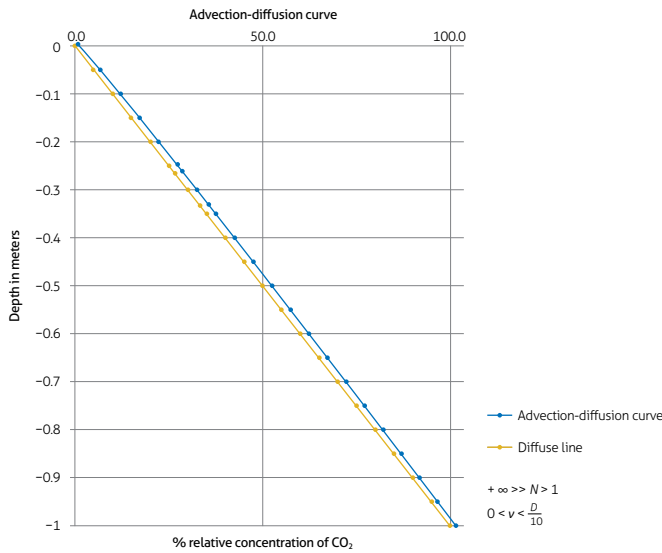


Figure 5. CO₂ percentage concentration with respect to depth for $+\infty \gg N > 1$, $0 < v < \frac{D}{10}$

In summary, the performance of the system is based on the fact that a gas exposed to another is mixed evenly due to its intrinsic gas movement (diffusion) and also simultaneously by a pressure gradient that generates a velocity v (advection). The value of N determines:

- » $N \gg 1$, there is almost no mass flux by diffusion.
- » $N > 1$, is only diffusive.
- » $N = 1$, it has an advective-diffusive transition.
- » $1 > N > 0$ is advective-diffusive.

Two NDIR sensors at two points in the DC are required to perform the CO₂ mass flux measurement and thus solve the equations for the two diffusive and advective phenomena within the physical kinematics of the gases.

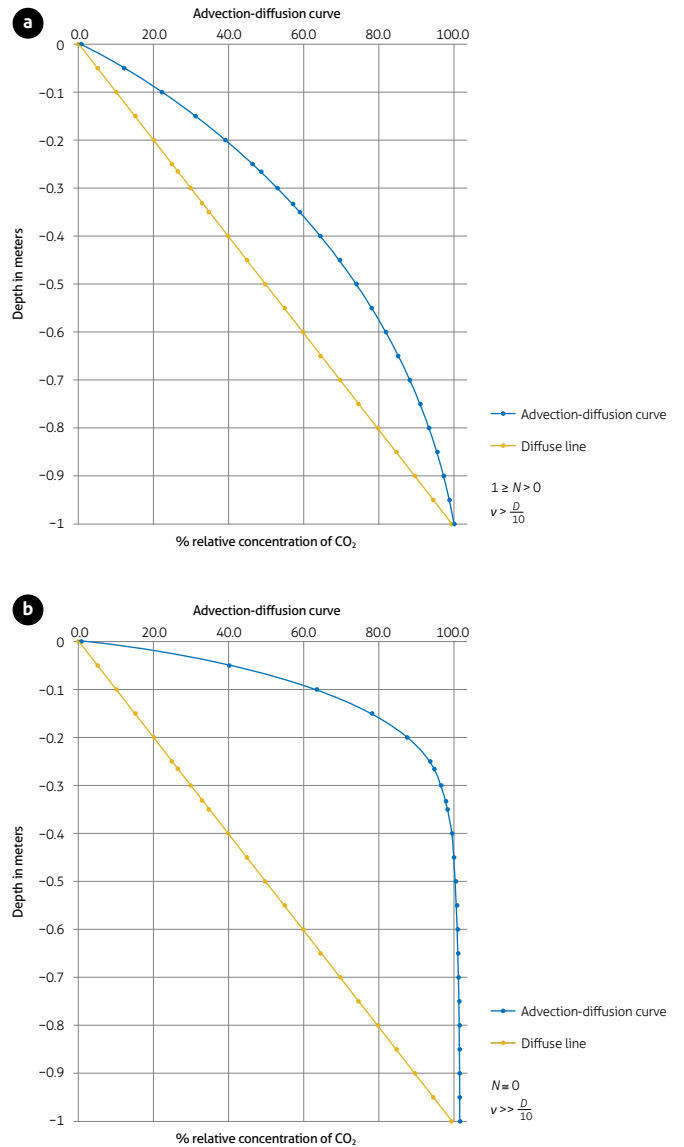


Figure 6. a) CO₂ percentage concentration with respect to depth for $1 \geq N > 0$, $v > \frac{D}{10}$; b) CO₂ percentage concentration with respect to depth for $N \approx 0$, $v \gg \frac{D}{10}$

5.3. Equation's approach

The approach of equation 14 in three points of the diffusion chimney allows to solve A , B , and v , and hence to find the J_i mass flux as a function of three concentrations C_{Soil} , C_{Upper} , $C_{Environment}$ and the constant parameters D , z_o , z_a , z_b . For an easier understanding, the next notation is defined:

- » $z = z_0 = 0$: Position at the top edge of the diffusion chimney.
- » $z = z_a$: Position in the upper third of the diffusion chimney (or in the middle).
- » $z = z_b$: Position in the soil of the diffusion chimney.
- » $C(z = z_0) = C_0 = C_{Environment}$: Example of environmental reference concentration 404ppm (for 2017) for this document (WMO, 2019).
- » $C(z = z_a) = C_a = C_{Upper}$: is the concentration at the point z_a .
- » $C(z = z_b) = C_b = C_{Soil}$: is the concentration at the point z_b .

Note 1: Each concentration given in ppm must be converted to $\left[\frac{mg}{m^3}\right]$, so the CO₂ measurements given by the NDIR sensors must be converted according to pressure and operating temperature.

Note 2: For all calculations, the coordinates axis will be positive upwards from the ground.

The detailed solution of this system can be found in the analytical solution in section 11.1. and have as a purpose two solutions: $z_b = 2 \times z_a$ and $z_b = 3 \times z_a$. The first is called a quadratic solution, and it is not practical because it limits the dynamic range. The second is called a cubic solution and fits well to the dynamic range due to the displacement of the concentration curve to the DC's upper third by the effect of the gas speed for $1 > N > 0$.

Figure 7 will be the reference for all explanations of the hypothetical assembly of the system for the CO₂ measurement in the other sections. In the case of $v = 0$, only the upper sensor shall be considered.

Table 1. Table of the physical model, boundary conditions, and equation 16

Diffusion chimney (DC)		Boundary conditions	Mathematical equation
	$z_0 = 0$ $C_0 = 404$	<ul style="list-style-type: none"> • $z = z_0 = 0$: Position at the upper edge of the diffusion chimney. • $C(z = z_0) = C_0$ $C_0 = C_{Environment} = 404ppm$ Example of environmental concentration reference. 	$C(z = z_0 = 0) = A \frac{D}{v} + B = C_0 = 404$ (16.1)
	z_a, C_a	<ul style="list-style-type: none"> • $z = z_a$: Position in the upper third of the chimney diffusion (or in the middle). • $C(z = z_a) = C_a$ $C_a = C_{Upper}$ Is the concentration at the point z_a. 	$C(z = z_a) = A \frac{D}{v} e^{\frac{v}{2D} z} + B = C_a$ (16.2)
	z_b, C_b	<ul style="list-style-type: none"> • $z = z_b$: Position in the soil of the diffusion chimney. • $C(z = z_b) = C_b$ $C_b = C_{Soil}$ Is the concentration at the point z_b. 	$C(z = z_b) = A \frac{D}{v} e^{\frac{v}{2D} z} + B = C_b$ (16.3)

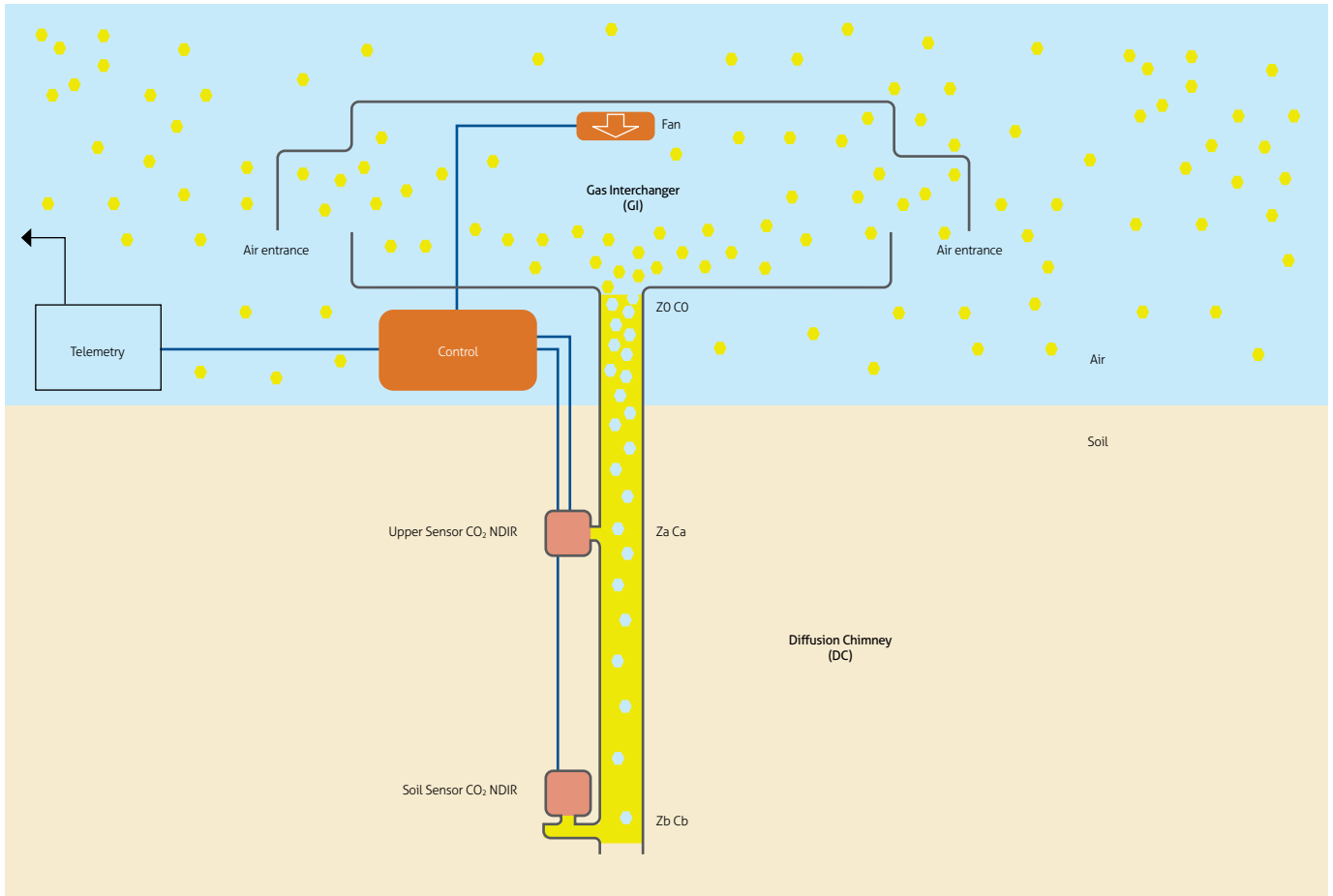


Figure 7. Assembly of a prototype embedded system for the measurement of CO₂ mass flux by diffusion and advection

6. MASS FLUX CALCULATION

$$J_i = B \times v \left[\frac{mg}{s \cdot m^2} \right] \quad (18)$$

6.1. The solution for $v = 0$

The calculation of the J_i mass flux for $v = 0$ is obtained by integrating equation 2 (Fick's first law), and for the point $z = z_a$ and the concentration C_a , it will be:

$$J_i(z, C) = \frac{-D(C_a - C_0)}{z} \left[\frac{mg}{s \cdot m^2} \right] \quad (17)$$

6.2. The solution for $v \neq 0$

The calculation of the J_i mass flux for $v \neq 0$ is determined by equation 9 with the solutions of equation 14 (see analytical solution number 11.1.2). After replacing the terms A , B , and v and simplifying, J_i will be as follows:

Where v is obtained from:

$$v = \frac{\ln(Y) \times D}{z_a} \quad (19)$$

And where Y is:

$$Y = \frac{-1 + \sqrt{1 - 4 \times \left(1 - \frac{(C_b - C_0)}{(C_a - C_0)} \right)}}{2} \quad (20)$$

Where:

- » $C_b > C_a > C_0$
- » $z_b = 3 \times z_a$ (is the cubic solution, see the analytic solution in 11.1.2)

The value of B is obtained as follows:

$$B = C_0 - \left(\frac{C_a - C_0}{e^{\frac{v}{D} \times z_a} - 1} \right) \quad (21)$$

This means that it is only necessary to know C_b , C_a , C_0 , D , and z_a to get A , B , and v , and thus obtain the J_i mass flux as long as it is satisfied that $C_b > C_a > C_0$ and $z_b = 3 \times z_a$.

7. THEORETICAL EXAMPLE

Suppose there is a diffusion chimney one inch in diameter and one meter long with a gas interchanger large enough to retain at its top a stable environmental concentration independent of the wind. There are two CO_2 concentration sensors, one at ground level at 1 m and the other at 0.333 m from the end of the chimney inwards. The system runs at 4,600 *masl* (Pressure 566 *hPa*), and the air temperature is almost constant at 10°C. Sensors after 45 minutes show the next concentrations at three different hours in the day: Measure 1: $C_a = 1,941.1 \text{ ppm}$ and $C_b = 5,000 \text{ ppm}$; Measure 2: $C_a = 17,490 \text{ ppm}$ and $C_b = 50,000 \text{ ppm}$; Measure 3: $C_a = 22,644.8 \text{ ppm}$ and $C_b = 50,000 \text{ ppm}$. Assume $C_0 = 404 \text{ ppm}$ as the reference concentration at $T = 25^\circ\text{C}$ and $P = 1,013 \text{ hPa}$; no adjustments are made for changes in atmospheric pressure, and it is recalled that length measurements are negative.

Questions:

- How much mass flux in $\left[\frac{\text{mg}}{\text{sxm}^2} \right]$ is being emitted for the measurements 1, 2, 3?
- Determine for measurements 1, 2, and 3 if the system is diffusive or advective-diffusive.

Data:

- » The 1-inch diameter data does not affect the measurement.
- » $z_a = -0.333 \text{ m}$.

Table 2. Measurement

	Measurement 1	Measurement 2	Measurement 3
C_0	404 ppm	404 ppm	404 ppm
C_a	1,941.1 ppm	17,490 ppm	22,644.8 ppm
C_b	5,000 ppm	50,000 ppm	50,000 ppm

- To calculate the mass flux, all values in *ppm* (the three measurements and points) should be changed to $\left[\frac{\text{mg}}{\text{m}^3} \right]$ and adjusted

for 4,600 *masl* and 10°C. Then the diffusion coefficient is calculated at the operating pressure and temperature. The mass flux velocity is then calculated using equations 20 and 19. The mass flux is calculated by equations 18 and 21.

- To determine whether the system is diffusive or advective-diffusive for all three cases, it is necessary to evaluate the velocity v obtained for the three cases and compare it with D by equation 15.

In the next sections, a step-by-step process is developed.

7.1. Calculation from ppm to mg/m³ unit

To convert the concentration C given in *ppm* to $\left[\frac{\text{mg}}{\text{m}^3} \right]$, it is necessary to multiply the *ppm* (ratio of CO_2 molecules to total molecules in one volume) by the molecular weight of CO_2 and divide it by the number of moles that fit in that volume according to the law of gases $V = \frac{R \times T}{P}$.

But since the system also works at a different pressure and temperature, the concentration C given in *ppm* should be passed to the concentration C given in $\left[\frac{\text{mg}}{\text{m}^3} \right]$ referenced to $P = 1,013 \text{ hPa}$ and temperature $T = 25^\circ\text{C}$.

$$C \frac{\text{mg}}{\text{m}^3} = \frac{Mw_{CO_2} \times C_{PPM}}{R \times T} \times 10^{-1} \left[\frac{\text{mg}}{\text{m}^3} \right]$$

$$C \frac{\text{mg}}{\text{m}^3} = \frac{P \times Mw_{CO_2} \times C_{PPM}}{R \times T} \times 10^{-1} \left[\frac{\text{mg}}{\text{m}^3} \right] \quad (22)$$

Where

- » $C \frac{\text{mg}}{\text{m}^3}$ is the concentration given in $\left[\frac{\text{mg}}{\text{m}^3} \right]$.
- » P is the pressure in [*hPa*].
- » Mw_{CO_2} is the CO_2 molecular weight in $\left[\frac{\text{g}}{\text{mol}} \right]$ (according to the periodic table 44.01).
- » C_{PPM} is the concentration given in *ppm* by the NDIR sensor.
- » R is the constant of the ideal gases that equals $8.315684 \text{ in } \left[\frac{\text{m}^2 \times \text{Pa}}{\text{K} \times \text{mol}} \right]$.
- » T is the temperature in Kelvin degrees [$^\circ\text{K}$]. (Sum 273.2 to the value in $^\circ\text{C}$ to get $^\circ\text{K}$).
- » 10^{-1} is the conversion factor of passing *hPascals* to *Pascals*, *ppm* to real value, and *grams* to *milligrams*:
 $10^{-1} = \frac{100 \text{ Pa}}{1 \text{ hPa}} \times 10^{-6} \times \frac{1,000 \text{ mg}}{1 \text{ g}}$.

For example, replacing $C_{PPM} = 5,000 \text{ ppm}$, $P = 566 \text{ hPascals}$ (4,600 *masl*), and 10°C the next result is obtained:

$$C \frac{mg}{m^3} = \frac{566 \times 44.01 \times 5,000}{8.315684 \times (273.2^\circ + 10^\circ)} \times 10^{-1} \left[\frac{mg}{m^3} \right]$$

$$C \frac{mg}{m^3} = 5,288.66 \left[\frac{mg}{m^3} \right]$$

Performing the calculations of the other values from *ppm* to $\left[\frac{mg}{m^3} \right]$ with pressure and temperature adjustment:

Table 3. Results

	Measurement 1	Measurement 2	Measurement 3
C ₀	404 ppm-> 427.32 $\left[\frac{mg}{m^3} \right]$	404 ppm-> 427.32 $\left[\frac{mg}{m^3} \right]$	404 ppm-> 427.32 $\left[\frac{mg}{m^3} \right]$
C _a	1,941.1 ppm-> 2,053.18 $\left[\frac{mg}{m^3} \right]$	17,490 ppm-> 18,499.7 $\left[\frac{mg}{m^3} \right]$	22,644.8 ppm-> 23,952 $\left[\frac{mg}{m^3} \right]$
C _b	5,000 ppm-> 5,288.66 $\left[\frac{mg}{m^3} \right]$	50,000 ppm-> 52,886 $\left[\frac{mg}{m^3} \right]$	50,000 ppm-> 52,886.6 $\left[\frac{mg}{m^3} \right]$

7.2. Velocity calculation

Then equations 19 and 20 are used to calculate the velocity of the gas. To determine measurement 1, the Table 3 values are used, then:

$$Y = \frac{-1 + \sqrt{1 - 4 \times \left(1 - \frac{(C_b - C_0)}{(C_a - C_0)} \right)}}{2} \quad (20)$$

$$v = \frac{\ln(Y) \times D}{z_a} \quad (19)$$

Replacing for measurement 1 in equation 20:

$$Y = \frac{-1 + \sqrt{1 - 4 \times \left(\frac{(5,288.66 - 427.32)}{(2,053.18 - 427.32)} \right)}}{2}$$

$$Y = 0.99666677$$

Replacing for the measurement 1 in equation 19 with the value of *D* adjusted to the pressure and temperature according to equation 3:

$$v = \frac{\ln(0.99666677) \times 2.66 \times 10^{-5}}{-0.333}$$

$$v = 2.66 \times 10^{-7} \left[\frac{m}{s} \right]$$

For the other measurements, see the following table:

Table 4. Results

	Measurement 1	Measurement 2	Measurement 3
Velocity	$2.66 \times 10^{-7} \left[\frac{m}{s} \right]$	$2.66 \times 10^{-6} \left[\frac{m}{s} \right]$	$2.66 \times 10^{-5} \left[\frac{m}{s} \right]$

7.3. Mass Flux calculation

Equation 18 is used to calculate the mass flux:

$$J_i = B \times v \left[\frac{mg}{s \times m^2} \right] \quad (18)$$

But *B* needs to be known, which can be obtained using equation 21

$$B = 427.3 - \left(\frac{-4,890.65 \times 2.66 \times 10^{-5}}{2.66 \times 10^{-7}} \right)$$

$$B = 489,492$$

Replacing *B* by the value in equation 18:

$$J_i = 489,492 \times 2.66 \times 10^{-7} \left[\frac{mg}{s \times m^2} \right]$$

$$J_i = 0.130 \left[\frac{mg}{s \times m^2} \right]$$

Comparing with the linear solution using equation 17 and its relative error:

Table 5. Results

	Measurement 1	Measurement 2	Measurement 3
Mass flux $\left[\frac{mg}{s \times m^2} \right]$	0.130 $\left[\frac{mg}{s \times m^2} \right]$	1.47 $\left[\frac{mg}{s \times m^2} \right]$	2.22 $\left[\frac{mg}{s \times m^2} \right]$
Mass flux $\left[\frac{mg}{s \times m^2} \right]$ (Solution for $v=0$)	0.129 $\left[\frac{mg}{s \times m^2} \right]$	1.47 $\left[\frac{mg}{s \times m^2} \right]$	1.879 $\left[\frac{mg}{s \times m^2} \right]$
Error	< 1%	< 1%	15%

7.4. Resolution of the type of transport of matter

For the determination of the type of transport of matter in the measuring system, that is, if it is diffusive or advective-diffusive, the parameter *N* of equation 15 is used, evaluated for the different speeds obtained from Table 4:

- » $N \gg 1$ there is no mass flux.
- » $N > 1$ is only diffusive.
- » $N = 1$ advective-diffusive transition.
- » $0 < N < 1$ is advective-diffusive.

$$\text{Note: } z = -1[m], D = 2.66 \times 10^{-5} \left[\frac{m^2}{s} \right]$$

Table 6. Results

Equation 15	Measurement 1	Measurement 2	Measurement 3
$N = \frac{D}{30 \times v \times z}$	10	1	0.1
Type of transport of matter	Diffusive	Advective-diffusive transition	Advective-diffusive

As seen in the theoretical exercise the system at low velocities delivers the same values as Fick's first law calculation. At higher velocities, the system estimates the advective process and obtains the value of the mass flux as the sum of the diffusive and advective process.

8. CORRECTIONS

The corrections of the system measurements associated with the changes in the physical-chemical parameters are:

- » Corrections for the isotopic composition of the gas.
- » Corrections for atmospheric pressure variations (not covered in this document).
- » Wind effect corrections are associated with the design of the gas interchanger (not covered in this document).

8.1. Corrections by gas isotopic composition

The carbon isotopic composition of CO_2 gas is an important marker for determining its origin in a volcano. The degassing of CO_2 in the upper magma shows typical values of $\delta^{13}C(CO_2)$ from -9% to -4% (Camarda et al., 2007). These variations will have little effect in the measurement system being converted from ppm to $\left[\frac{mg}{m^3}\right]$ (at the time of using the molecular weight of 44.01 of the CO_2). The reader could see that only hundredths could affect the molecular weight value, so the effect can be considered negligible if the units are given in $\left[\frac{mol}{m^2 \times day}\right]$. Studying the isotopic marker in the soil where the measurement will be made is more important than this small adjustment in the formulas to measure the mass flux.

9. COMPARISON BETWEEN MODELS

For practical purposes, the open chamber model (diffusion chimney) for $v = 0$ is compared due to the large numerical approximation of the results when the $+\infty \gg N > 1$ (without showing the errors) with the closed camera model (accumulation chamber) to see the differences between the measurement models.

Replacing equations 3 and 22 in equation 17, you get:

$$J_i(z, C) = 1.21787 \times 10^{-6} \times T^{0.75} \times (C_{PPM_a} - C_{PPM_0}) \left[\frac{mg}{s \times m^2} \right] \quad (23)$$

Where:

- » $J(z, C)$ is the CO_2 mass flux in $\left[\frac{mg}{s \times m^2} \right]$
- » C_{PPM_a} is the concentration in ppm of the meter located in the DC at a distance $z = z_a = -0.333$ meters.
- » C_{PPM_0} is the atmospheric concentration in ppm .
- » T is the operating temperature in $[^\circ K]$.

As can be seen, the mathematical model depends on a constant 1.21787×10^{-6} that includes the diffusion coefficient D , the distance $z = -0.333$ meters, the molecular weight of CO_2 , and other parameters that do not depend on any other variable. The dependent variable depends only on the temperature T and the concentration difference in ppm . In this model, the pressure P does not affect the model since replacing the equations is canceled.

For the model of the closed chamber (accumulation chamber), the following equation is used using a West Systems instrument with a LICOR LI-800 Non-dispersive infrared CO_2 detector (West Systems, 2012):

$$J(t, C) = \frac{P \times V (C_f - C_i)}{R \times T \times A \times t} = \frac{P \times V}{R \times T \times A \times 10^6} \times \frac{(C_f - C_i)}{t} \left[\frac{mol}{s \times m^2} \right]$$

Resemble equation 23 by adding molecular weight Mw_{CO_2} and 10^3 , which is the conversion factor from grams to milligrams to adjust units for analysis (without showing errors) and separating independent variable constants. The following equation is:

$$J(t, C) = \frac{P \times V (C_f - C_i)}{R \times T \times A \times t} = \frac{V \times Mw_{CO_2} \times 10^{-3}}{R \times A} \times \frac{P \times (C_f - C_i)}{T \times t} \left[\frac{mg}{s \times m^2} \right] \quad (24)$$

As it can be seen, the mathematical model depends on a constant $\frac{V \times Mw_{CO_2} \times 10^{-3}}{R \times A}$, which are the gas constant R , chamber volume V , chamber area A , molecular weight Mw_{CO_2} from the CO_2 , and the value 10^{-3} which is the compiled conversion factor of grams to milligrams and times of ppm . The dependent variable depends on pressure P , temperature T , and concentration difference in ppm . The $C_f - C_i$ value is the difference of concentrations in time t .

This latter equation 24 has more independent variables than equation 23. The interesting thing about this analysis is that the "open chamber" model in the diffuse state only needs to know the temperature and difference of ppm to calculate the mass flux. Many CO_2 sensors give this information, so the absolute pressure sensor for this model range is unnecessary, because variable P is canceled out in the mathematical development.

Table 7. Comparison of models

System	Constants	Independent variables	Simplified model
Open chamber (Diffusion chamber(DC)) Note: $\Delta z = 0.333$ immersed in 1.21787×10^{-6} and $v = 0$	1.21787×10^{-6}	$T^{0.75} \times (C_{ppm_a} - C_{ppm_0})$	$K_{CD} \times \frac{\Delta C}{\Delta z} \left[\frac{mg}{s \times m^2} \right]$
Closed chamber (Accumulation chamber (AC))	$\frac{V \times MW_{CO_2} \times 10^{-3}}{R \times A}$	$\frac{P \times (C_f - C_i)}{T \times t}$	$K_{AC} \times \frac{\Delta C}{\Delta t} \left[\frac{mg}{s \times m^2} \right]$

10. TECHNICAL ASPECTS OF IMPLEMENTATION

The GI is the key to the system since it is the one that allows the edge of the DC to occur at the reference concentration given by the atmosphere. Some recommendations of the system are:

- » A strong wind should not influenced it. This is a theoretical assumption that must be tested in practice. For this purpose, the GI must have protection so that the wind does not generate turbulence on the DC and does not affect the diffusive process at the beginning of the system. The wind must be perpendicular to the diffusive axis in the worst-case scenario.
- » There should be external light wind for the system to work well since the model assumes the atmosphere must give a concentration reference.
- » The area ratio between GI and DC should be at least 100, as a transition of the flux area of a magnitude of two orders reduces the maximum probable speed from $10^{-4} \left[\frac{m}{s} \right]$ to $10^{-6} \left[\frac{m}{s} \right]$, causing the GI to function under a diffusive regime. This allows for equalizing the external environmental concentration in the GI as a more precise measure of the CO₂ flux.

The sensitivity and response time of the system to CO₂ depends on:

- » The resolution of the NDIR detector of CO₂.
- » The volume ratio of DC and GI.
- » The length of the DC.
- » The ability of GI to mix gases without being affected by external wind turbulence.

11. ANALYTIC SOLUTION

11.1. Calculation of advective-diffusive mass flux

To obtain the mass flux equations, we start with the approach of equations 16.1, 16.2, and 16.3. From equation 18, it is observed

that in order to calculate the mass flux, the constant B must be calculated first, and for this, equation 16.1 is used:

$$C(z = z_0 = 0) = A \frac{D}{v} + B = C_0 \quad (16.1)$$

Where B will be:

$$B = C_0 - A \frac{D}{v}$$

As can be seen, B depends on A , and to calculate it, we use 16.2 and 16.3, replacing each one with the previous equation.

Replacing the previous equation in 16.2 and 16.3, respectively, and obtaining A :

$$A = \frac{v}{D} \times \frac{(C_a - C_0)}{e^{\frac{v}{D} z_0} - 1} \quad (21.1)$$

$$A = \frac{v}{D} \times \frac{(C_b - C_0)}{e^{\frac{v}{D} z_0} - 1} \quad (21.2)$$

Equation 21.1 and equation 21.2 are equalized so that only v is unknown:

$$A = \frac{(C_b - C_0)}{e^{\frac{v}{D} z_0} - 1} = \frac{(C_a - C_0)}{e^{\frac{v}{D} z_0} - 1}$$

Solving:

$$(e^{\frac{v}{D} z_0} - 1) (C_a - C_0) = (C_b - C_0) (e^{\frac{v}{D} z_0} - 1)$$

For practical purposes the following replacement is made $CC_b = C_b - C_0$, $CC_a = C_a - C_0$:

$$(e^{\frac{v}{D} z_0} - 1) CC_a = (e^{\frac{v}{D} z_0} - 1) CC_b$$

$$e^{\frac{v}{D} z_0} CC_a - e^{\frac{v}{D} z_0} CC_b + CC_b - CC_a = 0 \quad (25)$$

The solution to this equation has two parts, the quadratic solution when the sensor is in the middle of the DC and the cubic solution when the sensor is in the third part of the DC. The following substitution is performed for the solution:

- » To solve in a quadratic way, it is necessary to execute $z_b = 2 \times z_a$.
- » To solve in the cubic form, it is necessary to execute $z_b = 3 \times z_a$.

11.1.1. Mathematical solution (Quadratic)

The variables to be used are A , B , and v . To obtain B , equation 25 is used, substituting $z_b = 2 \times z_a$:

$$e^{\frac{v}{D} 2z_a} CC_a - e^{\frac{v}{D} z_a} CC_b + CC_b - CC_a = 0$$

A variable change is made $Y = e^{\frac{v}{D} z_a}$:

$$Y^2 CC_a - Y CC_b + (CC_b - CC_a) = 0$$

the quadratic equation solution is applied:

$$a = CC_a, b = -CC_b, c = CC_b - CC_a$$

$$Y = \frac{-(b) \pm \sqrt{b^2 - 4ac}}{2a}$$

$$Y = \frac{-(-CC_b) \pm \sqrt{(-CC_b)^2 - 4CC_a (CC_b - CC_a)}}{2CC_a}$$

The next solutions are obtained:

$$Y_1 = 1$$

$$Y_2 = \text{Valid solution}$$

Changing the variable, the velocity is obtained depending on C_0 , C_a , C_b , D , and z_a .

$$v = \frac{\ln(Y_2) D}{z_a}$$

This solution Y_2 will not be practical, but the solution $Y_1 = 1$ will be useful for the other solution by applying the substitution $z_b = 3 \times z_a$.

11.1.2. Mathematical solution (Cubic)

The cubic solution is developed in the same way as the quadratic solution until equation 25 is obtained:

$$e^{\frac{v}{D} 3z_a} CC_a - e^{\frac{v}{D} z_a} CC_b + CC_b - CC_a = 0 \tag{25}$$

Replacing $z_b = 3 \times z_a$, and doing $Y = e^{\frac{v}{D} z_a}$:

$$Y^3 CC_a - Y CC_b + (CC_b - CC_a) = 0$$

It is divided by CC_a

$$Y^3 - Y \frac{CC_b}{CC_a} + \frac{(CC_b - CC_a)}{CC_a} = 0$$

Which is a cubic equation of the form:

$$a_2 Y^3 + b_2 Y^2 + c_2 Y + d_2 = 0$$

In order to solve the cubic equation, the solution form will have the form $(Y - Y_1)(Y - Y_2)(Y - Y_3)$ whose solutions are matching term to term:

$$Y_1 + Y_2 + Y_3 = -\frac{b_2}{a_2} \tag{26}$$

$$Y_1 Y_2 + Y_1 Y_3 + Y_2 Y_3 = \frac{c_2}{a_2} \tag{27}$$

$$Y_1 Y_2 Y_3 = -\frac{d_2}{a_2} \tag{28}$$

As it is known from the previous quadratic solution that $Y_1 = 1$ which replaced in equations 26, 27, and 28, and, in addition, it is also known that $a_2 = 1$ and $b_2 = 0$.

- 1) $1 + Y_2 + Y_3 = 0 \Rightarrow Y_2 = -1 - Y_3$
- 2) $Y_2 + Y_3 + Y_2 Y_3 = c_2$
- 3) $Y_2 Y_3 = -d_2$

Since there are only two unknowns and three equations, only two equations are enough to solve the problem since one of the equations is linearly dependent on another. Therefore, Y_2 is obtained from the first and replaced in the second.

$$-1 - Y_3 + Y_3 + (-1 - Y_3) Y_3 = c_2$$

$$-1 - Y_3 - Y_3^2 = c_2$$

Organizing:

$$Y_3^2 + Y_3 + 1 + c_2 = 0 \tag{29}$$

Which is again a quadratic equation with the following coefficients:

$$a_3 = 1, b_3 = 1, c_3 = 1 + c_2$$

Where Y_3 has a quadratic solution:

$$Y_3 = \frac{-(b_3) \pm \sqrt{b_3^2 - 4a_3c_3}}{2a_3}$$

$$Y_3 = \frac{-(1) \pm \sqrt{(1)^2 - 4(1+c_2)}}{2(1)}$$

When replacing $c = \frac{C_b}{C_a}$, the next result is obtained:

$$Y_3 = \frac{-1 \pm \sqrt{1 - 4 \times \left(1 - \frac{(C_b - C_0)}{(C_a - C_0)}\right)}}{2}$$

The solution with the positive (+) sign is taken since the negative solution is a physically not possible solution for this model:

$$Y = \frac{-1 + \sqrt{1 - 4 \times \left(1 - \frac{(C_b - C_0)}{(C_a - C_0)}\right)}}{2} \quad (20)$$

Changing the variable again, the velocity is obtained in the function of C_0 , C_a , C_b , D and z_a :

$$v = \frac{\ln(Y) \times D}{z_a} \quad (19)$$

12. CONCLUSIONS

- » A stations network implementing the newly proposed technique would be possible to establish a continuous measurement of CO₂ per day emitted at a specific area of a volcano, and it could be validated with non-continuous and non-telemetric measurements, for instance, using the manual accumulation chamber portable instrument.
- » The solution of a 3 × 3 equations system using data from NDIR sensors and other parameters does not require knowledge of the soil characteristics that condition the speed of the gas that emerges due to advection-diffusion.
- » A new parameter in this paper called N will establish the state of the measurement system in a simplified way, defining the diffusive or advective-diffusive state and the inflection point.

- » The new element, called a gas interchanger, is key to the measurement system to avoid affectation by wind and external dust.
- » Any NDIR with a resolution of 10 ppm has sufficient capacity to measure a mass flow and the resolution is also determined by the gas interchanger that sets the external reference. Therefore, mathematically it can be verified that 10 ppm error generates approximately 1 % theoretical error in measuring the mass flux.
- » For the solution of the system of equations, it is necessary to have the environmental concentration of CO₂. The momentary agitation of the gas could obtain this value with an agitation fan in the diffusion chimney and the gas interchanger. The atmospheric concentration will be reported simultaneously by NDIR sensors at the time of shutting down the fan.
- » It is necessary to use an embedded system to determine the CO₂ mass flux from the volcano, using a good arrangement of the concentration, temperature, and pressure sensors in the tubes, controlling an agitation fan, and processing data remotely or locally. One difference with open chamber assemblies is that the inclusion of the gas interchanger is proposed here.

ACKNOWLEDGMENTS

The author wishes to especially thank his mother, Elzanna Margaret Mercado Weage, who revised the final manuscript in English. Additionally, a special thanks to the professional critic Carlos Laverde for his technical observations and edits to the first versions of this document, since he helped the evolution of this document to a more scientifically correct version. To Dario Corchuelo, who read the final document and made some edits which improved the final text. To Viviana Burbano, Luisa Mesa, and Zoraida Chacón of Colombia for their professional interests in using the analytical solution of the proposal for their professional activity. Sebastián Cajas made the formal translation of the document so that the scientific community would know it. Finally, the author thanks Yenny Cerquera and the anonymous reviewers for their valuable comments and suggestions, which helped improve the manuscript.

REFERENCES

- Allard P., Carbonnelle J., Dajlevic D., Le Bronec J., Morel P., Robe M. C., Maurenas J. M., Faivre-Pierret R., Martin D., Sabroux J. C., & Zettwoog P. (1991). Eruptive and diffuse emission of CO₂ from Mount Etna. *Nature*, 351, 387-391. <https://doi.org/10.1038/351387a0>
- Badalamenti, B., Gurrieri, S., Hauser, S., & Valenza, M. (1988). Ground CO₂ output in the island of Vulcano during the period 1984-1988: Gas hazard and volcanic activity surveillance implications. *Rend. Società Italiana di Mineralogia e Petrologia*, 43, 893-899.
- Baubron, J. C., Allard, P., & Toutain, J. P. (1990). Diffuse volcanic emissions of carbon dioxide from Vulcano island, Italy. *Nature*, 344, 51-53. <https://doi.org/10.1038/344051a0>
- Badalamenti, B., Gurrieri, S., Nuccio, P. M., & Valenza, M. (1991). Gas hazard on Vulcano Island. *Nature*, 350, 26-27.
- Bekku, Y., Koizumi, H., Nakadai, T., & Iwaki, H. (1955). Measurement of soil respiration using close chamber method: An IRGA technique. *Ecological Research*, 10(3), 369-373. <https://doi.org/10.1007/BF02347863>
- Busquets D. (2011). Difusión: 2º ley de Fick. Universidad Politécnica de Valencia. www.youtube.com/watch?v=HH-BvZDNvTic
- Camarda, M., De Gregorio, S., Favara, R., & Gurrieri, S. (2007). Evaluation of carbon isotope fractionation of soil CO₂ under an advective-diffusive regimen: A tool for computing the isotopic composition of unfractionated deep source. *Geochimica et Cosmochimica Acta*, 71(12), 3016-3027. <https://doi.org/10.1016/j.gca.2007.04.002>
- Camarda, M., Gurrieri, S., & Valenza, M. (2006). CO₂ flux measurements in volcanic areas using the dynamic concentration method: Influence of soil permeability. *Journal of Geophysical Research: Solid Earth*, 111(B5), B05202. <https://doi.org/10.1029/2005JB003898>
- Campbell, G. S. (1985). *Soil physics with basic transport models for soil-plant systems*. Elsevier.
- Callister W. D. (1995). *Introducción a la Ciencia e Ingeniería de los materiales*. Reverte.
- Cardellini, C., Chiodini, G., & Frondini, F. (2003). Application of stochastic simulation to CO₂ flux from soil: Mapping and quantification of gas release. *Journal of Geophysical Research. Solid Earth*, 108(B9), 2425.
- Chiodini, G., & Frondini, F. (2001). Carbon dioxide degassing from the Albani Hills volcanic region, Central Italy. *Chemical Geology*, 177(1-2), 67-83. [https://doi.org/10.1016/S0009-2541\(00\)00382-X](https://doi.org/10.1016/S0009-2541(00)00382-X)
- Chiodini, G., Cioni, R., Guidi, M., Raco, B., & Marini, L. (1998). Soil CO₂ flux measurements in volcanic and geothermal areas. *Applied Geochemistry*, 13(5), 543-552. [https://doi.org/10.1016/S0883-2927\(97\)00076-0](https://doi.org/10.1016/S0883-2927(97)00076-0)
- Ciotoli, G., Guerra, M., Lombardi, S., & Vittori, E. (1998). Soil gas survey for tracing seismogenic faults: A case-study in the Fucino basin (central Italy). *Journal of Geophysical Research*, 103(B10), 23781-23794. <https://doi.org/10.1029/98JB01553>
- Ciotoli, G., Della Seta, M., Del Monte, M., Fredi, P., Lombardi, S., Palmieri, E. L., & Pugliese, F. (2003). Morphological and geochemical evidence of neotectonics in the volcanic area of Monti Vulsini (Latium, Italy). *Quaternary International*, 101-102, 103-113. [https://doi.org/10.1016/S1040-6182\(02\)00093-9](https://doi.org/10.1016/S1040-6182(02)00093-9)
- Cropper Jr, W. P., Ewel K. C., & Raich, J. W. (1985). The measurement of soil CO₂ evolution in situ. *Pedobiologia* 28, 35-40.
- Diliberto, I. S., Gurrieri, S., & Valenza, M. (1993). Vulcano: Gas geochemistry. CO₂ flux from the ground. *Acta Vulcanologica*, 3, 272-273.
- García, I. (2020). *Fenómenos de transporte y conductividad electrolítica*. Universidad de Valencia.
- Gerlach, T. M., Doukas, M. P., McGee, K. A., & R. Kessler. (2001). Soil efflux and total emission rates of magmatic CO₂ at the Horseshoe Lake tree kill, Mammoth Mountain, California, 1995-1999. *Chemical Geology*, 177(1-2), 101-116. [https://doi.org/10.1016/S0009-2541\(00\)00385-5](https://doi.org/10.1016/S0009-2541(00)00385-5)
- Giammanco, S., Gurrieri, S., & Valenza, M. (1995). Soil CO₂ degassing on Mt. Etna (Sicily) during the period 1989-1993: Discrimination between climatic and volcanic influences. *Bulletin of Volcanology*, 57, 52-60. <https://doi.org/10.1007/BF00298707>
- Giammanco S., Gurrieri, S., & Valenza, M. (1998). Anomalous soil CO₂ degassing in relation to faults and eruptive fissures on Mount Etna (Sicily, Italy). *Bulletin of Volcanology*, 60, 252-259. <https://doi.org/10.1007/s004450050231>
- Guerra, M., & Lombardi, S. (2001). Soil-gas method for tracing neotectonic faults in clay basins: The Pisticci field (southern Italy). *Tectonophysics*, 339(3-4), 511-522. [https://doi.org/10.1016/S0040-1951\(01\)00072-5](https://doi.org/10.1016/S0040-1951(01)00072-5)
- Gurrieri, S., & Valenza, M. (1988). Gas transport in natural porous medium: a method for measuring soil CO₂ flows

- from the ground in volcanic and geothermal areas. *Rendiconti della Società Italiana di Mineralogia e Petrologia*, 43, 1151-1158.
- Hernández, P., Notsu, K., Salazar, J., Mori, T., Natale, G., Okada, H., Virgili, G., Shimoike, Y., Sato, M., & Pérez, N. (2001). Carbon dioxide degassing by advective flow from Usu Volcano, Japan. *Science*, 292(5514): 83-86. <https://doi.org/10.1126/science.1058450>
- Inguaggiato, S., Jácome Paz, M. P., Mazot, A., Delgado Granados, H., Inguaggiato, C., & Vita, F. (2013). CO₂ output discharged from Stromboli Island (Italy). *Chemical Geology*, 339, 52-60. <https://doi.org/10.1016/j.chemgeo.2012.10.008>
- Isachenko V., Osipova V., & Sukomel A. (1980). *Heat Transfer*. Mir Publisher.
- Jácome Paz, M. P., Taran, Y., Inguaggiato, S., & Collard, N. (2016). CO₂ flux and chemistry of El Chichón Crater Lake (México) in the period 2013-2015: Evidence for the enhanced volcano activity. *Geophysical Research Letters*, 43(1), 27-134. <https://doi.org/10.1002/2015GL066354>
- Janssens, I., Kowalski, A., Longdoz, B., & Ceulemans, R. (2000). Assessing forest soil CO₂ efflux: an in-situ comparison of four techniques. *Tree Physiology*, 20(1), 23-32. <https://doi.org/10.1093/treephys/20.1.23>
- Hernández, P. A., Salazar, J. M., Shimoike, Y., Mori, T., Notsu, K., & Pérez, N. M. (2001). Diffuse emission of CO₂ from Miyakejima volcano, Japan. *Chemical Geology*, 177(1-2), 175-185. [https://doi.org/10.1016/S0009-2541\(00\)00390-9](https://doi.org/10.1016/S0009-2541(00)00390-9)
- Moreno, J. (2005). *Metodología para el cálculo de incertidumbre*. Encuentro Nacional de metrología eléctrica, México.
- Nakadai, T., Koizumi, H., Usami, Y., Satoh, M., & Oikawa, T. (1993). Examination of the method for measuring soil respiration in cultivated land: Effect of carbon dioxide concentration on soil respiration. *Ecological Research*, 8(1), 65-71. <https://doi.org/10.1007/BF02348608>
- Norman, J. M., García, R., & Verma, S. B. (1992). Soil surface CO₂ fluxes and the carbon budget of a grassland. *Journal of Geophysical Research: Atmospheres*, 97(D17), 18845-18853. <https://doi.org/10.1029/92JD01348>
- Notsu, K., Mori, T., Chanchah, D., Vale, S., Kagi, H., & Ito, T. (2006). Monitoring quiescent volcanoes by diffuse CO₂ degassing: case study of Mt. Fuji, Japan. *Pure and Applied Geophysics*, 163(4), 825-835. <https://doi.org/10.1007/s00024-006-0051-0>
- Rogie, J. D., Kerrick, D. M., Sorey, G., Chiodini, M. L., & Galloway, D. L. (2001). Dynamics of carbon dioxide emission at Mammoth Mountain Continuous monitoring of diffuse CO₂ degassing, Horseshoe Lake, Mammoth Mountain, California. *Earth and Planetary Science Letters*, 188(3-4), 531-541. [https://doi.org/10.1016/S0012-821X\(01\)00344-2](https://doi.org/10.1016/S0012-821X(01)00344-2)
- Sahimi, M. (1995). *Flow and Transport in Porous Media and Fractured Rock: From Classical Methods to Modern Approaches*. Wiley-VCH Verlag GmbH & Co. <https://doi.org/10.1002/9783527636693>
- Salazar, J. M. L., Pérez, N. M., Hernández, P. A., Soriano, T., Barahona, F., Olmos, R., Cartagena, R., López, D. L., Lima, R. N., Melián, G., Galindo, I., Padrón, E., Sumino, H., & Notsu, K. (2002). Precursory diffuse carbon dioxide degassing signature related to a 5.1 magnitude earthquake in El Salvador, Central America. *Earth and Planetary Science Letters*, 205(1-2), 81-89. [https://doi.org/10.1016/S0012-821X\(02\)01014-2](https://doi.org/10.1016/S0012-821X(02)01014-2)
- Spicák, A., & Horálek, J. (2001). Possible role of fluids in the process of earthquakes swarm generation in the West Bohemia/Vogtland seismoactive region. *Tectonophysics*, 336(1-4), 151-161. [https://doi.org/10.1016/S0040-1951\(01\)00099-3](https://doi.org/10.1016/S0040-1951(01)00099-3)
- Tonani, F., & Miele, G. (1991). *Methods for measuring flow of carbon dioxide through soils in the volcanic setting*. International Conference Active Volcanoes and Risk Mitigation, IAVCEI, Naples, Italy.
- Wakita, H. (1996). Geochemical challenge to earthquake prediction. *PNAS*, 93(9), 3781-3786. <https://doi.org/10.1073/pnas.93.9.3781>
- West Systems. (2012). *Portable difusse flux meter with LI-COR CO₂ detector*. HandBook.
- Witkamp, M. (1966). Decomposition of leaf litter in relation to environment, microflora and microbial respiration. *Ecology*, 47(2), 194-201. <https://doi.org/10.2307/1933765>
- World Meteorological Organization (WMO). (2019). The State of Greenhouse Gases in the Atmosphere Based on Global Observations through 2018. *WMO Greenhouse Gas Bulletin*, (15).



Cerro Yuruma, Alta Guajira, Colombia
Fotografía de Pedro Patarroyo



This work is distributed under the Creative Commons Attribution 4.0 License.

Received: September 11, 2020

Revision received: July 26, 2021

Accepted: August 23, 2021

Published on line: September 24, 2021

The role of Rare Earth Elements in the deployment of wind energy in Colombia

El papel de los elementos de tierras raras en el despliegue de la energía eólica en Colombia

Carlos Andrés Gallego¹

1. Servicio Geológico Colombiano, Dirección de Recursos Minerales, Bogotá, Colombia

Corresponding author: cgallego@sgc.gov.co, carlosgallego80@gmail.com

ABSTRACT

The deployment of renewable energy technologies will play a crucial role in the global transition to a low-carbon economy and ultimately in the fight against global warming. However, this transition could face important problems because most of those technologies rely on the steady supply of critical minerals. Colombia, thanks to its hydrological resources, has relied on the hydro-power for electricity generation. However, the government has implemented measures to back-up the energy system in draught periods and, consequently, fossil fuels-based plants have increased the market share and with these, CO₂ emissions. This study assesses the mineral demand in Colombia in the period 2020-2050 for the rare earth elements embedded in the deployment of wind power technologies in four different climate policy scenarios in order to establish whether they could face geological bottlenecks that could ultimately hamper the transition to a low-carbon economy. The Gigawatts (GW) of future capacity additions in the energy system are converted into tons of metal using published metal intensities of use and assumptions of Colombia's technological pathway. Then, the cumulated mineral demand is compared against current mining production rates and geological reserves to establish geological bottlenecks. The results show that the reserves will not pose any threat to its transition. However, when compared to current mining rates, the mineral demand in 2050 could pose a problem for the supply of minerals. Finally, this study gives some policy recommendations that could be used to mitigate these issues, such as substitution, improved circular economy and sound technological choices.

Keywords: Renewable energy technologies, mineral demand, climate change mitigation, Dysprosium, Neodymium.

RESUMEN

El despliegue de tecnologías de energía renovable desempeñará un papel crucial en la transición mundial hacia una economía con bajas emisiones de carbono y, en última instancia, en la lucha contra el calentamiento del planeta. Sin embargo, esta transición podría enfrentar problemas importantes porque la mayoría de esas tecnologías dependen del suministro constante de minerales críticos. Colombia, gracias a sus recursos hidrológicos, ha dependido de la energía hidroeléctrica para la generación de electricidad. Sin embargo, el gobierno ha implementado medidas para respaldar el sistema energético en períodos de sequía y, en consecuencia, las plantas de energía basadas en combustibles fósiles han aumentado la cuota de mercado y con ellas las emisiones de CO₂. Este estudio evalúa la demanda de minerales de los elementos de tierras raras en Colombia en el período 2020-2050 incorporados en las tecnologías de energía eólica en cuatro escenarios de política climática con el fin de establecer si estas podrían enfrentar cuellos de botella geológicos que, en última instancia, podrían obstaculizar la transición a una economía baja en carbono. Los gigavatios (GW) de las futuras adiciones de capacidad en el sistema energético son convertidos en toneladas de metal utilizando intensidades de uso de metales publicadas y suposiciones de la trayectoria tecnológica de Colombia. Luego, la demanda acumulada de minerales es comparada con las tasas actuales de producción minera y las reservas geológicas para establecer los cuellos de botella geológicos. Los resultados muestran que las reservas no supondrán ninguna amenaza para la transición. Sin embargo, si se compara con las tasas de extracción actuales, la demanda de minerales en 2050 podría ser un problema para la oferta de minerales. Por último, en este estudio se formulan algunas recomendaciones de política que podrían utilizarse para mitigar estas cuestiones, como la sustitución, la mejora de la economía circular y las opciones tecnológicas racionales.

Palabras clave: Tecnologías de energía renovable, demanda de minerales, mitigación del cambio climático, Disprosio, Neodimio.

1. INTRODUCTION

The worldwide transition from high to low-carbon economies will require the extraction and processing of a significant volume of rare earth elements (REEs) and other minerals which are used in Renewable Energy Technologies (RETs). The future physical availability of some of those minerals has become a source of concern, because the reliability of their supply could disrupt this transition, the economic development and ultimately, the fight against climate change. Especially sensitive are the transportation and energy sectors, in which the metal intensity shows a dramatic increase in the years to come (Koning et al., 2018).

For the purpose of this paper, critical minerals are those minerals considered important for any type of technology and which at the same time could face supply disruptions, for instance, because the mineral deposits are concentrated in just a few countries (McCullough and Nassar, 2017). The REEs, —which are classified as critical minerals— play an important role in the development of RETs. They are used in a relatively large amount of applications in key technologies being developed to provide a sustainable mobility and energy supply (Alonso et al., 2012). Wind and solar photovoltaic technologies, which make up a segment of RETs, use a wide variety of

REEs. Thus, if they were to be deployed on a large scale, as will be expected to decarbonize the economy in the future, this could pose a threat to such a transition.

The demand for fossil fuels to power up the energy production in Colombia has been increasing steadily thanks to a growing economic sector. Thus far, most of electricity production has been supplied by large hydroelectric power stations, but because of climate change and seasonal climatic oscillations such as El Niño that make hydropower less reliable, fossil fuel-powered energy has been gaining share in electricity mix to back up the system in high demand conditions.

Colombia's low-carbon strategy is still in its initial stages. The 1715 law of 2014 aimed to implement plans, policies and projects to promote the mitigation of greenhouse gases (GHG) emissions without compromising social and economic growth (Calderón et al., 2016), as well as to incorporate RETs into the national electricity grid. However, thus far, Colombia has failed to set a course of direction for the implementation of such technologies and policies.

Since the 1980s, many authors (namely, Hayes and McCullough, 2018 and references therein) studied criticality issues and its effects on the global deployment of RETs. In recent years there has been a boom in the research dealing with how the future

global deployment of sustainable technologies could be affected by the physical availability of critical minerals, such as the REEs (Koning et al., 2018; Manberger and Stenqvist, 2018; Deetman et al., 2018). However, to date there has been a lack of studies on how the deployment of RETs in developing countries could impact the global market, and more specifically on how the implementation of different climate-policy scenarios in developing countries could affect the global demand for metals.

Therefore, this study aims to fill the research gap described above by analyzing how the adoption of RETs would affect the global demand for REEs in the near to medium future. This study is limited to two REEs (namely dysprosium and neodymium) that are embedded in the wind power generation plans in Colombia during the 2020-2050 period.

The analysis is conducted by using the outcome of Calderón et al. (2016), where they assess the effect of carbon taxes and abatement targets on CO₂ emissions in four different climate-policy scenarios using four models from the CLIMA-CAP-LAMP project (van der Zwaan et al., 2016), giving as a result multiple pathways of how the future energy technologies would deploy during the 2020-2050 period.

Specifically, the variable wind energy capacity additions (in GW) of their research will be used as the main input for the purposes of this research. They are converted here into quantity of metals (kg) embedded in the wind power generation systems by employing intensities of use obtained in the published literature. The derived demand for metals in Colombia is then compared against current mining rates and reserves, ultima-

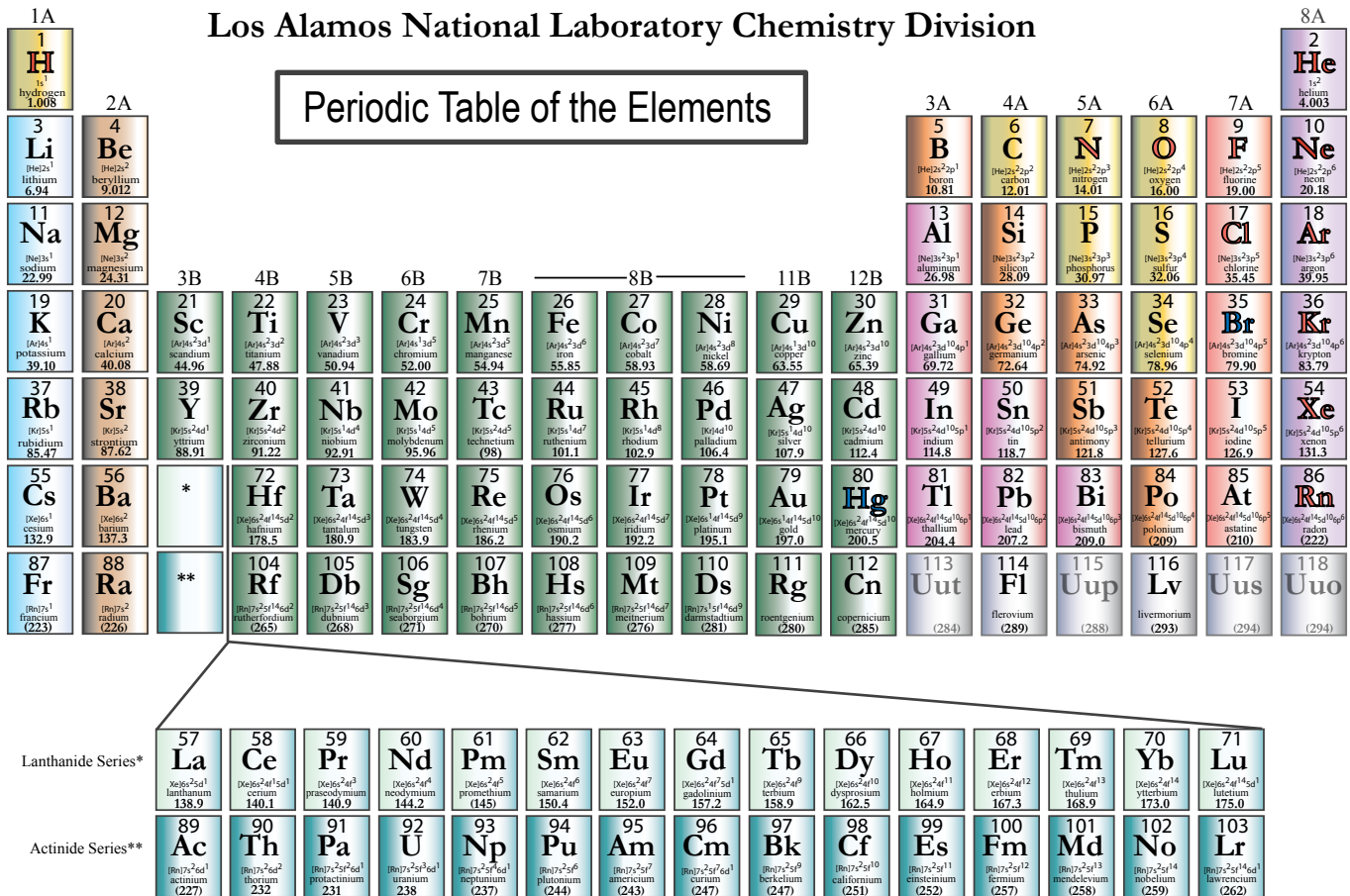


Figure 1. Periodic table of elements. The REEs are those elements highlighted by the rectangle. Source: Los Alamos National Laboratory, Chemistry Division, <https://periodic.lanl.gov/images/periodictable.pdf>



element names in **blue** are liquids at room temperature
 element names in **red** are gases at room temperature
 element names in **black** are solids at room temperature

tely allowing to establish whether the available resources are sufficient to meet future demand or whether there could be potential shortages of mineral resources that would affect the deployment of RETs. Finally, this study sheds light on whether the REEs would experience geological bottlenecks that could make them more expensive and concludes with a proposal for some policy options to deal with such issues.

2. BACKGROUND: RARE EARTH ELEMENTS, RENEWABLE ENERGY TECHNOLOGIES AND THE MINERAL REQUIREMENTS OF THE TRANSITION TO A LOW CARBON ECONOMY

2.1. Rare Earth Elements

Rare-earth elements (REEs) range from atomic number 57 (lanthanum) to 71 (lutetium) in the periodic table of elements and are commonly referred to as “lanthanides” (Figure 1, Table 1) (van Gosen et al., 2017). Yttrium (atomic number 39) and scandium (atomic number 21) are also regarded as REEs as they tend to occur in the same ore deposits as the lanthanides and show similar chemical and physical properties.

The term rare earth is really a misnomer, since they are not as rare as the name implies. Van Gosen et al. (2017) define its origin: “They were named rare earth because most were identified during the 18th and 19th centuries as ‘earths’, and, in comparison with other ‘earths’, such as lime or magnesia, they were relatively rare”. They are more abundant, on average, than silver, gold, or copper in the Earth’s crust (Table 1).

Not long ago, the REEs were familiar only for a relatively small number of people, such as chemists, engineers, and geologists. However, over the last decades these elements have gained considerable importance mainly due to three reasons: 1) their special properties which have made of them indispensable components of the modern technology; 2) the near-monopolistic market where China controls world production, and 3) the world’s heavy dependence on China’s production and its controlled supply (van Gosen et al., 2017).

Thanks to their unique magnetic, phosphorescent, and catalytic properties, over the last couple of decades the world has seen a noteworthy increase in the utilization of REEs in technologies deemed important such as clean energy sources and defense sectors.

Consequently, the strategic value of these elements was quickly recognized and the political and economic issues surrounding the global supply gained more visibility. Since then, the number of exploration activities aiming to discover economic deposits of REEs have dramatically increased (van Gosen et al., 2017).

Table 1. List of REEs with their crustal abundance

REEs	Symbol	Atomic number	Crustal abundance (ppm)
Lanthanum	La	57	39
Cerium	Ce	58	66.5
Praseodymium	Pr	59	9.2
Neodymium	Nd	60	441.5
Promethium	Pm	61	Does not occur in nature
Samarium	Sm	62	7.05
Europium	Eu	63	2.0
Gadolinium	Gd	64	6.2
Terbium	Tb	65	1.2
Dysprosium	Dy	66	5.2
Holmium	Ho	67	1.3
Erbium	Er	68	3.5
Thulium	Tm	69	0.52
Ytterbium	Yb	70	3.2
Lutetium	Lu	71	0.8
Yttrium	Y	39	33
Scandium	Sc	21	22

For the purpose of comparison, the average crustal abundances for silver, gold and copper are 0.075, 0.004, and 60, respectively. Source: van Gosen et al. (2014).

2.1.1. Demand and applications

The rate of economic growth and the development of new technologies are the two major drivers of demand for REEs (Mancheri et al., 2019). Sustainable technologies are one of the biggest sectors which requires REEs, including magnets, phosphors, catalysts, and batteries, and currently accounts for over 60% of the total demand; a tendency that will tend to increase fueled mostly by the heavy investments in clean energy.

The REEs are used in a variety of industrial and technological applications that take advantage of their unique physical and chemical properties. Table 2 shows the amount of REEs demanded by different intermediate products, which is expected to increase between 7-8% annually (Mancheri et al., 2019).

The main consumer of REEs are the permanent magnets made from REE alloys. Particularly important are the neodymium-iron-boron magnets since they are the strongest magnets currently known, especially when space and weight are critical variables. These magnets are used in hard disk drives, cell phones, electric motors for hybrid vehicles and windmills, and actuators in aircraft technologies (van Gosen et al., 2017).

Another major consumer are the catalytic converters based on cerium used in cars and the catalytic converters based on lanthanum used in the petroleum refining industry, followed by the use in the glass industry because they provide color and special optical properties to glass as well as glass polishing (cerium and lanthanum) (van Gosen et al., 2017).

Table 2. Global rare earth elements (metric tons of rare-earth-oxide (REO) equivalent) demand by type of intermediate product in 2017

Application	Total (tons)	Market share (%)
Magnets	51 000	30
Catalysts	30 000	18
Metal alloys	31 000	18
Polishing	22 000	14
Glass	9 500	6
Other	10 500	6
Ceramics	8 500	5
Phosphors	5 000	3
Total	167 500	100

Source: Mancheri et al. (2019).

The production of steel alloys and the removal of impurities in the steel-making industry uses cerium, lanthanum, neodymium, and praseodymium, commonly present in the form of a mixed oxide known as mischmetal.

Flat screens, some incandescent, fluorescent, and LED lighting used in phosphors consists of REEs, particularly yttrium, cerium, lanthanum, europium, and terbium. Medical applications such as magnetic resonance imaging (MRI) use gadolinium phosphors (van Gonsen et al., 2017).

2.1.2. Supply

China controls the global REEs industry and has established a dominant position in the entire value chain, from resource extraction to manufacturing of intermediate products such as magnets; products that are critical to high-growth industries such as the renewable energy technologies (RETs) (Mancheri et al., 2019).

Mine production data published by the United States Geological Survey (USGS, 1996-2020) indicate that China produced more than 90% of the total world supply between 2003 and 2012. Afterwards, its contribution to the total world supply has decreased from 86% in 2013 to 63% in 2019 (Figure 2, Table 3). However, it must be noted that the production volume shown for China in Table 3 does not include undocumented (“illegal”) production which can be rather significant. According to (Shen et al., 2020), there are estimates indicating that the illegal-sector production comprises, after 2017, between 20% and 50% of China’s total production, even after China announced new policies to curtail illegal production. As a result, total mine production in China, for example for 2019, can account for around 71% of the total world supply.

There are several reasons why China controls the REE market, including government support for the industry, low labor

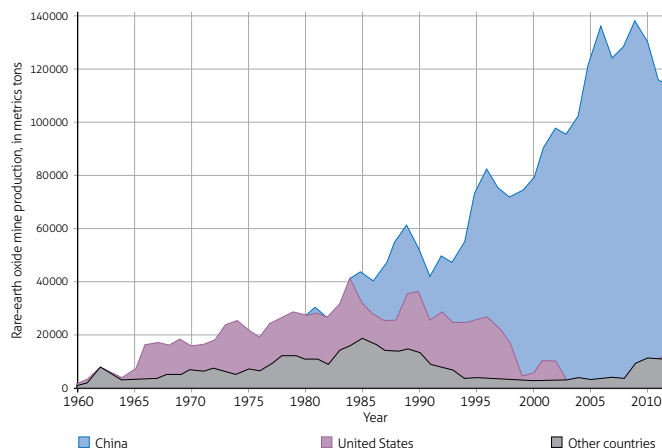


Figure 2. World mine production of rare-earth oxides by country and year since 1962 to 2012

Source: Taken from van Gonsen et al. (2017).

Table 3. Production and reserves of REEs (metric tons of rare-earth-oxide (REO) equivalent) for world producers

Country	Mine production (tons)			Reserves (tons)
	2017	2018	2019	
China	105 000 ¹	120 000 ¹	132 000 ¹	44 000 000
Brazil	1 700	1 000	1 000	22 000 000
Vietnam	200	400	900	22 000 000
Russia	2 600	2 600	2 700	12 000 000
India	1 800	1 800	3 000	6 900 000
Australia	19 000	21 000	21 000	3 300 000 ²
Greenland	-	-	-	1 500 000
United States	-	18 000	26 000	1 400 000
Tanzania	-	-	-	890 000
Canada	-	-	-	830 000
South Africa	-	-	-	790 000
Burma (Myanmar)	NA	19 000	22 000	NA [*]
Burundi	-	630	600	NA
Thailand	1 300	1 000	1 800	NA
Other countries	180 ³	60	-	310 000
World total	132 000	190 000	210 000	120 000 000

¹ Production quota; does not include undocumented production; ² For Australia, Joint Ore Reserves Committee-compliant reserves were 1.9 million tons; ³ Includes Malaysia; * Not available. Source: USGS (1996-2020).

and production costs, and a lax environmental regulatory framework (Zhou et al., 2016). These factors have allowed China to enjoy a monopolistic market, while countries like the US, which had to close mines such as Mountain Pass, began to import REEs to satisfy their demand (USGS, 1996-2020).

In 1999, China introduced an export quota on REEs “to control total production and illegal activities at the border of the country ...” and “...put specific restrictions on the structure of export quotas to support the development of the downstream sector” (Shen et al., 2020). These quotas reduced the

output of Chinese exports by nearly 60% compared to 2008 levels (Haque et al., 2014). Consequently, large price increases were common due to the mismatch between a growing demand and a declining supply. In 2014, China agreed to end those restrictions after multiple complaints from the World Trade Organization (WTO) and countries like USA, Japan, and the European Union.

After China started to impose quotas, licenses and taxes in 2010, citing as the main reasons the need to limit resources for domestic consumption and environmental concerns, the world reacted in different ways, including: increasing its stockpile; increasing exploration; developing new deposits; and increasing the efforts to reuse, recycle, and find new substitutes among the REEs.

Most of the world's REEs production comes primarily natural resources, although recycling as a source of raw materials is increasingly seen as a viable option. However, the recycling process is still in its initial stages and has to overcome several problems before being considered a realistic option, such as industrial scale recycling plants, and the small amount of these elements incorporated in the technological products which makes the recovery an expensive undertaking.

2.2. Wind power technologies

There are two ways to obtain energy from the wind, either by directly converting mechanical power or by transforming kinetic energy. The latter can be achieved through a wind turbine which converts wind energy into mechanical power, which can then be utilized for different purposes.

The wind turbines can be classified as either direct drive (no gear) or those who use gearbox electromagnets according to the drivetrain condition in a wind generator system (Figure 3) (Tong et al., 2010). In the first group the turbine blades are connected directly to the generator, which allows them to rotate at the same speed, but at low revolutions per minute (10-30 rpm) (Pavel et al., 2017). The electric energy is induced by a magnetic field which can be provided either by permanent magnet synchronous generators (PMSGs) or electromagnets which need excitation and consumes reactive power (Lacal-Arantequi, 2015). These types of turbines are popular among offshore windfarms because of their increased reliability and low maintenance costs (Habib and Wenzel, 2014).

Different metals can be employed to produce the permanent magnet. PMSG turbines with NdFeB (which stands for neodymium, iron, and boron) are the most common, however,

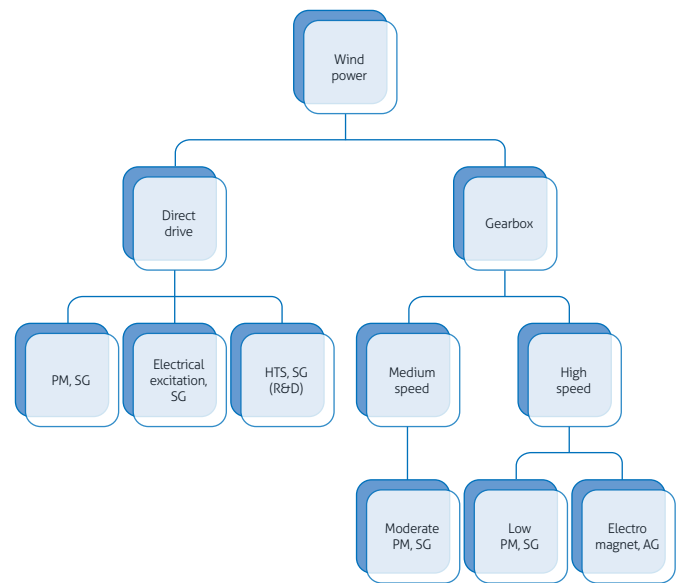


Figure 3. Wind power technologies

PM = permanent magnet, HTS = high-temperature super conductor, SG = synchronous generator, AG = asynchronous generator. Source: Taken from Manberger and Stenqvist (2018).

they contain low but vital amounts of praseodymium (Pr), dysprosium (Dy) and terbium (Tb), which some authors consider as critical minerals (Tokimatsu et al., 2018; Grandell et al., 2016; Brumme, 2011). The conventional electromagnets generators, which in 2015 made up to 77% of the global installed capacity, are produced using magnetic steel and copper windings (Pavel et al., 2017). These metals are not currently classified as critical minerals; however, these turbines are generally heavier and less efficient than turbines using permanent magnets (Manberger and Stenqvist, 2018). The latest generation among direct drive generators is the HTS (high-temperature superconductors), which allows for low weight turbines and do not require critical minerals except for yttrium. Nevertheless, they are currently in research stage (Manberger and Stenqvist, 2018).

Among the geared turbines, there are two groups: the mid-speed drive (≥ 80 rpm) and high-speed drive (≥ 900 rpm). Here, a gearbox allows for the generator to rotate faster than the blades to gain a higher power output (Pavel et al., 2017).

In the mid-speed geared turbines, the generator contains lower quantities of permanent magnets than the low speed configuration. In high-speed generators, a transmission system converts the low speed of the wind turbines into high speed in the generator (≥ 900 rpm). Currently, the onshore market is dominated by the traditional doubly-fed induction genera-

tor (DFIG), with capacities up to 6 MW, which is considered a high-speed technology (Pavel et al., 2017). Altogether, the geared drive system is heavier and requires more maintenance than the direct drive, which makes it less competitive for larger plants in offshore locations (Manberger and Stenqvist, 2018).

2.3. Mineral demand in a low carbon economy

There is a vast literature on the future availability of critical minerals such as the REEs in the deployment of RETs that would be required to meet certain climate mitigation targets. Thus, this section presents an overview of the major studies concerning renewable energy technologies.

Based on the future requirements for a low-carbon economy and energy technologies together with long-term socioeconomic scenarios, Koning et al. (2018) examine how the gradual introduction of climate policies by 2050 would prompt the onset of supply bottlenecks of a range of metals, including Fe, Al, Cu, Ni, Cr, In, Nd, Dy, Li, Zn, and Pb. Their results show that, compared with actual levels, the production of almost all metals analyzed would have to increase significantly to keep up with a low-carbon energy system transition. However, given their assumption that the supply of these metals used in other sectors of the society will increase gradually, the supply of metals for such a transition would not be a problem. Yet, the combination of special conditions, characteristics of the mining industry such as the lack of certainty on the return of investment, long lead times in expanding mining production, and social and environmental impacts that delay the expansion of mining capacity could create supply-demand imbalances. One aspect which is not considered in their paper is the importance of recycling and substitution in RETs.

Manberger and Stenqvist (2018) assess what makes a resource critical and how can it be mitigated, by analyzing different technological development trajectories affecting the demand for metals over time using technological substitutes and the role of recycling to meet supply needs. In their study, twelve metals were used, namely Co, Cu, Dy, Ga, In, Li, Nd, Ni, Pt, Se, Ag, and Te, which are critical for renewable energy production, storage or end-use technology up to 2060. They conclude that the growth rate of solar power, wind power, and electric motors is not likely to be constrained by the reserves of these metals, since they would continue growing to keep up demand. Therefore, given that metal use intensities have improved historically, and will continue to do so, the growth in mining intensity and cumulative demand will be much lower.

This would allow the recycling of metals to achieve a bigger share of the demand by 2060.

Tokimatsu et al. (2018) develop a bottom-up cost-minimizing model to calculate the aggregate metal requirements in energy technologies including hydrogen under several climate policy scenarios reflecting uncertainty in future metal intensities, recycling rate and the lifetime of energy technologies. Potentially “critical” metals were identified by comparing metal requirements to current production rates and resource estimates. Their model suggests that vanadium which is commonly used in nuclear, photovoltaic, carbon capture and storage, electric vehicles (plug-in hybrid) and fuel cell vehicles, is “critical” in all three energy policy scenarios, whereas selenium, indium, and tellurium are “critical” in photovoltaic systems, dysprosium in wind power, and nickel, platinum zirconium, yttrium, lithium, and lanthanum in fuel cell vehicles.

Deetman et al. (2018) take a broader approach in their research. They focus on developing climate policy scenarios for five metals like copper, tantalum, neodymium, cobalt, and lithium, used in three kind of applications: appliances, cars, and electricity technologies in 2050. The results show, unsurprisingly, that the demand for materials introduced by these products will increase significantly, regardless of anticipated climate policy ambitions. Similarly, the dominant factors for the demand are not climate policies but rather socioeconomic developments and technological change. Cars would be the major driver for the growth of metal demand, especially lithium and cobalt, which would be a consequence of the transformation of the traditional internal combustion engine car fleet into a hybrid/electric one.

Grandell et al. (2016) perform an analysis of the future availability of some critical minerals used in the clean energy technologies. These authors modeled the demand for 14 critical minerals (Ag, Nd, Pr, Dy, Tb, Yt, La, Ce, Eu, Co, Pt, Ru, In, Te) present in green energy technologies from 2010 up until 2050, including solar energy, wind energy, electric mobility, fuel cells, batteries, electrolysis and efficient lighting. The demand resulting from the expansion of the RET was compared against the known present state of global reserves and resources, and according to their results, the most serious problem could be the future availability of silver in the solar energy sector. Silver demand in 2050 will exceed known global resources by more than 300% and present reserves by almost 450%. Other possible material restriction might be given for indium, tellurium or ruthenium.

In a country-specific approach, Viebahn et al. (2015) assess whether the transformation of the German energy system by 2050, which will consist of a large deployment of renewable energy and GHGs emissions reduced between 80-90% matched against 1990 levels, would be affected by a lack of critical minerals. The main conclusion in their study shows that the deployment of most of the renewable energy would not be limited by the geological availability of minerals. However, possible criticality issues could arise for specific sub-technologies of wind power, photovoltaic, and battery storage. In the wind power technology, the main constraint is the development of technologies that involve the use of REEs. In the case of photovoltaic, the demand for selenium and indium in CIGS cells (Cu-In-Ga-diselenide) does not appear to be secured in the long term. Nonetheless, these restrictions could be overcome by establishing recycling systems.

Brumme's (2011) thesis reviews thoroughly the REEs used to produce wind turbines. She analyzed the REEs market and the requirements for the deployment of the wind power generation based on the projections of the International Energy Agency (IEA) Blue Map scenario for 2050. According to Brumme's results, the REE demand for wind turbines would rise between 66 to 500% -low and high scenarios, respectively- in 2050 compared to 2010 levels. Brumme ends by stating that the current level of supply is highly unlikely to be sufficient in the long run, and this could hamper a climate change mitigation measure, such as wind power generation.

3. COLOMBIAN ENERGY SECTOR

Thanks to its geographic location, historically the bulk of electricity generation has depended on hydropower. However, in recent decades there has been an increase in the production of electricity in thermal plants which could support the main system in cases of severe weather events, such as prolonged droughts. As a result, the production share of non-conventional renewable energy sources, (e.g. wind and solar power), has remained at negligible levels, far below other South American countries that have expanded renewable electricity generation, such as Chile and Brazil (Radomes and Arango, 2015).

The aim of this chapter is to provide an overview of the Colombian electric system, which will be covered in two parts. First, the generation system will be discussed and how it has changed over time, which will be followed by an overview of

the historical energy demand and its implication for future demand.

3.1. Electricity generation

Colombia is located in the north-western corner of South America, bordered by Brazil and Venezuela to the east, Ecuador and Peru to the south, by the Pacific Ocean to the west and the Atlantic Ocean to the north. The country has three mountain ranges which are sub-ranges of the Andes, and it has plenty of non-renewable resources like coal, nickel, and gold as well as abundant hydrologic resources represented in five great basins from the rivers: Magdalena, Cauca, Putumayo, Guaviare, and Amazon, among many others.

This plentiful of water resources are reflected in electricity generation mix. In 2017, total installed capacity was 17.3 GW, of which hydropower made up for 64.5%, while the thermal power (which includes gas turbines, oil and coal plants) accounted for 30.4%, small hydropower plants 5% and finally, wind power with 0.1%.

Historically, hydropower has been the traditional source of energy production, but since the early 1990s the thermal production has been increasing its share of electricity generation. Microclimatic phenomena such as "El Niño-Southern Oscillation" had severely affected the output of large hydro plants because of prolonged droughts (especially severe was the 1992 drought, see Figure 4). To overcome this vulnerability the government started to approach other sources of electricity as well as to give incentives to the private industry for the investment in thermal plants that could back up the system once climatic phenomena would affect hydropower production (Arango and Larsen, 2010).

The CO₂ emissions to the atmosphere in the energy production sector in Colombia have been relatively low due mainly to its hydropower dominance. However, given the increasing uncertainty of the effects of climate change on hydrologic resources and the increasing reluctance of communities to the installation of new hydroelectric projects given their environmental impact, the share of the thermal energy production will likely continue to grow and so will the share of CO₂ emissions into the atmosphere.

Regarding the non-conventional renewable energy production like wind and solar photovoltaic, in Colombia there is only one wind power plant with an installed capacity of 19.5 MW which accounts for the 0.11% of the 17.3 GW of the total capacity. Nevertheless, the potential for the installation of

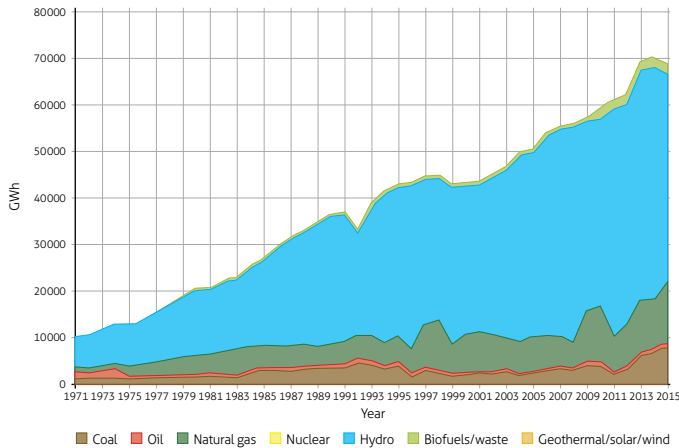


Figure 4. Colombian generation electricity power from 1971 to 2015
Source: Churio-Silvera et al. (2018).

new renewable energy capacity is good; the northern part of the country has been classified as having class 7 winds (over 10 m/s) and a total wind power potential of 25 GW, which is more than enough to meet the entire country demand (Gómez and Ribo, 2018). The solar photovoltaic installed capacity in 2010 was around 9 MW. However, by being located near the Equator, Colombia receives constant solar radiation (average 4.5 KWh/m²/day), which gives it relevant potential for this kind of energy source (Gómez and Ribo, 2018).

In October 2019, the Colombian government held the first of several renewable energy contract auctions, paving the way for the “Energy Transition” (Ministerio de Energía de Colombia, 2020). This plan aims to increase installed capacity from 50 MW to over 2500 MW in wind and solar energy with 14 projects (9 of them wind in La Guajira, and 5 solar in the departments of Cesar, Cordoba, Valle del Cauca and Tolima), which would represent 12% of the total energy mix by 2022.

3.2. Energy Demand

Colombia is the fourth largest economy in Latin America and the Caribbean, behind Brazil, Mexico, and Argentina. Since the early 1990s its gross domestic product (GDP) has been increasing considerably and consequently the energy requirements to sustain this growth. The energy demand during the period between 1990 and 2013 has nearly doubled, increasing from 28.85 to 55.73 TWh per year (Edsand, 2017). The most used energy sources are diesel and gasoline, both associated with the transportation sector, followed by natural gas used mainly in the industry sector. The housing sector uses most of the electricity generated, meanwhile the tertiary and industrial sectors use almost the same amount of electricity (Nieves et al., 2019).

According to the Mining and Energy Planning Unit of Colombia (UPME) in 2030, the demand for energy will increase to 105 000 GWh (UPME, 2016). However, Nieves et al. (2019) foresee that in 2030 the demand for electricity will fluctuate between 74 000 and 125 000 GWh; whereas in 2050, the electric energy demand could reach up to a maximum of 383 000 GWh.

4. METHOD AND DATA

This chapter’s aim is to outline the method employed to obtain the results as well as to discuss the data sources, which will be applied to estimate the derived demand of REEs embedded in RETs in Colombia during the period 2020-2050 (Figure 5).

The first part will briefly explain what scenario analysis is and the parameters used in this type of analysis. Next, it discusses the research of Calderón et al. (2016) and van der Zwaan et al. (2016). In their research they propose a pathway for the deployment of RETs through scenario analysis, the result of which –in this specific case, electricity capacity additions

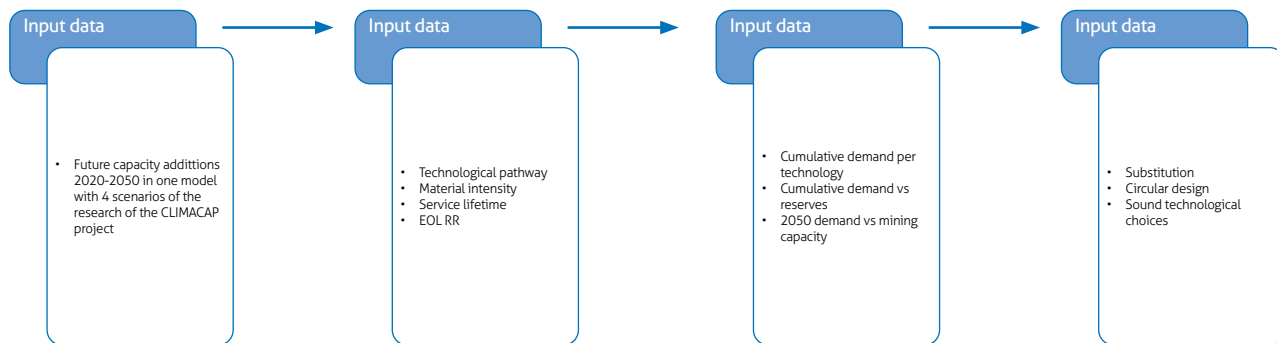


Figure 5. Diagram explaining the method used in this study

(GW) by type of energy source during the 2015-2050 period—will serve as the main input for the development of this study. Finally, it will establish the metal intensity of use of the REE incorporated in RETs, also taking into account possible future material improvements of these technologies. The cumulative demand is then calculated by multiplying the additional capacity (in GW) with the intensity of use of the REE embedded in the wind energy technologies.

4.1. Scenario Analysis

Scenario analysis is a method developed to explore future alternatives; it is an important tool for dealing with the complexity and uncertainty of the future. As Martinot et al. (2007) state:

They could be seen as ‘if... then’ queries: if policies accelerate the growth of renewables, what is the difference between situations with and without policies? If CO₂ emissions should be stabilized, what combinations of renewables and other technologies will achieve stabilization?

They can assist policy makers in decision-making strategies when it comes to long-term planning and are used especially in highly complex climate policy issues. However, emphasis should be given to the notion that scenarios are not predictions, but rather imaginative explanations of how possible futures might unfold (Kishita et al., 2017), and they do so by establishing a given set of assumptions and constraints.

There are three major categories of considerations when building a scenario analysis (TCFD, 2017). These will affect how the scenarios might unfold:

- » Parameters used: Discount rate, GDP and other macroeconomic and demographic variables.
- » Assumptions made: Assumptions related to policy changes, technology development/deployment, energy mix, price of key commodities or inputs, and timing of potential impacts, among others.
- » Analytical choices: choice of scenarios, time horizons, supporting data and models.

4.2. Colombian scenario description

This study is based on the outcomes of several previous studies (e.g. Calderón et al., 2016; van der Zwaan et al., 2016). which were designed to explore the implications of alternative CO₂

emission scenarios for Colombia and Latin America’s economy and energy system Their research was done under the CLIMACAP-LAMP project, -which stands for Integrated Climate Modelling and Capacity Building in Latin America- and assess the implementation of carbon taxes and abatement targets in reducing the emission of greenhouse gases (GHG) in key countries of the region (Science for Global Insight, 2015).

In this project, Colombia is assessed as a separate country rather than part of an aggregate region, such as Latin America. This allows to evaluate the implications of climate policy scenarios specifically, and thus the outcomes of their investigation form the basis of this study.

Four models were used to build the scenarios: two partial equilibrium models – The Global Change Assessment Model (GCAM), and the TIMES Integrated Assessment Model of the Energy Research Center of the Netherlands (TIAM-ECN)- and two Computable General Equilibrium models (CGE) – the Phoenix Model and Modelo de Equilibrio General para Colombia (MEG4C) (Calderón et al., 2016).

Of these four, this study uses the results of the TIAM-ECN model, which is a model for assessing long term energy systems and climate policy analysis (Table 4). It is based on energy cost minimization with a foresight until 2100 (Kober et al., 2014). The development of the global energy economy over time is simulated from the resource extraction to the final energy use. This model allows to establish future energy supply pathways including the set of possible fossil, nuclear and renewable energy technologies in Colombia (Calderón et al., 2016).

Once the model is established, the next step is the choice of the suitable scenarios. Calderón et al. (2016) chose four scenarios to assess how CO₂ emissions would deviate from baseline levels through the implementation of carbon taxes and abatement targets over the period 2020-2050 (Table 5).

By comparing different climate-policy scenarios with a business as usual scenario, the policy-makers are able to assess how the variables analyzed - in this case, CO₂ emissions - may deviate from the baseline level in the period of time established (Calderón et al., 2016). Specifically, the different pathways of how the energy mix will develop once adopted different climate mitigation policies is of particular importance for the outcome of this study.

The results obtained in their study were subsequently downloaded from the CLIMACAP website (International Institute for Applied Systems Analysis (IIASA) 2015), then filtered by country, model, scenarios; lastly, the capacity (in GW)

Table 4. Main features of and structural characteristics of the TIAM model

Model/Feature	TIAM-ECN
Economic coverage	Partial equilibrium
Calibrated years	2005, 2010
Endogenous variables	Energy supply, trade, emissions, prices (marginal costs)
Exogenous variables	End-use-demand (population, GDP), technology parameters, (investment costs, etc.)
Emission data sources	EDGAR, IEA
Population data sources	UN
GDP data sources	WB
Energy data sources	IEA
Covered sectors	Energy, Land use
Region	Global, Argentina, Brazil, Chile, Colombia, Mexico, Venezuela.
Covered gases	CO ₂ , CH ₄ , N ₂ O

EDGAR Emission Database for Global Atmospheric Research; IEA International Energy Agency; UN United Nations; WB World Bank; PV Photovoltaic; CSP Concentrated Solar Power. Source: Modified from Calderón et al. (2016) and van der Zwaan et al. (2016).

Table 5. Baseline and climate-policy scenarios explanation

Scenario	Scenario description
Core baseline	Business-as-usual scenario including climate and energy policies enacted prior to 2010.
High CO ₂ price	A carbon tax of 50 \$/tCO ₂ e is levied in 2020 growing each year at 4% to reach 165 \$/tCO ₂ e* in 2050.
50% abatement (GHG)	Greenhouse emissions, excluding Land Use Change CO ₂ , are reduced by 12.5% from 2010 levels by 2020, linearly increasing to 50% of 2010 levels by 2050.
50% abatement (FF&I)	Fossil fuels and industrial CO ₂ emissions are reduced by 12.5% from 2010 levels by 2050, linearly increasing to 50% of 2010 levels by 2050.

*US dollars/ton of CO₂ emitted. Source: Calderón et al. (2016).

variable was selected as the main input for the purposes of this study. The 2010-2050 period of their study is also in accordance with the scope of this study.

Figure 6 shows what will be the installed capacity by type of energy source for the different scenarios in Colombia for

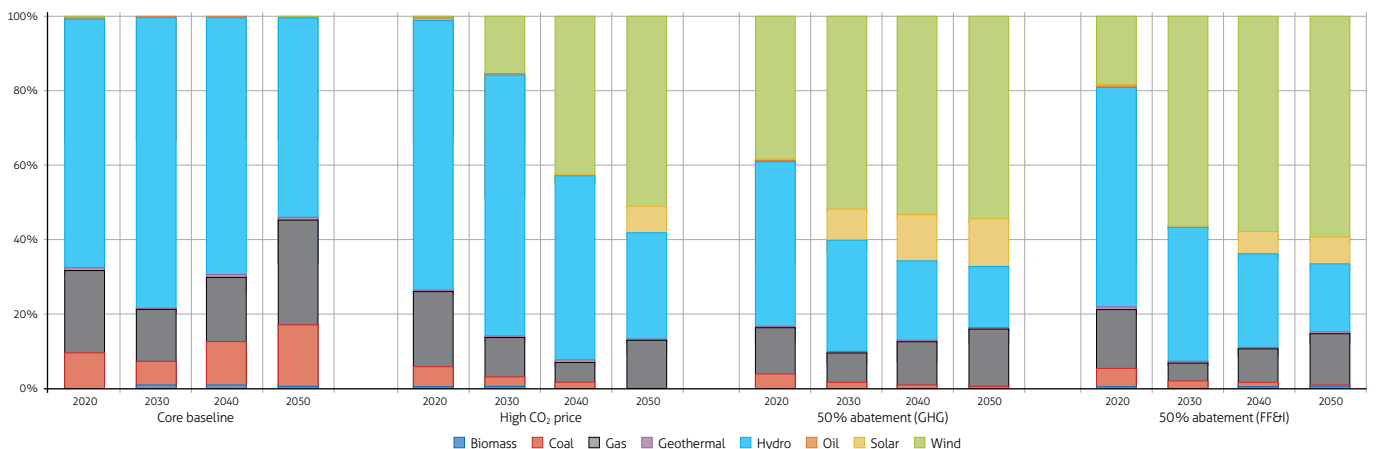


Figure 6. Development of electricity capacity from 2020 to 2050 in four climate policy scenarios, according to the outcomes of CLIMACAP project research (International Institute for Applied Systems Analysis (IIASA), 2015).

the 2020-2050 time interval according to the results of the CLIMACAP project. In the core baseline scenario, wind and solar energy capacity does not show a significant increase in the total capacity. Therefore, in this scenario, Colombia will continue to rely mainly on hydropower and fossil fuel-based technologies for electricity generation; whereas, in the most ambitious scenarios (50% abatement GHG and FF&I and the High CO₂ price), the renewable energy penetration rate could reach up to 60% of the total energy mix in 2050. In all of these scenarios, the wind power is the dominant renewable energy source.

4.3. Global metal intensities of use and market shares of the wind energy technologies

Once established the input data, the next step is to assign the metal intensity of use of the REEs embedded in the wind energy technologies. This will be based on the current published literature, taking into account possible future technical improvements, as well as recycling rates.

Regarding recycling, table 6 displays current and future recycling rates of selected REEs used in this study according to literature. Presently, recycling of rare earth elements is nearly absent, but will steadily increase mainly by concerns about future scarcity and rising prices of metals (Grandell et al., 2016).

Table 7 summarizes the metal intensity of use (IU) of the REEs present on the wind technologies used in this study, as well as a future projection of this parameter for the years 2025 and 2050. For this study, the average lifetime of the wind technologies is set to 25 years.

In addition, there are other factors when considering future deployment of the wind technology which are related to how the different sub-technologies will evolve over time. Table 8 shows the forecast of how wind energy will be shared between onshore and offshore technologies on a global basis/scale (DNV GL, 2017). Table 9 shows the market share evolution of the different subtypes of wind turbines from 2020 to 2050 for both onshore and offshore locations. The latter values were taken from the study of Viebahn et al. (2015), since there are no studies for Colombia regarding that matter.

Table 6. Current and future end of life recycling rates (EOL RR) for selected REEs

	Nd	Dy
Current EOL RR	<1%	<1%
2050 EOL RR	45%	45%

Future values were taken from Grandell et al. (2016) and Viebahn et al. (2015).

Table 7. Current and future metal intensities of use of wind technologies according to different authors

Sub-type	Element	This study*	2025**	2050**
Direct Drive (DD-PM)	Dysprosium	18	11.7	11.7
	Neodymium	199	162.5	130
Middle speed (MS)	Dysprosium	3.7	2.9	2.9
	Neodymium	49.6	40	32
High speed (HS)	Dysprosium	1.8	1.4	1.4
	Neodymium	24.8	20	16

All values are in t/GW; * Average values from Tokimatsu et al. (2018), Manberger and Stenqvist (2018), van Gosen et al. (2014), Viebahn et al. (2015), Habib and Wenzel, (2014), and Brumme (2011); ** Forecast of future IU according to Viebahn et al. (2015).

Table 8. Projection of the world share of wind energy according to its location

Location	2020	2030	2040	2050
Onshore	78.6%	66.7%	68.2%	76.9%
Offshore	21.4%	33.3%	31.8%	23.1%

Source: DNV GL (2017).

Table 9. Distribution of the wind energy according to type of location and windmill technology

Location	subtype	2020	2030	2040	2050
Onshore	AG [‡]	10.0%	6.6%	2.7%	1.5%
	SG [‡]	30.0%	15.6%	8.3%	3.8%
	HS	50.0%	51.1%	43.3%	42.2%
	MS	0.0%	4.7%	4.6%	12.5%
	DD-PM	10.0%	22.0%	41.1%	40.0%
Offshore	AG [‡]	61.0%	31.5%	11.5%	2.0%
	SG [‡]	0.0%	0.0%	0.0%	0.0%
	HS	0.7%	0.5%	0.3%	0.0%
	MS	38.3%	49.5%	59.2%	60.0%
	DD-PM	0.0%	18.5%	29.0%	38.0%

* These types of wind turbines do not use REEs. Modified from Viebahn et al. (2015).

5. DERIVED METAL DEMAND AND MATERIAL AVAILABILITY

This chapter aims to assess the demand for metals in a quantitative manner. The first step to calculate the metal requirement in the specified period is to divide the ten-year capacity additions into specific renewable energy technologies, as described in the previous chapter, by sub-type, location and market share. Then, for each scenario, the added capacity of a certain type of technology (e.g. DD-PM onshore wind turbines) is multiplied by its specific metal consumption in a given period.

Finally, the cumulated demand for the different elements is considered in relation not only to their current annual global extraction rate but also to estimates of world reserves. The reserves are defined by the (USGS, 1996-2020) as “that part of reserve base which could be economically extracted or produced at the time of the determination”, thus allowing to make a fair comparison with the amount of metals that can be mined at current market prices. Reserves are a dynamic measure, they can change due to alterations such as political and social factors, change in demand and price, as well as technological development (Davidsson and Höök, 2017).

5.1. Cumulative demand for REEs in the wind energy technologies

Figure 7 shows the cumulated demand for neodymium and dysprosium in the deployment of onshore wind technology in Colombia for the 2020-2050 period. The 50% abatement GHG scenario is the highest regarding REE demand, with a cumulated total demand of 6,150 tons of Nd and 498 tons of Dy. It is closely followed by the 50% FF&I scenario with 5,581 tons and 456 tons for Nd and Dy, respectively. This indicates that to halve emissions by 2050, the energy system will depend heavily on renewable energy technologies for electricity generation, and consequently, this will increase the amount of metals needed for such deployment.

In contrast, in the business-as-usual scenario (core baseline) the amount of metal needed is almost negligible because, as explained above, the energy mix in this scenario will rely mostly of hydropower, gas and coal for electricity generation. Interestingly, in the High CO₂ price scenario, which is a scenario where a growing tax on CO₂ emissions is levied, only moderate values of Nd and Dy 2050 demand are shown, with 2,135 tons and 181 tons respectively.

In offshore wind technology deployment, trends are similar but with lower general metal requirements (Figure 8). In

the 50% abatement GHG scenario, cumulated metal demand for Nd and Dy in 2050 is 2,609 tons and 192 tons, respectively, followed closely by the 50% abatement FF&I scenario with 2,403 tons and 177 tons of Nd and Dy.

The cumulated demand for Nd and Dy in the business-as-usual scenario is, as in the case of the onshore technology, negligible, with Nd and Dy values of metal demand in 2050 of just 1.33 tons and 0.10 tons, respectively.

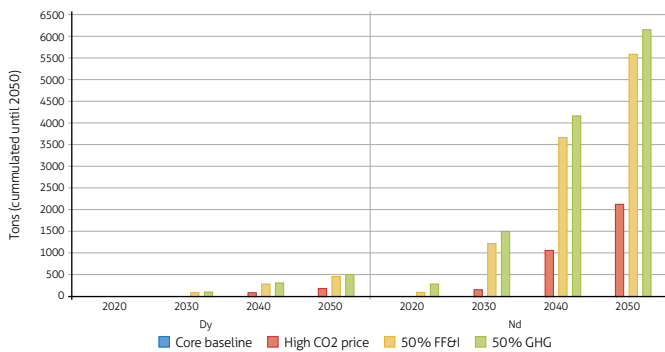


Figure 7. Cumulative metal demand for Nd and Dy in the onshore wind power in Colombia during the 2020-2050 period

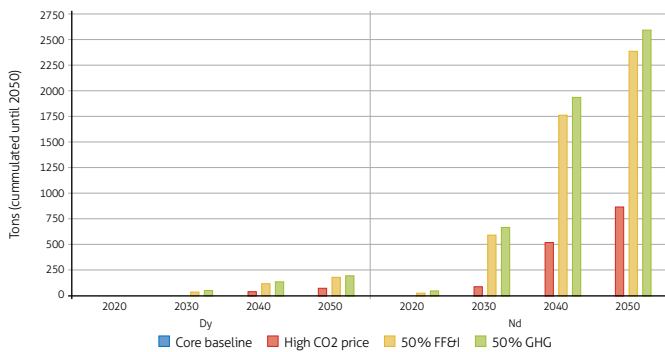


Figure 8. Cumulative metal demand for Nd and Dy in the offshore wind power in Colombia during the 2020-2050 period

5.2. Cumulative demand from a resource perspective

In this section the material requirement of REEs is compared to their annual global extraction rate as well as to the global reserves (Table 10). The comparison with the former provides insight as to what percentage of the current production would have to be employed to meet future rare earth demand from the wind industries. In contrast, the reserves will allow to establish comparison points with the geological availability of metals by considering current market prices.

Table 10. Production rates and reserves (in metric tons of rare-earth oxide (REO) equivalent content) for selected REEs

Element	Production rates (2016) in tons	Reserves (2016) in tons
Dy	1600 ¹	480 000 ²
Nd	7000 ²	800 000 ²

1) Grandell et al. (2016); 2) Arrobas et al. (2017).

Figure 9 shows the results of the estimated annual mineral demand in the year 2050 in relation with the actual annual production rates for the selected REEs analyzed. Nd and Dy embedded in wind technologies are the elements with the highest values in both of the abatement scenarios with ratios varying between 15% for Dy and 37% for Nd. Although in the High CO₂ price the percentage of Dy and Nd drops to 8% and 20% respectively. In the business-as-usual scenario the values are insignificant.

Figure 10 displays the ratio between cumulated metal demand for Nd and Dy and current reserves for those metals. Dysprosium shows values around 0.14% for both 50% abatement scenarios, whereas for the High CO₂ price is 0.05%. The values for the business-as-usual scenario are negligible. For neodymium the highest values are around 0.11% for both the 50% abatement scenarios, 0.04% for the High CO₂ price and 0% for the business-as-usual.

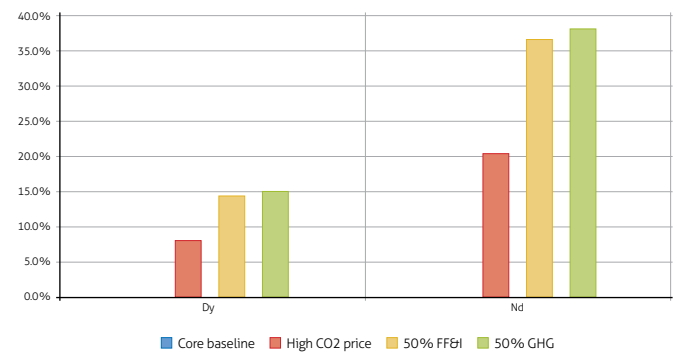


Figure 9. Ratio of the 2050 metal demand and 2016 production levels for selected REEs embedded in renewable energy technologies

6. DISCUSSION

This chapter discusses the main findings of the previous chapter, the assumptions made, the scope and limitations, concluding with some recommendations regarding the future availability of critical minerals for the deployment of RETs, not only in Colombia, but also taking into consideration a global perspective.

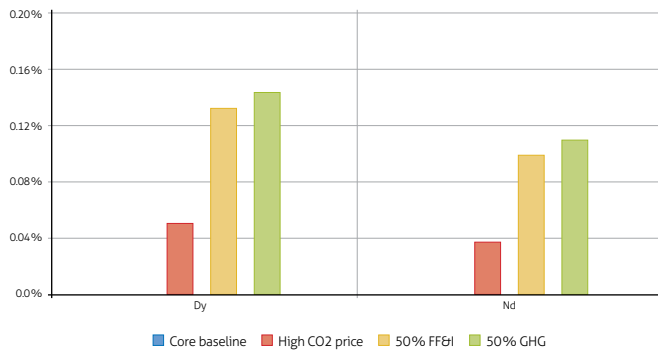


Figure 10. Ratio of cumulated metal demand and 2016 reserves for Dy and Nd embedded in renewable energy technologies

6.1. Future REEs availability

The future availability of critical metals, such as the REEs, can be estimated by combining the technology and resource development over long-term scenarios. This allows to assess the energy system transformation of a country, a region or even the whole world.

Assessments, such as the one presented, are only possible when certain assumptions are made. Assumptions like the technological pathway for the next 30 years or so in Colombia, including the market share of the sub-technologies (e.g. onshore vs. offshore), future improvements in the material intensity of use and end-of-life (EOL) recycling rates, can greatly affect the outcome of the cumulative demand of the selected REEs. Nonetheless, it is starting point for the development of more detailed methodological frameworks dealing with criticality assessments in developing countries such as Colombia.

Future assessments of the Colombian energy transformation could include a broader range of critical minerals, other than the REEs, such as copper, indium, tellurium, and could also take into consideration the deployment of other clean technologies (e.g. solar technologies, battery storage, and electric mobility, among others).

According to the results of this study, Dy and Nd are considered here as “critical” elements for the deployment of the renewable energy technologies in Colombia during the 2020-2050 period, with a total cumulated demand of 690 t and 8,758 t respectively, included in the wind energy technologies.

When the cumulated demand in Colombia for both wind energy technologies, in 2050, for Nd (8759 t) and Dy (648t) is compared to the global reserves (800 000 t and 480 000 t, respectively; see Table 10), it can be seen that the cumulated demand for Nd and Dy constitutes less than about 1.1% and

0.15% of the global reserve values. Therefore, from a reserve point of view, the geological availability of the REEs will not constrain growth rates and total penetration levels of wind power deployment in Colombia during the 2020-2050 period. Furthermore, given the fact that reserves include economic, social, environmental, and geological variables that can change over time, these will likely increase in the future through the discovery and commissioning of mines as demand rises.

Now, when it comes to current production rates, things are somehow different. The estimated Colombian annual mineral demand for Dy and Nd in the year 2050 would constitute 13% and 37% of the world’s current annual production rate, respectively. This will become an issue that needs careful consideration given the fact that by 2050 a massive deployment of the wind power for the global electricity generation is expected. Possible bottlenecks might arise and could influence the technology mix and maximum growth rates of some sub-technologies, such as the permanent magnet direct drive (PMDD).

Further sources of concern regarding mining production rates are competing demand from other technologies and recycling limitations. For the former, the increasing consumption of permanent magnets which utilizes Nd-Dy in other applications such as electric mobility will put more stress on the already strained production rates.

The supply of REEs come from two sources: either primary production, i.e. mining, or from secondary sources such as recycling. However, the secondary resources obtained through recycling are limited by several factors. Firstly, the limited EOL recycling rates – current levels are usually < 1% but will growth steadily to almost 45% by the end of the study period -; and secondly, the expected service life of RETs, which is 25 years, implies that only a small amount of the materials used in the period of the study will be available for recycling. In addition, even when EOL recycling rates improve, the recovery of the materials is not guaranteed, since many turbines that have reached the EOL have not been properly dismantled and recycled (Davidsson and Höök, 2017).

Furthermore, expanding mining capacity is not an easy task either. There are certain aspects of the REEs mining that makes it a complicated enterprise to achieve, including: 1) long lead times that take for a mineral deposit to become a producing mine, which oscillate between 10-20 years; 2) uncertainty of the return on investment caused by inherent mining factors; 3) environmental and social impacts that could delay the expansion of mines; and 4) the fact that these minerals are produced

as by-products, which means that as even their prices increase, the production does not necessarily increase immediately, since this normally implies a larger output of the material which is primarily mined (Davidsson and Höök, 2017).

All of these issues may cause supply-demand imbalances and consequently, price hikes could occur, especially if governments were to implement climate policy scenarios such as the 50% abatement GHG, where the renewable energy technologies play an important role in electricity generation.

6.2. Worldwide perspective

To put these results into perspective, they will be compared against the outcomes of other national and global studies. Viebahn et al. (2015) and Brumme (2011) performed assessments of the mineral demand for RETs in Germany during the 2010-2050 period and found that the supply of Dy and Nd (among other critical minerals) will be a source of concern, inasmuch as present levels of REEs supply will presumably not be able to satisfy a rising demand in the future.

The same trend is also observed on a global scale. Figure 11 shows the cumulative demand of several elements used in different clean energy applications. Here, Dy and Nd demand shows significant increments for each decade to keep up the

pace of the world deployment of renewable energy technologies, well above current mining production levels.

As it can be seen, the world could face potential shortages of metals such as Dy and Nd, and that could in turn, hinder the deployment of RETs and consequently, the fight against climate change.

6.3. Policy implications

Supply and demand policies can be used to mitigate the issues that the world could face related to the massive deployment of the renewable energy technologies and the mineral demand that a low-carbon economy could create. In this section, three policy options related with the mitigation of criticality issues are discussed.

6.3.1. Substitution

Material substitution is a way to decrease the amount of minerals utilized in RETs. It is an efficient measure to deal with criticality issues as long as the replacement is a more abundant material. However, this method has also certain drawbacks, such as the drop in performance of the technology when suboptimal materials are used. Moreover, it could also shift the criticality burden from one mineral to another, which could

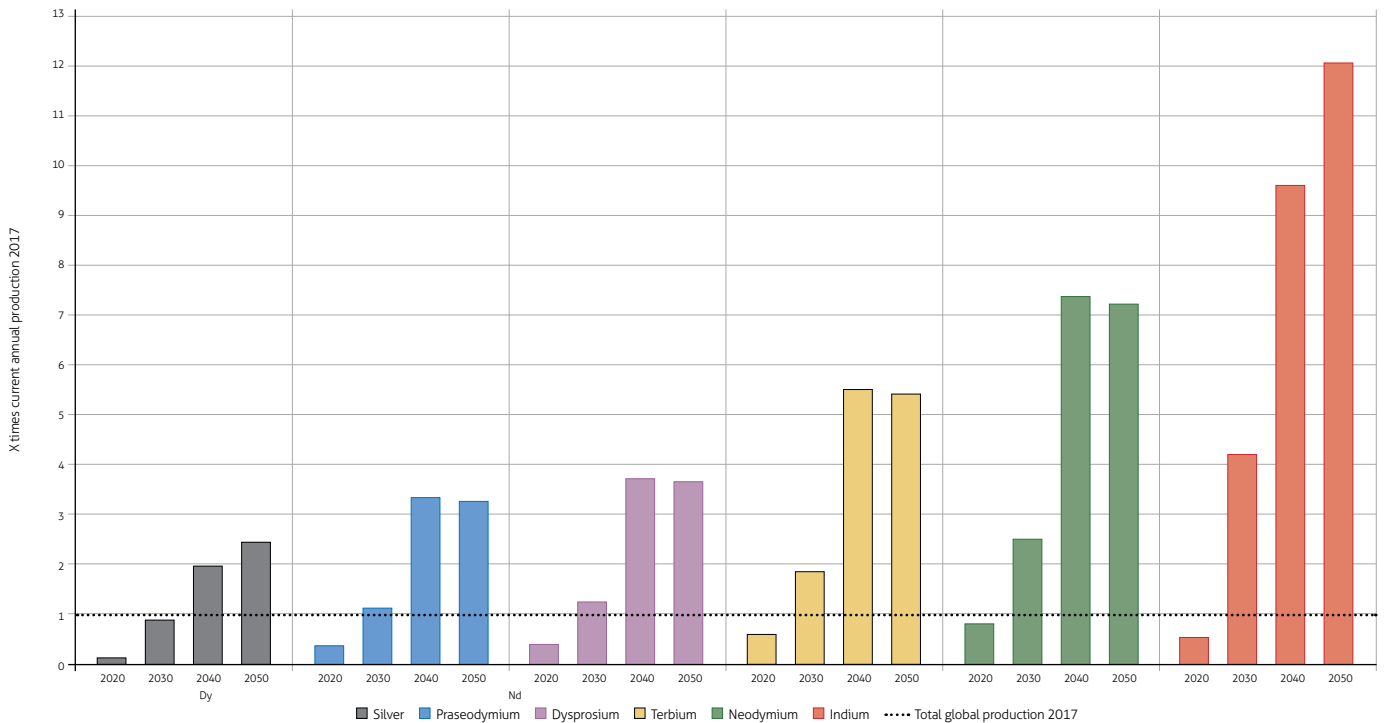


Figure 11. Metal demand for wind and photovoltaic power generation between the 2020-2050 period, compared against metal production (2017 = 1)
Source: Taken from van Exter et al. (2018).

worsen the issue. Many materials could become scarce at the same time if the global demand is high; this is likewise expected in the transition to a low carbon economy (van Exter et al., 2018).

6.3.2. *Improve circular design and recycling efforts*

In this group of policies there are two main considerations that could help reach a sustainable future in the renewable energy technologies:

1. Design products with longer lifespans
2. Improved modular design which facilitates the separation of components

For wind power, increasing the lifespan of turbines seems more relevant, given the fact that minimal material additions would be needed for producing electricity. For photovoltaic power, however, improvements in modular design seems more relevant. In addition, current recycling allows for most of the materials to be barely recycled. Therefore, areas for improving include the energy consumption associated with the recovery and increasing the purity of recovered materials (van Exter et al., 2018).

6.3.3. *Sound technological choices*

Policy-makers can influence the choice of technology a country or region could adopt when bottlenecks such as the mining capacity of critical elements are expected. The level of awareness among policy-makers has heightened, given that the increased use for critical materials such as Nd-Dy embedded in the renewable energy technologies may bring important issues for the development of a low carbon global economy.

6.3.4 *World's dependency on China*

The dependency on China's exports of REEs is being tackled on different fronts. In the United States, President Trump's Executive Order 13953, which addresses "the threat to the domestic supply chain from reliance on critical minerals from foreign adversaries and supporting the domestic mining and processing industries", was signed on 09/30/2020 and published on 10/05/2020 (see: Federal Register, Vol. 85, No. 193, Monday, October 5, 2020).

The decision of the Australian Government to strengthen its position in the world market of critical minerals, particularly REEs, with several projects currently at the feasibility stage that

include Nd and Pr (see: https://austrade.gov.au/ArticleDocuments/5572/Australian_Critical_Minerals_Prospectus.pdf. And also: <https://www.industry.gov.au/sites/default/files/2019-10/outlook-for-select-critical-minerals-in-australia-2019-report.pdf>).

Finally, the European Commission created ERECON (European Rare Earths Competency Network) as an initiative to strengthen the European Rare Earths supply chain. This network focuses on opportunities and road-blocks for primary supply of rare earths in Europe, European rare earths resource efficiency and recycling, and European end-user industries and rare earths supply trends and challenges. As stated by ERECON "rather than focusing on admonishing China over its REE policy, European industry and policy-makers must consider what they are prepared to do to support the development of a more diversified and sustainable supply chain" (European Commission, 2015; see also ERECON, 2015).

7. CONCLUSIONS

Overall, from a reserve perspective, the deployment of renewable energy technologies in Colombia during the 2020-2050 period and the associated mineral demand will not be affected by the worldwide geological availability of rare earth elements such as dysprosium and neodymium. Instead, certain sub-technologies, such as the permanent magnet direct drive in the wind power generation, could experience some future supply availability problems related to deficient mining capacity.

Demand from other industries such as electric mobility will also increase, and thus already troubled mining production rates will experience even more pressure. Consequently, the energy transition to a low-carbon economy and the fight against climate change could become a vulnerable process.

The supply of these minerals will come mainly from primary resources, as the supply from secondary sources will not be available in large quantities within the time frame of this analysis. In the extraction and refining processes, REEs only occur as byproducts, which means that these minerals are subject to supply restrictions related to the primary mineral with which they are associated. Therefore, even when prices increase, supply will not immediately increase, making it difficult to predict future availability. Recycling could become a significant mitigation measure, but only after 2050.

Policies that promote improved circular design, recycling, substitution, and sound technological choices are vital measures for achieving a more sustainable and resource-efficient fu-

ture. At the same time, these support strategies will help avoid potential shortcomings in the availability of critical minerals, such as the supply of rare earth elements, on a global scale.

Upcoming assessments of the Colombian energy system could use a broader range of critical minerals and include other clean energy technologies. There is also the need to improve the knowledge of the REEs in Colombia, which ensures the dissemination of accurate information to develop geological and mining projects, and consequently, help mitigate future supply constraints.

ACKNOWLEDGMENTS

This work is part of my master's thesis. Therefore, I would like to thank my advisor, Prof. Dr. Jan C. Bongaerts, of the T. U. Freiberg, who was always open to discussion and guidance at every stage of the process. The author thanks the anonymous reviewers for their valuable comments and suggestions, which helped to improve the original manuscript.

REFERENCES

- Alonso, E., Sherman, A., Wallington, T., Everson, M., Field, F., Roth, R., & Kirchain, R. (2012). Evaluating Rare Earth Element Availability: A Case with Revolutionary Demand from Clean Technologies. *Environmental Science & Technology*, 46(6), 3406-3414. <https://doi.org/10.1021/es203518d>
- Arango, S., & Larsen, E. (2010). The environmental paradox in generation: How South America is gradually becoming more dependent on thermal generation. *Renewable and Sustainable Energy Reviews*, 14(9), 2956-2965. <https://doi.org/10.1016/j.rser.2010.07.049>
- Arrobas, D. L. P., Hund, K. L., McCormick, M. S., Ningthoujam, J., & Drexhage, J. R. (2017). The Growing Role of Minerals and Metals for a Low Carbon Future. World Bank Group. <http://documents.worldbank.org/curated/en/207371500386458722/The-Growing-Role-of-Minerals-and-Metals-for-a-Low-Carbon-Future>
- Brumme, A. (2011). *Critical materials for wind power: The relevance of rare earth elements for wind turbines*. Chemnitz University of Technology [Master's Thesis]. Chemnitz University of Technology.
- Calderón, S., Álvarez, A., Loboguerrero, A., Arango, S., Calvin, K., Kober, T., Daenzer, K., & Fisher, K. (2016). Achieving CO₂ reductions in Colombia: Effects of carbon taxes and abatement targets. *Energy Economics*, 56, 575-586. <https://doi.org/10.1016/j.eneco.2015.05.010>
- Churio-Silvera, O., Vanegas, M., & Barros, P. (2018). Status of Non-Conventional Sources of Energy in Colombia: A Look at the Challenges and Opportunities of the Electric Sector. *Contemporary Engineering Sciences*, 11(44), 2163-2172. <https://doi.org/10.12988/ces.2018.85221>
- Davidsson, S., & Höök, M. (2017). Material requirements and availability for multi-terawatt deployment of Photovoltaics. *Energy Policy*, 108, 574-582. <https://doi.org/10.1016/j.enpol.2017.06.028>
- Deetman, S., Pauliuk, S., van Vuuren, D., van der Voet, E., & Tukker, A. (2018). Scenarios for Demand Growth of Metals in Electricity Generation Technologies, Cars, and Electronic Appliances. *Environmental Science & Technology*, 52(8), 4950-4959. <https://doi.org/10.1021/acs.est.7b05549>
- DNV GL. (2017). *Renewables, power and energy use forecast to 2050*. Energy Transition Outlook.
- Edsand, H.-E. (2017). Identifying barriers to wind energy diffusion in Colombia: A function analysis of the technological innovation system and the wider context. *Technology in Society*, 49, 1-15. <https://doi.org/10.1016/j.techsoc.2017.01.002>
- ERECON. (2015). *Strengthening the European rare earths supply chain: Challenges and policy options*. European Commission. <https://ec.europa.eu/DocsRoom/documents/10882/attachments/1/translations>
- European Commission. (2015). *European Rare Earths Competency Network (ERECON)*. https://ec.europa.eu/growth/sectors/raw-materials/specific-interest/erecon_en
- Gómez, T., & Ribo, D. (2018). Assessing the obstacles to the participation of renewable energy sources in the electricity market of Colombia. *Renewable and Sustainable Energy Reviews*, 90, 131-141. <https://doi.org/10.1016/j.rser.2018.03.015>
- Grandell, L., Lehtila, A., Kivinen, M., Koljonen, T., & Kihlman, S. (2016). Role of critical metals in the future markets of clean energy technologies. *Renewable Energy*, 95, 53-62. <https://doi.org/10.1016/j.renene.2016.03.102>
- Habib, K., & Wenzel, H. (2014). Exploring rare earths supply constraints for the emerging clean energy technologies and the role of recycling. *Journal of Cleaner Production*, 84, 348-359. <https://doi.org/10.1016/j.jclepro.2014.04.035>
- Haque, N., Hughes, A., Lim, S., & Vernon, C. (2014). Rare Earth Elements: Overview of Mining, Mineralogy, Uses, Sus-

- tainability and Environmental Impact. *Resources*, 3, 614-635. <https://doi.org/10.3390/resources3040614>
- Hayes, S., & McCullough, E. (2018). Critical minerals: A review of elemental trends in comprehensive criticality studies. *Resources Policy*, 59, 192-199. <https://doi.org/10.1016/j.resourpol.2018.06.015>
- International Institute for Applied Systems Analysis (IIASA). (2015). Integrated Climate Modelling and Capacity Building Project in Latin America (CLIMACAP). Retrieved (29/01/2019) from <https://tntcat.iiasa.ac.at/CLIMACAP-LAMPDB/dsd?Action=htmlpage&page=about>
- Kishita, Y., Nakatsuka, N., & Akamatsu, F. (2017). Scenario analysis for sustainable woody biomass energy businesses: The case study of a Japanese rural community. *Journal of Cleaner Production*, 142(4), 1471-1485. <https://doi.org/10.1016/j.jclepro.2016.11.161>
- Kober, T., van der Zwaan, B., & Rösler, H. (2014). Emission certificate trade and costs under regional burden-sharing regimes for a 2°C climate change control target. *Climate Change Economics*, 5(1), 1-32. <https://doi.org/10.1142/S2010007814400016>
- Koning, A., Kleijn, R., Huppel, G., Sprecher, B., Engelen, G., & Tukker, A. (2018). Metal supply constraints for a low-carbon economy? *Resources, Conservation & Recycling*, 129, 202-208. <https://doi.org/10.1016/j.resconrec.2017.10.040>
- Lacal-Arantequi, R. (2015). Materials use in electricity generators in wind turbines: state-of-the-art and future specifications. *Journal of Cleaner Production*, 87, 275-283. <https://doi.org/10.1016/j.jclepro.2014.09.047>
- Manberger, A., & Stenqvist, B. (2018). Global metal flows in the renewable energy transition: Exploring the effects of substitutes, technological mix and development. *Energy Policy*, 119, 226-241. <https://doi.org/10.1016/j.enpol.2018.04.056>
- Mancheri, N., Sprecher, B., Bailey, G., Ge, J., & Tukker, A. (2019). Effect of Chinese policies on rare earth supply chain resilience. *Resources, Conservation & Recycling*, 142, 101-112. <https://doi.org/10.1016/j.resconrec.2018.11.017>
- Martinot, E., Dienst, C., Weiland, L., & Qimin, C. (2007). Renewable Energy Futures: Targets, Scenarios, and Pathways. *Annual Review of Environment and Resources*, 32, 205-239. <https://doi.org/10.1146/annurev.energy.32.080106.133554>
- McCullough, E., & Nassar, N. (2017). Assessment of critical minerals: updated application of an early-warning screening methodology. *Mineral Economics*, 30(3), 257-272. <https://doi.org/10.1007/s13563-017-0119-6>
- Ministerio de Energía de Colombia. (2020, October 22). Histórico de Noticias - Ministerio de Energía. Retrieved from <https://www.minenergia.gov.co/historico-de-noticias?id-Noticia=24243663>
- Nieves, J., Aristizabal, A., Dyner, I., Báez, O., & Ospina, D. (2019). Energy demand and greenhouse gas emissions analysis in Colombia: A LEAP model application. *Energy*, 169, 380-397. <https://doi.org/10.1016/j.energy.2018.12.051>
- Pavel, C., Lacal-Arantequi, R., Marmier, A., Schüler, D., Tzimas, E., Buchert, M., Jenseit, W., & Blagoeva, D. (2017). Substitution strategies for reducing the use of rare earths in wind turbines. *Resources Policy*, 52, 349-357. <https://doi.org/10.1016/j.resourpol.2017.04.010>
- Radomes, A., & Arango, S. (2015). Renewable energy technology diffusion: an analysis of photovoltaic-system support schemes in Medellín, Colombia. *Journal of Cleaner Production*, 92, 152-161. <https://doi.org/10.1016/j.jclepro.2014.12.090>
- Science for Global Insight. (2015). CLIMACAP-LAMP Scenario database. Retrieved (25/11/2018) from <https://tntcat.iiasa.ac.at/CLIMACAP-LAMPDB/dsd?Action=htmlpage&page=about#intro>
- Shen, Y., Moomy, R., & Eggert, R. (2020). China's public policies toward rare earths, 1975-2018. *Mineral Economics*, 33, 127-151. <https://doi.org/10.1007/s13563-019-00214-2>
- Task Force on Climate Related Financial Disclosures (TCFD). (2017). *The Use of Scenario Analysis in Disclosure of Climate-Related Risks and Opportunities*. <https://www.tcfddhub.org/scenario-analysis/>
- Tokimatsu, K., Höök, M., McLellan, B., Wachtmeister, H., Murakami, S., Yasuoka, R., & Nishio, M. (2018). Energy modeling approach to the global energy-mineral nexus: Exploring metal requirements and the well-below 2 °C target with 100 percent renewable energy. *Applied Energy*, 225, 1158-1175. <https://doi.org/10.1016/j.apenergy.2018.05.047>
- Tong, W., Langreder, W., Schaffarczyk, A., Voutsinas, S., Cooper, P., & Lewis, C. (2010). *Wind Power Generation and Wind Turbine Design* (Wei Tong, ed.). WIT Press.
- Unidad de Planeación Minero Energética (UPME). (2016). *Proyección de la demanda de energía eléctrica y potencia máxima en Colombia*. http://www.siel.gov.co/siel/documentos/documentacion/Demanda/UPME_Proyeccion_Demanda_Energia_Electrica_Junio_2016.pdf

- USGS. (1996-2020). *Mineral Commodity Summaries*. Retrieved from <https://www.usgs.gov/centers/nmic/rare-earths-statistics-and-information>
- Van Gosen, B. S., Verplanck, P. L., Long, K. R., Gambogi, J., and Seal, R. R. (2014). *The Rare-Earth Elements— Vital to Modern Technologies and Lifestyles*. Fact Sheet 2014-3078. <https://doi.org/10.3133/fs20143078>
- Van der Zwaan, B., Kober, T., Calderón, S., Clarke, L., Daenzer, K., Kitous, A., Labriet, M., Lucena, A. F. P., Octaviano, C., & Sbroiavacca, N. (2016). Energy technology roll-out for climate change mitigation: A multi-model study for Latin America. *Energy Economics*, 56, 526-542. <https://doi.org/10.1016/j.eneco.2015.11.019>
- Van Exter, P., Bosch, S., Schipper, B., Sprecher, B., & Kleijin, R. (2018). *Metal demand for renewable electricity generation in The Netherlands*. Metabolic, Copper8 and Universiteit Leiden.
- Van Gosen, B., Verplank, P., Seal, R., Long, K., & Gambogi, J. (2017). Rare-Earth Elements. In K. Schulz, J. DeYoung, R. Seal, & B. Dwight (eds.), *Critical Mineral Resources of the United States—Economic and Environmental Geology and Prospects for Future Supply*. USGS. <https://doi.org/10.3133/pp1802>
- Viebahn, P., Soukup, O., Samadi, S., Teubler, J., Wiesen, K., & Rithhoff, M. (2015). Assessing the need for critical minerals to shift the German energy system towards a high proportion of renewables. *Renewable and Sustainable Energy Reviews*, 49, 655-671. <https://doi.org/10.1016/j.rser.2015.04.070>
- XM. (2017). Demanda de electricidad. Retrieved (27/02/2019) from <http://informesanuales.xm.com.co/2017/SitePages/operacion/4-1-Demanda-de-energia-nacional.aspx>
- Zhou, B., Li, Z., Zhao, Y., Zhang, C., & Wei, Y. (2016). Rare Earth Elements supply vs. clean energy technologies: new problems to be solve. *Mineral Resources Management*, 32(4), 29-44. <https://doi.org/10.1515/gospo-2016-0039>



Cordillera Occidental, sector de Jericó y río Cauca, Jericó, Antioquia, Colombia
Fotografía de Velásquez et al. (2021)



This work is distributed under
the Creative Commons Attribution 4.0 License.

Received: July 31, 2020

Revision received: July 2, 2021

Accepted: July 9, 2021

Published online: October 8, 2021

Geological modeling of a hydrocarbon reservoir in the northeastern Llanos Orientales basin of Colombia

Modelamiento geológico de un yacimiento de hidrocarburos ubicado al noreste de la cuenca de los Llanos Orientales de Colombia

Laura Juliana Rojas Cárdenas¹, Indira Molina¹

1. Universidad de los Andes, Bogotá, Colombia

Corresponding author: Laura Juliana Rojas, ljrojas@uniandes.edu.co

ABSTRACT

An hydrocarbon reservoir was characterized via a detailed geologic model, which allowed estimation of the original oil in place. The study characterizes a hydrocarbon reservoir of two fields of unit C7 of the Carbonera Formation within the Llanos Orientales basin of Colombia. This was done using well logs, the structural surface of the regional datum of the area, segments of the Yuca fault and a local fault of the reservoir, the permeability equation, and J functions of the reservoir provided by the operating company. With this information, a two-fault model and a grid with 3D cells was created. Each cell was assigned with a value of facies and petrophysical properties: porosity, permeability, and water saturation, to obtain a 3D model of facies and petrophysical properties. Subsequently, we used the constructed models and oil-water contacts to calculate the original oil in place for each field. Field 1 has a volume of six million barrels of oil and field 2 has 9 million barrels.

Keywords: geologic characterization, geologic modeling, well logs, original oil in place, petrophysics.

RESUMEN

El modelamiento geológico de un yacimiento de hidrocarburos permite la caracterización detallada y una estimación del aceite original en sitio acumulado en la trampa. Para este estudio, se realizó un modelamiento geológico de dos campos ubicados en la cuenca de los Llanos Orientales de Colombia, pertenecientes a un yacimiento de la unidad operacional M1 que hace parte de la unidad C7 de la Formación Carbonera, con el objetivo de realizar la caracterización geológica del yacimiento y obtener el volumen de aceite original en sitio. Asimismo, se emplearon registros eléctricos, la superficie estructural del *datum* regional del área de estudio, segmentos de la falla La Yuca, segmentos de la falla local del yacimiento, funciones J de Leverett, y la ecuación de permeabilidad del yacimiento, proporcionada por la empresa operadora. A partir de la información suministrada, se generó

un modelo con dos fallas y una cuadrícula con celdas en forma de prisma rectangular. Cada celda fue poblada con un valor de facies y propiedades petrofísicas: porosidad, permeabilidad, y modelo de saturación de agua por funciones J, para obtener así un modelo 3D de facies junto con las propiedades petrofísicas. Posteriormente, se emplearon los modelos generados y los contactos agua- petróleo, para calcular el volumen de aceite original en sitio de cada campo, dando un total de 6 millones de barriles para el Campo 1 y 9 millones para el Campo 2.

Palabras clave: caracterización geológica, registros de pozo, modelamiento geológico, aceite original en sitio, petrofísica.

1. INTRODUCTION

The Llanos Orientales is one of the most important oil basins in Colombia. The production of hydrocarbons and economic profitability of the development of fields in this basin have contributed to the country's energy supply. For this reason, it is essential for the oil industry to determine the volume of hydrocarbons in a reservoir. This is done through geologic modeling of the reservoir, with which geological and petrophysical aspects are determined and the volume of hydrocarbons in place is calculated.

During the drilling of a well, information is acquired to determine the geological and petrophysical properties of the subsoil by direct and indirect methods. Direct methods consist of core sampling and drill cuttings, corresponding to the extracted rock. These samples are studied to determine the lithology of the drilled formation and the cores are subjected to laboratory tests for direct measurement of the petrophysical properties of the formation, such as porosity and permeability.

Indirect methods consist of quantitative measurements of formation properties. These include electric well logs of gamma rays, density, and resistivity, using a sensor and receiver. These records provide indirect values of fluid saturation in the rock and serve as indicators of the lithology.

The main objective of the present work was to calculate the original oil in place (OOIP) from the geological modeling of a reservoir in two fields, with interest in unit C7 of the Carbonera Formation in the Llanos Orientales basin. The specific objectives were as follows: to conduct stratigraphic correlation of the major units of interest and a structural framework from the regional datum; to study the electric well logs for petrophysical evaluation; to analyze the results of that evaluation to characterize the operational units of the reservoir used in the modeling and perform the volumetric calculation of the OOIP in the area of interest.

To do the above, electric well logs and structural surfaces were used to generate a 3D model of the reservoir. This per-

mitted the calculation of the volume of hydrocarbons via the Petrel software. For the work, data from seven wells were used, which were provided by the operating company. Five wells correspond to Field 1 and two wells to Field 2.

2. GEOLOGICAL SETTING

The study area is in the northeastern Llanos Orientales basin of eastern Colombia, in the department of Arauca, near the municipality of Arauquita (Figure 1). Llanos Orientales is classified as an asymmetric foreland basin, defined as an elongated region formed between the orogenic belt of the Eastern Cordillera and the Guiana shield (Duarte et al., 2017).

The source rocks, deposited during the Cretaceous, are of marine origin and were buried during multiple orogeny events, which favored the formation of structural and stratigraphic traps (Campos and Mann, 2015). Source rocks of the Lower Cretaceous produced hydrocarbons over time, supporting substantial accumulations in Llanos Orientales basin (Mora, 2015).

The structural geology of the study fields corresponds to an anticline elongated in the northeast direction with closure in three directions, limited to the east by the La Yuca regional fault, which presents a strike-slip. The two fields of study are limited by a normal and local fault that is perpendicular to the main La Yuca fault.

Carbonera Formation. The Carbonera Formation dates from the Miocene at the top and early Eocene at the bottom. In the study area, at the northeast of the basin, this formation has an average thickness of 7053 feet, and is composed of sandstone and shale intercalations that permit division of the formation into eight units. Among these, the even numbers correspond to clay lithologies and the odd ones mainly to sands (Table 1). The formation was deposited in continental-type environments to the east and southeast of the Llanos Orientales basin, and in transitional environments to its west and northwest (Domínguez, 2014).



Figure 1. Location of study area
 a) Red polygon demarcates Llanos Orientales basin and green dot the location of the study area; b) Location of Llanos Orientales basin within Colombia.

Table 1. Study area column

Era	Period	Epoch	Formation		
Cenozoic	Neogene	Pliocene	Guayabo		
		Miocene		León	
		Paleogene	Oligocene	Upper Carbonera	C1
					C2
	C3				
	C4				
	C5				
	C6				
	Paleogene	Oligocene	Lower Carbonera	M1	
				Guafita	
M2					
M3					
Eocene		Mirador			
Paleocene		Los Cuervos			

Lower Carbonera. During the early Oligocene, regional sandstone deposition was caused by an increase in the supply of sediments, which facilitated the deposit of Unit C7 of the Carbonera Formation (De la Parra et al., 2015). This was integrated in only one unit called the lower Carbonera, composed of fine-grained facies, caused by a prograding wedge of braided fluvial deposits (Reyes-Harker et al., 2015) and facies of medium grain.

In the study area, the C7 unit has a thickness of 100–300 feet and the companies divide it into the operational units M1, M2 and M3, which consist of massive sandstone bodies separated by a regional shale called guafita, with intercalations of sandstones-siltstones. The sandstone deposits correspond to a fluvial-deltaic environment that accumulates hydrocarbons in the operational production unit M1.

The marker of the area of interest is the guafita shale, which corresponds to the maximum flooding surface that is homogeneously distributed in the northeastern basin. This marker was used as a regional datum because it was identified in all study wells.

3. METHOD

We used information from seven wells, five in Field 1 and two in Field 2, that have directional files, electric well logs of gamma ray (GR), resistivity (RT), and density (RHOB). Likewise, we took as reference the regional datum and its structural surface, the faults in the two fields of study, the permeability equation as a function of effective porosity found from data of tests on rock core plugs, and the J functions determined from reservoir capillary pressure curves. The cores were not available for facies analysis. In the following, we describe and explain the steps in the study.

3.1. Stratigraphic model

We conducted a stratigraphic correlation based on the regional datum of the study area. The datum was located at each well and the well tops of the operational units that belonged to the C7 unit of the Carbonera Formation were defined as: M1, M2_1, M2_2, and M3. These were identified based on the response of the GR log.

In the analysis of electrofacies, we identified the facies of the depositional environment of the studied intervals according to patterns of electric well logs established and accepted in the geological literature.

To determine the facies, we analyzed forms of the GR log, which indicated a relative variation of grain size related to the depositional environment. The large values of the log indicate the presence of clays and small values the presence of sands. The main forms of the log responses are divided into cylinder, funnel, and bell. Each form can be associated with more than one depositional environment.

3.2. Structural model

The structural surfaces of operational units M1, M2_1, M2_2, and M3, were generated from the structural surface to the top of the guafita regional datum and isopachous maps of each unit that were obtained from the correlation between wells. We created fitted surfaces to the well tops of the units by adding or subtracting the average thickness of each surface. This operation implies an addition of thicknesses if the unit is above the guafita surface, or a subtraction if it is below.

3.3. Fault model

We used fault segments supplied by the operator company as a result of seismic interpretation, which correspond to deep fault lines of the reservoir. By interpolating these segments, we obtained the plane of the fault in depth. The segments become fault pillars, a set of lines with upper, middle, and lower nodes that define the shape and location of the fault surfaces in the model.

3.4. Petrophysical model

The petrophysical properties used for modeling the reservoir were effective porosity, permeability, and water saturation. For the porosity model of units M1, M2_1, M2_2 and M3, we used effective porosity (ϕ_e) furnished by the operating company, which is calculated from the total porosity (ϕ_T) based on the density log and corrected by the clay volume (V_{sh}). This model is related to the reservoir facies. The permeability model (k) is based on an equation that relates porosity:

$$\phi_e = \phi_T - (V_{sh} \times \phi_{sh}) \quad (1)$$

$$\text{Log}_{10}k = m\phi_e + c \quad (2)$$

Here, m is the slope and c a constant that indicates the cutoff point with the permeability, when porosity has a value of zero (Satter et al., 2008). This equation is established from

core samples in the laboratory. Then, based on the permeability equation, the modified Lorenz method was applied (Craig, 1972) to determine the various rock types in the reservoir.

Rock typing consists of grouping rocks that have similar petrophysical properties of the different flow units comprising the reservoir (Guo et al., 2005). For this, we used the modified Lorenz method, which normalizes and graphs values of the effective porosity and permeability. Each slope on the graph indicates a type of rock.

Thereafter, we grouped the rock types of the formation using the flow zone indicator (FZI) method, which uses the fraction of effective porosity ϕ_z and the rock quality index RQI, based on the relationship between permeability and porosity (Lis-Śledziona, 2019).

$$RQI = 0.0314 \times \sqrt{\frac{k}{\phi_e}} \quad (3)$$

$$FZI = \frac{RQI}{\phi_z} \quad (4)$$

The values from Equation (4) are grouped to classify and graph the effective porosity and permeability ranges for each rock type. The trend equation is a mathematical expression of permeability as a function of porosity. A permeability function was established for each rock type via a permeability vs. porosity graph, and using a software calculator, the functions were applied to generate the permeability model.

The water saturation model starts from the rock types and water-oil contact, related to the capillary pressure curves and functions $J(S_w)$ provided by the company. These functions were determined from the capillary pressure curves of the cores, which were averaged to obtain a representative curve for the area of interest, called the J function. This is a dimensionless function that correlates the capillary pressure to the reservoir pore structure in terms of porosity and permeability (Donnez, 2007). The functions are specific to each rock type and are implemented in the software to generate the water saturation model of each field.

$$J(S_w) = \frac{C P_c}{\sigma \cos \theta} \sqrt{\frac{k}{\phi_e}} \quad (5)$$

Here, $J(S_w)$ is the J function, P_c the capillary pressure, k the permeability, ϕ_e the effective porosity, θ the contact angle, and σ the interfacial tension.

3.5. Construction of 3D geologic model

Using the previous models, we constructed the geologic model with standardized and normalized data. This model includes the construction of a cell grid with dimensions X, Y and Z, limited by the structural surfaces at the top of each unit (M1, M2_1, M2_2, and M3) and by the fault surfaces.

We constructed the model grid using the fault surfaces as the framework. This grid was divided into three skeletons, upper, middle and lower, related to the nodes of the fault columns. The grid is composed of cells with a rectangular prism shape that the software defined in the I, J and K directions, corresponding to the directions X and Y (I and J) with depth K, equivalent to Z, with sizes defined on each axis. The grid has 337 cells in direction I, 334 in direction J, and 178 layers in direction Z. This results in a total of 20035324 cells, corresponding to a geocellular model of high resolution.

Horizons and layers were created by incorporating structural surfaces to the top of each unit (M1, M2_1, M2_2 and M3) in the 3D grid, and vertically subdividing each unit limited by surfaces by a determined number of layers. The number of vertical layers of each unit was determined from the minimum thickness to preserve geological bodies of minimal thickness, which corresponds to the vertical resolution of the model.

After determining the facies, we did the upscaling, which consists of taking information from the scale of well logs to that of the geologic model. These scaled cells were the main input to the 3D modeling. Each cell traversed by a well corresponds to only one value of the scaled property of the wells, either discrete or continuous. For facies, these are discrete quantities because there can only be an integer value associated with a facies. Petrophysical properties are continuous variables that take on decimal values within a specific range. The scaled properties in this case are the facies and effective porosity. For the permeability and water saturation, we used equations implemented in the software calculator, which are a function of the previously established properties.

After scaling the facies in each well, we used a geostatistical analysis module, which was applied to the discrete values of the facies in order to spatially populate the cells. This module is based on the deterministic or stochastic modeling algorithms – sequential indicator simulator (SIS) and object modeling. The SIS algorithm generates a pixel model of the facies distribution, following the probability tendencies of these and extrapolation using variograms obtained for each facies of each unit. Object modeling represents the geometry of geological bodies such

as channels, bars and fans, in order to reliably represent the distribution of those bodies. This information is acquired via an analysis of seismic interpretation (seismic attributes), data of outcrops and/or known analogue fields, which facilitate acquisition of the directions and dimensions of modeled bodies.

After modeling the facies, we modeled the petrophysical properties. For the porosity model, we used the scaled log and conducted a geostatistical analysis, generating variograms for the porosity of each facies of each unit. The permeability was modeled using an equation related to the reservoir porosity, from which was determined the rock types. Each type had its range of permeability and porosity. Then we found a function for each rock type and extrapolated to the model by applying this equation in the software calculator. The J functions of unit M1 were used to obtain the water saturation model, which is based on the identified rock types and permeability model.

3.6. Contacts and volumetric computations

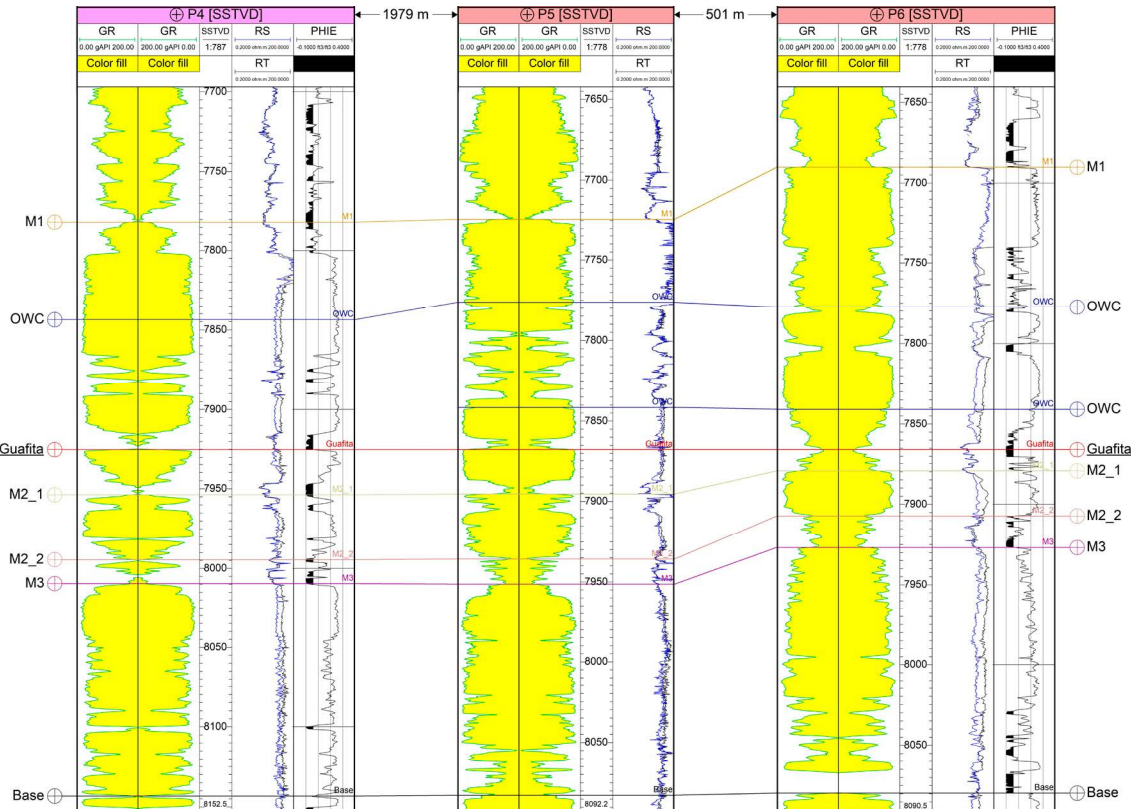
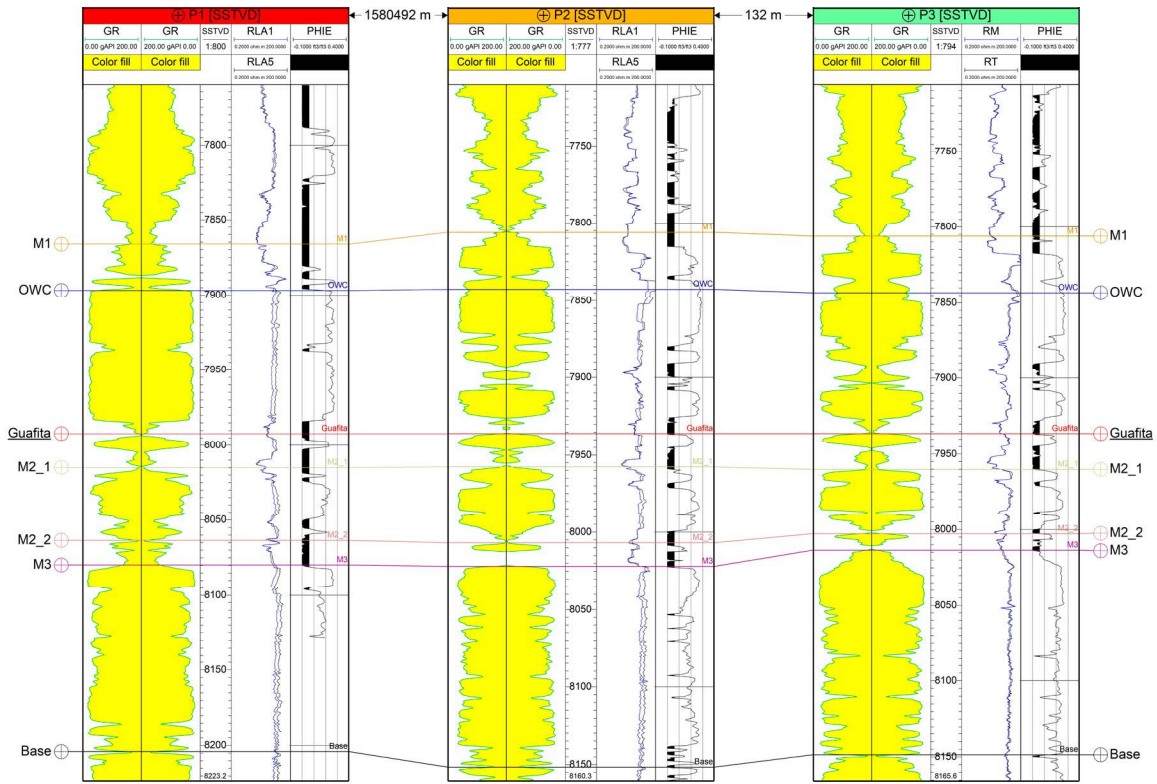
For each field, we determined the water-oil contact through the resistivity log and tests of well production. We used the volume calculation module for the OOIP and selected the oil-water contact, water saturation model, porosity model, facies model, and oil volumetric factor. From the above models, the software calculated the OOIP of each field.

4. RESULTS AND DISCUSSION

4.1. Facies model

The study interval corresponds to the operational units M1, M2 and M3, among which M1 is the unit of interest. A stratigraphic correlation was carried out at the level of these units, taking as a starting point the regional datum of the study area. Figures 2 and 4 show this correlation, wherein the tops M1, M2_1, M2_2 and M3 are identified based on the response of the GR and density logs. Unit M2 corresponds to thin intercalations of sands and shales. Unit M2_1 consists of clean sands, according to smaller GR values. Unit M2_2 had larger values in this log, owing to the clay content in the sands. Units M1 and M3 are relatively homogeneous and correspond to packets of sandstone with intercalations of shales. We are only interested in the top of unit M3, so it was assigned a lower limit corresponding to the base of the model.

Based on regional studies and those of the cores of neighboring fields of the operating company and of similar fields, it was established that the studied reservoir was deposited in



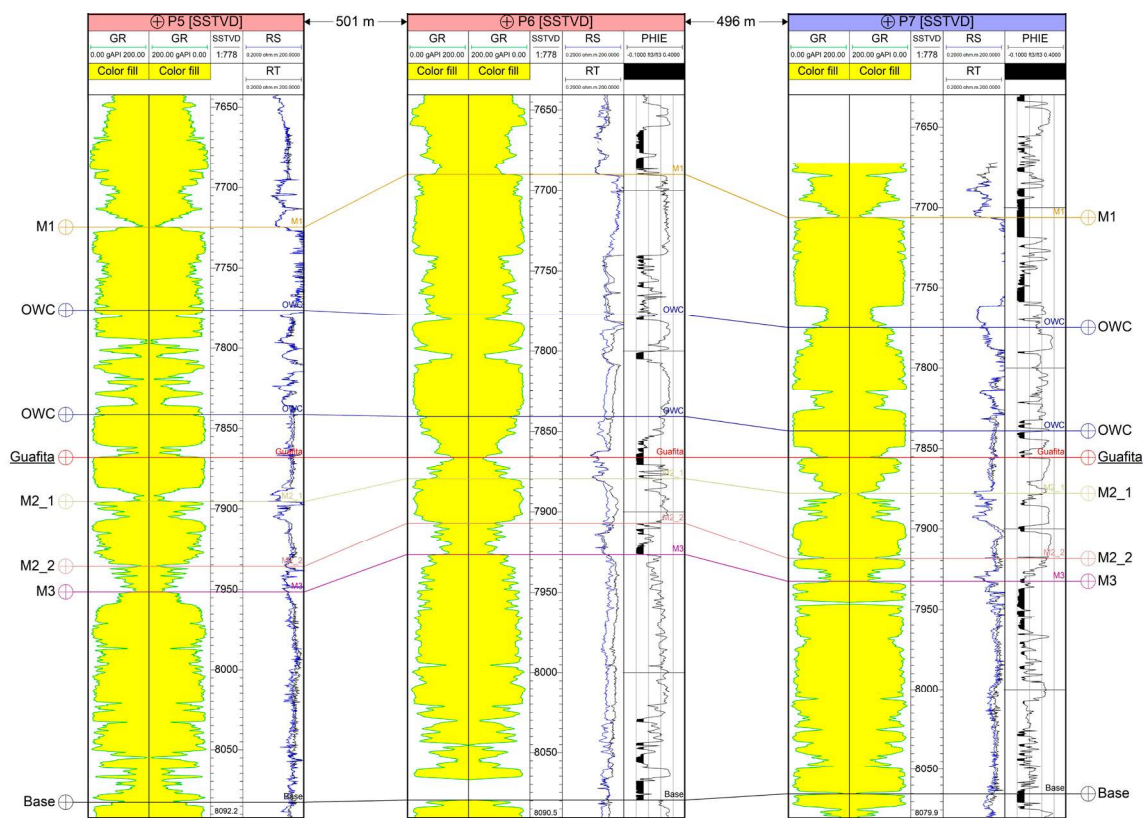


Figure 2. Stratigraphic correlation of the seven wells
Field 1: P1, P2, P3, P4, P5; Field 2: P6, P7

a fluvial-deltaic environment. Four main facies were determined, channel, deltaic front, overflow fan, and floodplain. Figure 3 shows the facies model.

The channel facies correspond to massive sand bodies of units M1 and M3, and smaller sand packets for the channels of M2_1. The signature of clean sand channels in the GR log were identified with cylinder shape, indicating small GR values and uniform lithology. These facies are the most important of the study because they have greater flow and storage capacity, owing to their petrophysical properties of porosity and permeability.

Floodplains are flat areas adjacent to the round of a river, or long-range areas composed of fine sediment lithologies. The floodplain facies are identified by large values in the GR log, which correspond to areas of fine-grained lithology such as shales and are local seals of the reservoir. These facies are present in operational units M1, M2_1 and M2_2, and to a lesser extent in M3.

An overflow fan is generated when a river breaks its barrier and pulses of sand are released, creating fan-shaped sedimentary

bodies. These bodies are recognized in the logs by a sawn-off funnel shape with a coarsening-upward sequence. This is because they have fine-grained deposits at the base and, as the river relea-

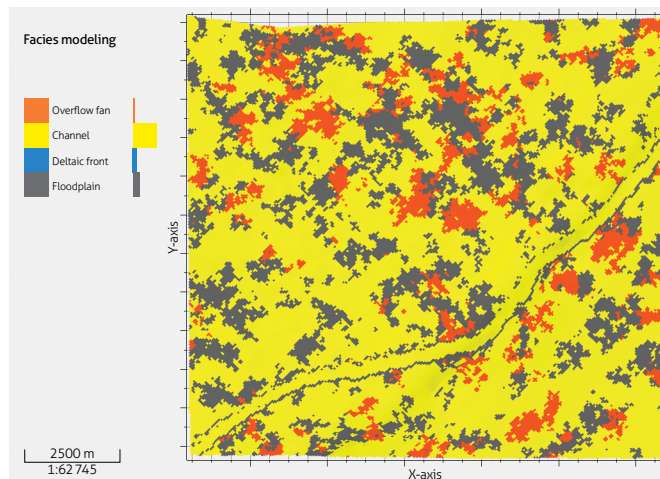
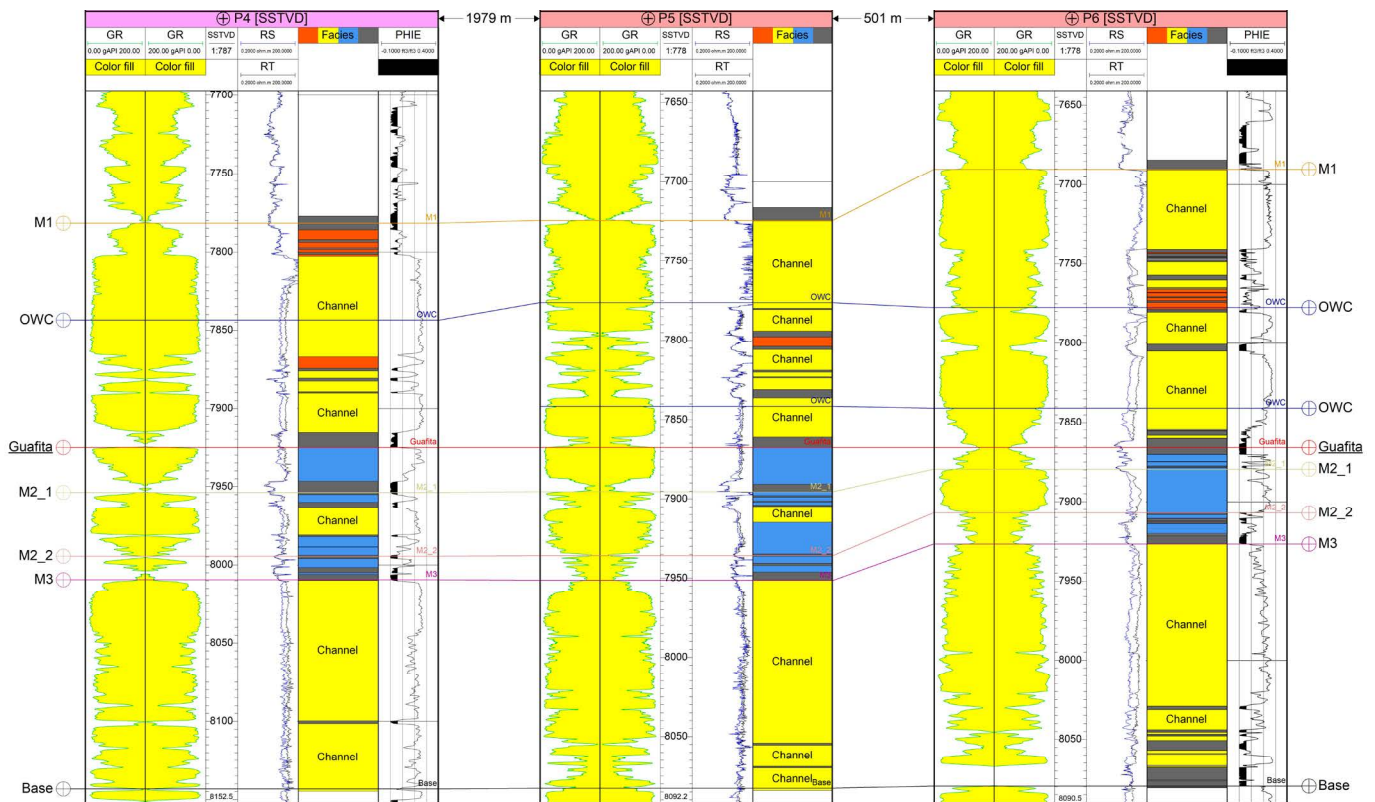
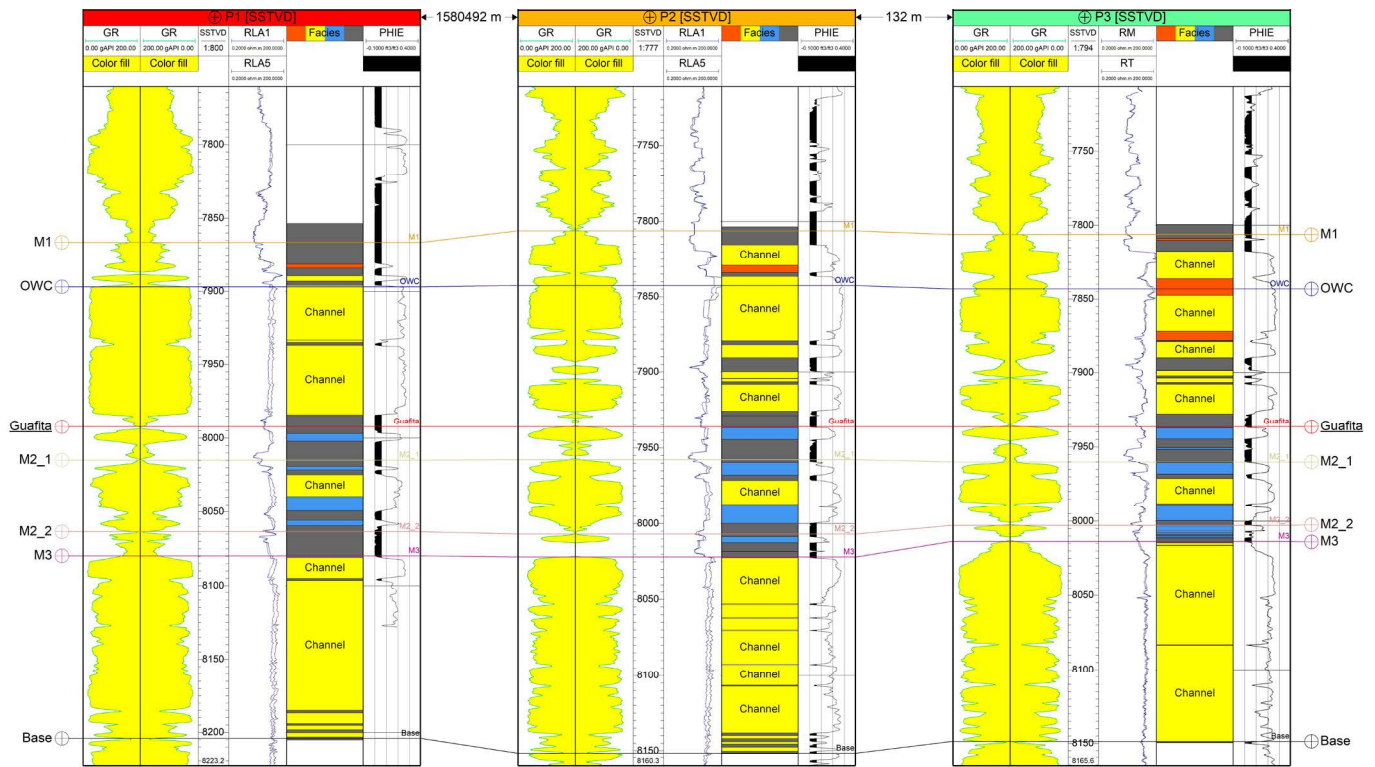


Figure 3. Plan view of layer 1 facies modeling



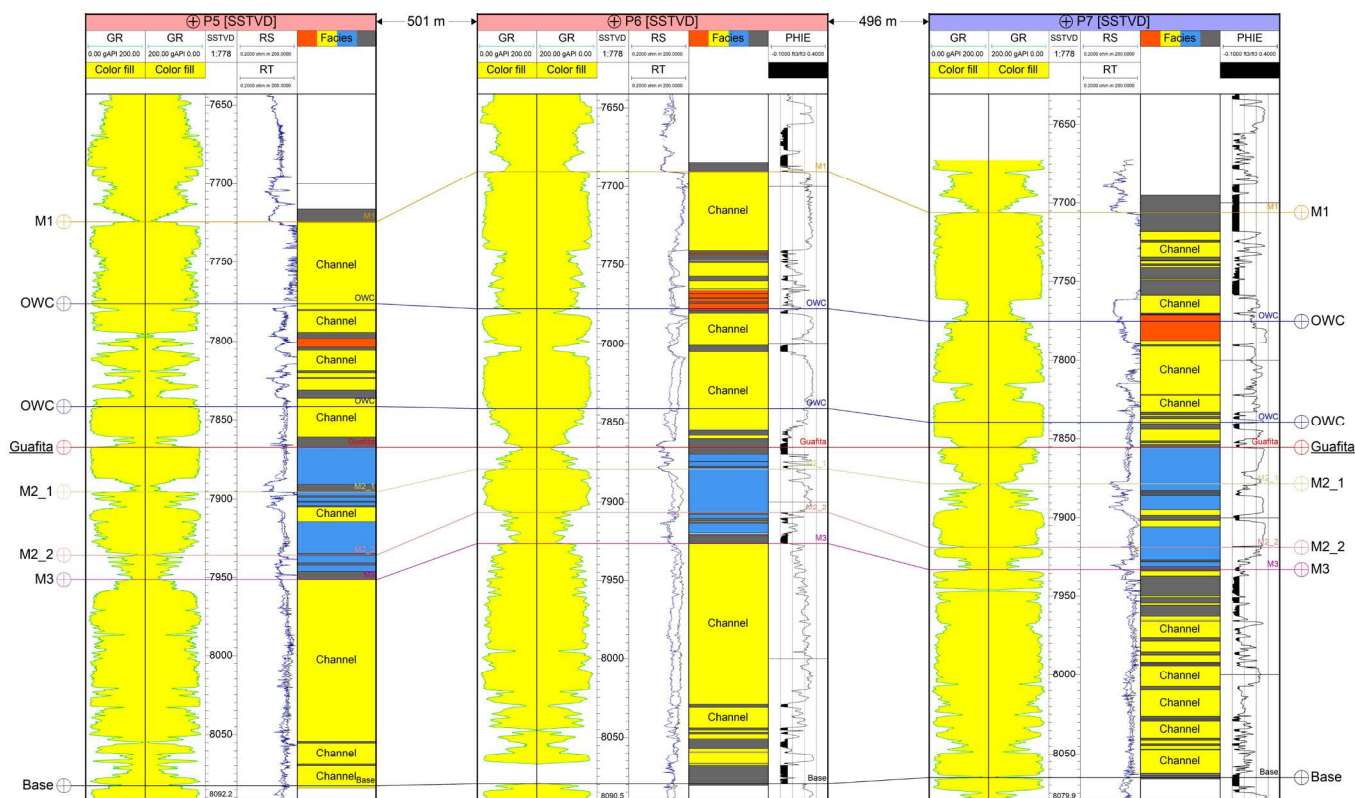


Figure 4. Stratigraphic correlation with the relationship of the facies defined from seven wells, based on the response of well logs Field 1: P1, P2, P3, P4, P5; Field 2: P6, P7

ses sands, they increase toward the top. These facies are present in the upper part of unit M1 and are in a fluvial environment.

The deltaic front facies mark a transition zone between a continental and marine environment. The deltaic front corresponds to the shallow part of a delta receiving sediment from river channels and, for this reason, in the log analysis there was a coarsening-upward response in the shape of a non-sawed-off funnel. It was also identified that they are heterogeneous bodies that are interspersed with channels due to the channel-front interaction of waves and sediment redeposition. These intercalations are evident in unit M2_1.

4.2. Structural model

The structural model of the fields corresponds to an anticline elongated in the northeast direction with closure in three directions. It was obtained from the structural surface in depth at the top of the guafita marker and the faults affecting it. The top surfaces of each unit were created using isopachous thicknesses. Figure 5 shows a 3D view of the structural surface at the top of the producer unit M1.

4.3. Petrophysical model

The modeled porosity is discriminated by the facies of each unit. Figure 6 shows a plan view of this variable, where it is seen that the model adequately represented the porosities of the facies. The channel facies has high porosity values of 22%–27%, the delta front facies 18%–22%, and the facies floodplain < 5%.

To find the model permeability (K), we used the data on reservoir permeability furnished by the operating company.

$$K = 0.0698 \times e^{(39.369 \times \phi_e)} \quad (6)$$

We determined the rock types of the reservoir with the modified Lorenz method. Figure 7 shows three different slopes, corresponding to rock types categorized in ascending order of porosity: Rock 0, related to floodplain facies; Rock 1, related to channel facies; Rock 2, related to deltaic front facies.

We obtained an FZI range for the Rock 2 type at 0–1.65, for Rock 1, 1.66–11, and for Rock 0, 12–8312. For the permeability model, equations were established for each rock type using a graph of permeability vs. effective porosity.

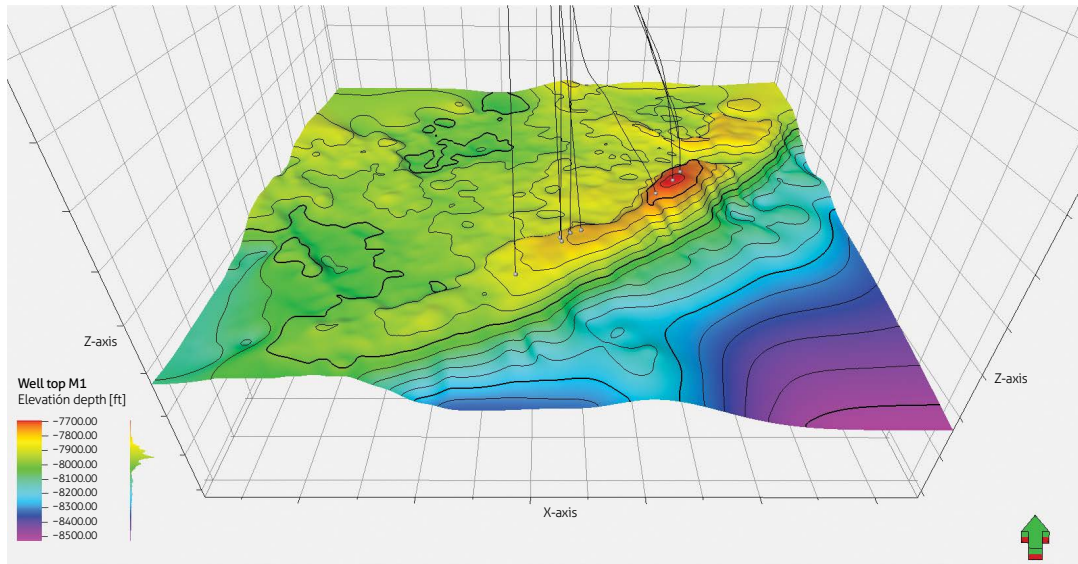


Figure 5. Structural surface to the top of producer unit M1.

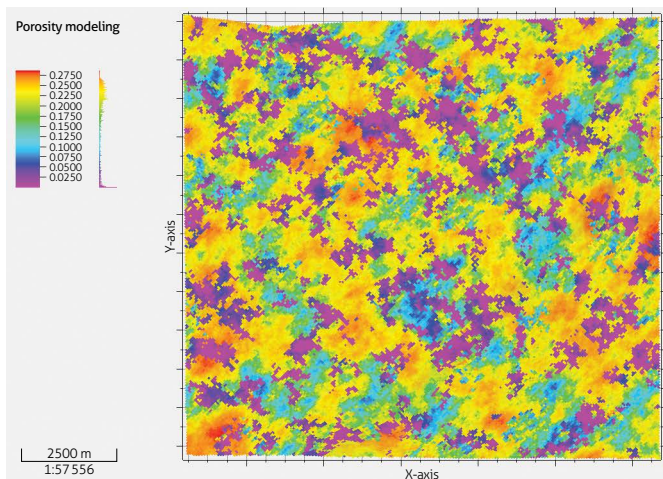


Figure 6. Plan view of porosity modeling, layer 1

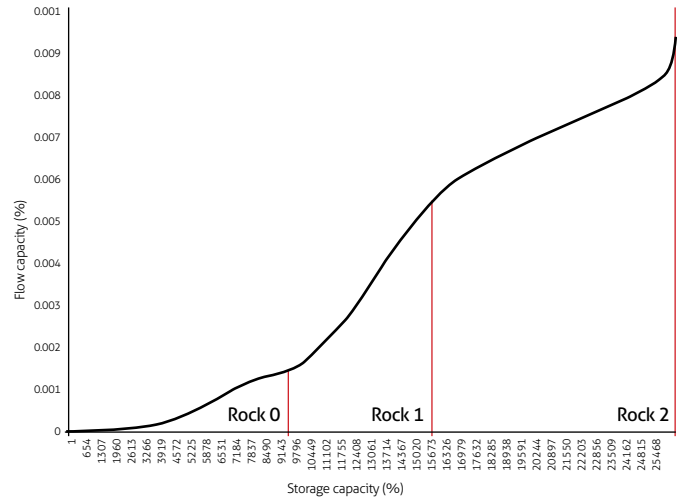


Figure 7. Modified Lorenz graph

$$K_{R0} = 23\,006 \times (\text{Porosity Model}) - 42.561 \quad (7)$$

$$K_{R1} = 0.0698 \times (e^{39.359 \times (\text{Porosity model})}) \quad (8)$$

$$K_{R2} = 67.916 \times (\text{Porosity Model}) - 3.7608 \quad (9)$$

A permeability model discriminated by rock type and effective porosity was constructed. Figure 8 shows a plan view of the modeled permeability, where it is seen that the facies model and rock types are coherent. The high permeabilities

(> 100 mD) correspond to rock types 1 and 2, which are related to the channel and deltaic front facies.

The following table shows average porosity and permeability values for each facies present in each unit.

The water saturation model has as input the permeability model by rock type, executing the *J* functions for operational unit M1. Based on information of pressure, logs and production tests, we determined the water-oil contact at Field 1 at a true vertical depth subsea depth of -7848 feet. At Field 2, this was -7777 feet.

Table 2. Average values of porosity and permeability models for each facies in each unit

Unit	Facies	Porosity (%)	Permeability (md)
M1	Channel	21.77	955.87
	Overflow fan	16.31	81.45
	Floodplain	2.69	0.18
M2_1	Channel	21.97	458.96
	Deltaic Front	18.88	94.98
	Floodplain	2.24	0.23
M2_2	Deltaic Front	11.9	31.59
	Floodplain	1.28	0.13
M3	Channel	18.58	351
	Floodplain	2.85	0.27

J functions were run for each field in the software calculator. Figures 9 and 10 depict the water saturation model for unit M1 of the two fields studied. The area of interest corresponds to saturations from 20% to 30% in the structurally higher part of the reservoir, corresponding to channel facies.

4.4. Calculating OOIP volume

The software included the previous models to do the volume calculation of the OOIP of unit M1 of each field. An oil volume factor of 1.06 was used for both calculations. For Field 1, we obtained a value of six million barrels of OOIP, and 9 million barrels for Field 2. Figures 11 and 12 show OOIP maps, indicating the area of oil accumulation.

The values obtained were used to calculate the current recovery factor, based on August 2019 production data. For this we divided the accumulated production of each field by the calculated OOIP. Field 1 has a current recovery factor of 1.5% and Field 2 has 22%.

5. CONCLUSIONS

From the stratigraphic correlation of the wells, we identified four units of the lower Carbonera Formation, M1, M2_1, M2_1, and M3. The unit of interest was M1, because in it lie clean sands that store hydrocarbons.

The deposit environment of the reservoir is fluvial-deltaic and the most important facies is that of the channel in operational unit M1. There, clean sands predominate, which are identified as the main pool of the reservoir. The floodplain facies are hallmarks of the reservoir that are present mainly in units M2_1 and M2_2. Facies of the deltaic front reservoir and overflow fan are lower quality reservoirs in comparison with the channel facies.

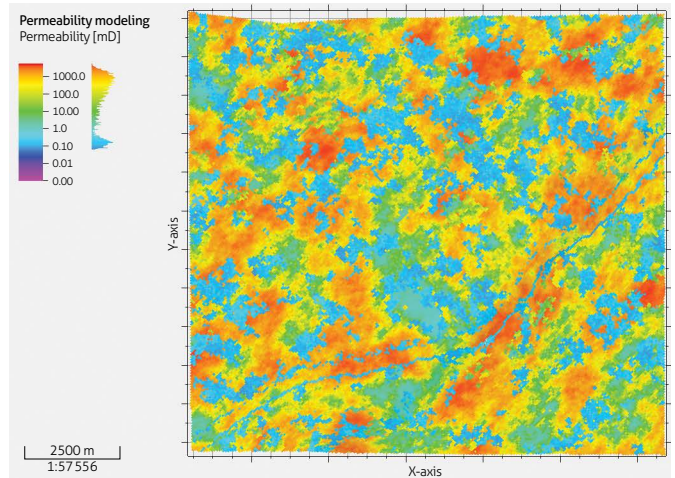


Figure 8. Plan view of layer 1 permeability modeling

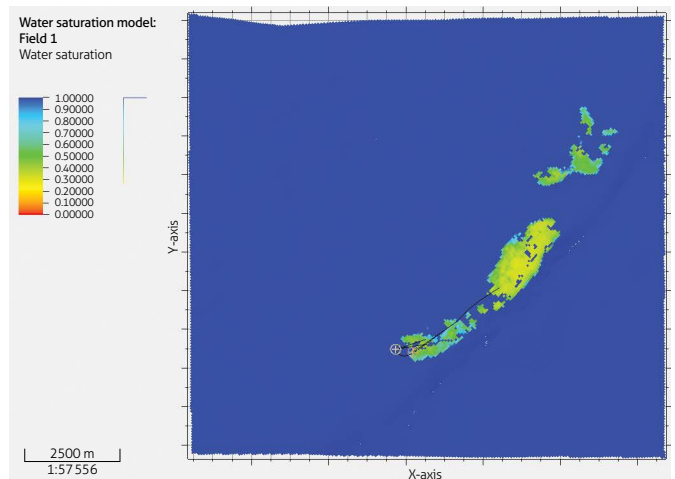


Figure 9. Layer 1 of water saturation modeling for unit M1 of Field 1

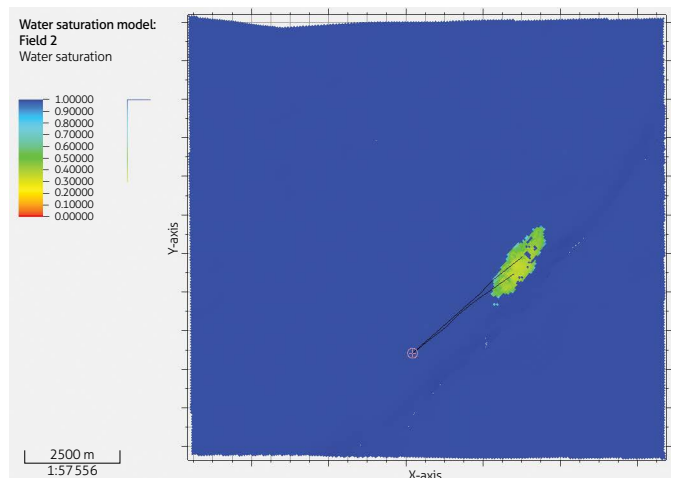


Figure 10. Layer 1 of water saturation modeling for unit M1 of Field 2

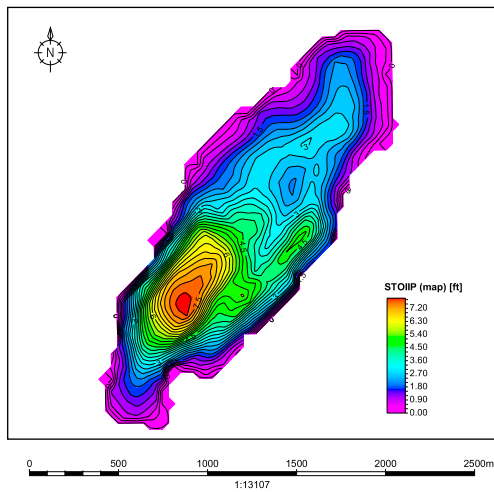


Figure 11. Field 1 OOIP Map

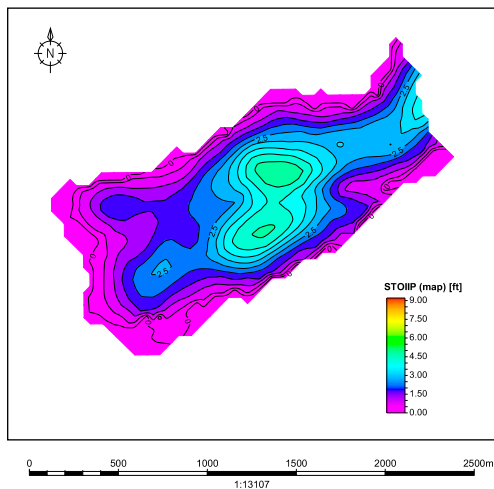


Figure 12. Field 2 OOIP Map

Petrophysical properties such as effective porosity indicate that unit M1 is the most prone to accumulate hydrocarbons, as it has the greatest porosities in the channel facies (22%–27%). We integrated the stratigraphic, structural, petrophysical models through 3D geological modeling, from which the OOIP was calculated in each field.

Field 1 has 1.5% recovery factor. This indicates that the sands of unit M1 can produce oil with recovery factors up to that of Field 2, which is 22%.

ACKNOWLEDGMENTS

We thank the Department of Geosciences at the Universidad de los Andes, Colombia, and the operating company for authorization to use the data. We also thank the editorial group of the *Boletín Geológico*, and the anonymous reviewers who helped improve the manuscript with their valuable comments.

REFERENCES

- Campos, H., & Mann, P. (2015). Tectonostratigraphic Evolution of the Northern Llanos Foreland Basin of Colombia and Implications for Its Hydrocarbon Potential. In *Petroleum geology and potential of the Colombian Caribbean margin* (pp. 517-546). American Association of Petroleum Geologists. <https://doi.org/10.1306/16531948M1083651>
- Craig, F. F. (1972). *The Reservoir Engineering Aspects of Waterflooding*. SPE Monograph 3. Society of Petroleum Engineers.
- De la Parra, F., Mora, A., Rueda, M., & Quintero, I. (2015). Temporal and spatial distribution of tectonic events as deduced from reworked palynomorphs in the eastern Northern Andes. *AAPG Bulletin*, 99(8), 1455-1472. <https://doi.org/10.1306/02241511153>
- Domínguez, A. (2014). *Análisis Sismoestratigráfico de la Formación Carbonera Miembro C7 (Municipios de Orocué y San Luis de Palenque, Cuenca Llanos Orientales), Colombia* [Undergraduate thesis]. Universidad Nacional de Colombia, Bogotá, Colombia.
- Donnez, P. (2007). Reservoir rock properties. In *Essentials of reservoir engineering* (pp. 19-20). Editions Technip.
- Duarte, E., Bayona, G., Jaramillo, C., Parra, M., Romero, I., & Mora, J. (2017). Identificación de los máximos eventos de inundación marina miocenos y su uso en la correlación y análisis de la cuenca de antepaís de los Llanos Orientales, Colombia. *Boletín de Geología*, 39(1), 19-40. <http://dx.doi.org/10.18273/revbol.v39n1-2017001>
- Guo, G., Díaz, M. A., Paz, F., Smalley, J., & Waninger, E. A. (2005). *Rock Typing as an Effective Tool for Permeability and Water-Saturation Modeling: A Case Study in a Clastic Reservoir in the Oriente Basin*. SPE Annual Technical Conference and Exhibition. <https://doi.org/10.2118/97033-MS>
- Lis-Śledziona, A. (2019). Petrophysical rock typing and permeability prediction in tight sandstone reservoir. *Acta*

- Geophysica*, 67, 1895-1911. <https://doi.org/10.1007/s11600-019-00348-5>
- Mora, A. (2015). Petroleum systems of the Eastern Cordillera, foothill basins, and associated Llanos basin: Impacts on the prediction of large scale foreland and foothill petroleum accumulations. *AAPG Bulletin*, 99(8), 1401-1406. <https://doi.org/10.1306/bltnintro032615>
- Reyes-Harker, A., Ruiz-Valdivieso, C. F., Mora, A., Ramírez-Arias, J. C., Rodríguez, G., De la Parra, F., Caballero, V., Parra, M., Moreno, N., Horton, B., Saylor, J., Silva, A., Valencia, V., Stockli, D., & Blanco, V. (2015). Cenozoic paleogeography of the Andean foreland and retroarc hinterland of Colombia. *AAPG Bulletin*, 99(8), 1407-1453. <https://doi.org/10.1306/06181411110>
- Rider, M. (2000). *The geological interpretation of well logs*. Rider-French Consulting Ltd.
- Satter, A., Iqbal, G. M., & Buchwatter, J. L. (2008). *Practical enhanced reservoir engineering*. PennWell Corporation.
- Vayssaire, A., Abdallah, H., Hermoza, W., & Negri, E. G. F. (2014). *Regional Study and Petroleum System Modeling of the Eastern Llanos Basin*. AAPG Search and Discovery.



Sector del Cerro Yuruma, Alta Guajira, Colombia
Fotografía de Pedro Patarroyo



This work is distributed under the
Creative Commons Attribution 4.0 License.

Received: August 28, 2020

Revision received: August 2, 2021

Accepted: August 2, 2021

Published online: October 29, 2021

Relevant aspects to the recognition of extensional environments in the field

Aspectos relevantes para el reconocimiento de ambientes
extensionales en campo

Ana Milena **Suárez Arias**, Julián Andrés **López Isaza**¹, Anny Julieth **Forero Ortega**¹, Mario Andrés **Cuéllar Cárdenas**¹, Carlos Augusto **Quiroz Prada**¹, Lina María **Cetina Tarazona**¹, Oscar Freddy **Muñoz Rodríguez**¹, Luis Miguel **Aguirre Hoyos**¹, Nelson Ricardo **López Herrera**¹

¹ Dirección de Geociencias Básicas, Servicio Geológico Colombiano, Bogotá, Colombia.

Corresponding author: Ana Milena Suárez Arias, anasuarezgeo@gmail.com

ABSTRACT

The understanding of each geological-structural aspect in the field is fundamental to be able to reconstruct the geological history of a region and to give a geological meaning to the data acquired in the outcrop. The description of a brittle extensional environment, which is dominated by normal fault systems, is based on: (i) image interpretation, which aims to find evidence suggestive of an extensional geological environment, such as the presence of scarp lines and fault scarps, horst, graben and/or half-graben, among others, that allow the identification of the footwall and hanging wall blocks; ii) definition of the sites of interest for testing; and iii) analysis of the outcrops, following a systematic procedure that consists of the observation and identification of the deformation markers, their three-dimensional schematic representation, and their subsequent interpretation, including the stereographic representation in the outcrop. This procedure implies the unification of the parameters of structural data acquisition in the field, mentioning the minimum fields necessary for the registration of the data in tables. Additionally, the integration of geological and structural observations of the outcrop allows to understand the nature of the geological units, the deformation related to the extensional environment and the regional tectonic context of the study area.

Keywords: Normal fault, deformation, stress, extensional environment.

RESUMEN

El entendimiento de cada aspecto geológico-estructural en campo es fundamental para poder reconstruir la historia geológica de una región y dar un sentido geológico a los datos adquiridos en afloramiento. La descripción de un ambiente extensional frágil, el cual está dominado por sistemas de fallas normales, se basa en: i) la interpretación de imágenes, que tiene como objetivo encon-

trar evidencias que sugieran un ambiente geológico extensional, como lo son la presencia de líneas de escarpe y escarpes de falla, pilares tectónicos y grábenes y/o semigrábenes, entre otros, que permitan la identificación de los bloques yacente y colgante; ii) definición de los sitios de interés para comprobación; y iii) análisis de los afloramientos, siguiendo un procedimiento sistemático que consiste en la observación e identificación de los marcadores de deformación, su representación esquemática tridimensional, y su posterior interpretación, incluyendo la representación estereográfica en el afloramiento. Este procedimiento implica la unificación de los parámetros de adquisición de datos estructurales en campo, mencionando los campos mínimos necesarios para el registro de los datos en tablas. Adicionalmente, la integración de las observaciones geológicas y estructurales del afloramiento permite entender la naturaleza de las unidades geológicas, la deformación relacionada con el ambiente extensional y el contexto tectónico regional del área de estudio.

Palabras clave: Falla normal, deformación, esfuerzo, ambiente extensional.

1. INTRODUCTION

The observations of geological structures in the field allow the understanding of the geological processes that occur in the earth's crust, product of the dynamics of tectonic plates through geological time (Frisch et al., 2011; Moores and Twiss, 2000). The integration of sedimentological, petrological, stratigraphic and structural studies of a region allows establishing the geological environment, which is related to the tectonic regime (extensional, contractional and transcurrent) operating at a given time. One of these environments is extensional, which is associated with different geological processes (Frisch et al., 2011) such as intracontinental rift systems (Corti, 2009; Dickinson, 2002), mid-oceanic ridge systems (Batiza, 1996), basins (Yoon et al., 2014) and passive continental margins (Trumpy, 1980, cited in Frisch et al., 2011), among others.

At the structural level, the style of deformation in an extensional environment is dominated by normal fault systems that together form graben and semigraben structures (Fossen, 2010; Groshong, 1999; McClay, 1987; Moores and Twiss, 2000; Ragan, 2009). Each fault within the normal fault system records a spatial and temporal evolution with respect to the geological units it affects (Cowie et al., 1998; Cowie et al., 2000; Hus et al., 2005; Tanner and Brandes, 2020; Walsh et al., 2002). These faults can be classified according to their geometry, displacement magnitude, temporality and depth (Fossen, 2010; Twiss and Moors, 2007), thus obtaining the fault activity history.

The understanding of each geological-structural aspect in the field is fundamental to be able to reconstruct the geological history of a region and to give a geological sense to the data acquired in the outcrop. This review is aimed at non-specialists, or professionals from other disciplines who are dealing, or are

faced, with the management of faults in extended zones. The paper proposes a methodology for the recognition of extensional environments that integrates pre-field photogeological interpretation, the establishment of a systematic process for data acquisition and structural analysis with a stereographic projection grid. Additionally, some basic concepts for the description and understanding of the structures and the mechanisms that generate them are included, in order to provide greater clarity. Next, the definition of several previous concepts is presented:

» **Deformation.** Geological structures observed in the field are deformations that represent the structural configuration of the Earth's crust. Deformation is the transformation of an initial geometry to a final geometry through distortion, rotation and translation (Figure 1a) (Ragan, 2009; van der Pluijm and Marshak, 2004). However, the latter two components are difficult to determine in practice, with distortion being the most commonly used in structural analysis, which involves a change of shape (Fossen, 2010; Ragan, 2009; Tanner and Brandes, 2020; van der Pluijm and Marshak, 2004). In addition, continuous medium mechanics, which analyses the physical behavior of matter (e.g. rock) at the meso- and macroscopic scale, without considering discontinuities at the microscopic level, is used to study the deformation of a rock body (Pollard and Fletcher, 2005; Ragan, 2009; Ramsay and Lisle, 2000).

The deformation can be homogeneous or heterogeneous (Fossen, 2010; Ragan, 2009; Tanner and Brandes, 2020; van der Pluijm and Marshak, 2004). The former happens when a body that is subjected to deformation the lines that were parallel in the pre-deformation state stay parallel, or when a circumference in the pre-deformation

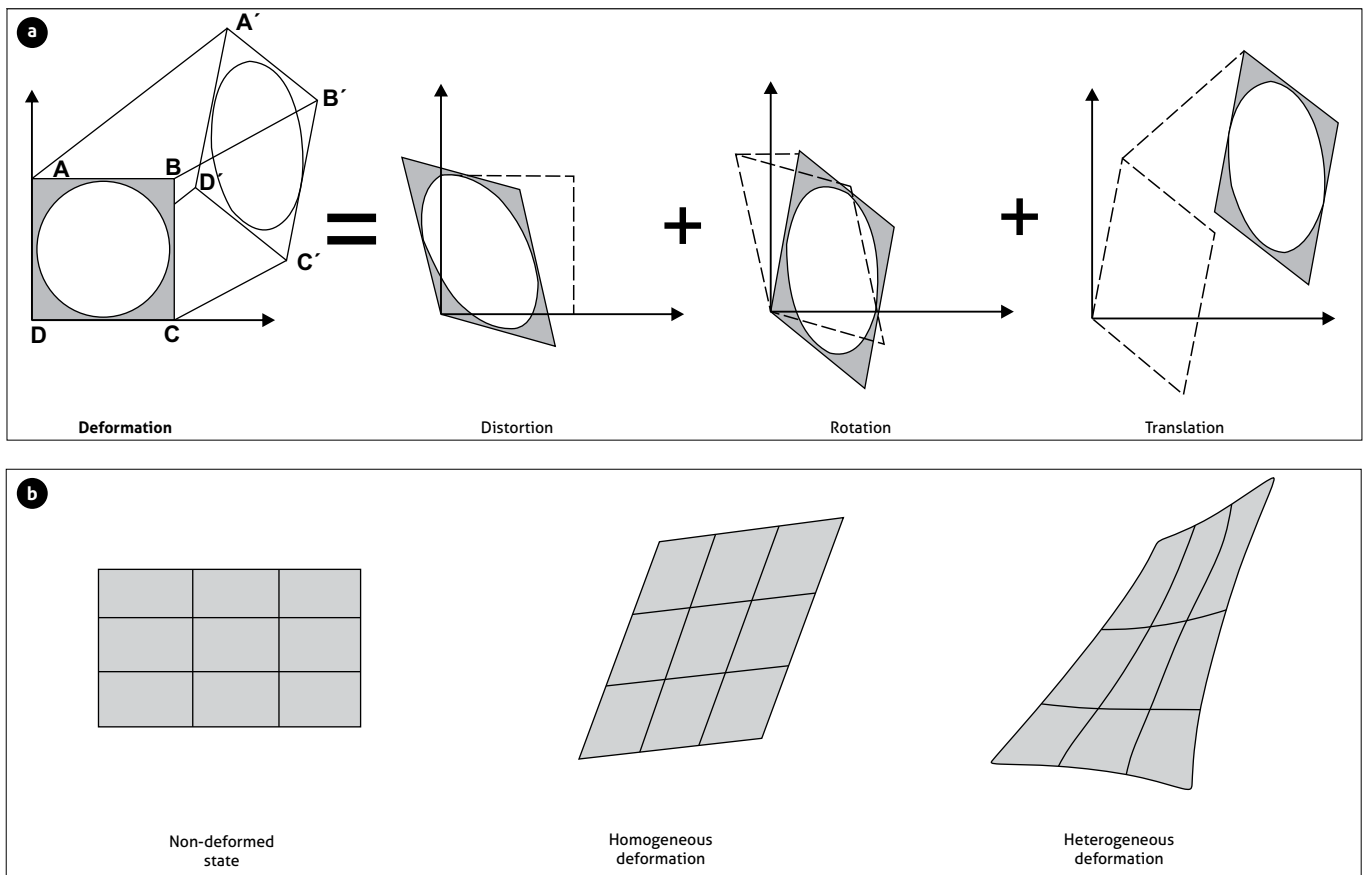


Figure 1. Deformation concepts

a) Deformation of a square as the result of three independent components: distortion, rotation and translation. b) Homogeneous and heterogeneous types of deformation. Source: modified from van der Pluijm and Marshak (2004).

state becomes an ellipse in the deformed state (Ragan, 2009; van der Pluijm and Marshak, 2004); if this does not occur, the result is heterogeneous deformation (Figure 1b). In the analysis of homogeneous deformation, material lines formed by a series of points on a body are taken as reference material lines that serve as deformation markers and are recognizable throughout the deformation process (van der Pluijm and Marshak, 2004).

For a two-dimensional body (e.g. a circle), when deformed homogeneously, there will be at least two material lines that do not rotate with respect to each other, thus forming the principal axes of the deformation ellipse (Figure 2a). Similarly, in three dimensions one has three material lines that remain perpendicular after deformation, which correspond to the principal axes of a deformation ellipsoid (Fossen, 2010; Ramsay and Huber, 1986; van der Pluijm and Marshak, 2004). Homogeneous deformation without

volume change can be decomposed into pure shear and/or simple shear (Fossen, 2010; Ragan, 2009; Twiss and Moors, 2007; van der Pluijm and Marshak, 2004) (Figure 2b). Pure shear consists of coaxial or irrotational deformation where material lines parallel to the principal axes of deformation do not rotate and do not have no shear deformation, whereas simple shear consists of non-coaxial or rotational deformation where material lines rotate, passing through the principal axes of deformation; the only material lines that do not rotate are those parallel to the shear direction (Ragan, 2009; Twiss and Moors, 2007; van der Pluijm and Marshak, 2004).

» **Stress.** The structural analysis of a deformed rock body determines the possible stress field to which the body was subjected. The term stress is defined as the force (F) divided by the surface area (A) on which the force acts (Fossen,

2010; Means, 1976; Twiss and Moors, 2007). The mechanical behavior of a rock that is subjected to stress varies depending on its rheology and is conditioned by factors such as time, stress intensity, temperature and pressure (Means, 1976; Pollard and Fletcher, 2005; Ramsay and Huber, 1986).

» **Faults.** The generation of a fault in a homogeneous body responds to the Mohr-Coulomb fracture criterion ($|\tau| = C + \mu\sigma_n$), which postulates that a fault develops following the plane where the shear stress (τ) is equal to or greater than the body cohesion (C) plus the internal friction (μ) of the material multiplied by the normal stress (σ_n) (Means, 1976; Pollard and Fletcher, 2005). Generally speaking, a fault is a fracture over which relative motion occurs between two blocks that are separated by that fracture (Groshong, 1999; McClay, 1987; Ragan, 2009); that relative motion is called net slip and is represented geometrically by a vector connecting two originally adjacent points that are now on opposite sides of the fault (red dots in Figure 3) (Lisle and Walker, 2013; van der Pluijm and Marshak, 2004; Xu et al. 2009; Yamada and Sakaguchi, 1994). According to the components of the net slip vector, faults are classified

according to whether the slip direction is parallel to the dip direction (normal fault or reverse fault) or to the strike direction (right lateral fault or left lateral fault), although it may happen that the slip is neither parallel to the dip direction nor to the strike direction (oblique faults, Figure 3) (Allmendinger, 2017; Groshong, 1999; van der Pluijm and Marshak, 2004).

The evolution of a normal fault begins with a nucleation point in the crust, followed by lateral growth (Burbank and Anderson, 2011; Gupta and Scholz, 2000; Peacock and Sanderson, 1991; Tanner and Brandes, 2020). There are two models of fault growth, the isolated propagation model (conventional model) and the constant-length coherent model (Cowie et al., 1998; Tanner and Brandes, 2020; Walsh et al., 2002). The conventional model states that faults nucleate randomly in space and their lateral growth occurs by systematic increases in both maximum displacement and fault length, or by the interaction of smaller faults fortuitously aligned to form a single transverse structure (Cowie et al., 1998). In turn, the coherent model proposes that in an early stage the fault lengths are constant and their kinematic components are inherited from an initial structure, and that, in the final stage, these faults interact to form a single continuous structure (Walsh et al., 2002).

The distribution of displacements on a fault ranges from zero at fault terminations to a maximum value at some point along the fault trace (Stewart, 2001). Muraoka and Kamata (1983) determined two patterns of normal fault profiles from displacement distribution plots (length [L] vs. displacement [D]), thus obtaining C-type faults, cone-shaped

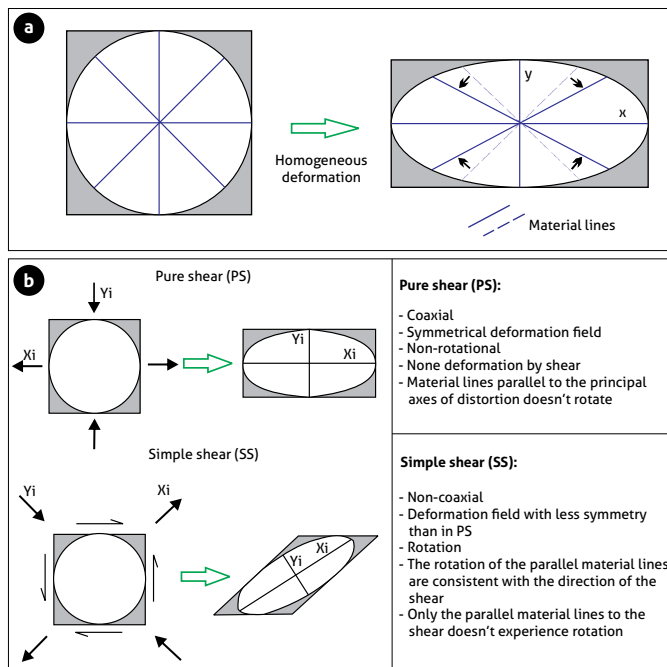


Figure 2. Homogeneous Deformation Concepts
 a) Homogeneous deformation of a circle; b) Types of deformation by pure shear and simple shear. Source: modified from van der Pluijm and Marshak (2004).

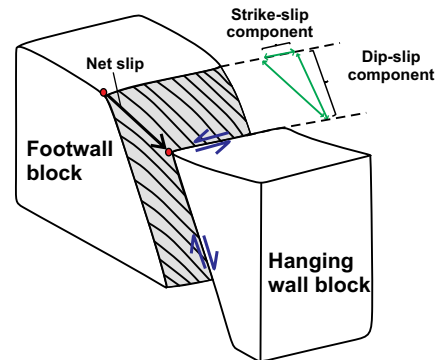


Figure 3. Schematic of a normal fault illustrating the net slip vector and its components in strike and dip
 Source: modified from van der Pluijm and Marshak (2004).

and symmetric with smooth change in displacement, and M-type faults, table-shaped, with a profile that has a broad central part with little variation in displacement and steep slopes toward the ends of the structure. The distribution and displacement profiles show three types of faults, based on their evolution and growth: isolated faults, echelon fault array, with soft links forming relay ramps with other faults, and fault arrays with strong links (Xu et al., 2014).

In nature there are deformation zones that are generated at different depths, giving rise to brittle, brittle-ductile, and ductile shear zones (Fossen, 2010; Fossen and Cavalcante, 2017; Forero-Ortega et al., 2021; Mitra and Marshak, 1988; Sibson, 1977; Sibson, 1980). Brittle structures are generated in shallow structural levels, where the rock loses cohesion, generating the rupture of the rock; however, structures generated by ductile shear can be found originated in deeper structural levels, where the movement occurs without loss of cohesion (Jiang and White, 1995; Sibson, 1977; Sibson, 1980; Twiss and Moores, 2007). Those structural levels of deformation from brittle to ductile level present intrinsic characteristics depending on the temperature and pressure at which the deformation occurred (Forero-Ortega et al., 2021; Fossen and Cavalcante, 2017; Hatcher, 1995; Sibson, 1980).

2. RECOGNITION OF EXTENSIONAL ENVIRONMENTS IN THE FIELD

The fieldwork is supported by the bibliographic review of the geological and geodynamic context of the area of interest, and of the sites planned from the interpretation of images. To recognize an extensional environment in the field, all observations of the outcrop that lead to a hypothesis about the nature of the geological units and the deformation being observed must be integrated. The observations will be focused on recognizing the formation environment of the rocks, the geometry of the structures and the temporal and spatial relationships of the stratigraphic units.

2.1. Image interpretation

Image interpretation aims to find evidence that suggests a particular geological environment, in this case, extensional. A normal fault corresponds to a fault in which the hanging wall block slides downward with respect to the footwall block, on a fault plane, driven by gravity (Anderson, 1951; van der Pluijm and Marshak, 2004). The normal faults that are generated in such an environment develop in the topography different geometries (Faulds and Varga, 1998) and types of structures (Figure 4), such as: fault scarps, grabens, half-graben, horst, and ba-

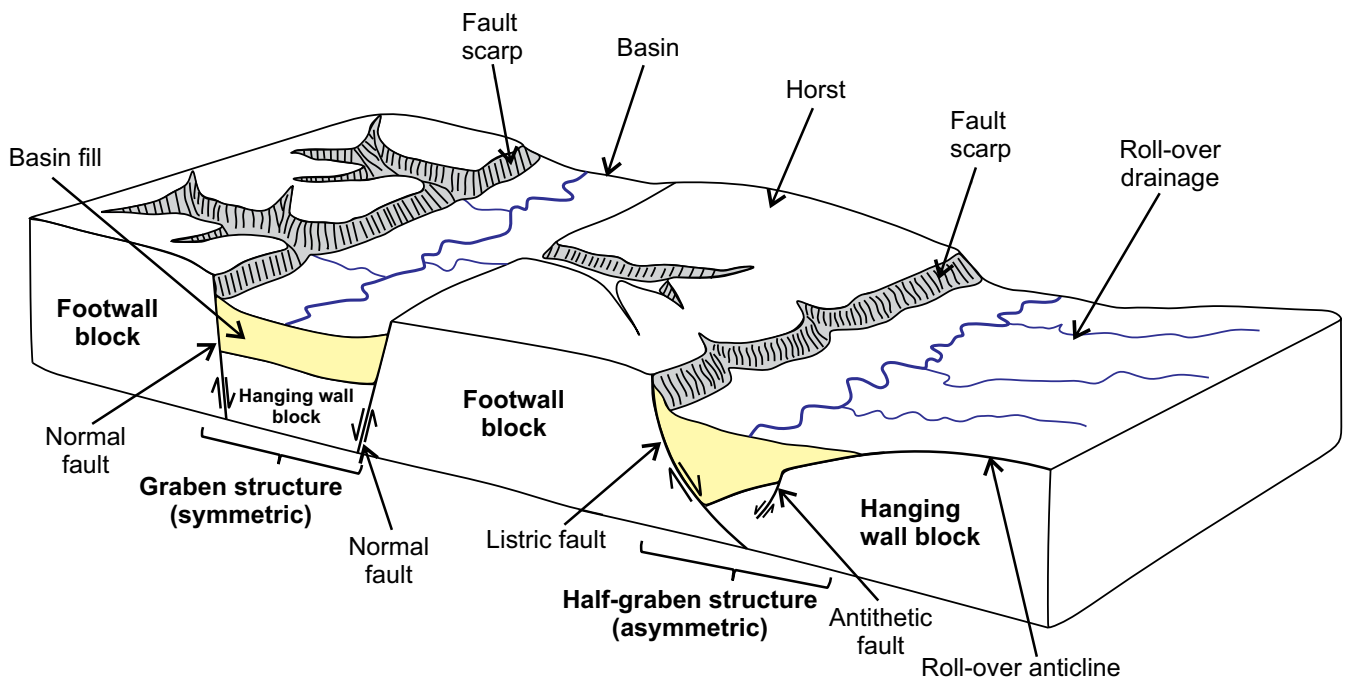


Figure 4. Block diagram showing some of the tectonic structures generated in extended zones
Source: modified from Huggett (2007).

sins, among others (Bull, 2008; Burbank and Anderson, 2011; Huggett, 2007; McCalpin, 2009; Peacock et al., 2000). Synthetic and antithetic normal faults can occur, which correspond to secondary faults that define their orientation and kinematics with respect to the main or master fault. A synthetic fault is parallel to the main fault and has the same shear direction, while an antithetic fault is a fault conjugate to the main fault, with an opposite shear direction (Twiss and Moors, 2007). A listric normal fault corresponds to a rotational fault that presents a curved surface, where the dip decreases with increasing depth

(Fossen, 2010; Hartcher, 1995; Twiss and Moors, 2007), and a rotational fault with a domino arrangement occurs when rotation is simultaneous between faults and layers (Axen, 1988; Stewart and Argent, 2000; Xu et al., 2004). Other characteristic features are the development of roll-over anticlines and horst. A roll-over anticline develops on a hanging wall block of a rotational listric normal fault (Fossen, 2010; Groshong, 1999; Twiss and Moors, 2007). A horst corresponds to an uplifted tectonic block resulting from a normal fault (Fossen, 2010; Groshong, 1999; Hartcher, 1995; Huggett, 2007; Twiss and Moors, 2007).

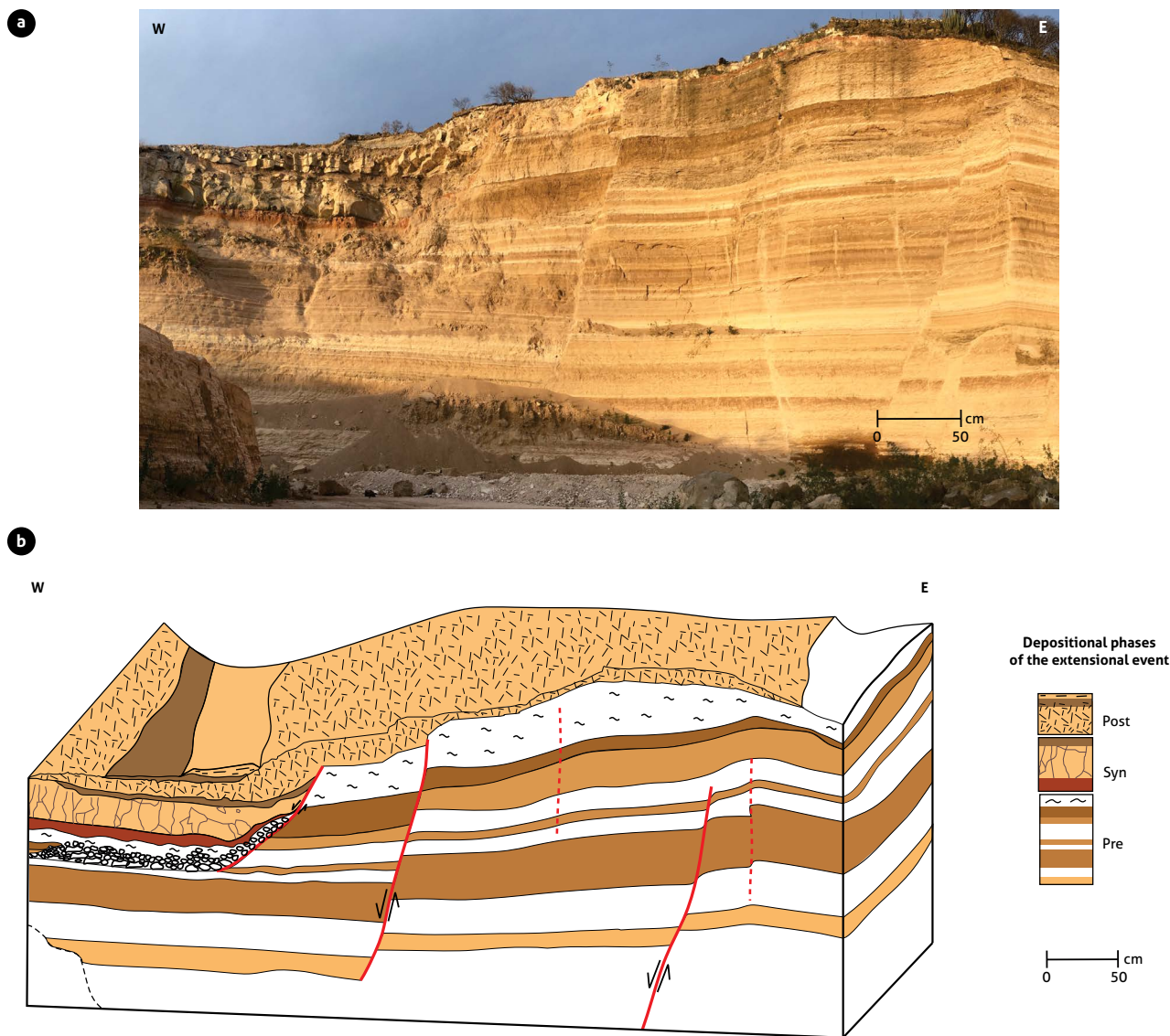


Figure 5. Three-dimensional schematic of an outcrop with evidence of faulting associated with an extensional environment a) Outcrop of volcanic rocks affected by normal faults evidencing an extensional environment; b) Block diagram representing outcrop observations (geological structures and fault shear relationships). For the definition of the temporal evolution of the structure, the depositional phases are established in relation to the extensional event. Photograph taken in Querétaro, Mexico.

Scarps are features in the landscape characterized by steep slopes in the topography (Huggett, 2007). There are two types: fault scarps, which correspond to a linear break in slope that is generated as a result of fault movement, and fault line scarps, which correspond to a new form of relief resulting from erosion of the fault scarp (Twiss and Moors, 2007). Grabens are symmetrical extensional structures, which are bounded by two conjugate, non-rotational master faults (Twiss and Moors, 2007). Their morphological feature is evidenced by two horst, which represent the footwall blocks of the conjugate faults, which limit the hanging wall block, generating a basin where sediments accumulate. The half-graben correspond to asymmetric extensional structures, which are formed by a listric and rotational master fault (Twiss and Moors, 2007).

2.2. Field data acquisition

To study each site or outcrop in the field, it is proposed to apply the following systematic procedure for the acquisition of geological and structural data.

1. Observe the structural arrangement of the outcrop where deformation markers such as faults, folds or fractures are identified. In an extensional environment, normal faults predominate that are dip-slip type, where the hanging wall block has descended with respect to the footwall block, generating a displacement. These structures are characterized by stratigraphic truncation in their vertical section, putting younger rocks in contact with older rocks.
2. Make a three-dimensional schematic of the outcrop where the observed deformation markers are identified (Figure 5). The three-dimensional schematic in Figure 5 illustrates the different rock shear relationships and depositional phases with respect to the extensional deformational event (pre-extension, syn-extension and post-extension).
3. Describe the rock type being observed (Table 1) and establish the possible formation, emplacement and/or depositional environment of outcropping stratigraphic units (Hollocher, 2014; Jerram and Petford, 2011; Stow, 2005).
4. Description of the geological structures of the outcrop. To understand the spatial and temporal distribution of geological structures, it must be established whether those observed in the field correspond to primary or secondary structures (Hatcher, 1995; McClay, 1987; Mitra and Marshak, 1988). Primary structures form simultaneously with rock formation (e.g. stratification, sedimentary structures,

lamination, dykes, melts or lava flows) and secondary structures are generated after lithification (e.g. folds, faults, foliation) (Hatcher, 1995; McClay, 1987; Mitra and Marshak, 1988).

5. Measurement of the geological structures of the outcrop. Geological structures observed at the mesoscopic scale will be measured first, then located in the three-dimensional scheme of the outcrop and written down in the structural data table (table 2). Subsequently, the detailed outcrop structures will always be measured, classifying their shear and temporal relationship between each one, from most to least old.

Table 2 presents the structural data recording scheme for measurements of geological structures or rock fabric elements (López-Isaza et al., 2021). Structural data can be recorded in different ways, according to the different types of notation that exist (azimuthal or quadrant direction, right hand rule or dip line direction), but it is recommended to the reader to adopt only one type of notation for the measurement and its

Table 1. Important aspects for the description of sedimentary, igneous or metamorphic rocks in the field

Type of rock	Description
Sedimentary rocks	Texture, mineralogical composition (%), granulometry, matrix, cementitious, shape and roundness, degree of lithification and classification.
	Thickness and shape of strata, layer recognition, alternation of lithologies, sedimentation rhythm, sequence polarity, fossiliferous content.
Igneous rocks	Identification of primary and secondary structures.
	Color index, degree of weathering, texture, mineralogical composition (%), habit and crystal size.
Metamorphic rocks	Rock classification.
	Identification of primary and secondary structures.
Metamorphic rocks	Color index, structure (foliated or non-foliated), texture, mineralogical composition (%), index minerals, mineral size and classification.
	Identification of secondary structures.

Table 2. Data register scheme for geological structures or fabric elements

Plane		Lineation	
Structural data	Planar type ¹	Structural data	Lineation type
	Planar fabric elements (S)		
Dip → Dip Direction (Dip → Dir) ²	S ₀		Linear fabric elements (L)
	S ₁ – S _n	Plunge → Azimuth Plunge ²	Mineral line
Quadrants	S _{n+1} – S _{n+n}		Hinge line of folds
Right Hand Rule	Axial axis plane	Pitch or Rake and Pitching direction	Crenulation
Strike Azimuth	Veins		Intersection line
	Contacts		
	Joints (J)		

¹ Designation of the type of plan, i.e. S_n- Foliation.

² Notation taken from McClay (1987). Source: modified from López-Isaza et al. (2021).

respective recording. In addition, different nomenclatures are indicated in the table, corresponding to: L for lineations, S for planar surfaces, and the subscripts that accompany this ($S_0, S_1 - S_n, S_{n+1} - S_{n+n}$), which indicate the relative chronology of each structure - for a deeper understanding of the types of linear and planar structures the reader is suggested to review McClay (1987), Twiss and Moors (2007) and López-Isaza et al. (2021).

The recognition and description of a normal fault in an outcrop starts with the identification of structural discontinuities, lithological discontinuities and deformation zones that have associated fault rocks, either breccias, cataclasites, or mylonites, among others (Forero-Ortega et al., 2021). Then, the kinematics of the fault is established (Figure 6), with the help of stratigraphic markers, riedel structures or kinematic indicators (Doblas, 1998; Doblas et al., 1997; Petit, 1987; Sugden, 1987). When the kinematics of the fault have been determined, the structures will be measured in a systematic way (table

3), starting from one end of the deformed zone. In addition to this, it will be of great importance to establish the main plane of the structure (Y), in order to define the orientation of the fault trace on the geological map.

2.3. Structural analysis with stereographic network

The careful analysis of the structural data of faults will be one of the key tools to understand and reconstruct the deformation history observed in the field, for which it is necessary to perform a kinematic analysis (Marrett and Allmendinger, 1990) and, later, a dynamic analysis (Angelier, 1984; Angelier, 1990; Simpson, 1997). The kinematic analysis is based on the geometric analysis of the structures, where the orientation of the main axes of shortening and elongation is determined (Figure 7a). For this analysis, the orientation and inclination of the fault plane, the pole of the fault plane, the direction and inclination of the slickenline and the sense slip must be plotted in

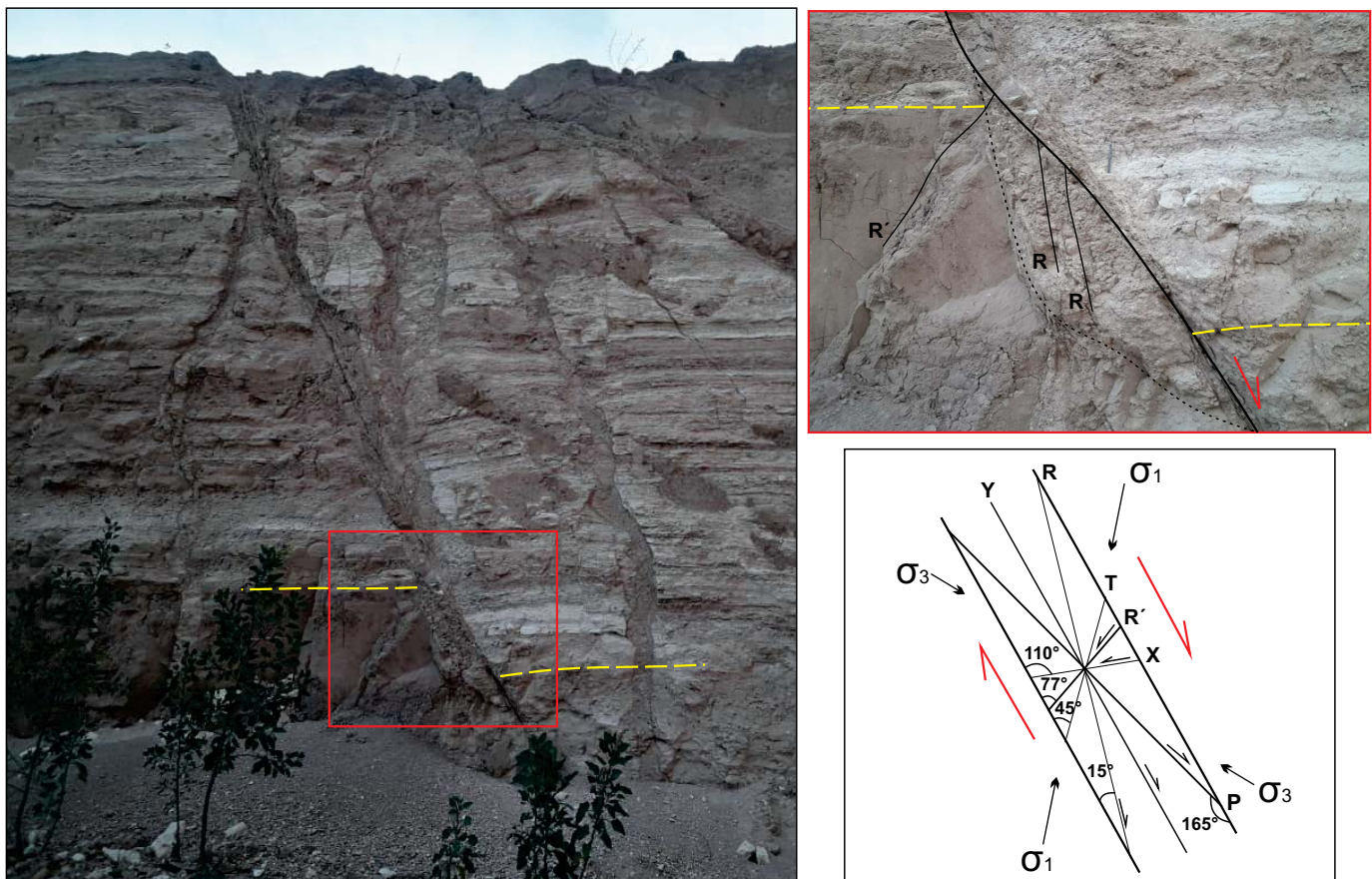


Figure 6. Outcrop of volcanic rocks affected by normal faulting. The red box is a zoom of the fault core where it is determined by stratigraphic markers (yellow lines), riedel structures (R and R') and kinematic indicators, that the kinematics of fault is normal. Photograph taken in Querétaro, Mexico.

the stereographic projection grid –for the projection of planes and lines in the stereographic network, the reader is suggested to review Ramsay and Huber (1983) and López-Isaza et al. (2021)–. The orientation of the main axes of elongation and shortening are found in the plane of motion, which contains the slip vector (slickenline) and the vector normal to the fault plane (pole), and forms 45° angles with each of the vectors (Figure 7a) (Marrett and Allmendinger, 1990).

In the dynamic analysis, the orientation of the principal stresses σ_1 , σ_2 and σ_3 is obtained, which would be adjusted to the deformation of the faults observed in the outcrop. Anderson (1951) proposed for conjugate and two-dimensional faults that: the orientation of the maximum principal stress axis (σ_1) is determined by the vector bisecting the acute angle between the two conjugate faults, the orientation of the intermediate prin-

cipal stress axis (σ_2) is the intersection of the two fault planes and the orientation of the minimum principal stress axis (σ_3) corresponds to the vector bisecting the obtuse angle between two conjugate faults (Figure 7b). In the case of normal faults, the principal orientation of the shortening axis is vertical and corresponds to the orientation of the maximum principal stress axis (σ_1), and the orientation of the elongation axis corresponds to the orientation of the minimum principal stress axis (σ_3).

3. CONCLUSIONS

The recognition of any geological environment in the field is based on image interpretation, direct observation of the outcrop, establishment of the rock-forming environment, and careful and systematic recording of the structural data revealed

Table 3. Data register scheme for geological faults measured in the field

Plane (fault)	Line (slickenline)	Block	Planar type	Kinematics	Certainty	Remarks
Direction and inclination	Direction and inclination	Footwall Block (BF)	Plane or fault	Right lateral (RL)	Low (kinematic: supposed)	Kinematic indicators
			Shear type Riedel (R, R', P, T, X)	Left lateral (LL)		
		Hanging wall block (BH)	Main plane (Y)	Normal (N)	Medium (kinematic: possible or probable)	
				Thrust (T)	High (kinematic: true)	
				Oblique (O)		

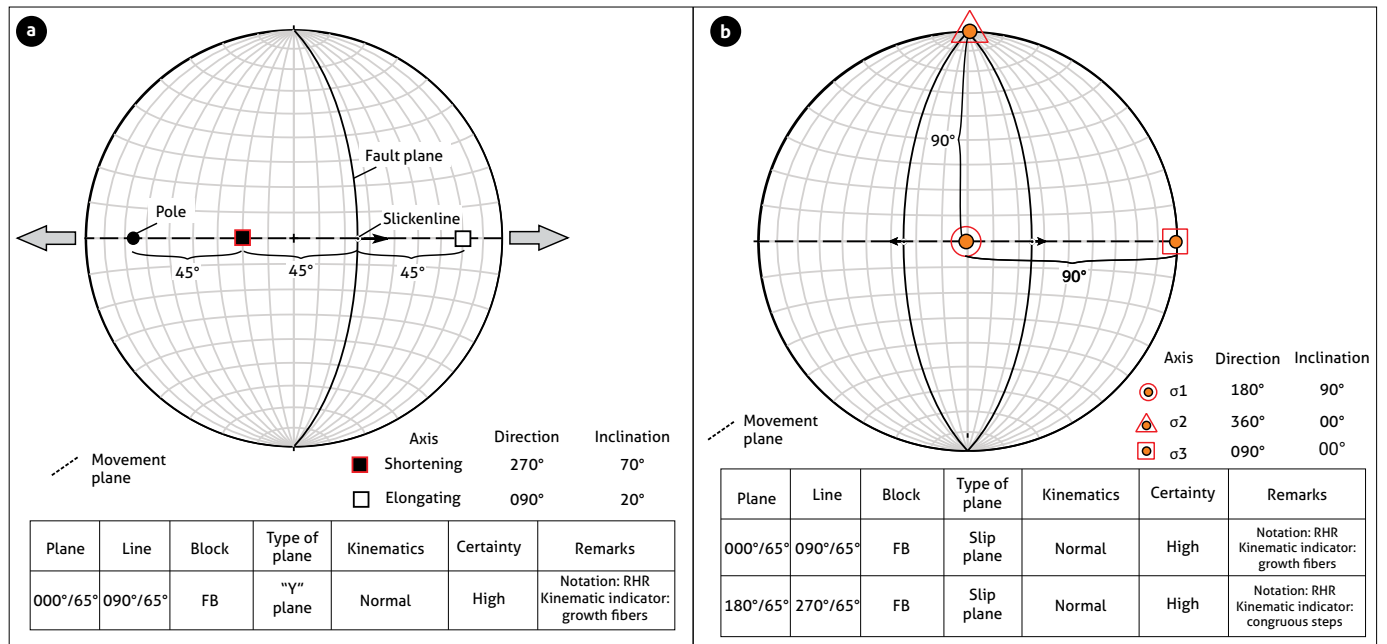


Figure 7. Structural analysis with stereographic network

a) Kinematic analysis of a fault, where the principal orientations of the shortening and elongation axes are determined. The gray arrows indicate the main elongation direction; b) Dynamic analysis for two conjugate faults, where the orientation of the principal stresses is defined. The data were plotted on the Schmidt stereographic projection grid, lower hemisphere. BF: footwall block, RHR: right hand rule.

by each outcrop. The determination of a regional-scale extensional environment associated with a given geological process (intracontinental rift systems, mid-oceanic ridge systems, basins, passive continental margins, etc.) requires bringing together all the geological evidence (morphological features associated with normal faulting, stratigraphic relationships, structural style and unconformities) collected in different outcrops, which implies the understanding of the spatial and temporal distribution of geological units and the hierarchization of deformation structures present in the study area. In addition, the integration of different tools from other branches of geology, such as geochronology, geochemistry and geophysics, is necessary. The results obtained with each tool should be consistent with the stratigraphic and structural relationships observed in the field.

ACKNOWLEDGEMENTS

This contribution was made in the framework of the *Tectonic Model of Colombia Project* of the Tectonics Group of the Dirección de Geociencias Básicas of the Servicio Geológico Colombiano. The authors wish to express their gratitude to the geological engineer Ricardo Milián de la Cruz for the field appreciations and technical contributions that improved the present article, as well as to the reviewers of this contribution. Finally, the authors thank the anonymous reviewers for their comments that improved the original manuscript.

REFERENCES

- Allmendinger, R.W. (2017). *Modern Structural Practice. A structural geology laboratory manual for the 21st Century*. V.1.7.0. <http://www.geo.cornell.edu/geology/faculty/RWA/structure-lab-manual/>
- Anderson, E. M. (1951). *The dynamics of faulting and dike formation with application to Britain*. Oliver and Boyd.
- Angelier, J. (1984). Tectonic analysis of fault slip data sets. *Journal of Geophysical Research: Solid Earth*, 89(B7), 5835-5848. <https://doi.org/10.1029/JB089iB07p05835>
- Angelier, J. (1990). Inversion of field data in fault tectonics to obtain the regional stress-III. A new rapid direct inversion method by analytical means. *Geophysical Journal International*, 103(2), 363-373. <https://doi.org/10.1111/j.1365-246X.1990.tb01777.x>
- Axen, G. (1988). The geometry of planar domino-style normal faults above a dipping basal detachment. *Journal of Structural Geology*, 10(4), 405-411. [https://doi.org/10.1016/0191-8141\(88\)90018-1](https://doi.org/10.1016/0191-8141(88)90018-1)
- Batiza, R. (1996). Magmatic segmentation of mid-ocean ridges: a review. In C. J. MacLeod, P. A. Tyler, & C. L. Walker (eds.), *Tectonic, Magmatic, Hydrothermal and Biological Segmentation of Mid-Ocean Ridges* (pp. 103-130). Special Publications 118. Geological Society.
- Bull, W. B. (2008). *Tectonic geomorphology of mountains: a new approach to paleoseismology*. John Wiley & Sons.
- Burbank, D. W., & Anderson, R. S. (2011). *Tectonic geomorphology*. John Wiley & Sons.
- Corti, G. (2009). Continental rift evolution: from rift initiation to incipient break-up in the Main Ethiopian Rift, East Africa. *Earth-Science Reviews*, 96(1-2), 1-53. <https://doi.org/10.1016/j.earscirev.2009.06.005>
- Cowie, P. A. (1998). A healing-reloading feedback control on the growth rate of seismogenic faults. *Journal of Structural Geology*, 20(8), 1075-1087. [https://doi.org/10.1016/S0191-8141\(98\)00034-0](https://doi.org/10.1016/S0191-8141(98)00034-0)
- Cowie, P. A., Gupta, S., & Dawers, N. H. (2000). Implications of fault array evolution for synrift depocentre development: insights from a numerical fault growth model. *Basin Research*, 12(3-4), 241-261. <https://doi.org/10.1111/j.1365-2117.2000.00126.x>
- Dickinson, W. R. (2002). The Basin and Range Province as a composite extensional domain. *International Geology Review*, 44(1), 1-38. <https://doi.org/10.2747/0020-6814.44.1.1>
- Doblas, M. (1998). Slickenside kinematic indicators. *Tectonophysics*, 295(1-2), 187-197. [https://doi.org/10.1016/S0040-1951\(98\)00120-6](https://doi.org/10.1016/S0040-1951(98)00120-6)
- Doblas, M., Mahecha, V., Hoyos, M., & López-Ruiz, J. (1997). Slickenside and fault surface kinematic indicators on active normal faults of the Alpine Betic cordilleras, Granada, southern Spain. *Journal of Structural Geology*, 19(2), 159-170. [https://doi.org/10.1016/S0191-8141\(96\)00086-7](https://doi.org/10.1016/S0191-8141(96)00086-7)
- Faulds, J. E., & Varga, R. J. (1998). The role of accommodation zones and transfer zones in the regional segmentation of extended terranes. *Geological Society of America, Special Papers*, 323, 1-45. <https://doi.org/10.1130/SPE323>
- Forero-Ortega, A. J., López-Isaza, J. A., López Herrera, N. R., Cuéllar-Cárdenas, M. A., Cetina Tarazona, L. M., & Aguirre Hoyos, L. M. (2021). Geological-structural mapping and geochronology of shear zones: A methodologi-

- cal proposal. *Boletín Geológico*, 48(1), 81-122. <https://doi.org/10.32685/0120-1425/bol.geol.48.1.2021.524>
- Fossen, H. (2010). *Structural geology*. Cambridge University Press.
- Fossen, H., & Cavalcante, G. C. G. (2017). Shear zones - A review. *Earth-Science Reviews*, 171, 434-455. <https://doi.org/10.1016/j.earscirev.2017.05.002>
- Frisch, W., Meschede, M., & Blakey, R. (2011). *Plate Tectonics: Continental drift and mountain building*. Springer.
- Groshong Jr, R. H. (1999). *3D structural geology: a practical guide to surface and subsurface map interpretation*. Springer.
- Gupta, A., & Scholz, C. H. (2000). A model of normal fault interaction based on observations and theory. *Journal of Structural Geology*, 22, 865-879. [https://doi.org/10.1016/S0191-8141\(00\)00011-0](https://doi.org/10.1016/S0191-8141(00)00011-0)
- Hatcher Jr. R. D. (1995). *Structural geology. Principle, concepts and problems*. Prentice Hall.
- Hollocher, K. (2014). *A pictorial guide to metamorphic rocks in the field*. CRC Press.
- Huggett, R. (2007). *Fundamentals of geomorphology*. Routledge.
- Hus, R., Acocella, V., Funicello, R., & De Batist, M. (2005). Sandbox models of relay ramp structure and evolution. *Journal of Structural Geology*, 27(3), 459-473. <https://doi.org/10.1016/j.jsg.2004.09.004>
- Jerram, D., & Petford, N. (2011). *The field description of igneous rocks*. John Wiley & Sons.
- Jiang, D., & White, J. C. (1995). Kinematic of rock flow and the interpretation of geological structures, with particular reference to shear zones. *Journal of Structural Geology*, 17(9), 1249-1265. [https://doi.org/10.1016/0191-8141\(95\)00026-A](https://doi.org/10.1016/0191-8141(95)00026-A)
- Lisle, R. J., & Walker, R. J. (2013). The estimation of fault slip from map data: The separation-pitch diagram. *Tectonophysics*, 583, 158-163. <https://doi.org/10.1016/j.tecto.2012.10.034>
- López Isaza, J. A., Cuéllar Cárdenas, M. A., Cetina Tarazona, L. M., Forero Ortega, A. J., Suárez Arias, A. M., Muñoz Rodríguez, O. F., Aguirre Hoyos, L. M., & Gutiérrez López, M. J. (2021). Graphical representation of structural data in the field: A methodological proposal for its application in deformed areas. *Boletín Geológico*, 48(1), 123-139. <https://doi.org/10.32685/0120-1425/bol.geol.48.1.2021.504>
- Marrett, R., & Allmendinger, R. W. (1990). Kinematic analysis of fault-slip data. *Journal of Structural Geology*, 12(8), 973-986. [https://doi.org/10.1016/0191-8141\(90\)90093-E](https://doi.org/10.1016/0191-8141(90)90093-E)
- McCalpin, J. P. (2009). *Paleoseismology*. Academic Press.
- McClay, K. R. (1987). *The mapping of geological structures*. John Wiley & Sons.
- Means, W. D. (1976). *Stress and Strain. Basic concepts of continuum mechanics for geologists*. Springer-Verlag.
- Mitra, G., & Marshak, S. (1988). *Basic methods of structural geology*. Prentice Hall.
- Moores, E., & Twiss, R. (2000). *Tectonics*. W. H. Freeman and Company.
- Muraoka, H., & Kamata, H. (1983). Displacement distribution along minor fault traces. *Journal of Structural Geology*, 5(5), 483-495. [https://doi.org/10.1016/0191-8141\(83\)90054-8](https://doi.org/10.1016/0191-8141(83)90054-8)
- Peacock, D. C., Knipe, R. J., & Sanderson, D. J. (2000). Glossary of normal faults. *Journal of Structural Geology*, 22(3), 291-305. [https://doi.org/10.1016/S0191-8141\(00\)80102-9](https://doi.org/10.1016/S0191-8141(00)80102-9)
- Peacock, D. C. P., & Sanderson, D. J. (1991). Displacements, segment linkage and relay ramps in normal fault zones. *Journal of Structural Geology*, 13(6), 721-733. [https://doi.org/10.1016/0191-8141\(91\)90054-M](https://doi.org/10.1016/0191-8141(91)90054-M)
- Petit, J. P. (1987). Criteria for the sense of movement on fault surfaces in brittle rocks. *Journal of Structural Geology*, 9(5-6), 597-608. [https://doi.org/10.1016/0191-8141\(87\)90145-3](https://doi.org/10.1016/0191-8141(87)90145-3)
- Pollard, D., & Fletcher, R. C. (2005). *Fundamentals of structural geology*. Cambridge University Press.
- Ragan, D. M. (2009). *Structural geology. An introduction to geometrical techniques*. Cambridge University Press.
- Ramsay, J. G., & Huber M. I. (1983). *The techniques of modern structural geology. Volume 1: Strain Analysis*. Academic Press.
- Ramsay, J. G., & Huber M. I. (1986). *The techniques of modern structural geology. Volume 2: Folds and Fractures*. Academic Press.
- Ramsay, J. G., & Lisle, R. J. (2000). *The techniques of modern structural geology. Volume 3: Applications of continuum mechanics in structural geology*. Academic Press.
- Sibson, R. H. (1977). Fault rocks and fault mechanisms. *Journal of the Geological Society*, 133, 191-213.
- Sibson, R. H. (1980). Transient discontinuities in ductile shear zones. *Journal of Structural Geology*, 2(1-2), 165-171.
- Simpson, R. W. (1997). Quantifying Anderson's fault types. *Journal of Geophysical Research: Solid Earth*, 102(B8), 17909-17919.
- Stewart, S. A. (2001). Displacement distributions on extensional faults: Implications for fault stretch, linkage, and seal. *AAPG Bulletin*, 85(4), 587-599. <https://doi.org/10.1306/8626C951-173B-11D7-8645000102C1865D>

- Stewart, S. A., & Argent, J. D. (2000). Relationship between polarity between extensional fault arrays and presence of detachments. *Journal of Structural Geology*, 22(6), 693-711. [https://doi.org/10.1016/S0191-8141\(00\)00004-3](https://doi.org/10.1016/S0191-8141(00)00004-3)
- Stow, D. A. (2005). *Sedimentary Rocks in the Field: A color guide*. Gulf Professional Publishing.
- Sugden, T. (1987). Kinematic indicators: structures that record the sense of movement in mountain chains. *Geology Today*, 3(3-4), 93-99. <https://doi.org/10.1111/j.1365-2451.1987.tb00496.x>
- Tanner, D., & Brandes, C. (2020). *Understanding Faults: Detecting, Dating, and Modeling*. Elsevier. <https://doi.org/10.1016/C2017-0-03320-7>
- Twiss, R. J., & Moores, E. M. (2007). *Structural geology*. W. H. Freeman and Company.
- Van der Pluijm, B. A., & Marshak, S. (2004). *Earth Structure. An introduction to structural geology and Tectonics*. W. W. Norton & Company.
- Walsh, J. J., Nicol, A., & Childs, C. (2002). An alternative model for the growth of faults. *Journal of Structural Geology*, 24(11), 1669-1675. [https://doi.org/10.1016/S0191-8141\(01\)00165-1](https://doi.org/10.1016/S0191-8141(01)00165-1)
- Xu, S., Nieto-Samaniego, A. F., & Alaniz-Álvarez, S. A. (2004). Tilting mechanism in domino faults of the Sierra de San Miguelito, Central Mexico. *Geologica Acta*, 3, 189-201. <https://doi.org/10.1344/105.000001426>
- Xu, S., Nieto-Samaniego, A. F., & Alaniz-Álvarez, S. A. (2009). Quantification of true displacement using apparent displacement along an arbitrary line on a fault plane. *Tectonophysics*, 467(1-4), 107-118. <https://doi.org/10.1016/j.tecto.2008.12.004>
- Xu, S. S., Nieto-Samaniego, A. F., & Alaniz-Álvarez, S. A. (2014). Estimation of average to maximum displacement ratio by using fault displacement-distance profiles. *Tectonophysics*, 636, 190-200. <https://doi.org/10.1016/j.tecto.2014.08.023>
- Yamada E., & Sakaguchi, K. (1994). Fault-slip calculation from separations. *Journal of Structural Geology*, 17(7), 1065-1070. [https://doi.org/10.1016/0191-8141\(95\)00003-V](https://doi.org/10.1016/0191-8141(95)00003-V)
- Yoon, S. H., Sohn, Y. K., & Chough, S. K. (2014). Tectonic, sedimentary, and volcanic evolution of a back-arc basin in the East Sea (Sea of Japan). *Marine Geology*, 352, 70-88. <https://doi.org/10.1016/j.margeo.2014.03.004>



This work is distributed under the
Creative Commons Attribution 4.0 License.

Received: May 25, 2021

Revision received: August 9, 2021

Accepted: September 12, 2021

Published on line: November 5, 2021

Yuruma Formation (Barremian - lower Aptian?) In the Yuruma hill and Punta Espada, Alta Guajira, Uribia, Colombia

Formación Yuruma (Barremiano – Aptiano inferior?) en el cerro
Yuruma y Punta Espada, Alta Guajira, Uribia, Colombia

Pedro Patarroyo¹

¹ Departamento de Geociencias, Universidad Nacional de Colombia, Bogotá, Colombia.

Corresponding author: pcpatarroyog@unal.edu.co

ABSTRACT

The Yuruma Formation in the Yuruma hill area its type locality can be differentiated into two stratigraphic intervals. The lower and upper intervals of the Yuruma Formation can also be subdivided into two segments. The lithological, sedimentological and fossiliferous characteristics support this differentiation, which allows to interpret the accumulation energy influences over the sea floor. The lower interval is characterized by intercalations of very fossiliferous marlstones and biomicrites with benthonic and nektonic fossils from the lower Barremian. The upper interval is represented by marlstones and biomicrites with poor benthonic and nektonic fossils from the upper Barremian and probably from the lower Aptian. In the Punta Espada area, whit scarce lithological controls over the lower and upper parts of the Yuruma Formation, were found biomicrites with benthonic and nektonic fossils of the lower Barremian to the lower part, and to the top were recognized biomicrites that underlie beds with lower Aptian ammonites.

Keywords: Yuruma Formation, lower cretaceous, type locality, La Guajira, Colombia.

RESUMEN

La sucesión de los depósitos de la Formación Yuruma, con base en la sección del cerro Yuruma, su localidad tipo, se puede diferenciar en dos intervalos estratigráficos, el inferior y el superior, que a su vez pueden subdividirse en dos segmentos cada uno. Las características litológicas, sedimentológicas y fosilíferas sustentan esta diferenciación, permitiendo interpretaciones de la energía de acumulación sobre el fondo del depósito. El intervalo inferior está caracterizado por presentar intercalaciones de lodolitas calcáreas muy fosilíferas y biomicritas con fósiles bentónicos y nectónicos del Barremiano inferior. El intervalo superior se caracteriza por presentar lodolitas calcáreas y biomicritas con poca fauna bentónica y nectónica del Barremiano superior y posiblemente de

parte del Aptiano inferior. Para el sector de Punta Espada, a partir de reconocimientos puntuales de la parte inferior y superior de la Formación Yuruma, se identificaron respectivamente biomicritas con fósiles bentónicos y nectónicos del Barremiano inferior y biomicritas del techo de la unidad a pocos metros del registro de amonitas del Aptiano inferior.

Palabras clave: Formación Yuruma, Cretáceo inferior, localidad tipo, La Guajira, Colombia.

1. INTRODUCTION

Knowledge of the Cretaceous lithostratigraphic units of the Alta Guajira, Colombia (Figure 1) continues to be scarce, and the few publications related to the Cretaceous stratigraphy and paleontology of the La Guajira Peninsula are not very detailed. Renz (1956, 1960), Bürgl (1960) and Rollins (1960, 1965) introduced valuable stratigraphic data but did not illustrate the fossils reported. Zuluaga et al. (2009) synthesized the existing Cretaceous stratigraphy into geological maps. Salazar (2010) investigated the Palanz Formation, which involves continental and transitional deposits. Patarroyo (2020) and Patarroyo and Götz (2020)

described the Barremian and Aptian deposits and fossils. Based on ammonites, other mollusks and echinoderms, Renz (1956, 1960), Bürgl (1960), Rollins (1960, 1965), Patarroyo (2020) and Patarroyo and Götz (2020) recognized the existence of calcareous deposits of the Lower Cretaceous in the Alta Guajira.

The sedimentary succession and fossil association of the Yuruma Formation (Alta Guajira) allow a separation in intervals and stratigraphic ranges, which clearly involve the Barremian and probably the lower part of the lower Aptian, providing evidence of the sedimentological and environmental differences related to the contemporary deposits of the Cretaceous basin in central Colombia.

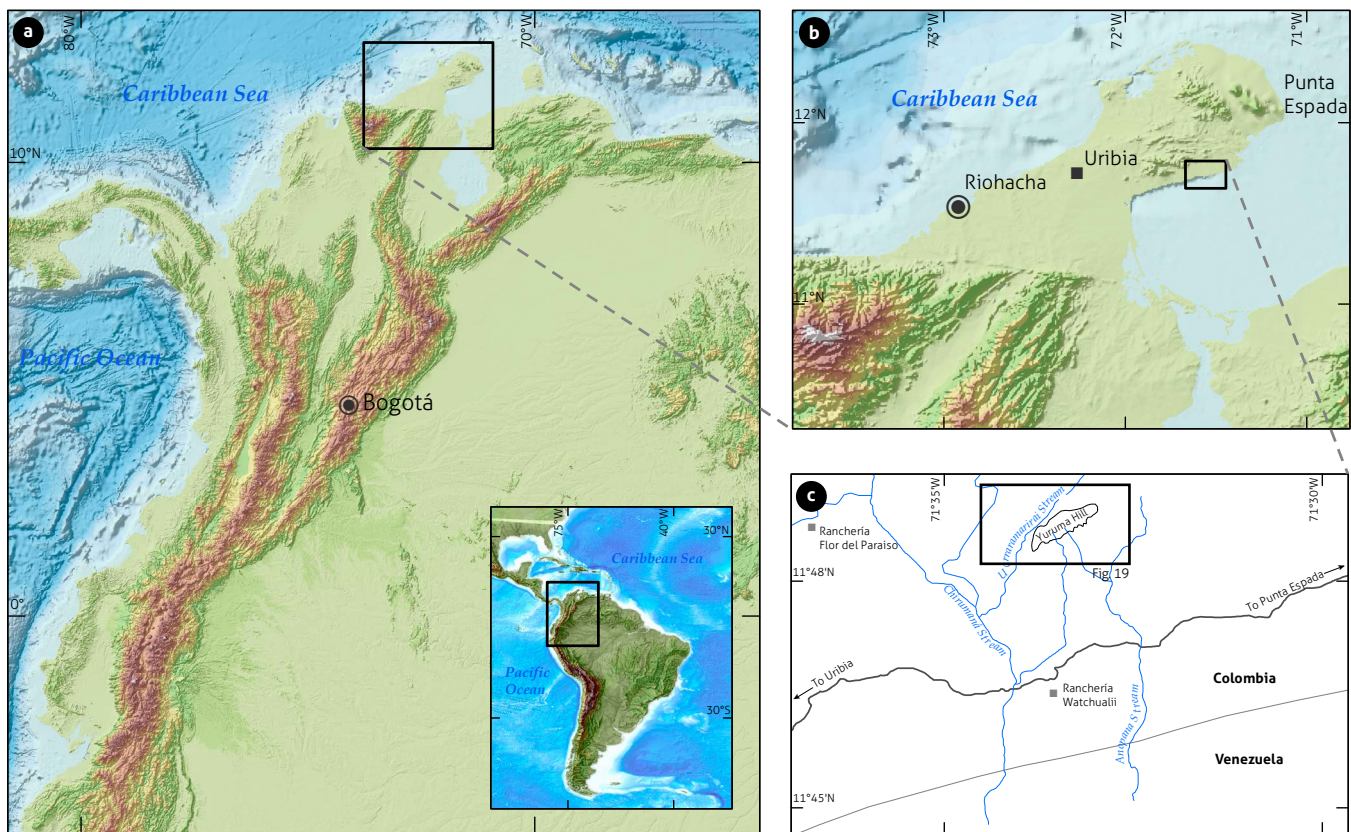


Figure 1. Location of the study area

a) location of La Guajira in northern Colombia; b) department of La Guajira, with the locations of Riohacha, Uribia and Punta Espada; c) Yuruma hill sector, near to ranchería Watchualí (IGAC, Instituto Geográfico Agustín Codazzi), 10Bis-I-A topographic map.

Thus, the present contribution seeks to provide data on the lithostratigraphy, nomenclature and biostratigraphy of the Yuruma Formation in its type locality, as well as nearby outcrops located to the north in Punta Espada (Uribia, La Guajira-Colombia).

1.1. Location

Yuruma hill is located at 8.5 km N of ranchería Wuatchuali (in the Wayuunaiki language) or Wuatchuari (Spanish), approximately 90 km from the urban center of Uribia, in the La Guajira Peninsula (Figure 1) and very close to the border with Venezuela; to the NE of this sector, Punta Espada is located approximately 70 km away.

2. METHOD

The initial input focused on a bibliographic analysis, which allowed the locations of the areas of interest to be recognized, including the Cretaceous sedimentary succession and the Yuruma Formation deposits in the Alta Guajira.

Since mid-2009, based on personal research carried out in the Punta Espada area, the Cretaceous deposits and marine fossils of the Alta Guajira (Patarroyo, 2011, 2020; Patarroyo and Götz, 2013, 2014, 2020) have been recognized from field

trips by the Department of Geosciences at the Universidad Nacional de Colombia in Bogotá. Later, between the end of February and the beginning of March 2018, under the auspices of the Servicio Geológico Colombiano, the Yuruma hill (Figure 2) was surveyed to advance the work related to the book of *The Geology of Colombia* (Patarroyo, 2020). During this last visit, since the base (northwestern side) until the upper part of the Yuruma hill (side southeast), the sedimentary succession was measured using a Jacob's staff; additionally, rock samples and macrofossils were collected, and the thickness and geometry of the beds were determined following Campbell (1967), moreover comparatively was obtained the color of the rocks with a reference table. To achieve continuous recognition of the succession, bed levels were followed laterally, therefore controls were performed at different sites of the hill, from which four partial columns were obtained.

The rock samples allowed a conventional macroscopic description of the different types of lithologies. The macrofossils were collected directly in the field, prepared or cleaned with conventional techniques using hammers, chisels, needles and pneumatic hammers. These fossils were coated with ammonium chloride, photographed and then digitally processed. The fossil taxonomy is mainly based on Jaworski (1938), Etayo-Serna (1985), Guzmán (1985) and Patarroyo (2020).

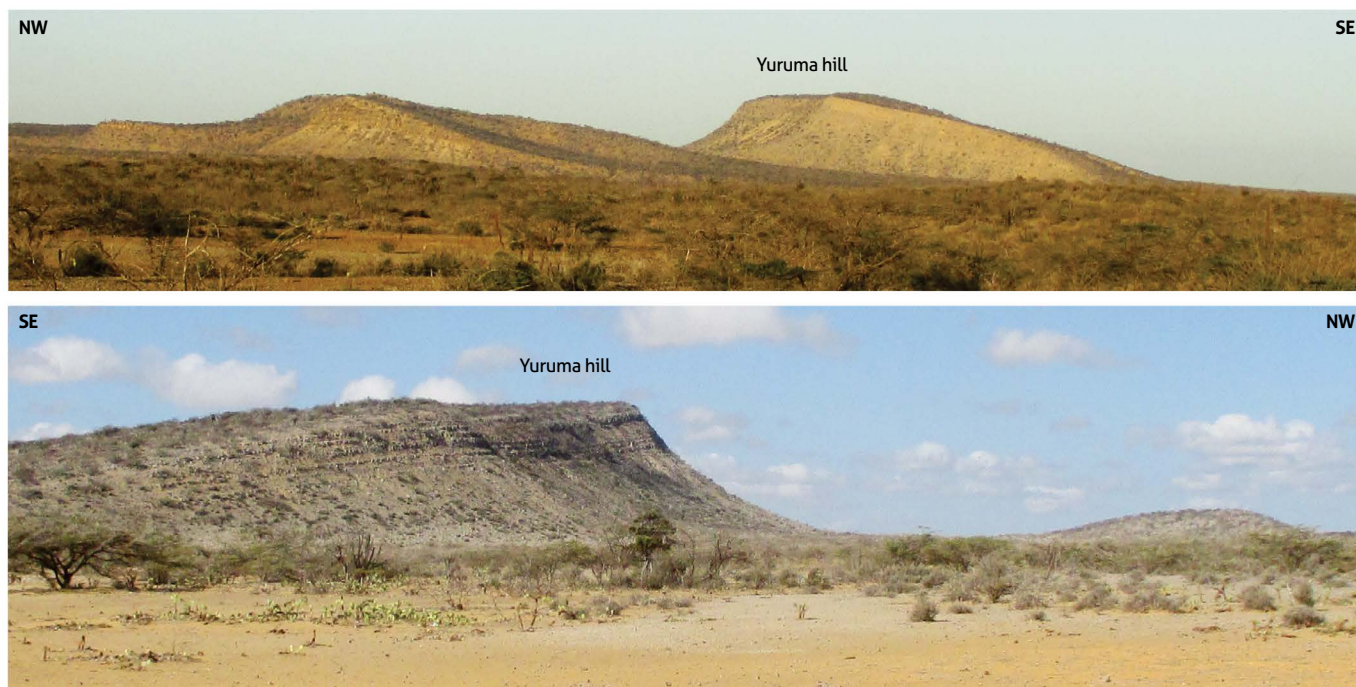


Figure 2. Panoramas of the Yuruma hill north of ranchería Wuatchuali from two locations to the SW and NE

In Punta Espada area, with the help of the collected fauna, were identified lower Barremian deposits of the Yuruma Formation (Patarroyo, 2011, 2020) and higher stratigraphically probably lowest Aptian deposits of the Yuruma Formation because they underlay beds with lower Aptian ammonites (Patarroyo and Götz, 2020).

3. GEOLOGICAL FRAMEWORK

The geology in the continental northern area of Colombia is very particular because the Caribbean plate has exerted a great tectonic influence on the geological blocks in this area, so regionally, the Oca, Cuisa (or Cuiza) and Huimatirra faults are recognized (cf. Álvarez, 1967; Colmenares et al., 2019; Gómez, 2001; Irving, 1971; MacDonald, 1964, 1965; Patarroyo and Götz, 2020; Renz, 1960; Rollins 1960, 1965), which constitute the main lineaments of the allochthon blocks of the Media and Alta Guajira. The Oca and Cuisa faults (Figure 3) are considered dextral strike-slip faults, so they have continuity toward Venezuela. To the south and north of the Cuisa Fault, it is possible to find Cretaceous deposits, whose rock bodies are recog-

nized under the same names. The Cretaceous deposits of the Alta Guajira are included in the Palanz, Moina, Yuruma, “Cogollo”, “Maraca”, “La Luna”, Guaralamai and Parauinkrein (Parabanden) formations, following Renz (1960), Bürgl (1960), Rollins (1960, 1965), Zuluaga et al. (2008 a and b, 2009), Salazar (2010), Patarroyo (2011, 2020) and Patarroyo and Götz (2013, 2014, 2020).

3.1. Nomenclature of the Yuruma Formation

The Yuruma Formation is one of the lithostratigraphic units that includes marine deposits of the Lower Cretaceous of the Alta Guajira. Rollins (1960, 1965) and Julivert et al. (1968) indicate that the denomination Yuruma was first used by geologists at the Richmond Exploration Company in approximately 1947.

Related with Yuluma (in the Wayuunaiki language) or Yuruma (Spanish) hill, the lithostratigraphic denomination arises under the term Yuruma Formation, formalized by Renz (1956) to refer to a Hauterivian - Barremian succession, which differentiated into “lower Yuruma” and “upper Yuruma”. Later, Renz (1960) restricted the term Yuruma Formation to the

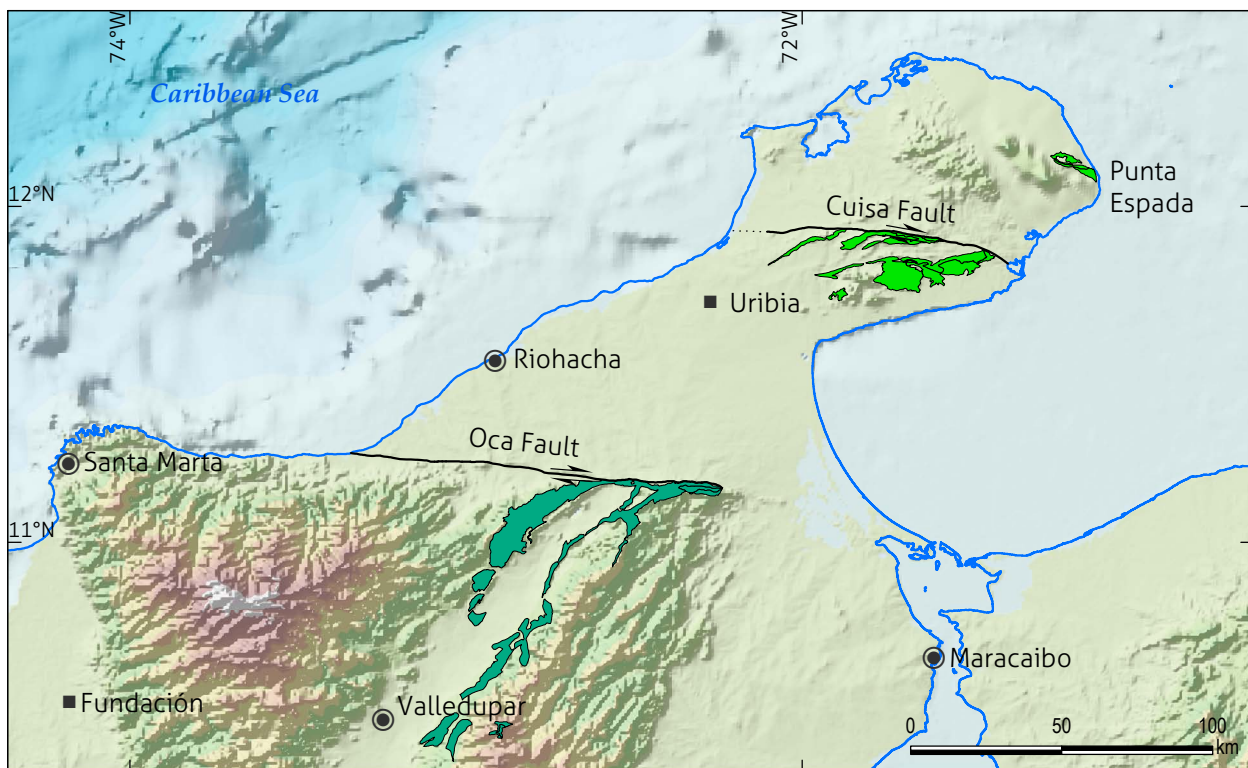


Figure 3. Location of the La Guajira province, showing the outcrop distribution of the Cretaceous deposits to the south and north of the Oca and Cuisa faults. General location in Figure 1b.

Table 1. Comparative diagram of the lithostratigraphic units of the Lower Cretaceous and their stratigraphic range and limits

Valanginian - Barremian (?)	Cenomanian		Aptian		Patarroyo and Götzt (2020) and this work
	Renz (1956)	Renz (1960)	Rollins (1960, 1965)		
upper Yuruma F.	Yuruma F.	Yuruma F.	"Cogollo" Group	"Maraca" F.	?
				lower "Cogollo" F.	?
				upper Yuruma F.	Yuruma F.
lower Yuruma F.	Moina F.	Moina F.	Yuruma Group	Moina F.	Moina F.
Río Negro F.	Palanz F.	Palanz F.		Palanz F.	

Source: Based on Renz (1956, 1960), Rollins (1960, 1965), and Patarroyo and Götzt (2020).

“upper Yuruma” succession with Barremian fossils, so he designated the “lower Yuruma” as the Moina Formation.

According to the proposal of Renz (1960), the Yuruma Formation underlies the Moina Formation of the Valanginian - Hauterivian (in the sense of Rollins, 1960, 1965) or the “lower Yuruma” of Renz (1956), which underlies the “Cogollo” Formation. Notably, Rollins (1960, 1965) modified the top boundary of the Yuruma Formation, placing it higher stratigraphically (Table 1), therefore the succession becomes thicker than that considered by Renz (1960). It means that according to Renz (1956, 1960), part of the lower interval of the Cogollo

Formation became the highest segment of the Yuruma Formation (Rollins 1960, section BB’ and plate 4 of the geological map of the La Guajira Peninsula; 1965) proposal followed in this study.

Related with the type locality, Rollins (1960, 1965) indicated a thickness of 269 m for the upper Yuruma, which should be understood as the succession of the Yuruma Formation. Although there are other known outcrops of the Yuruma Formation in the Alta Guajira, which, according to the literature, show some thickness and lithological variations, in the Yuruma hill (Figure 2), there is a very good exposure. Some outcrops near Punta Espada, NE of the type locality, are recognized by Barremian fossil fauna; thus, they are associated with this lithostratigraphic unit, as also was recognized by Renz (1960), Bürgl (1960), Rollins (1960, 1965), Patarroyo (2011, 2020) and Patarroyo and Götzt (2013, 2014, 2020).

4. RESULTS

The literature analysis, moreover the fieldwork in the Yuruma hill and in the Punta Espada area, were the fundamental inputs to obtaining the results of this contribution.

4.1 Lithostratigraphy

At the base of the Yuruma hill, along the Uarraramarirai or Uarramaralijai Stream (Figures 1c and 4), the sharp contact between the bioclastic levels with ostreids to the top of the Moina Formation and the marlstones at the base of the Yuruma Formation is observed. There structural orientation of the beds toward the lithostratigraphic boundary is N70° E/11° SE.



Figure 4. Surface of the sharp contact between the top bed of the Moina Formation and the base of the Yuruma Formation, Uarraramarirai Stream Lower Yuruma hill section

A large part of the succession described here, since the base (Uarraramarirai or Uarramaralijai stream) until the upper part of Yuruma hill, has a thickness of approximately 190 m (Figures 2 and 5), measured directly with a Jacobs staff and with glo-

bal positioning system (GPS) control. Based on fieldwork and lithological characteristics, the succession can be divided into two stratigraphic intervals (Figure 5), coinciding with observations proposed by Rollins (1960, 1965). The lower interval,

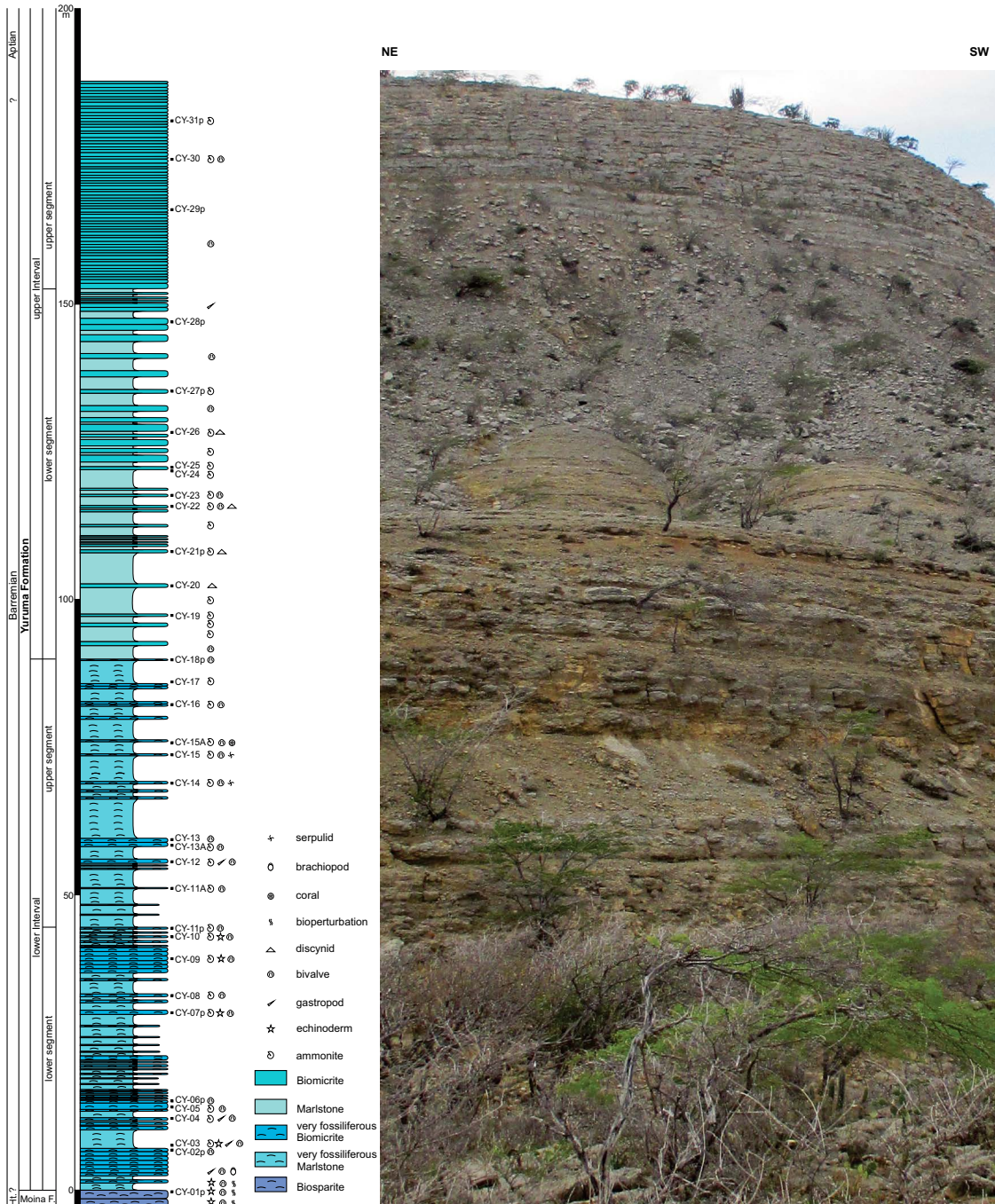


Figure 5. Stratigraphic section of the sedimentary succession of the Yuruma Formation in the Yuruma hill area and panoramic view of the succession since the Uarraramarirai Stream until the upper part of the hill (Uribia, La Guajira) Includes the top of the Moina Formation and a large part of the Yuruma Formation.

90 m, shows intercalations of very fossiliferous to fossiliferous biomicrites and very fossiliferous marlstones with mollusks, echinoids, articulated brachiopods, serpulids and colonial corals, with thin to very thick beds and irregular to regular geometries. To the upper interval was possible to described only 100 m (Figure 5), without reaching the top of the unit, represented by intercalations of poor fossiliferous biomicrites and marlstones. The fossil content of this interval varies markedly compared with its underlying beds because the fossil amount decreases. In addition, benthic organisms are scarce and the few that exist have thin shells (bivalves and disarticulated brachiopods). Likewise, the change in the sedimentological characteristics is perceived; there is a tabular geometry in the beds with flat to parallel wavy lamination, scarce macrofauna (microfauna is predominant) and without fragmentation of the fossils.

The upper boundary with the “Cogollo” Formation was not recognized in the Yuruma hill area in this study. Based on Rollins (1960, Figure 6, BB' section and plate 4 of the geological map of the La Guajira Peninsula; 1965, Figure 6), for this sector, the boundary of the Yuruma Formation is found at the limestones with ostreids in the SE margin of the Yuruma hill. In the sector of the Punta Espada, following Patarroyo and Götz (2020), the upper boundary of the Yuruma Formation is located in the highest structural plane of biomicrites of the upper interval, coinciding with a very prominent morphological change (Figure 6).

Similarly, each of the aforementioned intervals can be subdivided into two segments. For the lower interval, the lower segment (Figures 5, 7 and 8) has 44.5 m of intercalations, in which there is a greater predominance of biomicrites (N1-N5) with irregular geometries of thin, medium and thick beds on very fossiliferous marlstones (N1) (Figure 8).

Whole fossils are in the marlstones, while in the biomicrites, thick-shelled benthic fossils are more frequent, which present principally aleatory distributions and, in many cases, fragmentation. There may also be bioperturbations in some of the strata.

The upper segment of the lower interval (Figures 5 and 7), with thickness of 45.5 m, has a higher proportion of marlstones (N1) than biomicrites (N1-N5). The marlstone beds are very thick, and the biomicrite layers are medium to thin. The fossils in the marlstones show parallel orientations according to the stratification plane, while in the biomicrites, the thick shell benthic fossils mainly present aleatory distributions and, in some cases, fragmentation. Bioperturbation may occur in some strata. In the succession of the lower interval, trigonids (*Pterotrigonia* sp.), ostreids (*Ceratostreon* sp.), gastropods of variable sizes (*Nododelphinula* sp.), ammonoids, irregular echinoderms, serpulids, articulated brachiopods, and others are either fragmented or complete (whole).

For the upper interval, the lower segment (Figures 5 and 9) is 65 m thick with intercalations between weathered marlstones (N1, 5YR 4/1) and biomicrites (N1, N2, N3, N4, 5YR 2/1, 5YR



Figure 6. Biomicrite strata at the top of the Yuruma Formation in the Punta Espada area. The morphological change in the structural plane with strong tectonic and karstic effects dips to the N, coinciding with the lithostratigraphic boundary (photographic capture from the N, Piedra del Destino valley, cf. Patarroyo and Götz, 2020, Figure 2).

4/1, 5YR 6/1). The tabular beds of marlstones are very thick, and the biomicrites are medium thick (Figure 10), mainly with flat parallel lamination. In both the marlstones and biomicrites, the fossils have the same orientations as the bedding plane, and the few benthic fossils (bivalves and discynid brachiopods) have thin shells (Figure 10). In the upper segment of the upper interval (Figures 5, 9 and 10), only 35 m of strata are described, represented by tabular, medium to thick beds, mainly containing biomicrites with dominantly parallel flat lamination; the

benthic and nektonic fauna are scarce, while the microfossils (foraminifera?) are more abundant.

In other controls of the Punta Espada area, thin beds of biomicrite (Figure 11) were recognized, in which abundant benthic fossils with thick shells appear, mainly disjointed and fragmented, and nektonic fossils are less frequent. These lithostratigraphic characteristics are similar to those observed in the lower segment of the lower interval of the Yuruma hill sector.

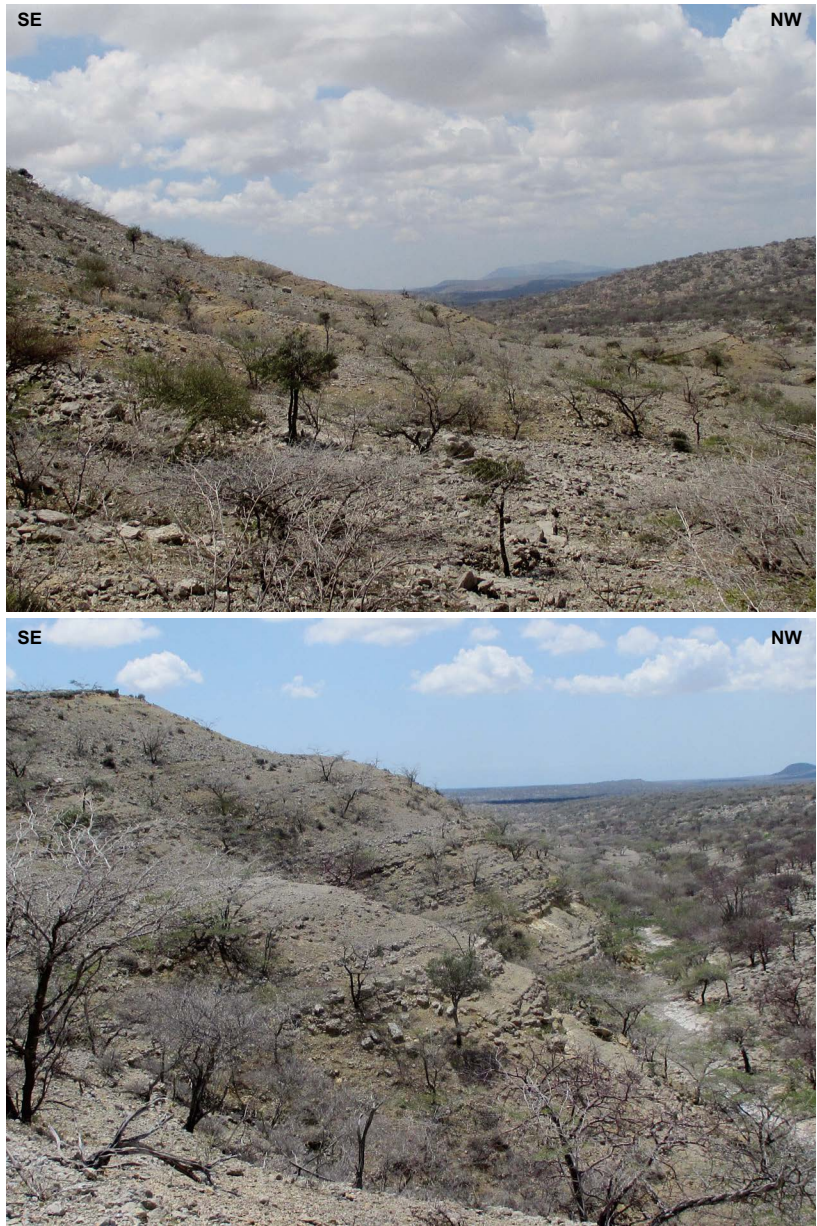
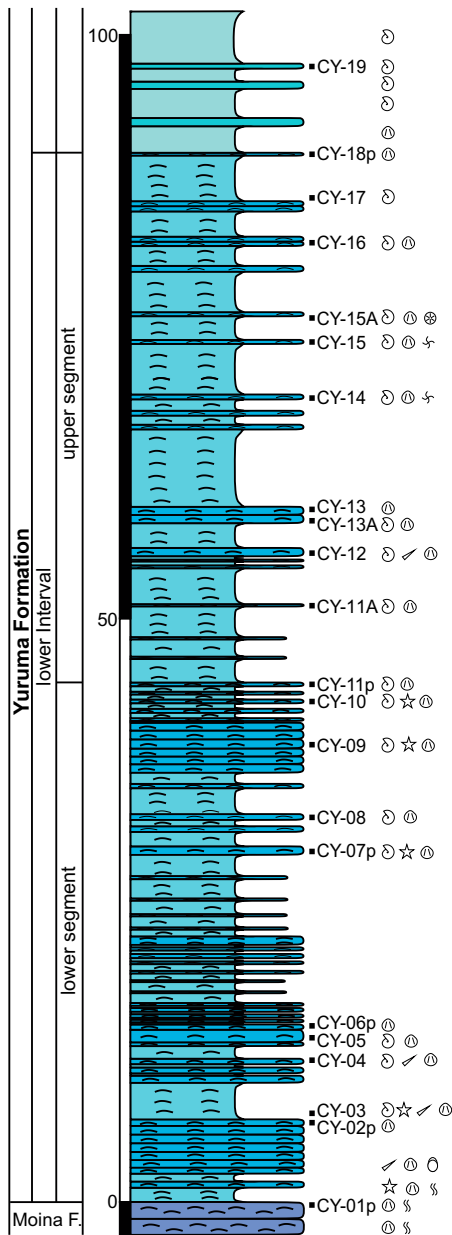


Figure 7. Stratigraphic succession and outcrops of the lower interval of the Yuruma Formation, Yuruma hill section

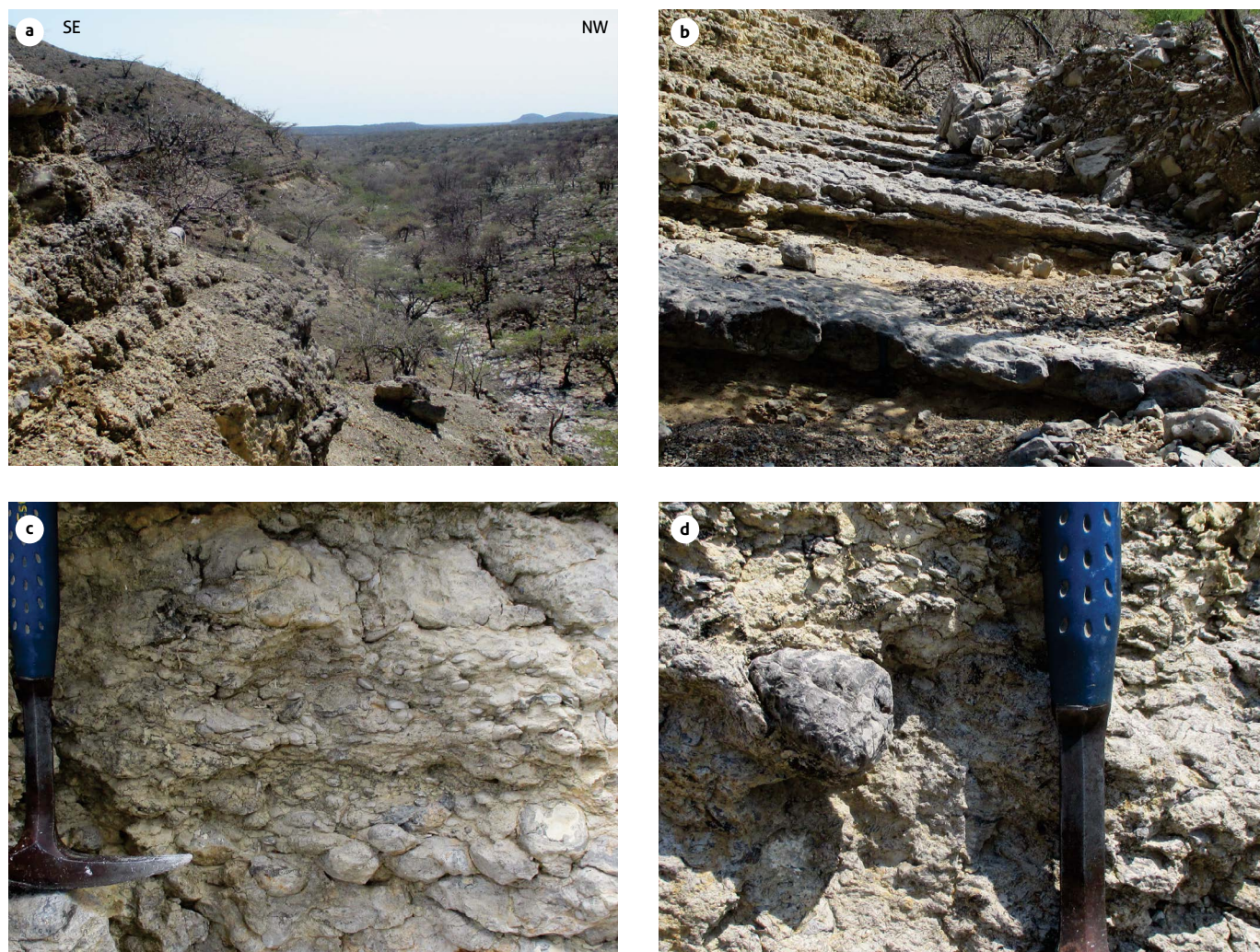


Figure 8. a) Sedimentary outcrops of the entire lower segment of the lower interval of the Yuruma Formation; b) close up picture, where the irregular geometries of the thin beds are notorious (meters 37 to 39); c and d) fossils and their bed distribution; and d) *Pterotrigonia* sp.

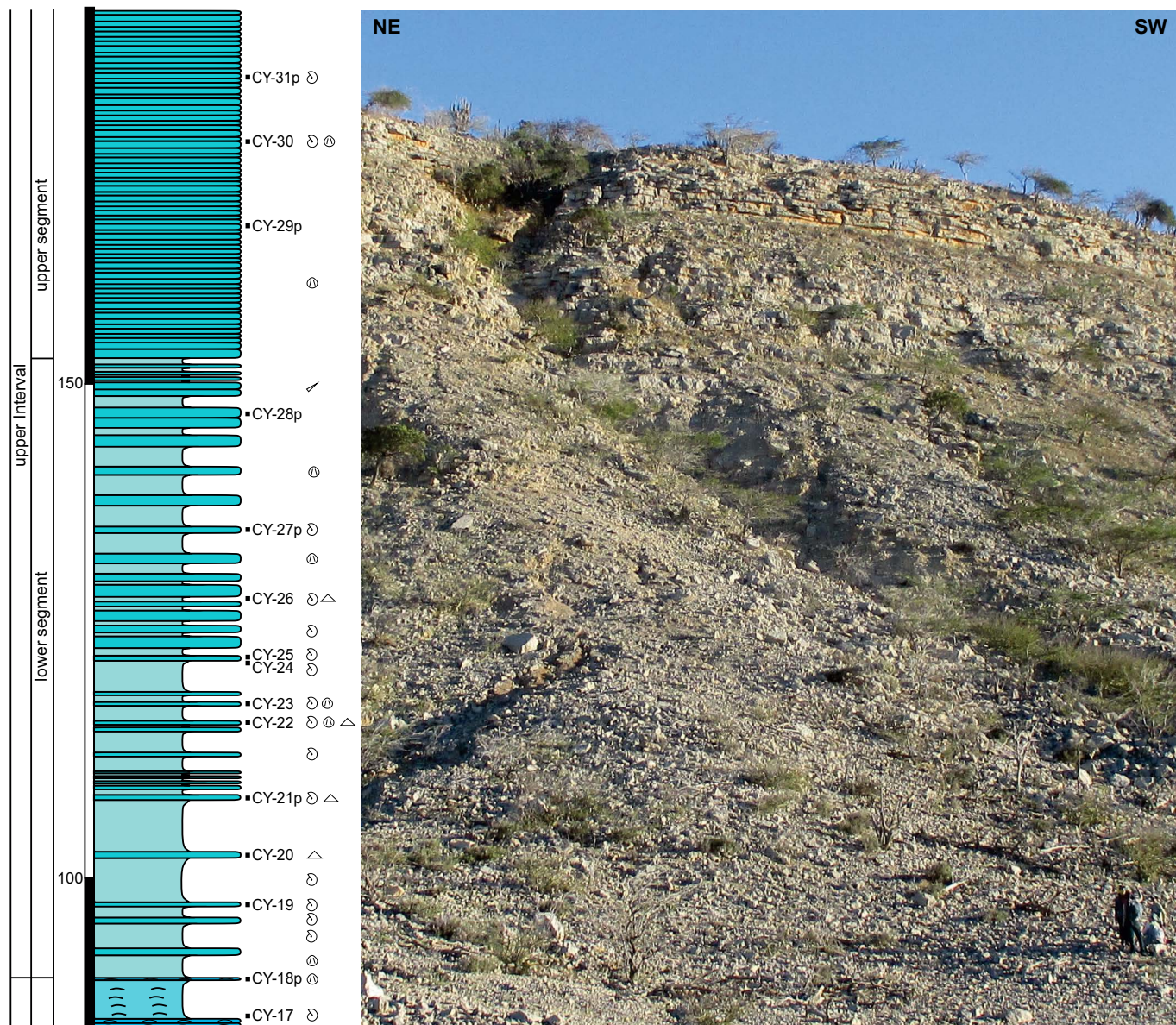


Figure 9. Stratigraphic succession and outcrops of the upper interval of the Yuruma Formation Medium to upper Yuruma hill section.



Figure 10. Details of the outcrops of the tabular beds of marlstones and biomicrotites of the upper interval and some of their macrofossils a and c) biomicrotites and weathered marlstones of the lower segment; b, d and e) biomicrotites of the upper segment; f) biomicrotite with an ammonoid fragment; and g) biomicrotite with a bivalve, in which soft thickening of the growth lines is observed. Fossils remain in the field.



Figure 11. Succession of the lower part of the Yuruma Formation at Punta Espada
In the background, the coastline and the Punta Espada lighthouse can be seen.

4.2 Biostratigraphy and stratigraphic range

Based on the fossil vertical distribution, especially the ammonoids, it is possible to identify the stratigraphic range of the Yuruma hill succession following postulates for the equivalent Cretaceous successions of central Colombia.

In the upper section of the Moina Formation (Figure 12), the predominance of the ostreid *Ceratostreon* sp. may be present in both the Hauterivian and Barremian deposits, a case that is similar to what occurs in the stratigraphic section at the top of the Rosablanca Formation in the middle of Magdalena Valley.

Within the lower segment of the lower interval of the Yuruma Formation (Figure 12), the following fossils are recognized: sample CY-03, *Nicklesia pulchella* (d'Orbigny, 1840) (Figure 13a), *Nicklesia karsteni* (Uhlig, 1882) (Figure 13b), *Karsteniceras beyrichi* (Karsten, 1858) (Figure 13c), *Karsteniceras cf. beyrichi* (Figure 13 d and e), and *Neithea* sp. (Figure 13f); sample CY-04, *Karsteniceras cf. beyrichi* (Figure 13g, e, i), *Karsteniceras* sp. (Figure 13 h), and *Nododelphinula* sp. (Figure 13j) in the sense of Jaworski (1938, pl. 23, 5); sample CY-05, *Nicklesia cf. karsteni* (Figure 13k, l); samples CY-07 and CY-08, *Pulchellia galeata* (von Buch, 1838) (Figure 13 m and n); sample CY-08, *Pulchellia* sp. (Figure 13o); sample CY-09, *Karsteniceras* sp. (Figure 14a); sample CY-10, *Pulchellia* sp. (Figure 14b), *Moutoniceras?* sp. (Figure 14c), and *Pulchellia cf. galeata* (Figure 14 d and e); and sample CY-11A; *Nicklesia pulchella* (Figure 14f).

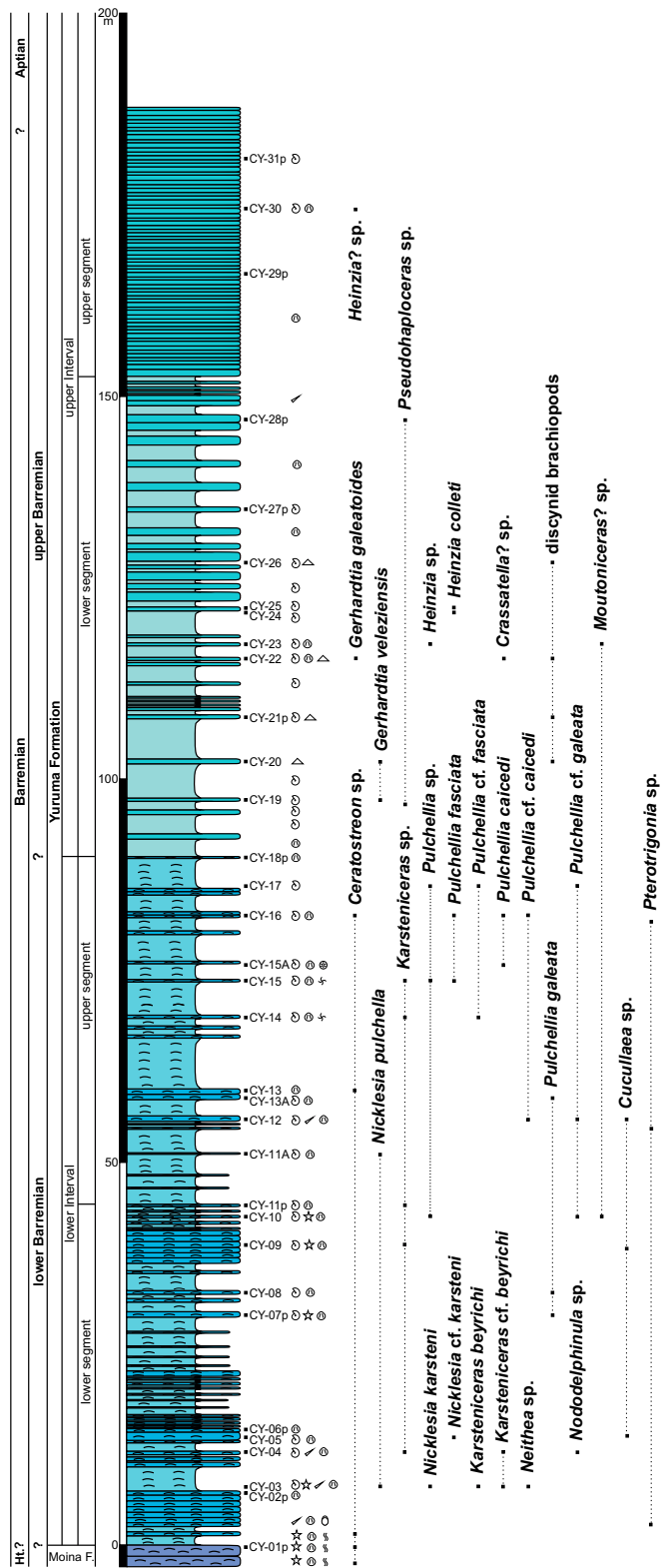


Figure 12. Sedimentary succession of the Yuruma hill section with the vertical fossil distribution

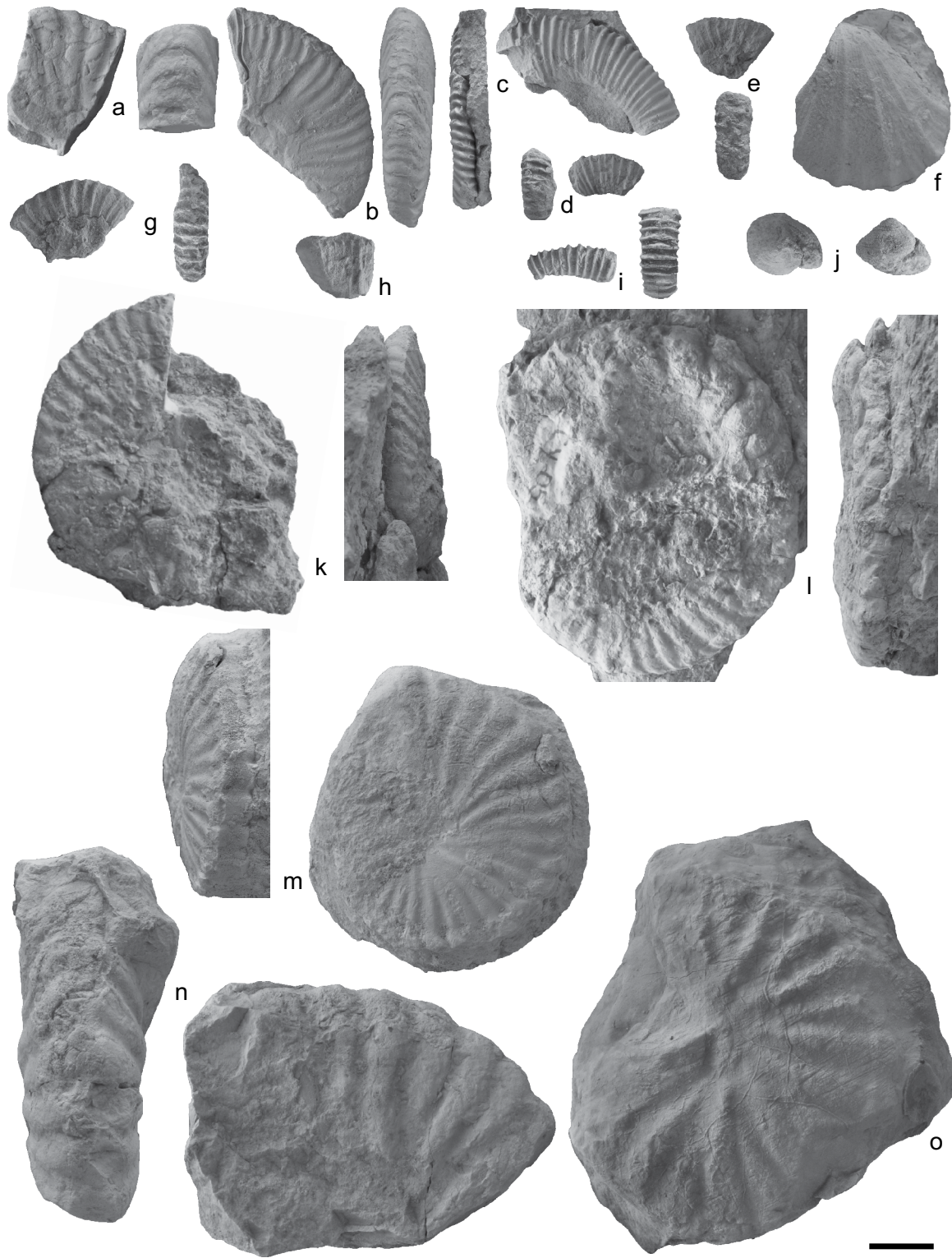


Figure 13. a) *Nicklesia pulchella* (CY-03); b) *Nicklesia karsteni* (CY-03); c) *Karsteniceras beyrichi* (CY-03); d and e) *Karsteniceras cf. beyrichi* (CY-03); f) *Neithea* sp. (CY-03); g, e, i) *Karsteniceras cf. beyrichi* (CY-04); h) *Karsteniceras* sp. (CY-04); j) *Nododelphinula* sp. (CY-04); k, l) *Nicklesia cf. karsteni* (CY-05); m, n) *Pulchellia galeata* (CY-07 and CY-08); and o) *Pulchellia* sp. (CY-08) [Graphic scale: 10 mm]



Figure 14. a) *Karsteniceras* sp. (CY-09); b) *Pulchellia* sp. (CY-10); c) *Moutoniceras?* sp. (CY-10); d and e) *Pulchellia* cf. *galeata* (CY-10); f) *Nicklesia pulchella* (CY-11A); g) *Pulchellia* cf. *galeata* (CY-12); and h) *Pulchellia* cf. *caicedi* (CY-12) [Graphic scale: 10 mm]

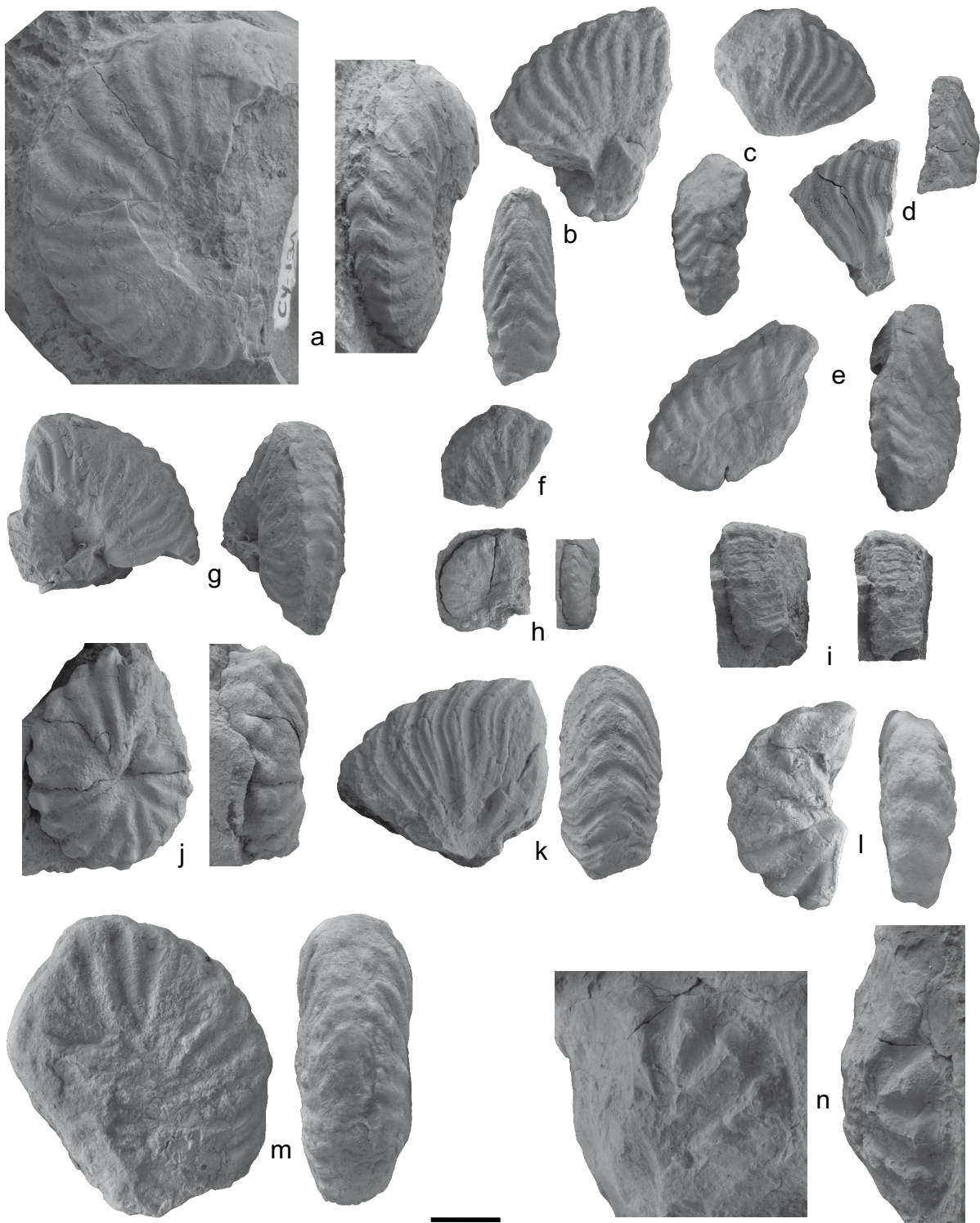


Figure 15. a) *Pulchellia galeata* (CY-13A); b, c, d, e and f) *Pulchellia cf. fasciata* (CY-14); g) *Pulchellia fasciata* (CY-15); h) *Pulchellia* sp. (CY-15); i) *Karsteniceras* sp. (CY-15); j) *Pulchellia caicedi* (CY-15A); k) *Pulchellia fasciata* (CY-16); l) *Pulchellia cf. caicedi* (CY-16); m) *Pulchellia cf. galeata* (CY-16); and n) *Pulchellia caicedi* (CY-16) [Graphic scale: 10 mm]

For the upper segment of the lower interval, the following fossils are recognized: sample CY-12, *Pulchellia* cf. *galeata* (Figure 14g) and *Pulchellia* cf. *caicedi* (Karsten, 1858) (Figure 14h); sample CY-13A, *Pulchellia galeata* (Figure 15a); sample CY-14, *Pulchellia* cf. *fasciata* (Gerhardt, 1897) (Figures 15 b, c, d, e and f); sample CY-15, *Pulchellia fasciata* (Figure 15 g), *Pulchellia* sp. (Figure 15 h) and *Karsteniceras* sp. (Figure 15i); sample CY-15A, *Pulchellia caicedi* (Figure 15j); sample CY-16, *Pulchellia fasciata* (Figure 15k); sample CY-16, *Pulchellia* cf. *caicedi* (Figure 15l), *Pulchellia* cf. *galeata* (Figure 15m) and *Pulchellia caicedi* (Figure 15n); and sample CY-17, *Pulchellia* cf. *fasciata* (Figure 16a), *Pulchellia* sp. (Figure 16b) and *Pulchellia* cf. *galeata* (Figure 16c). In addition, *Pterotrigonia* sp. (Figure 8d), *Ceratostreon* sp., *Pholadomya* sp., *Pinna* sp., gastropods of small size (*Nododelphinula* sp.) large (internal molds with low spire), irregular echinoderms (cf. Figure 18), and articulated brachiopods and colonial corals are found.

Thus, based on the ammonoids finding in the lower interval, this stratigraphic section involves deposits of the Lower Barremian taking into account the index species of the unnamed interval biozones of *Nicklesia pulchella* and *Pulchellia galeata* (cf. Patarroyo, 1999, 2000 a and b, 2004, 2020).

To the other hand, within the succession of the Lower Barremian of the Yuruma Formation (Figure 12), a stratigraphic level is recognized, in which individuals of *Nicklesia* and *Pulchellia* coincide, similar to that is found in the center of Colombia (Patarroyo, 1999, 2000 a and b, 2004, 2020). Given this finding and its constancy through Colombia, from the biostratigraphic point of view, it would be more appropriate to propose a concurrent range subzone for this interval than a new biozone for the lower Barremian. Thus, the subzone in which *Nicklesia* and *Pulchellia* coexist is restricted to the lower part of the interval biozone (based on lowest occurrences) of *Pulchellia galeata* (Patarroyo, 1999, 2000 a and b, 2004, 2020).

In the lower segment of the upper interval, the following fossils are present in the samples: CY-19 and CY-20, *Gerhardtia veleziensis* (Hyatt, 1903) (Figure 16d and e); CY-20 and CY-22, discynid brachiopods (Figures 16f and 17a), *Gerhardtia galeatoides* (Karsten, 1858) (Figure 17b), and *Crassatella?* sp. (Figures 17c and 18h); CY-23, *Heinzia* sp. (Figure 17d) and *Moutoniceras?* sp. (Figure 17e); CY-24 and CY-25, *Heinzia colleti* (Bürgl, 1956) (Figures 17 f and g) and *Pseudohaploceras* sp. (Figure 18i); and for the upper segment of the upper interval, in CY-30, *Heinzia?* sp. (Figure 17 h).

Based on the collected ammonoids in the upper interval, this stratigraphic succession involves deposits of the Upper Barremian, as indicated by the presence of the index species of the biozone of *Gerhardtia veleziensis* (cf. Patarroyo, 1999, 2000 a and b, 2004, 2020). It is not possible to indicate a clear stratigraphic range for the highest deposits of the Yuruma Formation in Yuruma hill because the recovery of ammonoids in these strata unfortunately was not successful. Furthermore, it was not possible to describe there the succession until the boundary with the overlying “Cogollo” Formation. However, in the sector of Punta Espada, a few meters from the upper boundary of the Yuruma Formation and toward the base of the “Cogollo” Formation, *Dufrenoyia* cf. *hansbuerglii* Etayo-Serna of the Lower Aptian (Patarroyo and Götz, 2020) was found; thus, the possibility remains that part of the deposits in the upper segment of the upper interval in the Yuruma Formation may be represented the lowest part of the Lower Aptian.

Similarly, at Punta Espada, the sample PEY-1 contains *Nicklesia* sp. (Figure 17i) and *Epistomina caracola*, which were identified in the thin section of the same sample. This material is from the lower Barremian and is related to the lower stratigraphic level of the Yuruma Formation (Figure 11) in this sector of the Alta Guajira.

The citation of *Pedioceras*, *P. caquesense* or *P. caquensense* (sic) to the upper Barremian in the upper part of the Yuruma Formation (Rollins, 1960, p. 29, Figure 6, Figure 10; 1965, p. 53, Figure 6, Figure 10) is highly controversial because in the central Cretaceous marine deposits of Colombia, *Pedioceras* is restricted to the lower part of the lower Barremian (cf. Etayo-Serna, 1964; Patarroyo, 1995, 2000 a and b, 2004, 2020).

4.3 Environmental considerations

Considering the lithological, sedimentological and fossil variations, preliminary environmental interpretations of the sedimentary succession of the Yuruma hill can be proposed.

The environmental conditions of the upper part of the Moína Formation indicate currents with high energy levels over the bottom of the deposit, as demonstrated by the mechanical accumulation of mollusks (Figure 18a) and the fragmentation of shells and carapaces.

The sharp contact between the top bed of the Moína Formation and the lower bed of the Yuruma Formation (Figure 4) indicates a change in the sedimentary conditions of the medium since there is an increase in the content of calcareous mud without decreases benthic macrofauna. Thus, a transgressive

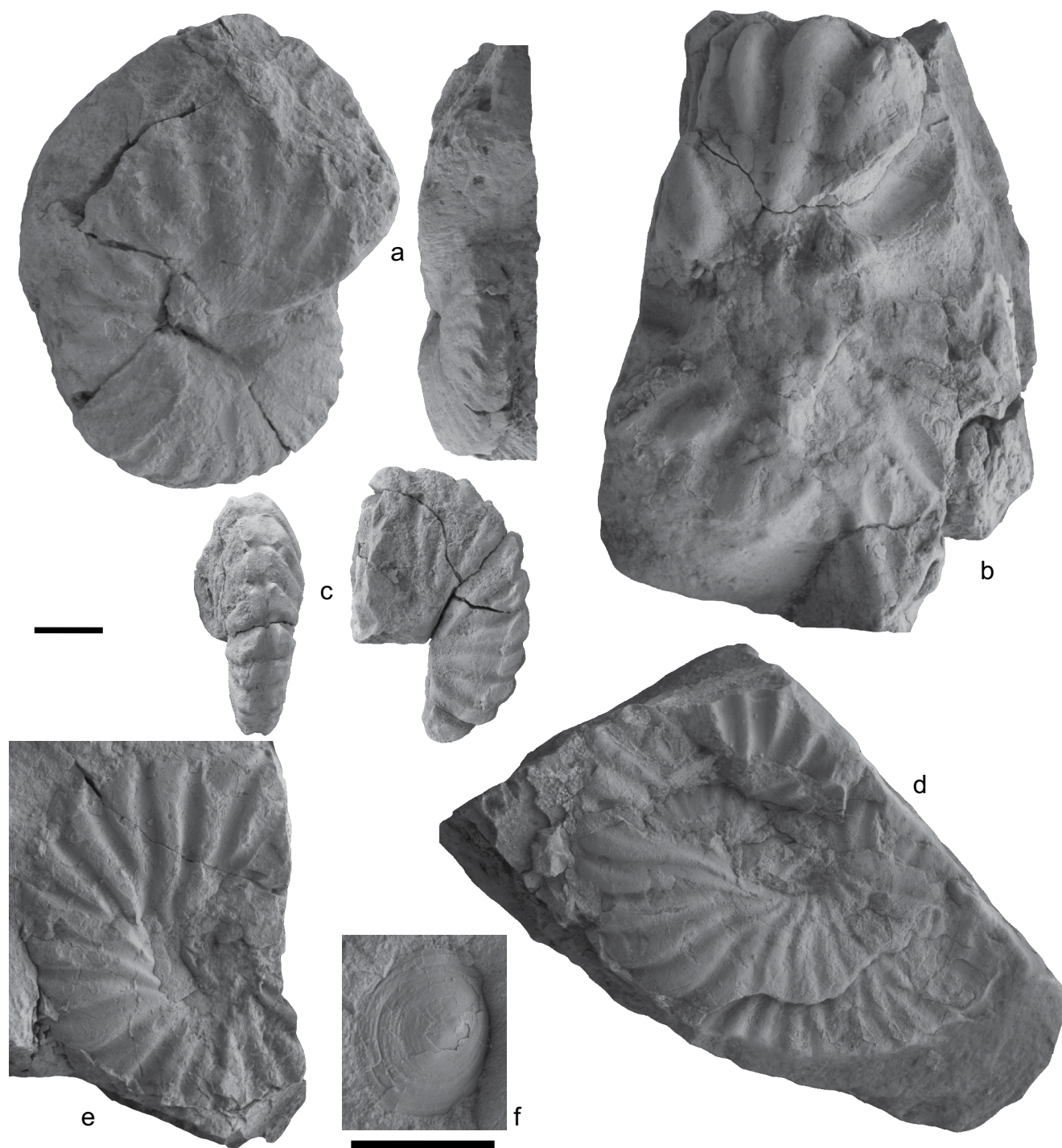


Figure 16. a) *Pulchellia* cf. *fasciata* (CY-17); b) *Pulchellia* sp. (CY-17); c) *Pulchellia* cf. *galeata* (CY-17); d and e) *Gerhardtia veleziensis* (CY-19 and CY-20); and f) discynid brachiopod (CY-20) [Graphic scales (a, e) 10 mm and (f) 5 mm]

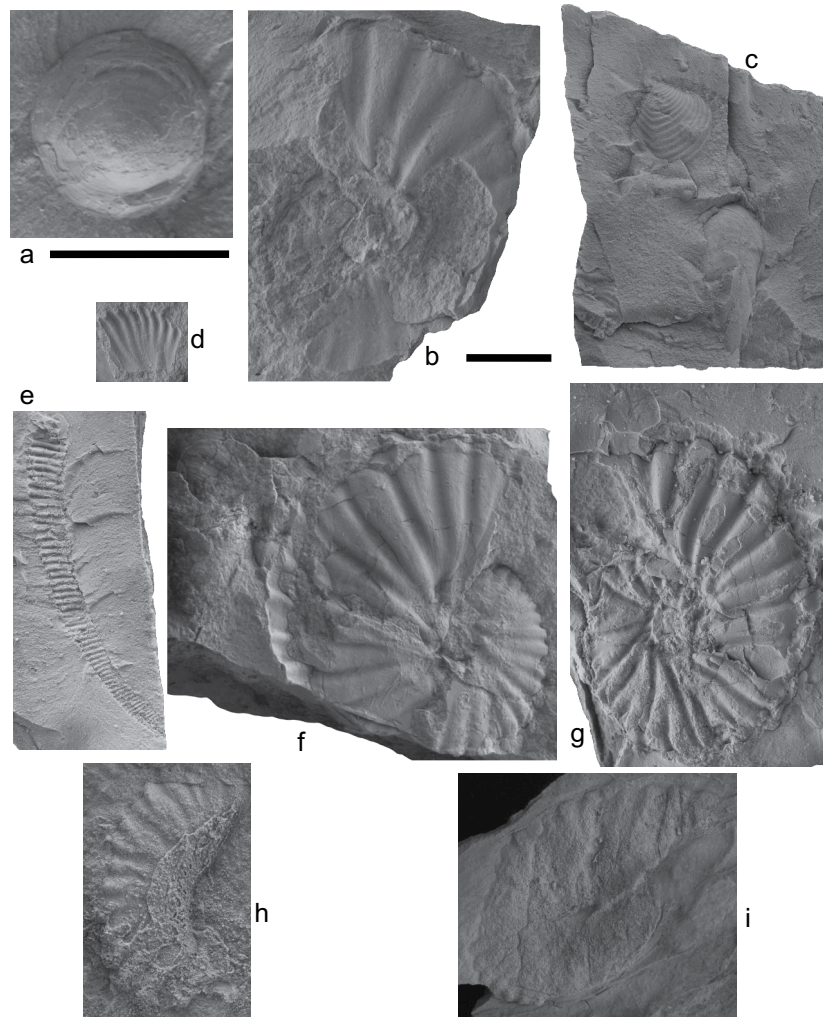


Figure 17. a) Brachiopod discynid (CY-22); b) *Gerhardtia galeatoides* (CY-22); c) *Crassatella?* sp. (CY-22); d) *Heinzia* sp. (CY-23); e) *Moutoniceras?* sp. (CY-23); f and g) *Heinzia colleti* (CY-24 and CY-25); h) *Heinzia?* sp. (CY-30); and i) *Nicklesia* sp. (PEY-1. Punta Espada) [Graphic scales (a) 5 mm and (b, i) 10 mm]

surface is identified as a consequence of deepening of the bottom of the deposit and a decrease in energy levels. The alternation between very fossiliferous marlstones and biomicrites with irregular layers allows to interpret variations in the depth of the deposit bottom and consequently in the energy flow over it. These variations in the lower interval deposits were more constant in the lower segment than in the upper segment because the biomicrites are subordinate to the marlstones.

In the upper interval, calmer environmental conditions are identified as a result of a greater deepening of the bottom of the deposit. The tabular beds geometries and the continuous or discontinuous plane-parallel internal lamination, plus the scarce presence of benthic fauna, corroborate this postulate.

4.4 Geology of Cerro Yuruma

Considering the stratigraphic findings at the Yuruma hill and in its surroundings, it was possible to recognize and differentiate the deposits of the upper part of the Moina Formation in the Uarramarirai or Uarramaralijai Stream (Figures 1c and 4); consequently, the sharp boundary of the base of the Yuruma Formation and from there, stratigraphically ascending, the following succession of the Yuruma Formation until the upper part of the Yuruma hill (overview, Figures 2 and 19).

Based on the data obtained in this contribution, related with the 10Bis-I-A topographic map of the IGAC (scale 1:25,000), the lateral boundaries continuity between the formations was projected based on public satellite images, pano-

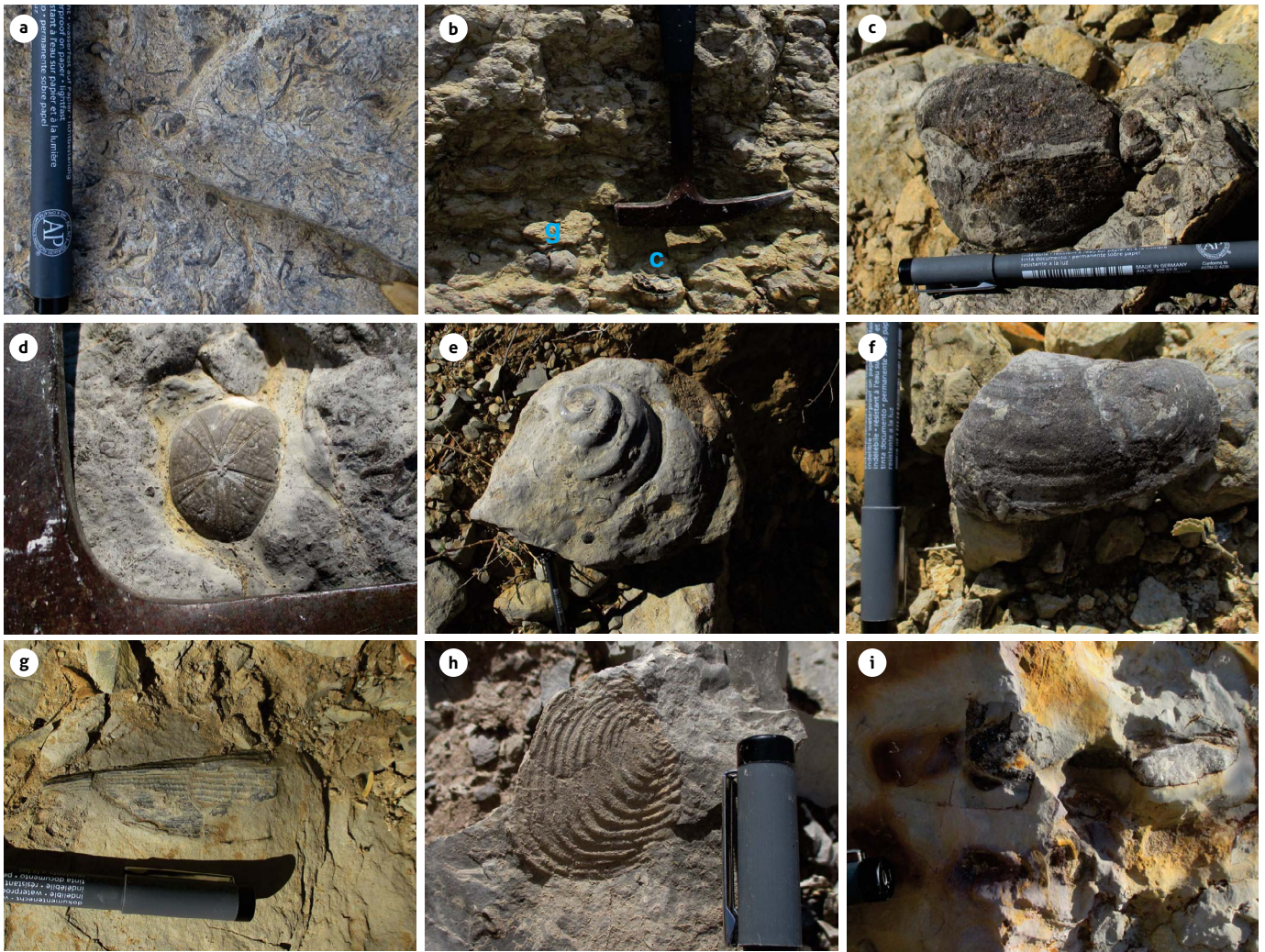


Figure 18. Other macrofossils of the Yuruma hill section that remain in the terrain a) mechanical accumulation of mollusks in the upper part of the Moina Formation with *Ceratostreon* sp.; b) small gastropod (g) and *Ceratostreon* sp. (c) with articulated shells and parallel orientation to the bedding plane at the base of the Yuruma Formation; c) *Cucullaea* sp.; d) irregular echinoid; e) internal mold of a large gastropod; f) *Pholadomya* sp.; g) *Pinna* sp.; h) *Crassatella*? sp.; and i) biomicrite bed with the whorl section of *Pseudohaploceras* sp. and parallel orientation to the bedding plane.

ramic observations, field controls (compass and GPS data) and the morphology of the lithostratigraphic units. Although the upper boundary of the Yuruma Formation with the base of the “Cogollo” Formation was not recognized in the adjacent area of the Yuruma hill, the morphological change between these units was considered (Figures 2 and 19), which is coincident with the proposition and mapping of Rollins (1960, 1965). Therefore, a geological map of this sector was obtained (Figure 19), which shows the relationship of the rocks of the Yuruma Formation, following Rollins (1960, 1965), with the underlying Moina Formation and with the overlying “Cogollo” Formation.

This last contact is sharp, according to Patarroyo and Götz (2020, Figure 2), as is recognized in the Punta Espada area.

The geological map, Plate 10Bis Rancho Grande (Yuruma hill) and Plate 6 Castilletes (Punta Espada) of Zuluaga et al. (2008 a and b) show different geological interpretations because they do not consider the same lithostratigraphic boundary between the Yuruma Formation and the “Cogollo” Formation. As it was discussed this boundary is taken following Rollins (1960 and 1965) to the Yuruma hill (panoramic Figure 19) and to Punta Espada area (cf. Patarroyo and Götz, 2020).

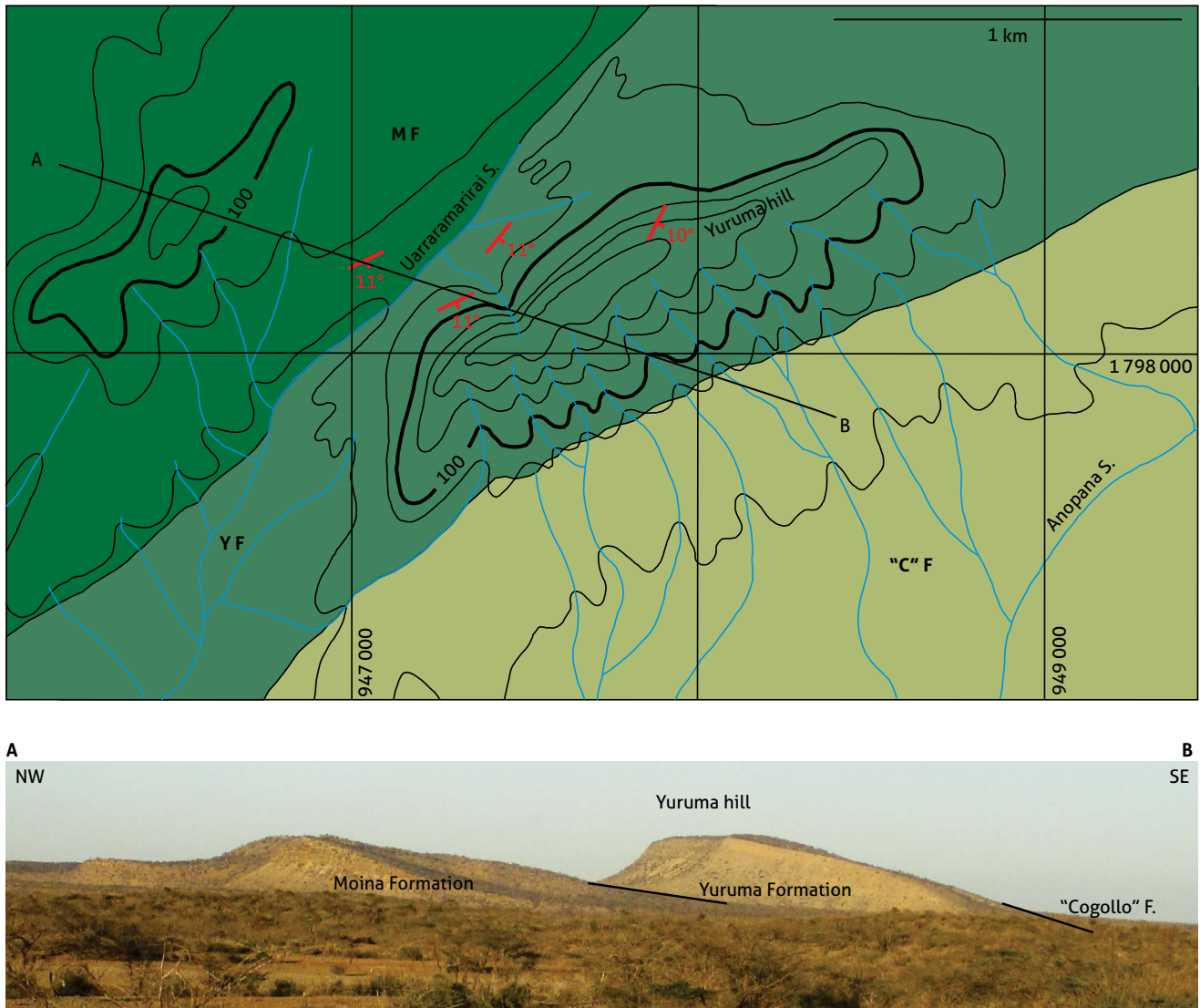


Figure 19. Geological map of the Yuruma hill area based on the 10Bis-I-A topographic map of the IGAC and obtained from field data, morphological expression, panoramic photographs and satellite images

The two stratigraphic intervals of the Yuruma Formation in the Yuruma hill present variable morphological characteristics; thus, initially in the relief, the succession is principally competent although incompetent beds appear as intercalations (Figures 4, 5, 7 and 8); in the intermediate part, a morphological depression is manifested by the predominance of incompetent beds (Figures 5, 7 and 9). Finally, for the upper part, there is a pronounced escarpment (Figures 5, 9 and 10). In the Yuruma hill and Punta Espada area, to the upper interval, karst phenomena are evident, so much so that in the upper sector

of the Yuruma hill, travertine associated with speleothems is recognized.

The sharp contact between the highest bioclastic bed of the Moina Formation and the lower marlstone beds of the Yuruma Formation is associated with a morphological change representing a transgressive surface that was developed very close to the Hauterivian-Barremian boundary. At the top of the Yuruma Formation, the boundary with the marlstones of the “Cogollo” Formation is sharp, based on geological controls recognized in Punta Espada (Patarroyo and Götz, 2000) following the postulates of Rollins (1960 and 1965, Figure 6).

5. DISCUSSION

The Yuruma Formation of the Barremian - lower Aptian? is a lithostratigraphic unit with marine deposits that are geologically associated with the Alta Guajira block. Its lower boundary is sharp with the Moina Formation at the type locality, as was recognized by Renz (1960) and Rollins (1960, 1965), and its upper boundary is sharp with the Cogollo Formation, following Rollins (1960, 1965). Based on the lithostratigraphic limits used here and the geomorphology of the Yuruma Formation, it is clearly better to follow the proposals of Rollins (1960, 1965) than those of Renz (1960) to obtain a geological mapping.

The Yuruma Formation and the Moina Formation do not crop out to the south in the Perijá Mountain range, where the type locality of the “Cogollo” Group or Formation is found (cf. Patarroyo and Götz, 2020). Care must be taken to extend regionally the lateral continuity of the lithostratigraphic units of the Perijá Mountain range because the tectonic and paleotectonic of the Oca and Cuisa faults indicate that the northern blocks of the Alta Guajira were originally located to the west of their current position. This type of misstatement generates unnecessary stratigraphic confusion.

The paleotectonic, paleoecological and sedimentological deposits conditions of the Yuruma Formation are not directly related to the equivalent deposits of the central Cretaceous basin in Colombia, although they show similar biostratigraphic elements in the nektonic fauna, which enables the establishment of their stratigraphic range (cf. Patarroyo, 2020).

6. CONCLUSIONS

In the studied section of the Yuruma hill, the succession of the Yuruma Formation can be differentiated into two stratigraphic intervals, lower and upper intervals, which in turn can be subdivided into two segments each.

The lower interval is characterized by intercalations of very fossiliferous marlstones and biomicrites with benthic and nektonic fossils of the lower Barremian. *Nicklesia pulchella*, *N. karsteni*, *N. cf. karsteni*, *Karsteniceras* sp., *K. beyrichi*, *K. cf. beyrichi*, *Neitheia* sp., *Nododelphinula* sp., *Pulchellia* sp., *P. galeata*, *P. cf. galeata*, *P. caicedi*, *P. cf. caicedi*, *P. fasciata*, *P. cf. fasciata*, *Moutoniceras?* sp., *Pterotriconia* sp., *Ceratostreon* sp., *Pinna* sp., small and large gastropods, echinoderms, brachiopods and corals were found.

The upper interval is characterized by marlstones and biomicrites with scarce benthic and nektonic fauna of the upper Barremian and possibly part of the lower Aptian. *Gerhardtia veleziensis*, *G. galeatoides*, *Heinzia* sp., *H. colleti*, *H.? sp.*, *Moutoniceras?* sp., *Pseudohaploceras* sp., *Crassatella?* sp. and discyrid brachiopods are found. In the Punta Espada area, a few meters from the top of the Yuruma Formation, *Dufrenoyia* cf. *hansbuerglii* Etayo-Serna from the lower Aptian was found toward the base of the “Cogollo” Formation (Patarroyo and Götz, 2020).

Considering the lithological and sedimentological variations in the succession of the Yuruma hill, variable environmental conditions can be interpreted. At the top of the Moina Formation, the sea bottom experienced high energy influxes with the accumulation of shell and carapace fragments. In the lower deposits of the Yuruma Formation, there is a change in the environmental conditions of the deposit due to the presence of marls, an indicator of deepening for the lower interval succession where very fossiliferous marlstones and biomicrites with dominant benthic macrofossils are present. Then, there is a greater deepening related with the upper interval succession, where poor fossiliferous marlstones and biomicrites appear with scarce benthic and nektonic macrofossils.

ACKNOWLEDGMENTS

My sincere thanks to the communities of Wuatchuali and Punta Espada, to Edwar Salazar, and to the students of the field trip (2009) from the Department of Geosciences, Universidad Nacional de Colombia, for all the support provided. In the same way, I extend my gratitude to Jorge Gómez Tapias, María Fernanda Almanza, Lisbeth Fog and Alejandra Cardona (Servicio Geológico Colombiano) for their support, accompaniment and the opportunity to carry out the research on Yuruma hill. I also thank the two anonymous reviewers who contributed to the enrichment of this work.

REFERENCES

- Álvarez, W. (1967). *Geology of the Simarua and Carpintero áreas, Guajira península, Colombia* [Ph.D. Thesis]. Princeton University, USA.
- Bürgl, H. (1956). Catálogo de las amonitas de Colombia. Parte I. Pulchelliidae. Instituto Geológico Nacional. *Boletín Geológico*, 4(1), 1-119.

- Bürgl, H. (1960). Geología de la Península de la Guajira. Servicio Geológico Nacional. *Boletín Geológico*, 6(1-3), 129-168.
- Campbell, C. V. (1967). Lamina, Laminaset, bed and bedset. *Sedimentology*, 8, 7-26.
- Colmenares, F., Román García, L., Sánchez, J. M., & Ramírez, J. C. (2019). Diagnostic Structural Features of NW South America: Structural Cross Sections Based Upon Detailed Fields Transects. In F. Cediél, & R. P. Shaw (eds.), *Geology and Tectonics of Northwestern South America*, Frontiers in Earth Sciences. Chapter 9. Springer.
- d'Orbigny, A. (1840). *Paléontologie française. Terrains Crétacés. Céphalopodes*. Tomo I. Masson.
- Etayo Serna, F. (1964). Posición de las faunas en los depósitos cretácicos colombianos y su valor en la subdivisión cronológica de los mismos. *Boletín de Geología*, 16-17, 1-141.
- Etayo-Serna, F. (1985). Paleontología estratigráfica del Sistema Cretácico en la Sierra Nevada del Cocuy. In F. Etayo-Serna, & F. Laverde Montaña (eds.), *Proyecto Cretácico* (pp. XXIV1-XXIV47). Publicaciones Geológicas Especiales 16. Ingeominas.
- Gerhardt, K. (1897). Beitrag zur Kenntniss der Kreideformation in Columbien. In G. Steinmann (ed.), Beiträge zur Geologie und Paläontologie von Südamerika, 5. *Neues Jahrbuch für Mineralogie, Geologie und Palaeontologie*, XI. Beilage-Band, 118-208.
- Gómez, I. (2001). *Structural style and evolution of the Cuisa Fault System, Guajira, Colombia* [Master thesis]. University of Houston.
- Guzmán, G. (1985). Los grifeidos infracretácicos *Aetostreon couloni* y *Ceratostreon boussingaulti*, de la Formación Rosablanca, como indicadores de oscilaciones marinas. In F. Etayo-Serna, & F. Laverde Montaña (eds.), *Proyecto Cretácico* (pp. XIII1-XIII16). Publicaciones Geológicas Especiales 16. Ingeominas.
- Hyatt, A. (1903). Pseudoceratites of the Cretaceous. *USGS Monograph*, 44, 1-250.
- Irving, E. M. (1971). La evolución estructural de los Andes más septentrionales de Colombia. *Boletín Geológico*, 19(2), 1-89.
- Jaworski, E. (1938). *Gasterópodos del Cretácico inferior de Colombia. Estudios geológicos y paleontológicos sobre la cordillera Oriental de Colombia, parte tercera, folleto de texto*. República de Colombia, Ministerio de Industrias y Trabajo, Departamento de Minas y Petróleos.
- Julivert, M., Barrero, D., Botero Arango, G., Duque Caro, H., Hoffstetter, R., Navas, J., de Porta, J., Robbins, R. K., Tabora Arango, B., Téllez, N., & Zamarreño de Julivert, I. (1968). *Colombie. Précambrien, Paléozoïque, Mésozoïque, et intrusions d'âge mésozoïque – tertiaire. Lexique Stratigraphique International*, (V, 4a), première partie. Centre National de la Recherche Scientifique.
- Karsten, H. (1858). Über die geognostischen Verhältnisse des westlichen Columbien, der heutigen Republiken Neu-Granada und Equador. *Amtlicher Bericht über die 32 Versammlung der Deutschen Naturforscher und Ärzte zu Wien*, 1856, 80-116.
- MacDonald, W. D. (1964). *Geology of the Serranía de Macuira Area. Guajira Peninsula, Colombia* [Ph.D. Thesis]. Princeton University, USA.
- MacDonald, W. D. (1965). Geology of the Serranía de Macuira area, Guajira Peninsula, Northeast Colombia. In J. B. Saunders (ed.), *Transactions, Fourth Caribbean Geological Conference, 1965* (pp. 267-274). Caribbean Printers.
- Patarroyo, P. (1999). *Die Entwicklung der Ammoniten der Familie Pulchelliidae aus dem Barrême von Zentral-Kolumbien* [Dr. Thesis]. Universität Giessen, Alemania.
- Patarroyo, P. (2000a). Amonitas del Barremiano en Villa de Leyva-Boyacá (Colombia-Sur America): Datos bioestratigráficos preliminares. *Zentralblatt der Geologie und Paläontologie*, 1, 789-798.
- Patarroyo, P. (2000b). Distribución de amonitas del Barremiano de la Formación Paja en el sector de Villa de Leyva (Boyacá, Colombia): Bioestratigrafía. *Geología Colombiana*, 25, 149-162.
- Patarroyo, P. (2004). Die Entwicklung der Ammoniten der Familie Pulchelliidae aus dem Barrême von Zentral-Kolumbien. *Révue de Paléobiologie*, 23(1), 1-65.
- Patarroyo, P. (2011). *Observaciones sobre la geología de las sedimentitas del Cretácico (Barremiano-Coniaciano) del sector de Punta Espada, Alta Guajira (Uribe-Guajira-Colombia)*. XIV Congreso Latinoamericano de Geología, XIII Congreso Colombiano de Geología [Memories], Medellín.
- Patarroyo, P. (2020). Barremian deposits of Colombia: A special emphasis on marine successions. In J. Gómez, & A. O. Pinilla-Pachón (eds.), *The Geology of Colombia, Volume 2 Mesozoic* (pp. 445-474). Publicaciones Geológicas Especiales 36. Servicio Geológico Colombiano. <https://doi.org/10.32685/pub.esp.36.2019.12>

- Patarroyo, P., & Götz, S. (2013). Dufrenoyia y Amphitriscoelus en depósitos del Aptiano de la Formación Cogollo (Guajira - Colombia). XIV Congreso Colombiano de Geología, Bogotá.
- Patarroyo, P., & Götz, S. (2014). Aptian ammonite and rudist association, Cogollo Formation (Guajira, Colombia). Paleobiogeographic significance to North Colombia. 23rd Latin American Colloquium on Earth Sciences (abstracts). In C. Ifrim, P. Bengtson, F. J. Cueto Berciano, & W. Stinnesbeck (eds.), *23rd International Colloquium on Latin American Earth Sciences, Abstracts and Programme. GAEA heidelbergensis 19* (p. 123). https://www.geow.uni-heidelberg.de/md/chemgeo/geow/tagung/lak2014/lak2014_gaea19_small.pdf
- Patarroyo, P., & Götz, S. (2020). Depósitos del Aptiano inferior con amonitas y rudistas, Punta Espada, Alta Guajira (Uribia - Colombia). Litoestratigrafía y apreciaciones regionales. *Boletín de Geología*, 42(3), 227-241. <https://doi.org/10.18273/revbol.v42n3-2020010>
- Renz, O. (1956). Cretaceous in Western Venezuela and the Guajira (Colombia). 20 Congreso Geológico Internacional, México (pp. 1-13).
- Renz, O. (1960). Geología de la parte sureste de la Península de la Guajira (República de Colombia). *Mem. 1161, Congreso Geológico Venezolano, 1*. Publicación Especial 3, 317-347. Ministerio de Minas e Hidrocarburos.
- Rollins, J. F. (1960). *Stratigraphy and Structure of the Goajira Peninsula, Northwestern Venezuela and Northeastern Colombia* [Ph.D. Thesis]. University of Nebraska, USA.
- Rollins, J. F. (1965). Stratigraphy and Structure of the Goajira Peninsula, Northwestern Venezuela and Northeastern Colombia. *Papers from the University of Nebraska series*. 76. <https://digitalcommons.unl.edu/cgi/viewcontent.cgi?article=1076&context=univstudiespapers>
- Salazar, E. (2010). *Análisis estratigráfico y determinación de ambientes de depósito para la Formación Palanz. Inicio de la sedimentación cretácica en la Alta Guajira, Colombia* [Master Thesis]. Universidad Nacional de Colombia, Bogotá.
- Uhlig, V. (1882). Die Wernsdorfer Schichten und ihre Äquivalente. *Sitzungsberichte der kaiserlichen Akademie der Wissenschaften. Mathematisch-Naturwissenschaftliche, Classe 86*, pp. 86-117.
- Von Buch, L. (1838). Über den zoologischen Character der Secundär-Formationen in Süd-Amerika. *Bericht über die zur Bekanntmachung geeigneten Verhandlungen der Königlischen Preussischen Akademie der Wissenschaften zu Berlin*, 54-67.
- Zuluaga, C., Ochoa A., Muñoz, C., Dorado, C., Guerrero, N., Martínez, A., Medina, P., Ocampo, E., Pinilla, A., Ríos P., Rodríguez, P., Salazar, E., & Zapata, V. (2008a). *Geología de la Plancha 6 Castilletes (Escala 1:100000)*. Universidad Nacional de Colombia - Ingeominas. <http://recordcenter.sgc.gov.co/B12/23008010024231/mapa/pdf/2105242311300010.pdf>
- Zuluaga, C., Ochoa A., Muñoz C., Dorado, C., Guerrero, N., Martínez, A., Medina, P., Ocampo, E., Pinilla, A., Ríos P., Rodríguez, P., Salazar, E., & Zapata, V. (2008b). *Geología de la Plancha 10Bis Rancho Grande (1:100000)*. Universidad Nacional de Colombia - Ingeominas. <http://recordcenter.sgc.gov.co/B12/23008010024231/mapa/pdf/2105242311300014.pdf>
- Zuluaga, C., Ochoa A., Muñoz, C., Guerrero, N., Martínez, A., Medina, P., Pinilla, A., Ríos P., Rodríguez, P., Salazar, E., & Zapata, V. (2009). *Memoria de las planchas 2, 3, 5, y 6 (con parte de las planchas 4, 10 y 10bis)* [Proyecto de investigación: Cartografía e historia geológica de la Alta Guajira, implicaciones en la búsqueda de recursos minerales]. Universidad Nacional de Colombia - Ingeominas. <http://recordcenter.sgc.gov.co/B12/23008010024231/documento/pdf/2105242311101000.pdf>



Sector desembocadura del Río Arma en el río Cauca, La Pintada, Antioquia, Colombia
Fotografía de Velásquez et al. (2021)



This work is distributed under the
Creative Commons Attribution 4.0 License.

Received: May 15, 2020

Revision received: January 30, 2021

Accepted: July 21, 2021

Published online: November 22, 2021

Seismic hazard assessment of the urban area of Ambato, Ecuador, in deterministic form

Evaluación de la peligrosidad sísmica del área urbana de Ambato, Ecuador, en forma determinística

Roberto Aguiar Falconi¹, Paola Serrano Moreta²

¹ Department of Earth Sciences and Construction, Universidad de las Fuerzas Armadas ESPE, Sangolquí, and Faculty of Engineering, Universidad Laica Eloy Alfaro de Manabí, Manabí, Ecuador

² Universidad de las Fuerzas Armadas ESPE, Sangolquí, Ecuador

Corresponding author: Paola Serrano, pcserrano@espe.edu.ec

ABSTRACT

Seismic microzonation of the urban area of Ambato was done in 2018 in a probabilistic and a deterministic manner. This type of calculation is presented in the first part of the article. For this purpose, three geologic faults and three strong-motion equations were considered. For each geologic fault, recurrence periods are determined using two methods. It is seen that a magnitude 6.3 earthquake associated with the blind faults traversing Ambato may occur in 80 to 100 years, and one of magnitude 6.5 in the next 300 years. Geophysical and geotechnical studies of the urban area of the city of Ambato are presented. These permitted the acquisition of curves with the same period of soil vibration and equal speed of the shear wave in the first 30 m, plus the classification of soils of the city. Later, six models of strong soil movements were considered and horizontal acceleration spectra of the soil were obtained in a mesh of points separated every 500 m, for each soil profile. Average spectra were found for soil profiles C, D and E when making comparisons with the spectra found in the 2018 study. Based on the results of the present study and those from 2018, new spectral forms are proposed for the urban area of the city of Ambato (called spectral envelopes) and compared to spectra reported by seismic regulations in force in Ecuador (NEC-15).

Keywords: Deterministic seismic hazard, acceleration spectra.

RESUMEN

La microzonificación sísmica del área urbana de la ciudad de Ambato fue realizada en 2018, en forma probabilística y en forma determinística; esta última forma de cálculo es la que se presenta en la primera parte del artículo. Para el efecto se consideraron tres fallas geológicas y tres ecuaciones de movimientos fuertes. Para cada una de las fallas geológicas se determinan los periodos de recurrencia empleando dos métodos: i) método del terremoto característico, y ii) método de Gutenberg y Richter

modificado, por medio de lo cual se ve que un sismo de magnitud 6,3, asociado a las fallas ciegas que atraviesan Ambato, puede registrarse dentro de 80 a 100 años, y uno de magnitud 6,5 en los próximos 300 años. Por otra parte, se presentan los estudios geofísicos y geotécnicos que se han realizado en el área urbana de la ciudad de Ambato, para obtener curvas de igual periodo de vibración del suelo, así como de igual velocidad de la onda de corte en los primeros 30 m y finalmente clasificar los suelos de la ciudad. Posteriormente, se consideraron seis modelos de movimientos fuertes del suelo y se obtuvieron espectros de aceleración horizontal del suelo en una malla de puntos separados cada 500 m, para cada perfil de suelo. Se hallaron espectros promedio para perfiles de suelo C, D y E al hacer comparaciones con los espectros hallados en el estudio de 2018. Con base en los resultados hallados ahora y en los de 2018, se proponen nuevas formas espectrales para el área urbana de la ciudad de Ambato, denominadas de espectro envolvente, las cuales se comparan con los espectros que reporta la normativa sísmica vigente en Ecuador, NEC-15.

Palabras clave: Peligrosidad sísmica en forma determinística, espectros de aceleración.

1. INTRODUCTION

An earthquake on April 16, 2016 ($M = 7.8$) left about six 600 dead and collapsed several dozen structures, most of them reinforced concrete of between three and seven floors in cities as important as Manta and Portoviejo, where the famous zero zone was established (Aguiar et al., 2016). Following this, municipalities in much of Ecuador did studies to determine the type of soil on which they sit, determining spectra for the design and/or repair of structures and the degree of seismic vulnerability of existing structures.

Such studies are fully justified because the zero zone of the cities mentioned and others like Pedernales and Bahía de Caráquez, which appeared like war zones with very destructive bombing. Unfortunately, many buildings built during the 1980s in Pedernales, Manta, and Portoviejo were destroyed. Other buildings of reinforced concrete with medium height (about ten floors) withstood the quake but with considerable damage in Bahía de Caráquez and Manta (Aguiar, 2017). However, their owners decided to tear them down, e.g., the Salango and Fragata buildings.

Four years have passed since the earthquake and there are empty lots in the aforementioned cities where there were buildings that were apparently earthquake resistant. Thus, the question arises: Why did these buildings have considerable damage, especially those built five years or less before the 2016 earthquake?

There are many factors leading to poor seismic behavior of structures, one being the amplification of seismic waves as an effect of soil type. For example, in the sector known as La Puntilla, in Bahía de Caráquez, modern midrise buildings su-

ffered extensive damage. These sat atop a type C soil profile (a suitable soil), according to the classification of the Ecuadorian Construction Standard NEC-15. There was strong amplification of the waves because the vibration period of the ground was ~ 0.9 s. This is a large value, which shows that it is not adequate to classify soils with the speed of the shear wave in the first 30 m (V_{s30}) or based on the number of blows in the standard penetration test (N_{60}). It is also necessary to include the vibration period in the soil classification (Aguiar and Zambrano, 2018). Thus, the principal municipalities of Ecuador do well in conducting geophysical and geotechnical studies to classify soils from a seismic standpoint.

There are three fundamental factors for the performance of a structure during an earthquake: i) the soil (the more it is known the better); ii) the spectrum or spectra considered for design; iii) good structural performance.

The structures with poor seismic behavior during the 2016 earthquake were flexible, designed for low spectral order. Under these conditions, spectra obtained from the earthquake records were greater than those used in the design.

2. WORKS IN AMBATO

Microzonation studies were conducted in 2018 in the city of Ambato, in the center of Ecuador, which has strong commercial activity. The population in that year was $\sim 180,000$ (Aguiar and Rivas, 2018). Two methods were used to define the acceleration spectra of ground movement: probabilistic, in which geological faults are grouped into seismic sources, and deterministic, wherein the hazard for specific geological faults is evaluated.

In this article, the second method is followed. It might be asked why, if the work was already done in 2018, it was done again in 2020. The reason is that there is a new model of strong motion (Zhao et al., 2016), which the authors of the Ambato seismic microzonation study were unaware of when they did their work in the first half of 2018.

The working models in Zhao et al. (2016) are very interesting, because much of the database was obtained regarding *cangahuas*, which can be considered a rock like that in Ecuador. The previous model of Zhao et al. (2006) is very simple, because with a single equation one can obtain spectra and attenuation ratios of soil movement for three types of seismic sources, i.e., interphase, intraplate, and cortical.

The previous model of Zhao et al. (2006) has been used to compare the attenuation of soil movement from acceleration records of the 2016 Ecuador earthquake, so that use of the standard deviation gives reasonably good correlation.

For the deterministic calculation in the hazard study of 2018, the following strong motion equations were used: Campbell and Bozorgnia (2013), abbreviated C&B; Abrahamson et al. (2013), ASK; Chou and Youngs (2014), CY.

In 2018, we worked with three models of strong motion, whereas now we are working with six, the three above and the additional ones of Zhao et al. (2016), Boore and Atkinson (2008), and Akkar et al. (2014). Moreover, Aguiar and Rivas (2018) did not determine the recurrence period of the three blind faults traversing Ambato. This was determined in the present work, using the methods of the characteristic earthquake and modified Gutenberg and Richter, complementing the earlier study.

3. MODEL OF ZHAO ET AL. (2016)

Two aspects are important in the model of Zhao et al. (2016). The first is incorporation of the soil period in the classification of seismic profiles, which was mentioned in the first section. The second has to do with the incorporation in the model of earthquakes associated with a volcano, an effect that is always important in a volcanic area. For the present study, the area is somewhat distant, so we considered minimum values recommended by the authors, but we nevertheless present four possible cases. Before this, we discuss the executive form of the Zhao et al. (2016) model, which includes two equations. One is for crustal earthquakes (source shallower than 25 km) and the other for upper mantle earthquakes (source deeper than

25 km). In our case, for the seismogenic characteristics of the three faults, we treated crustal earthquakes.

Crustal earthquakes

$$\log_e(y_{i,j}) = f_{mcr} + g_{cr} \log_e(r_{i,j}) + g_{crL} \log_e(x_{i,j} + 200.0) + g_N(c_{i,j}) + e_{cr} x_{i,j} + e_{cr}^v x_{i,j}^v + \gamma_{cr} + \log_e(A^{cr}) + \xi_{ij} + \eta_i \quad (1)$$

Upper mantle earthquakes

$$\log_e(y_{i,j}) = f_{mum} + g_{um} \log_e(r_{i,j}) + g_{crL} \log_e(x_{i,j} + 200.0) + g_N(x_{i,j}) + e_{um} x_{i,j} + e_{cr}^v x_{i,j}^v + \gamma_{cr} + \log_e(A^{um}) + \xi_{ij} + \eta_i \quad (2)$$

In the equations, subscript *cr* indicates that these are crustal earthquakes and subscript *um* refers to the upper mantle. With this clarification, the functions without the subscript are as follows: f_m represents the source effect, a function of the magnitude, focal depth, and type of fault; g is the rate of geometric attenuation, a function of distance and magnitude, considering in the model equations for the near field (g_N) and long distance (g_{crL}). e is the rate of anelastic attenuation, e_{cr}^v is the rate of anelastic attenuation associated with the volcanic path (discussed below), and A^{cr} corresponds to site functions.

The soil classification in Zhao et al. (2016) is indicated in Table 1. In the first column is the nomenclature for soil types and in the last column, their similarity to the classification of the National Earthquake Hazards Reduction Program (NEHRP) (FEMA, 2015). The second column presents a description of the soil. The third column lists classifications according to the vibration period of the soil (which is interesting). The fourth shows the value of V_{s30} . It is important to recognize that the periods of the soils affect their classification, and that if there are soil periods > 0.6 s, one must be concerned with problems of seismic wave amplification.

Table 1. Soil classification considered by Zhao et al. (2015) and similarity with NEHRP

Soil profile	Description	Period (s)	V_{s30} (m/s)	Soil profile NEHRP
SC I	Rock	$T < 0.2$	$V_{s30} > 600$	A + B + C
SC II	Hard soil	$0.2 \leq T < 0.4$	$300 < V_{s30} \leq 600$	C
SC III	Medium soil	$0.4 \leq T < 0.6$	$200 < V_{s30} \leq 300$	D
SC IV	Soft soil	$T \geq 0.6$	$V_{s30} \leq 200$	E + F
SC IV1		$0.6 \leq T < 1.0$	$120 < V_{s30} \leq 200$	E
SC IV2		$T \geq 1.0$	$V_{s30} \leq 120$	F

Source: Zhao et al. (2015) and FEMA (2015).

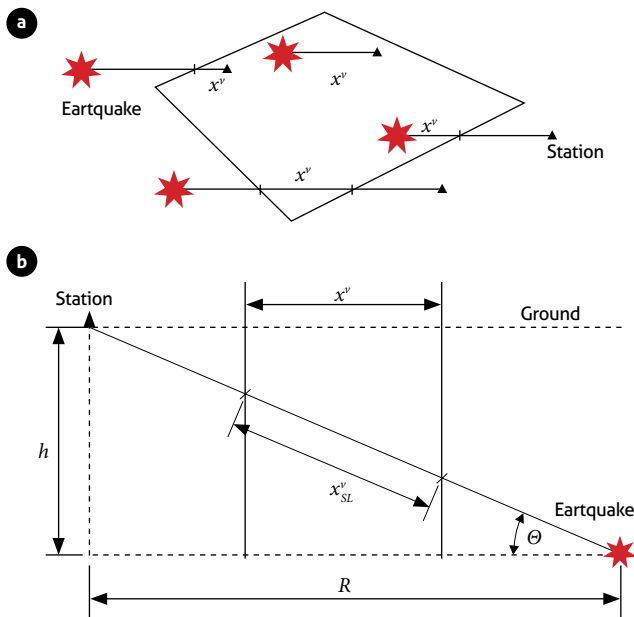


Figure 1. a) Definition of volcanic trajectory for four cases; b) volcanic distance, horizontal and inclined
Source: Zhao et al. (2016).

In some places in the city of Guayaquil, there are soil periods in the order of 3 and 4 s. However, piles are used in building foundations in such a way that in relation to the soils of most of that city, the soils of La Puntilla of Bahía de Caráquez are suitable. Nonetheless, there were substantial amplifications of seismic waves, despite the placement of gravel piles in the reinforcement of some buildings, which stiffen the soil and decrease its period.

Thus, we have the lesson that it is inadequate to classify soil according to shear wave speed because of seismic wave amplification. Thus, it is necessary to know the vibration period of the soil, as has been done for Ambato.

The other important aspect of the Zhao et al. (2016) model is its consideration of volcanism, for which four cases are defined and shown in Figure 1: i) epicenter outside the volcanic zone (VZ) and station or point of interest within the VZ; ii) station and epicenter within the VZ; iii) epicenter in the VZ and station outside it; iv) station and epicenter outside the VZ but they cross it. In all cases, the distance x^v is within the VZ.

4. BLIND FAULTS IN CITY OF AMBATO

Very likely, 90% of the structural designers of the city of Ambato do not know that they are doing calculations for buildings

on an active reverse fault and that an earthquake < 20 km deep is possible. This type of earthquake is known as impulsive and is characterized by a short duration but a dominant pulse that causes great damage to structures if they have not been properly designed.

In this regard, Ambato is built on *blind* geologic faults, i.e., they have no surface outcrop. Therefore, parameters such as fault type, geometry, and length have been obtained from a catalog of active faults (Eguez et al., 2003).

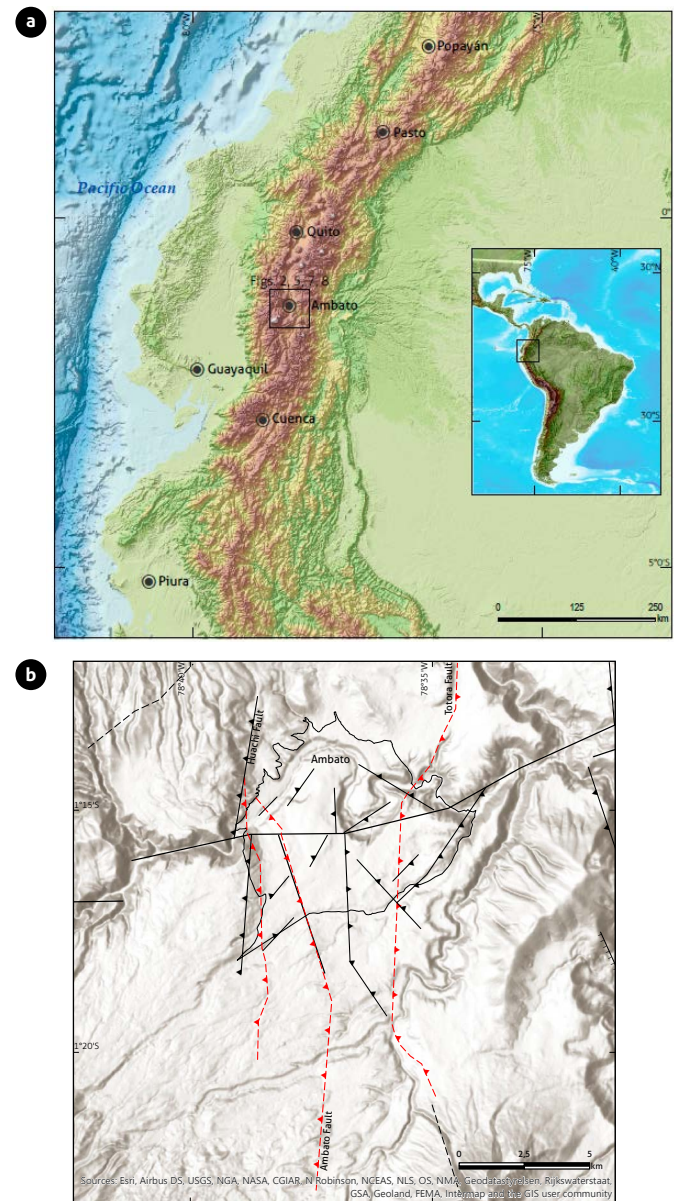


Figure 2. a) General location; b) Geologic faults selected in study of seismic hazard in urban area of Ambato
Source: Eguez et al. (2003); Chunga and Mulas (2018).

The urban area of the city of Ambato is traversed by three faults, which are shown in Figure 2. In the upper left of the figure there is Huachi, a reverse fault with length ~ 12.04 km. At right is Totoras, the longest fault. It is a lateral reverse fault of length 17.65 km. At bottom is Ambato, which is a reverse fault of 16.3 km length (Eguez et al., 2003; Chunga and Mulas, 2018).

It is important that the city of Ambato is in a valley, surrounded by mountains with steep slopes on which there is construction. Thus, there is a strong probability of landslides of large soil masses in an earthquake on one of the reverse faults. In addition, this construction mostly belongs to people with few economic resources.

Table 2 presents the faults of the study, indicating the maximum magnitude expected for each. These were found using Equations (3) and (4), proposed by Leonard (2010), and Equation (5), formulated by Wells and Coppersmith (1994) from the relationship between fault length (L), area (A), and width (W). The magnitude was found with these three proposed equations. Then, the average was obtained and rounded to the next larger value.

$$M_w = 1.52 \log(L) + 4.4 \quad (3)$$

$$M_w = 1.0 \log(A) + 4.0 \quad (4)$$

$$M_w = 1.22 \log(L) + 5.0 \quad (5)$$

Table 2. Parameters of blind faults traversing urban and rural areas of city of Ambato

Fault	δ	λ	M	L (km)	A (km ²)	W (km)	Type
Ambato	45	90	6.5	16.3	97.80	6	Blind reverse
Huachi	45	90	6.3	12.04	72.24	6	Blind reverse
Totoras	45	90	6.5	17.65	105.90	6	Lateral blind reverse

Source: Aguiar and Rivas (2018).

5. RECURRENCE PERIOD

The recurrence period is different from the return period, widely used in seismic regulations for the publication of design spectra. The recurrence period is the period between earthquakes of a certain magnitude. The return period is a statistical term that relates the useful life of a structure with the probability of exceeding parameters considered in soil motion.

The two periods are complementary because it is important to know, for example, the time (in years) that it takes for a magnitude 6.5 earthquake to occur on the Totoras fault. Ob-

viously, this time corresponds to a model calculation and will therefore have some uncertainty, but in this way the structural designer will have an idea that will help him or her determine the safety to ascribe to a project.

Likewise, it is important that the structural designer know the probability of exceedance of the spectrum to be used, thereby obtaining spectra for a lower or higher probability of exceedance, combined with the recurrence period.

Again by way of example, in the analysis of the 100-year recurrence period associated with a geologic fault, it is necessary to work with an exceedance probability of $< 10\%$, because the recurrence period of a geologic fault is short and the beginning time of that period is unknown.

The first model for calculating the recurrence period is called the characteristic earthquake method, which assumes that earthquakes occur with perfect periodicity. This is a simple model that equates the accumulated seismic moment of the fault with the seismic moment released during the maximum earthquake on fault M_0 (Rivas, 2014).

$$T_r = \frac{M_0}{M_w} \quad (6)$$

$$M_0 = \mu \dot{u} A \quad (7)$$

$$M_0 = 10 \frac{(M_w + 10.7)^3}{2} \quad (8)$$

The as yet undefined variables are: μ , stiffness modulus or shear ($\mu \approx 3 \times 10^9 \frac{\text{kgf}}{\text{m}^2}$); the slip rate \dot{u} , area of the fault plane A ; magnitude of the moment M_w .

On the other hand, the Gutenberg and Richter (1944) model, modified by Cosentino et al. (1977), assumes that during the recurrence period there may be earthquakes of lesser magnitude, for the maximum quantity of which one wishes to calculate T_r . The calculation equations are as follows.

$$\dot{N}_{(m)} = \dot{N}_{M_{min}} * \left[\frac{e^{-\beta(m)} - e^{-\beta(M_{max})}}{e^{-\beta(M_{min})} - e^{-\beta(M_{max})}} \right] \quad (9)$$

$$\dot{N}_{M_{min}} = \frac{\dot{M}_0 (\bar{d} - \beta) (e^{-\beta M_{min}} - e^{-\beta M_{max}})}{\beta [e^{-\beta M_{max}} M_0 (M_{max}) - e^{-\beta M_{min}} M_0 (M_{min})]} \quad (10)$$

$$M_0 (M_{min}) e^{(\bar{c} + \bar{d} M_{min})} - M_0 (M_{max}) e^{(\bar{c} + \bar{d} M_{max})} \quad (11)$$

$$\bar{c} = 16.05 * \ln(10) \quad \bar{d} = 1.5 * \ln(10) \quad (12)$$

Here, $\dot{N}_{(m)}$ is the accumulated rate of earthquakes with magnitude $\geq m$. It is the accumulated rate of earthquakes of

magnitude $\geq M_{min}$ (the minimum magnitude). M_{max} is the maximum magnitude considered. β is a parameter of fault seismicity. $M_0(M_{min})$ is the minimum seismic moment and $M_0(M_{max})$ the maximum seismic moment.

Once the considered magnitude has been obtained, we determine $\dot{N}_{(m)}$ and the non-annual accumulated rate of earthquakes $\hat{N}_{(m)}$, which is obtained by subtracting the accumulated annual rate of two consecutive quantities to ultimately determine the recurrence period, which is the inverse of the non-accumulated annual rate.

It is important to note that the accumulated rate of seismic moment is assumed to be released by earthquakes of different magnitudes and is between M_{min} and M_{max} , the latter determined by the size of the fault plane.

Considering the equation of Gutenberg and Richter (1944), it follows that

$$\log N = a - b M \tag{13}$$

Here, N is the number of earthquakes of magnitude $\geq M$ and a and b are seismicity parameters of the fault. However, the Ambato, Huachi and Totoras faults are in source zone 6 of the model of Beauval et al. (2018), and for that zone (known as the Pallatanga fault) these parameters are: $a = 2.8012$, $b = 0.73$, which were adopted for the three blind faults in the city of Ambato. Equation (13) can then be written as follows.

$$\ln N = \alpha - \beta m \tag{14}$$

$$\alpha = a \ln 10 \quad \beta = b \ln 10 \tag{15}$$

In Equation (15) we have the parameter β , which appears in Equations (9) and (10). Finally are defined all calculation equations to determine the recurrence period in the two models. It only remains to mention that we took $\dot{u} = 3.5$ mm/yr, because Alvarado et al. (2014) stated that for a fault system, the rate of motion is between 3.0 and 4.0 mm/yr.

Figure 3 presents graphically the recurrence period results for each blind fault crossing Ambato. Figure 3a shows results of the characteristic earthquake method and Figure 3b those from Gutenberg and Richter.

Based on the results, we can say that for a magnitude of maximum moment = 6.5, associated with the blind faults of Ambato and Totoras, the period is ~600 years. For an earth-

quake of magnitude of maximum moment = 6.3, related to the Huachi fault, that period is ~400 years.

The city of Ambato was founded on August 24, 1534, and was destroyed by an earthquake on June 20, 1698, which was short-lived. We assume that this was associated with one of the blind faults in the city. Therefore, a second foundation of the city occurred in 1698, and since that time there have been no earthquakes that could be associated with the blind faults of Ambato.

The Riobamba earthquake of February 4, 1797 completely destroyed the ancient city of Riobamba and caused very severe damage in Ambato, but it was not related to the blind faults of the city. Something similar can be said of the earthquake on August 5, 1949, which also destroyed Ambato but whose epicenter was in Pelileo, distant from the city.

The faults portrayed in Figure 2 are in source zone 6, known as the Pallatanga fault from the model of Beauval et al. (2018). We cite this reference because we used the seismicity parameters $a = 2.8012$ and $b = 0.73$ from the classical model of Gutenberg and Richter $\log N = a - b M$, whose values were found for source zone 6.

Table 3 lists the calculated recurrence periods associated with Ambato fault, and Table 4 the values for Huachi and Totoras faults.

The characteristic earthquake method assumes that earthquakes occur with perfect periodicity, obtaining a return period

Table 3. Recurrence period from GR model modified for Ambato fault

m	Accumulated annual rate $\dot{N}_{(m)}$	Non-accumulated annual rate $\hat{N}_{(m)}$	Recurrence period (years)
4.5	0.0490	0.0289	34.65
5.0	0.0201	0.0125	80.31
5.5	0.0077	0.0054	186.11
6.0	0.0023	0.0023	431.28
6.5	0.0000	0.0001	676.45

Table 4. Recurrence period from GR model modified for Huachi and Totoras faults

Huachi				Totoras			
m	$\dot{N}_{(m)}$	$\hat{N}_{(m)}$	T_r (years)	m	$\dot{N}_{(m)}$	$\hat{N}_{(m)}$	T_r (years)
4.5	0.0510	0.0305	32.82	4.5	0.0530	0.0312	32.04
5.0	0.0205	0.0131	76.05	5.0	0.0218	0.0135	74.25
5.5	0.0074	0.0057	176.24	5.5	0.0083	0.0058	172.06
6.0	0.0017	0.0017	276.43	6.0	0.0025	0.0025	398.73
6.3	0.0000	0.0000	336.54	6.5	0.0000	0.0000	625.40

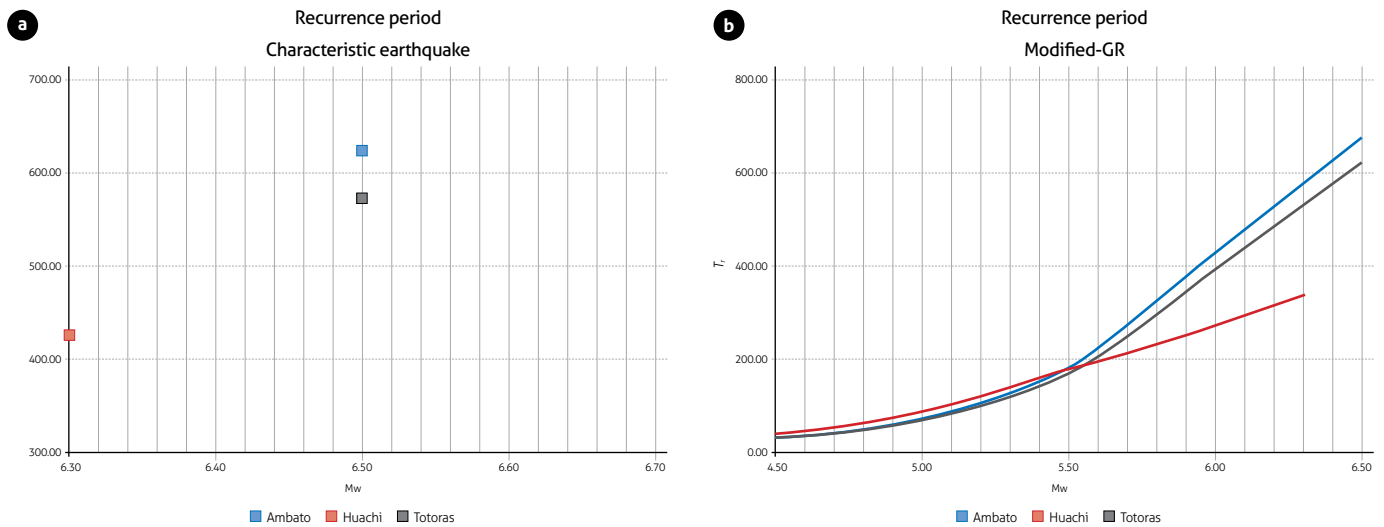


Figure 3. Recurrence periods for blind faults crossing Ambato. a) characteristic earthquake method; b) modified Gutenberg and Richter method.

for a specific moment magnitude, whereas the Gutenberg and Richter model treats the probability that a fault produces earthquakes of different magnitudes with varying recurrence periods.

Given the above, 1698 can be considered the start year to determine roughly when the next earthquake associated with the Huachi, Ambato and Totoras faults will occur. Based on our results, an earthquake of magnitude 6.3, associated with Huachi, is expected between 80 and 100 years hence, and a magnitude 6.5 in ~80–700 years.

A major problem is that a sizeable part of the city would not be able to withstand a magnitude 6.3 quake with focal depth ~10 km. This is asserted based on the Study of Seismic Vulnerability for the city of Ambato, in which a seismic analysis of ~450 structures was carried out (Aguiar, 2018).

6. GEOPHYSICAL AND GEOTECHNICAL STUDIES

At nine sites in the urban area of the city of Ambato (indicated in Figure 4), data of the active source were obtained from an impact that generated waves recorded by geophones (active source) and environmental vibration (passive source, MASW). We applied the combined method to these two databases and determined the shear wave speed V_s , reaching at least 50 m depth, to obtain V_s in the first 30 meters (designated V_{s30}) as one of the parameters used for the soil classification (Aguiar and Rivas, 2018).

The period of soil vibration was obtained for the above locations using other measurement equipment (SARA), using environmental vibration and the Nakamura method.

The periods of vibration found determined curves of the same period (Figure 5a), which varied between 0.11 and 0.45 s. Thus, from the point of view of seismic wave amplification, soils of the city of Ambato can be classified as favorable.

Furthermore, using the values of V_{s30} , we constructed the curve of equal shear wave speed values in the first 30 m (Figure 5b), which is generally between 300 to 450 m/s. These values correspond to favorable soil from a seismic perspective. There are very specific sites corresponding to creek fills that had V_{s30} on the order of 120 m/s.

To classify soils seismically requires determination of the number of blows (N_{60}) obtained with the standard penetration test (SPT), for which we conducted geotechnical studies at the same locations as the geophysical studies (Figure 6; also shown in the photos of Figure 4).

Drillings to 30-m depth did not reach the water table, which helped further validate that the soils of Ambato are resistant. In addition to finding the value of N_{60} , during the test we obtained unaltered soil samples at some sites, and at other sites altered. With these, we performed triaxial laboratory tests to determine cohesion and the friction angle of the soil (Aguiar and Rivas, 2018).

The soils of Ambato were classified following the NEC-15 classification method and using the following information: V_{s30} , period of vibration of the soil T_s , N_{60} , values of cohesion c , angle of internal friction Φ , and ground shear. The results are presented in Figure 7.

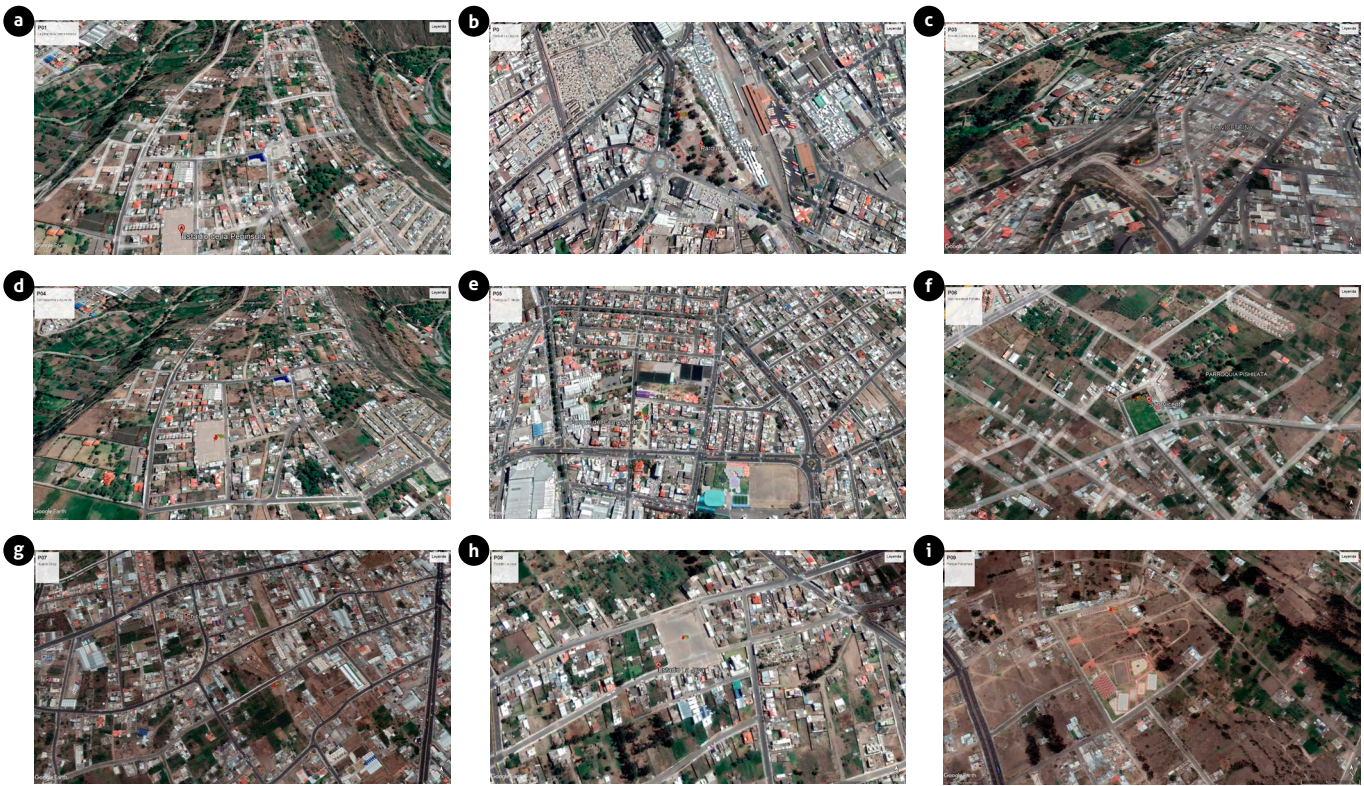


Figure 4. Sites of geophysical studies
 a) San Luis stadium; b) La Laguna park; c) La Floreana stadium; d) La Península neighborhood league; e) Celiano Monje park; f) San Vicente de Pishilata neighborhood league; g) green area of Huachi Chico; h) La Joya stadium; i) Pasochoa park. Source: Aguiar and Rivas (2018).

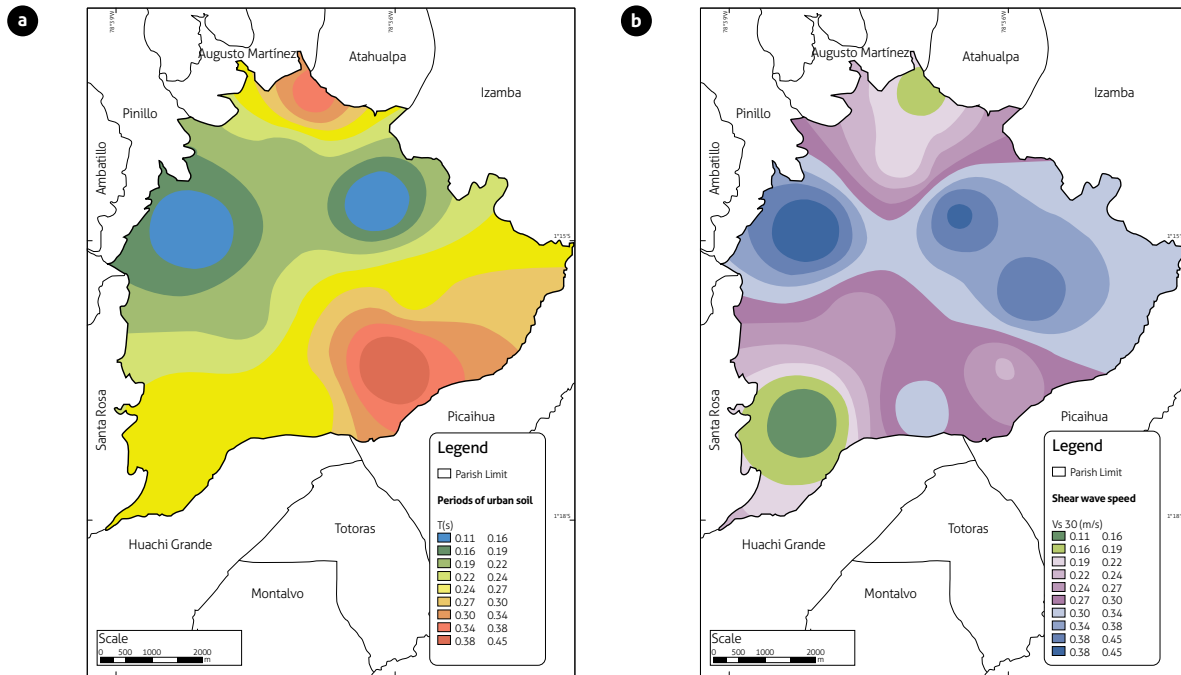


Figure 5. Studies of seismic hazard of urban area of city of Ambato: a) soil vibration period; b) shear wave speed in the first 30 m
 Source: Aguiar and Rivas (2018).



Figure 6. Sites of standard penetration tests (SPT), at the same locations as the geophysical studies
Source: Aguiar and Rivas (2018).

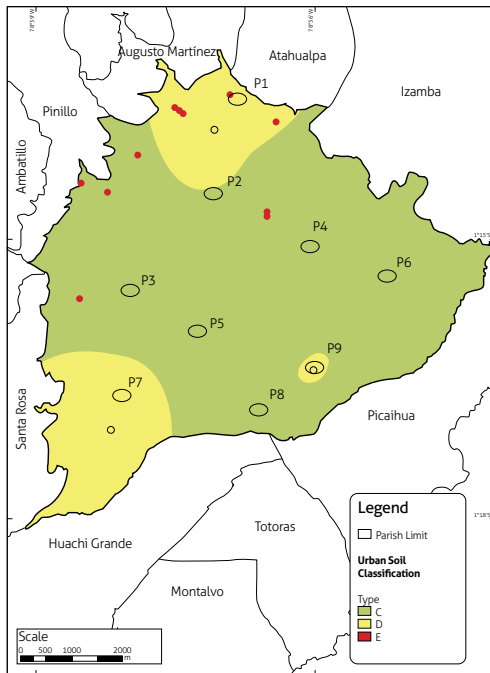


Figure 7. Classification of soils in city of Ambato from standpoint of seismic hazard
Source: Aguiar and Rivas (2018).

Figure 7 reveals that most of the soils of Ambato are of type C and D. As indicated, there are several parameters involved in the soil classification, but V_{s30} is the most used in the models of strong motion, For this reason, the range of V_{s30} according to soil type is indicated very briefly below, following the NEC-15 standard (Table 5).

Table 5. Soil classification according to NEC-15 and NEHRP (FEMA, 2015)

Soil profile	V_{s30}
A	$V_{s30} > 1500 \text{ m/s}$
B	$760 \text{ m/s} < V_{s30} \leq 1500 \text{ m/s}$
C	$360 \text{ m/s} < V_{s30} \leq 760 \text{ m/s}$
D	$180 \text{ m/s} < V_{s30} \leq 360 \text{ m/s}$
E	$V_{s30} \leq 180 \text{ m/s}$

Source: NEC-15.

7. SPECTRA OF HORIZONTAL ACCELERATION

To calculate the acceleration spectra with respect to the horizontal component of soil movement using the deterministic

method, the urban area of the city of Ambato was divided into three grids with points separated by 500 m in both horizontal directions. Figure 8a shows the grid in a general way and Figure 8b the grid for soil profiles C, D and E.

The horizontal acceleration spectra were calculated for each soil profile, considering an earthquake of maximum magnitude on each of the blind faults (Huachi, Ambato and Totoras). The focus of this earthquake was located at the center of gravity of the fault. For each equation of strong motion, we found control spectra at all grid points, ultimately obtaining an average. These spectra are presented below and were determined using an EXCEL program developed for the purpose.

For a soil profile C, the calculation was done using $V_{s30} = 340 \text{ m/s}$. For a soil profile D, $V_{s30} = 300 \text{ m/s}$, and for a soil profile E, $V_{s30} = 180 \text{ m/s}$.

Figure 9a shows average spectra for an earthquake of maximum magnitude ($M = 6.3$) on the Huachi fault, for which the spectra were determined at each grid point and the average value was established. This was done for each strong motion equation. The model of Zhao et al. (2016) produced the largest spectral ordinates, in an area with short periods.

The spectra in Figure 9b correspond to the average of values from each of the six models, which is identified as “Spectra 2020”. The average spectra from three equations of strong motion used in the 2018 study are labeled “Spectra 2018”.

Figure 9c and d is analogous, but for a maximum-magnitude earthquake on the Ambato fault ($M = 6.5$). Finally, Figure 9e and f shows results for a maximum-magnitude earthquake ($M = 6.5$) on the Totoras fault. It is interesting to compare the spectra of Figures 9 b, d and f, which is done in the next section.

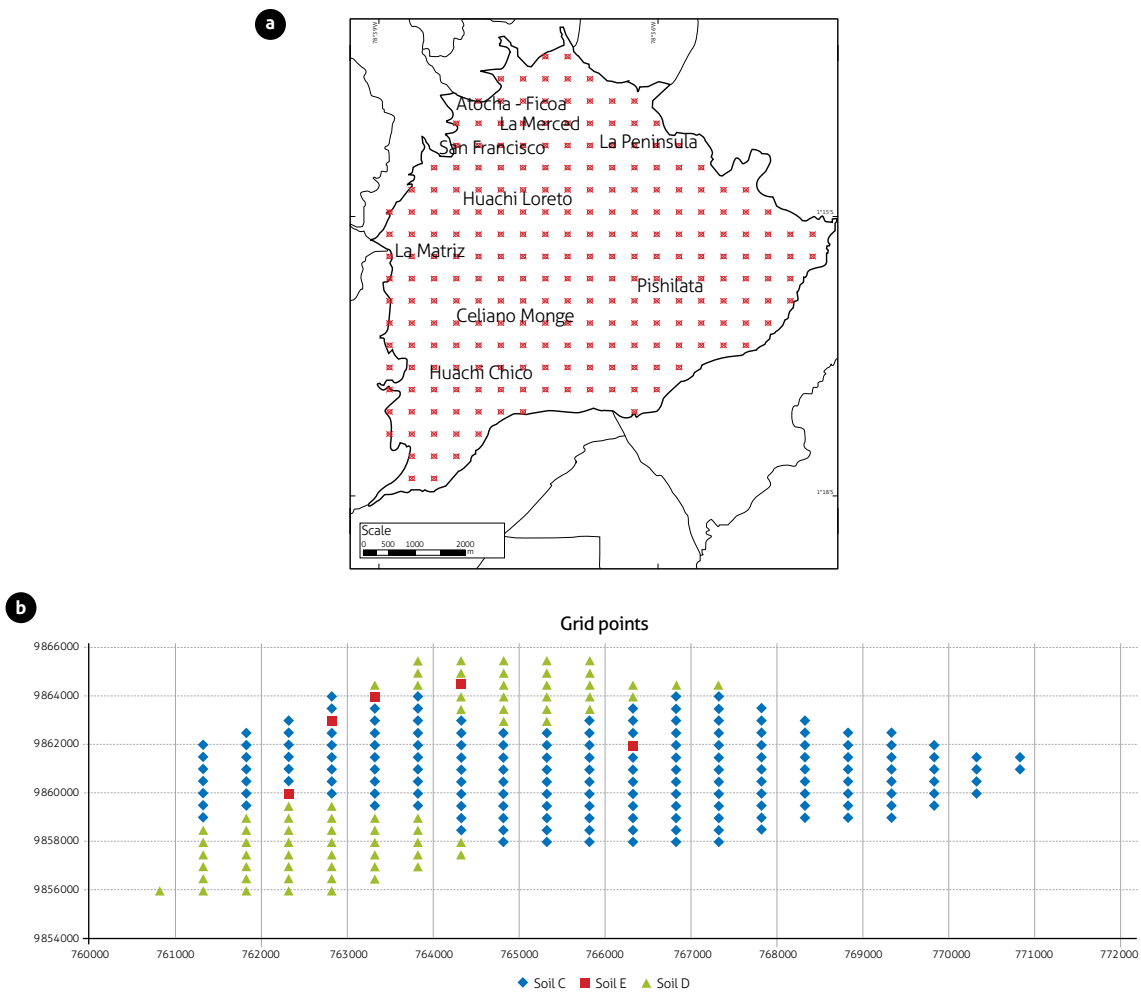


Figure 8. a) Grid points in urban area of Ambato; b) profiles of soils C, D and E

As with the type C soil profile, we proceeded with the type D and E soils in the city of Ambato, obtaining the average spectra in Figures 10 and 11 (considering an earthquake of maximum magnitude on each fault).

In general, Spectra 2020 has greater ordinates than Spectra 2018, but not in all periods. Indeed, for an earthquake on

the Totoras fault ($M = 6.5$), the spectral ordinates of Spectra 2018 are slightly greater. However, for short periods, the spectral ordinates of Spectra 2020 are slightly greater than those of Spectra 2018, but for the remaining periods they are very similar.

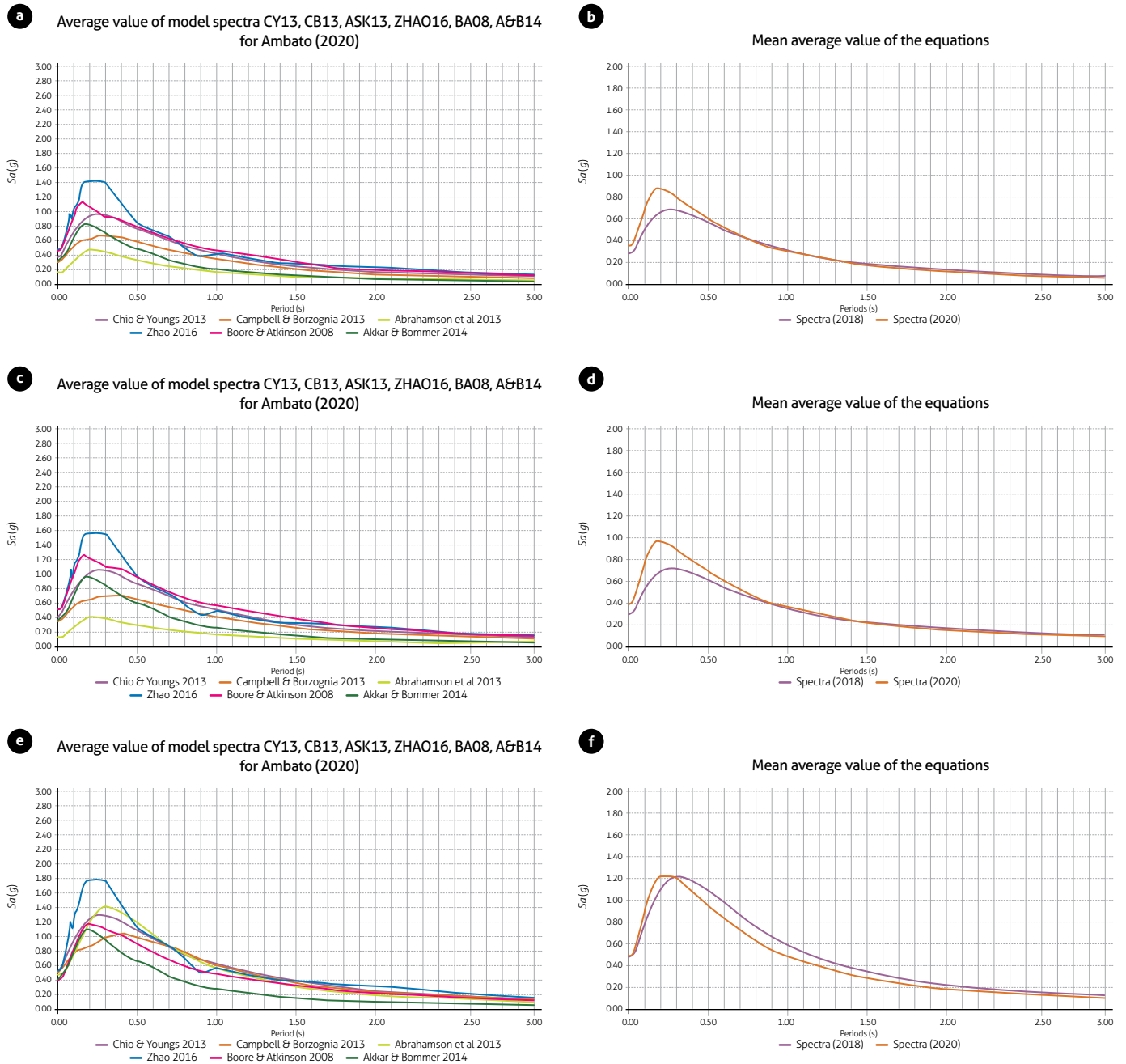


Figure 9. Spectra in a C soil profile
 a) Earthquake on Huachi fault from all models; b) average spectra from studies of 2018 and 2020; c) earthquake on Ambato fault from all models; d) average spectra from studies of 2018 and 2020; e) earthquake on Totoras fault from all models; f) average spectra from studies of 2018 and 2020.

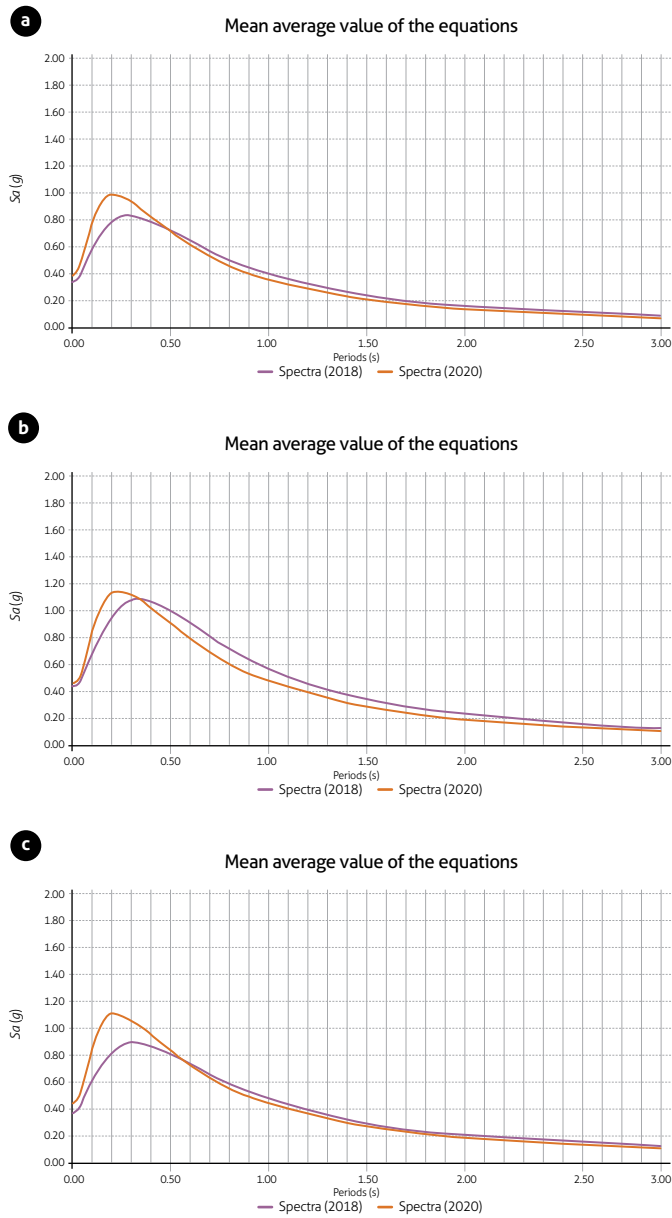


Figure 10. Average spectra in a soil profile D, found using the six equations of strong motion in present study and three equations from study of 2018 a) Earthquake on Huachi fault; b) earthquake on Ambato fault; c) earthquake on Totoras fault.

8. SPECTRAL ENVELOPES

With the values of Spectra 2020 and Spectra 2018 we determined a spectral envelope from averages of seismic hazard studies in 2018 and 2020 for soil type C shown in Figure 9b, d and f. For soil type D we considered the spectra of Figure 10, and for type E those of Figure 11.

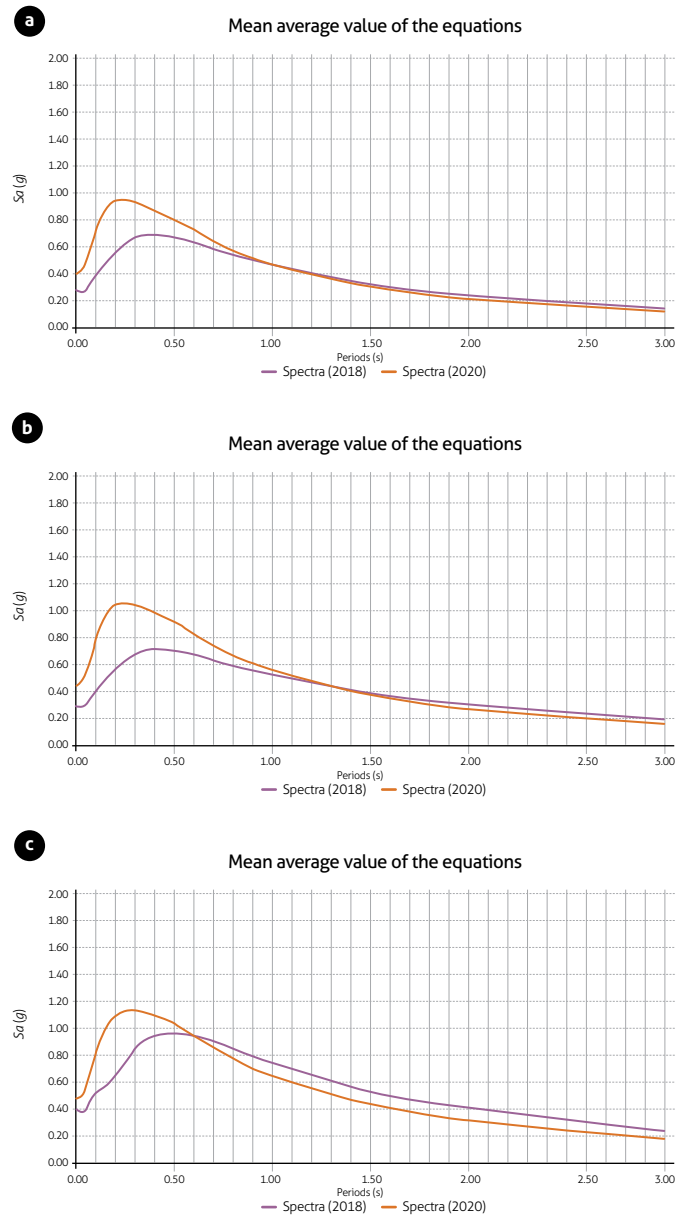


Figure 11. Average spectra in soil profile E, found using the six equations of strong motion in present study and three equations of study of 2018 a) Earthquake on Huachi fault; b) earthquake on Ambato fault; c) earthquake on Totoras fault.

For the spectra associated with type D soil from each strong motion model, Figure 12 presents these values and the spectral envelope.

There are clearly periods in which the spectral ordinate found by a model is greater than the spectral envelope, but the values are < 10% of the probability of exceedance.

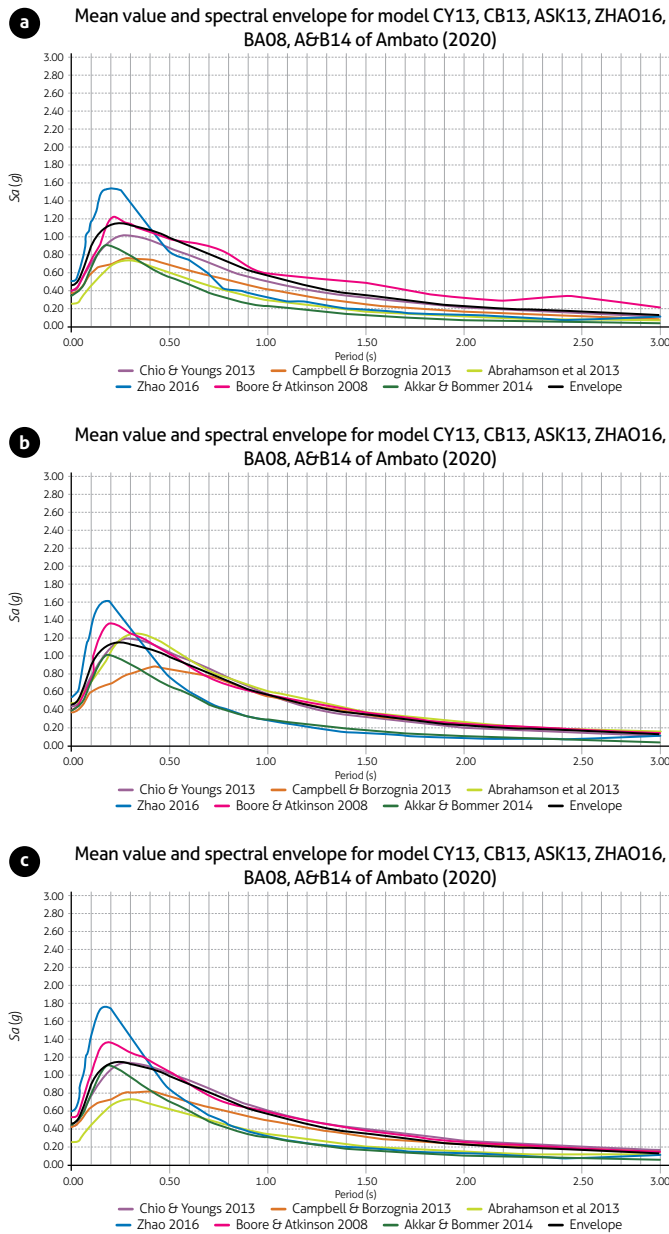


Figure 12. Spectra from each of six models in the study and spectral envelope derived from average values of seismic hazard studies in 2018 and 2020
 a) Earthquake on Huachi fault ($M = 6.3$); b) earthquake on Ambato fault ($M = 6.5$); c) earthquake on Totoras fault ($M = 6.5$).

We then compared spectral envelopes with reports in the Ecuadorian Standard of Construction (NEC-15) for three soil profiles (Figure 13a) in a C seismic soil profile. There was a good approximation between the two.

Figure 13b compares the spectra for a soil profile D, which suggests a reduction in spectral shape for long periods. Finally, Figure 13c shows the spectra for a soil profile E, which differ

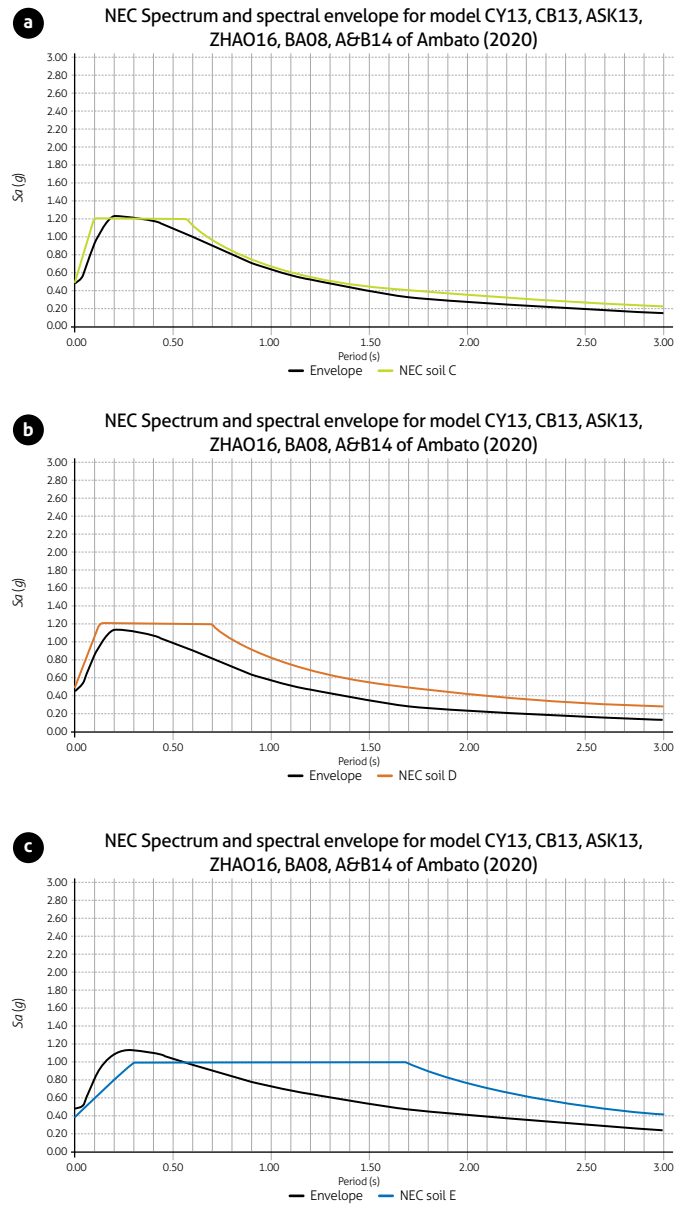


Figure 13. Comparison of spectral envelopes with those reported in NEC-15
 a) Soil type C; b) soil type D; c) soil type E.

the most with respect to the spectrum of NEC-15. Here, for the constant acceleration platform, the spectral ordinates are $\sim 1.2 g$.

The results of our study are very valuable and make an important contribution to comparing spectra obtained from the probabilistic method, in order to finally determine the shape of the spectra for the city of Ambato.

9. COMMENTS AND CONCLUSIONS

After the 2016 earthquake of Pedernales ($M = 7.8$), which left much destruction and death in the provinces of the northern coast of Ecuador, some municipalities decided to conduct seismic hazard studies. Among these were Ambato, where it was decided to do a seismic microzoning of the urban area in 2018. In these studies, two methods (probabilistic and deterministic) were used to find the spectra vs. the horizontal component of ground movement. For the last method, values were acquired from three models of strong motion, which have been called in this article Spectra 2018.

In the 2018 study, geophysical and geotechnical studies were done in different places of the city, at least one in each parish, to determine the vibration period of the soil, speed of the shear wave in the first 30 m, number of blows in the SPT, and other parameters from which the soils were classified from a seismic perspective.

For each seismic soil profile, the 2018 Spectra were found by considering a seismic event of maximum magnitude on each of three blind faults traversing the city. In this endeavor, the recurrence period of an earthquake of maximum magnitude was first determined for each fault, using the two aforementioned methods. Results were analyzed in relation to the historical seismicity of the city, discovering that an earthquake with magnitude 6.3 can occur in the next 80 to 100 years, and one of magnitude 6.5 during the next 300 years.

In the same way, spectra were obtained using the deterministic method, but considering six models with strong motion equations, among them that of Zhao et al. (2016). These were obtained from Spectra 2020, which are very similar to those of 2018. Therefore, we decided to consider as a contribution to the studies of 2018 the spectral envelopes, the same that were compared to the spectra that would be obtained in each soil seismic profile for earthquakes of maximum magnitude on each fault, and were compared with the spectra reported in the Ecuadorian Standard of Construction (NEC-15). There was strong correlation for soil profile C, whereas for profile D, there was a reduction of spectral ordinates for long periods. For soil profile E, it is suggested to increase the spectrum plateau to 1.2 g.

ACKNOWLEDGMENTS

The authors thank the anonymous reviewers for their contribution to improve the manuscript.

REFERENCES

- Abrahamson, N., Silva, W., & Kamai, R. (2013). *Update of the AS08 Ground Motion Prediction Equations based on the NGA-West2 Data Set*. Pacific Earthquake Engineering Research Center, PEER.
- Aguiar, R. (2017). No se acepta el diseño por ductilidad. Caso del Edificio Fragata que incurrió en el rango no lineal. *Revista Internacional de Ingeniería de Estructuras*, 22(3), 327-391.
- Aguiar, R. (2018). Vulnerabilidad sísmica de Ambato [Consulting carried out for Ambato].
- Aguiar, R., & Rivas, A. (2018). Espectros de peligro sísmico uniforme para la ciudad de Ambato. In R. Aguiar, & A. Rivas (eds.), *Microzonificación sísmica de Ambato* (pp. 103-119). Instituto Panamericano de Geografía e Historia.
- Aguiar, R., & Zambrano, V. (2018). Relation H/T in structures of Bahía de Caráquez and the 2016 earthquake. *Revista Internacional de Ingeniería de Estructuras*, 23(2), 227-241.
- Aguiar, R., Zevallos, M., Palacios, J., García, L., & Menéndez, E. (2016). *Reforzamiento de estructuras con disipadores de energía. Caso del terremoto del 16 de abril de 2016*. Instituto Panamericano de Geografía e Historia (IPGH).
- Akkar, S., Sandıkkaya, M., & Bommer, J. (2014). Empirical ground-motion models for point- and extended-source crustal earthquake scenarios in Europe and the Middle East. *Bulletin of Earthquake Engineering*, 12, 359-387. <https://dx.doi.org/10.1007/s10518-013-9461-4>
- Alvarado, A., Audin, L., Nocquet, J., Lagreulet, S., Segovia, M., Font, Y., Lamarque, G., Yepes, H., Mothes, P., Rolandone, F., Jarrin, P., & Quidelleur, X. (2014). Active tectonics in Quito, Ecuador, assessed by geomorphological studies, GPS data, and crustal seismicity. *Advancing Earth and Space Science*, 33, 67-83. <https://doi.org/10.1002/2012TC003224>
- Beauval, C., Marinier, J., Yepes, H., Audin, L., Nocquet, J., Alvarado, A., Baize, S., Aguiar, J., Singaicho, J. C., & Jomard, H. (2018). A New Seismic Hazard Model for Ecuador. *Bulletin of the Seismological Society of America*, 108(3A), 1443-1464. <https://doi.org/10.1785/0120170259>
- Boore, D., & Atkinson, G. (2008). Ground Motion Prediction Equations for the Average Horizontal Component of PGA, PGV, and 5 %-Damped PSA at Spectral Periods between 0.01 s and 10.0 s. *Earthquake Spectra*, 24(1), 99-138. <https://doi.org/10.1193/1.2830434>

- Campbell, K., & Bozorgnia, Y. (2013). NGA-West2 Ground Motion Model for the Average Horizontal Components of PGA, PGV, and 5% damped linear acceleration response spectra. *Earthquake Spectra*, 30(3), 1087-1115. <https://doi.org/10.1193/062913EQS175M>
- Choiu, B., & Youngs, R. (2014). Update of the Choiu and Youngs NGA ground motion model for average horizontal component of peak ground motion and response spectra. *Earthquake Spectra*, 30(3), 1117. <https://doi.org/10.1193/072813EQS219M>
- Chunga, K., & Mulas, F. (2018). Zonificación geológica, volcánica y sísmica. In R. Aguiar, & A. Rivas (eds.), *Microzonificación Sísmica de Ambato* (pp. 120-172). Instituto Panamericano de Geografía e Historia.
- Cosentino, P., Ficarra, V., & Luzio, D. (1977). Truncated Exponential Frequency-Magnitude Relationship in Earthquake Statistics. *Bulletin of the Seismological Society of America*, 67(6), 1615-1623.
- Eguez, A., Alvarado, A., & Yepes, H. (2003). *Database and Map of Quaternary Faults and Folds of Ecuador and its offshore regions* [Open File Report]. U. S. Geological Survey.
- Federal Emergency Management Agency of the U.S. Department of Homeland Security (FEMA). (2015). NEHRP Recommended seismic provisions for new buildings and other structures Volume I: Part 1 Provisions, Part 2 Commentary.
- Gutenberg, B., & Richter, F. (1944). Frequency of Earthquakes in California. *Bulletin of the Seismological Society of America*, 34(4), 185-188. <https://doi.org/10.1785/BSSA0340040185>
- Leonard, M. (2010). Earthquake fault scaling: Self-consistent relating of rupture length, width average displacement and moment release. *Bulletin of the Seismological Society of America*, 100(5A), 1971-1988. <https://doi.org/10.1785/0120090189>
- NEC-15. (2015). *Norma ecuatoriana de la construcción SE-DS. Cargas sísmicas. Diseño sismo resistente*. NEC-SE-DS.
- Rivas, A. (2014). *Contribución metodológica para incorporar fallas activas en la modelización de la fuente dirigida a estimaciones de peligrosidad sísmica. Aplicación al sur de España* [Ph.D. Thesis]. Universidad Politécnica de Madrid.
- Wells, D., & Coppersmith, J. (1994). New Empirical Relationship among Magnitude, Rupture Length, Rupture Width, Rupture Area, and Surface Displacement. *Bulletin of the Seismological Society of America*, 84(4), 974-1002.
- Zhao, J., Zhang, J., Asano, A., Ohno, Y., Oouchi, T., Takahashi, T., Ogawa, H., Irikura, K., Hong, K., Somerville, P., Fukushima, Y., & Fukushima, Y. (2006). Attenuation Relations of Strong Ground Motion in Japan Using Site Classification Based on Predominant Period. *Bulletin of the Seismological Society of America*, 96(3), 898-913. <https://doi.org/10.1785/0120050122>
- Zhao, J., Zhou, S., Gao, P., Long, T., Zhang, Y., Thio, H., Lu, M., & Rhoades, A. (2015). An earthquake classification scheme adapted for Japan determined by the goodness-of-fit for ground-motion prediction equations. *Bulletin of the Seismological Society of America*, 105(5), 2750-2763. <https://doi.org/10.1785/0120150013>
- Zhao, J., Zhou, S., Zhou, J., Zhao, C., Zhang, H., Zhang, Y., Gao, P., Lan, X., Rhoades, D., Fukushima, Y., Somerville, P., & Irikura, K. (2016). Ground-Motion Prediction Equations for Shallow Crustal and Upper-Mantle Earthquakes in Japan Using Site Class and Simple Geometric Attenuation Functions. *Bulletin of the Seismological Society of America*, 106(4), 1552-1569. <https://doi.org/10.1785/0120150063>



Boletín Geológico

Editorial Policy

Boletín Geológico is a serial scientific publication of the Servicio Geológico Colombiano (SGC), active since 1953, aiming to promote and disseminate research in the Earth sciences. *Boletín Geológico* publishes original scientific manuscripts of research, reflections, reviews, data and case reports on the Earth sciences, in Spanish or English.

Objective and scope

To disseminate scientific knowledge in the following fields of research:

- » Stratigraphy, sedimentology, structure and evolution of basins.
- » Geochemistry, geophysics, volcanology, igneous and metamorphic petrology.
- » Tectonics, seismotectonic and geodynamic modeling.
- » Hydrogeology, oceanography and geothermal energy.
- » Economic geology, mineralogy, metallogenesis, hydrocarbon genesis and reservoirs.
- » Geomorphology, geological hazards, environmental geology, soil research, climate change and geological heritage.
- » Paleontology, paleoclimatology, Quaternary geology and geoaerchology.
- » Software applications and artificial intelligence in Earth sciences.

Boletín Geológico may also include compilations, short notes and manuscripts on the state of knowledge and special research on critical and relevant issues.

Articles from authors linked or not linked to the Servicio Geológico Colombiano are accepted.

Periodicity

Biannual publication with online publishing in June and December of each year.

Publishing costs

The contents of the journal are freely available without charge to readers and can be reused after download with proper bibliographic reference.

The journal does not charge authors any fees for sending or receiving their article, for the editorial process, or for publishing. It is completely funded by the Servicio Geológico Colombiano.

Open Access Statement

The content of the journal is protected under a Creative Commons - attribution license. Consequently, the work may be copied, redistributed, remixed, adapted, transformed, and built upon to create new works from the content for any purpose (including commercial purposes). The journal guarantees open access to all published content, users can read, download, copy, distribute,

print, search or link the full texts of the articles. Whoever exercises any of the aforementioned rights must adequately credit the copyright on the original work and indicate if the work was modified.

The Servicio Geológico Colombiano is not responsible for any damage or harm derived from the exercise of the rights granted under the Creative Commons attribution license, nor does it offer guarantees of any kind in relation to the licensed material.



Attribution (CC BY)

Archive and preservation

Boletín Geológico uses the LOCKSS system to create a storage system that allows the creation of permanent files for conservation and restoration purposes.

Instructions to Authors

Authorship

The authorship of a postulated article should include those who actively and substantially contributed to the intellectual content and the analysis or interpretation of the data; as such, the authors are publicly responsible for the article submitted. The list and order of the authors should be reviewed before submitting the work the first time for publication. After submitting an article, authorship changes are not accepted.

Transfer of patrimonial copyright to the Servicio Geológico Colombiano

The authors of an article approved for publication transfer patrimonial copyright to the Servicio Geológico Colombiano for its subsequent dissemination, reproduction and distribution in the printed and digital media available to the Servicio Geológico Colombiano, as well as for its inclusion in national or international databases and indexes.

Author requirements

- » Understand the editorial policy of the *Boletín Geológico* and the derived processes, and be in agreement with them.
- » Include all the people who contributed to the preparation of the manuscript as authors.
- » Abide by all ethical guidelines for authors and reviewers.
- » In the event that the reviewers of the article/publication suggest the need to make changes or adjustments before their approval, the authors agree to make such adjustments in the time required by the *Boletín Geológico*.

The obligations of the authors are included in the letter of authorship found [HERE](#), or in the corresponding steps when submitting an article. Sending the letter of authorship is an essential requirement for the submission of an article.

1. SUBMISSION CRITERIA

All articles submitted for consideration for publication must meet the following submission criteria:

- » Only original and unpublished articles are accepted. The content of the articles must not have been published, totally or partially, in another journal or publication.
- » Articles must be sent in Word format by the web page <https://revistas.sgc.gov.co/index.php/boletingeo>, in the “Submit article” tab.
- » The title, in Spanish and English, should be concise and reflect the subject matter.
- » The name, the complete institutional affiliation of each author, and the email of the corresponding author must be included.
- » The abstract and keywords must be included in both Spanish and English. Images must be attached as individual graphics files, with a minimum resolution of 300 dpi.
- » If acknowledgments, acknowledgments to entities, publication permits, etc., are required, they should be included at the end of the text and before the references.
- » The text must comply with the references and style requirements indicated in the editorial standards.

2. EDITORIAL GUIDELINES

a. Tables

Tables must be submitted in an editable format, not as images, and they must be accompanied by an explicit legend and source. They must be referenced in the text, and they must be essential to explain or further support the argument of the article.

b. Figures

Figures, such as diagrams, photographs or maps, should be sent in graphics files with a minimum resolution of 300 dpi. Each figure must be cited in the text and be accompanied by an explanatory legend that includes the source.

Images from sources other than the authors of the article must have the permission from the authors of the original image, be free of copyright conflicts or have a Creative Commons license (for further information, please refer to: <https://co.creativecommons.org/>). Maps, aerial photographs and satellite images should include a graphic scale.

c. Citations

The citation format of *Boletín Geológico* is APA style (Seventh Edition). In the text, citations must include the author's name and date of publication, and all references must be listed in the references section.

When several works by the same author are cited, they must be organized in chronological order and will be shown separated by a comma: (Groat, 2014).

When a reference has two authors, the surnames of both authors must be cited and separated by the conjunction “&”: (Pokrovski and Dubessy, 2014) or Pokrovski and Dubessy (2014).

When the reference has three or more authors, only the first author must be cited, followed by the abbreviation “et al.”: (Feneyrol et al., 2013) or Feneyrol et al. (2013).

In the case of a corporate author, the name of the organization must be written the first time with the acronym in parentheses, followed by the year; subsequently, only the acronym will be mentioned (Servicio Geológico Colombiano (SGC), 2017).

When citing several references, they must be chronologically sorted and separated by semicolons: (Mantilla et al., 2013; Van der Lelij et al., 2016; Rodríguez et al., 2017). When a specific page of a reference is cited, the page number must be included after the year and be preceded by the abbreviation p., or pp. in the case of several pages: (Groat, 2014, p. 48).

d. Quotes

When the quote is shorter than forty words, it must be written within the paragraph, in quotation marks and without italics. The reference must be included at the end of the quote (Groat, 2014, p. 48).

When the quote is longer than forty words, it must be written in a separate paragraph, with a 2.5-cm left indent, without quotation marks or italics and with a font size one point smaller than the body text. The reference must be included at the end of the quotation (Groat, 2014, p. 48).

e. References

According to the APA format, only the first letter (initial) of the first names of the authors is provided. In the case where two surnames are included, they must not be separated by a hyphen. References must be written in single-space format and with a 1-cm hanging indent (in a hanging indent, the first line of the paragraph is not indented, and all subsequent lines are indented, in this case, 1 cm). If the documents have a Digital Object Identifier (DOI), this identifier must be included at the end of the reference.

Books

Only the first letter (initial) of the first word and of proper names, if any, in the titles of books are capitalized. The titles should be italicized, and the subtitle separated from the title by a colon, not by a period. In Spanish, the first letter of a word following a colon is written in uppercase font; in English, this letter is capitalized.

The information provided must strictly match that included in the following examples and follow the same rules of punctuation between each element of the reference:

Lee, M. S. (2012). *Mass Spectrometry Handbook* (Vol. 1). Wiley.

Bormann, P. (2013). *New Manual of Seismological Observatory Practice 2 (NMSOP-2)*. Deutsches GeoForschungsZentrum. https://doi.org/10.2312/GFZ.NMSOP-2_DS_3.1

Book chapters

Book chapters follow the same rules as those of book titles, except for one difference: the titles of book chapters must not be italicized. The title of the book must be italicized and preceded by the preposition “In”.

The information provided must strictly match that included in the following examples and follow the same rules of punctuation between each element of the reference:

Horstwood, M. (2008). Data reduction strategies, uncertainty assessment and resolution of LA–(MC–) ICP–MS isotope data. In P. Sylvester (Ed.), *Laser ablation–ICP–MS in the Earth Sciences: Current practices and outstanding issues*. Mineralogical Association of Canada.

Reimann, C., Birke, M., Demetriades, A., Filzmoser, P., & O'Connor, P. (2014). The gemas project - concept and background. In C. Reimann, A. Demetriades, M. Birke, & I. Schoeters (Eds.). *Chemistry of Europe's Agricultural Soils, Part A*. Bundesanstalt für Geowissenschaften und Rohstoffe.

Journal articles

Titles of journal articles follow the same rules as those of titles of book chapters, except for one difference: the first letters of all meaningful words (first word, names, verbs and adjectives) of titles of journal articles must be written in uppercase font and italicized, but they must not be preceded by the preposition “In”.

The information provided must strictly match that included in the following examples and follow the same rules of punctuation between each element of the reference:

Domeier, M., & Torsvik, T. (2014). Plate tectonics in the late Paleozoic. *Geoscience Frontiers*, 5(3), 303-350. <https://dx.doi.org/10.1016/j.gsf.2014.01.002>

Konstantinou, K. (2015). Tornillos modeled as self-oscillations of fluid filling a cavity: application to the 1992-1993 activity at Galeras volcano, Colombia. *Physics of the Earth and Planetary Interiors*, 238, 23-33. <https://dx.doi.org/10.1016/j.pepi.2014.10.014>

Thesis works

Saylor, J. (2008). *The Late Miocene Through Modern Evolution of the Zhada Basin, South-Western Tibet* (Ph. D. Thesis). The University of Arizona, Tucson.

Conferences, seminars and others

The titles of talks given in these contexts are written without italics, and only the first letter of the first word and proper nouns, if included, are capitalized. All meaningful words in event names are capitalized.

The information provided must strictly match that included in the following example and follow the same rules of punctuation between each element of the reference:

Sulochana, V., Francis, A., & Tickle, A. (2015). Morphology based radon processed neural network for transmission line fault detection. 2015 International Conference on Advances in Computing, Communications and Informatics (ICACCI).

Maps

The information provided must strictly match that included in the following example and follow the same rules of punctuation between each element of the reference:

Bacchin, M., Miligan, P. R., Wynne, P., & Tracey, R. (2008). *Gravity anomaly map of the Australian region, 3rd edn, 1:5,000,000*. Geoscience Australia.

Web pages

EURACHEM/CITAC. (2016). *Guide to quality in analytical chemistry an aid to accreditation*. Retrieved from www.eurachem.org

Suggested links

- » Keywords in the Geosciences: <https://www.americangeosciences.org/georef/georef-thesaurus-lists>
- » Creative Commons: <https://co.creativecommons.org/>



Alta Guajira, Colombia. Autor: Patarroyo.

CONTENTS

- 3 Editorial**
Mario Maya
- 7 Historical memory of the geology of Antioquia: Emil Grosse and The Carboniferous Tertiary of Antioquia**
Felipe Velásquez Ruiz, Marion Weber Scharff, Verónica Botero Fernández
- 41 Analytical solution of CO₂ mass flux measurement with Non-Dispersive Infrared sensors for soil in diffusive and advective-diffusive regime: Tool for the continuous and telemetric measurement of volcanic gases in an open chamber**
Nicolás Oliveras
- 61 The role of Rare Earth Elements in the deployment of wind energy in Colombia**
Carlos Andrés Gallego
- 81 Geological modeling of a hydrocarbon reservoir in the northeastern Llanos Orientales basin of Colombia**
Laura Juliana Rojas Cárdenas, Indira Molina
- 95 Relevant aspects to the recognition of extensional environments in the field**
Ana Milena Suárez Arias, Julián Andrés López Isaza, Anny Julieth Forero Ortega, Mario Andrés Cuéllar Cárdenas, Carlos Augusto Quiroz Prada, Lina María Cetina Tarazona, Oscar Freddy Muñoz Rodríguez, Luis Miguel Aguirre Hoyos, Nelson Ricardo López Herrera
- 107 Yuruma Formation (Barremian - lower Aptian?) In the Yuruma hill and Punta Espada, Alta Guajira, Uribia, Colombia**
Pedro Patarroyo
- 131 Seismic hazard assessment of the urban area of Ambato, Ecuador, in deterministic form**
Roberto Aguiar Falconi, Paola Serrano Moreta

